DECAY ANOTHER DAY

SEARCH OF HIGGS PRODUCTION WITH DECAY INTO THE Z BOSON AND A PHOTON IN PP COLLISIONS WITH THE ATLAS DETECTOR AT THE LHC

Proefschrift

ter verkrijging van de graad van doctor
aan de Radboud Universiteit Nijmegen
op gezag van de rector magnificus prof. dr. J. H. J. M. van Krieken,
volgens besluit van het college van decanen
in het openbaar te verdedigen op woensdag 27 oktober 2021
om 10:30 uur precies

door

NADEZDA PROKLOVA

geboren op 26 mei 1992
te Komsomolsk, Oekraïneë

PROMOTOREN	Prof. dr. N. DE GROOT Prof. dr. A. ROMANIOUK (MEPhI, Rusland)
COPROMOTOR	Dr. T. ÇUHADAR-DÖNSZELMANN (UCI, Verenigde Staten)
MANUSCRIPTCOMMISSIE	Prof. dr. S.J. DE JONG Prof. dr. M. KHLOPOV (MEPhI, Rusland) Dr. E. SOLDATOV (MEPhI, Rusland) Prof. dr. Th. PEITZMANN (Universiteit van Utrecht) Dr. H. SNOEK (Universiteit van Amsterdam)

DECAY ANOTHER DAY - Search of Higgs production with decay into the Z boson and a photon in pp collisions with the ATLAS detector at the LHC
Thesis, Radboud University Nijmegen

Cover design by Sergey Moskvin
Printing: Ipskamp Printing

Contents

Introduction

“Knowledge, absolutely sure of its infallibility, is faith."

- Yevgeny Zamyatin, *We*

There is a long-standing question of what one can believe in, or more what belief should be based on when it comes to the understanding of nature surrounding us. The belief in the way natural phenomena happen often starts with the observation and further development of some initial idea with the help of certain expectations based on the current knowledge. Centuries of philosophical research showed that belief has to be rather replaced by the objective truth, which, in turn, evolved into certain principles. The way of looking for the truth in natural science is the subject to the so-called *scientific method*, which defines a set of ethical principles and rules to help correctly explore the world and understand the laws of nature. Generally accepted rules in the modern scientific community include the formation of a hypothesis, which has to be tested on data through experiment. The development of the philosophy of science in the past century added an important condition to the formation of the hypothesis - it has to be falsifiable, meaning it can be contradicted by evidence. This leads to a more concrete idea that a hypothesis is considered scientific only if it can be tested by experiment and its predictions can be disproved through that test.

The search for the truth is a continuous, long process, where laws of Nature can be finally defined through means of theories. After the initial stage of formation, they start to get developed through time and extend into different domains with the help of the new falsifiable hypothesis, based on the same principles and ideas. One can compare the development of most of the modern scientific theories to the growth of an onion core, containing initial theoretical assumptions. It then gets new layers of expendable hypotheses and discoveries, which enhance and support the core. However, sometimes it also happens, that the theory can grow a set of critical anomalies, which can no longer be explained by it. A so-called "paradigm shift" happens when a proposal to the new theory appears, which can both replace the old theory and explain those anomalies. This has been formulated by Th. Kuhn and I. Lakatos (latter by using the term of "research programme" replacement), and recent cases include the transition from Newtonian gravity to general relativity and replacement of classical mechanics at microscopic scales with quantum mechanics.

The formation of the prediction of the hypothesis is followed by its testing through experiment and completed with the statistical analysis of the collected data. For example, many of the modern research programmes in particle physics are performed at CERN’s Large Hadron Collider (LHC). One of the main approaches in conducting experiments to minimise possible human bias (among minimisation of the other possible errors) is blinded data analysis. The bias can happen due to participants’

expectations of what the evidence data might look like. Such blinding is widely used in searches for new particles. The unblinding of the data happens typically after the analysis is complete and evidence can be claimed or not.

The best tested and most thoroughly developed theory in particle physics is the Standard Model, which describes interactions between matter and provides the classification of elementary particles. Its formation, over time, included a high precision theoretical description with a successful experimental confirmation. One of the main missing blocks in its description was the experimental proof (or exclusion) of the Higgs boson - an elementary particle, which was thought to be responsible for the origin of other particles' masses through the Higgs mechanism. On July 4th 2012, the ATLAS and CMS collaborations announced the observation of a particle, which was later confirmed to have the expected behaviour of the Higgs boson.

The Standard Model proved to describe certain laws of nature at an unprecedented level. It however leaves some open questions in its construction. Being the theory that unites electromagnetic, weak, and strong interactions, it fails to provide satisfactory unification with the last missing interaction - gravity, which is currently described by general relativity. Other problems include matter-antimatter asymmetry, description of the Dark Energy, and Dark Matter. It is possible to assume that the Standard Model is a subset of a larger theory, which could adopt all of its anomalies, and it would be possible to observe another paradigm shift.

Besides, it has not yet been determined if the Higgs boson is indeed the particle, described by the Standard Model. To definitely establish the Higgs mechanism, it is necessary to check all of its possible properties, one of such property being all of the decay channels, predicted by the Standard Model. Any possible deviation leads to Beyond Standard Model (BSM) theories, which are intended to expand the Standard Model theory. BSM theories predict, in many cases, the existence of new particles, which can be possibly found at the LHC. Many BSM theories provide an encouraging completion of the Standard Model. However, no such theories have yet been confirmed.

One of the ways to both precisely test Standard Model predictions and BSM theories is to search for the rare Higgs boson decay channels at the LHC. Decays mediated through loop diagrams, such as $H \to Z\gamma$, can be sensitive to any changes in their branching ratios due to the existence of new particles in loop-induced processes. In particular, the $H \to Z\gamma$ decay channel, which remains still unobserved at the LHC, has a relatively small branching ratio predicted to be $B(H \to Z\gamma) = (1.54 \pm 0.09) \times 10^{-3}$. Leptonic final states (electron or muon) of the Z boson decay are of particular interest because they provide a clear signal with a good invariant mass resolution, with a small background from pp collisions.

The first attempt to measure the $H \to Z\gamma$ decay by the ATLAS collaboration was in Run-1 of the LHC, at the centre-of-mass energy of $\sqrt{s} = 7$ TeV and 8 TeV, with a small subset of data collected at 13 TeV during Run-2 of the LHC. With all data combined, no significant excess above the expected background was observed. The next attempt of the search is presented in this thesis, using 139 fb^{-1} of the collected data during Run-2 of the LHC at $\sqrt{s} = 13$ TeV. There are several improvements concerning the first attempt, one of the main ones is coming from the newly proposed analysis strategy, which includes enhanced event categorisation and optimised lepton and photon identification criteria. Other major improvements come from the increased production cross-section and size of the dataset compared to Run-1.

In addition to physics analysis, the current thesis includes detector-based studies and performance studies, with the main focus on photons. The first part is dedicated to the calibration of the performance of the Transition Radiation Tracker (TRT), one

of three sub-detectors of the ATLAS Inner Detector. The detector's precise calibration is necessary for the studies, presented later in the thesis, as the TRT plays important role in the charged particle identification, such as electrons. Electrons are used, for example, in Z boson identification (with the decay to $Z \to ee$), and in photon identification, in cases where a photon can convert to a pair of electrons in the TRT detector material. The second part of the thesis includes photon performance studies, where the efficiency of the identification of photons is estimated using radiative Z decays. Photons are involved in various Standard Model analyses, such as searches for Higgs boson decays into two photons or to $Z\gamma$, and in many BSM searches (for example, anomalous triple and quartic gauge couplings). Results of the photon studies are implemented in the last chapter of the thesis for the search of the $H \to Z\gamma$ decay.

Outline

Chapter 1 presents a brief overview of the Standard Model, along with Higgs phenomenology, Higgs production modes, and decay channels. In addition, some of the Beyond Standard Model theories are reviewed. The chapter provides the theoretical background for the rest of the thesis. Chapter 2 describes of the LHC and the ATLAS detector, which is necessary to carry the experiment and to obtain data for the analysis. The summary is based on the Technical Design Reports. Chapter 3 gives a more detailed description of the TRT detector and its performance. Chapter 4 reviews the reconstruction algorithms, necessary for the correct definition of the physics objects of the analysis, such as electrons, photons, muons, and jets. The chapter focuses on the reconstruction of objects from the initial detector information, calibrations techniques, and final identification of the particles. Chapter 5 presents studies of the photon reconstruction at the low energy scale, using photon from radiative Z boson decays. Finally, chapter 6 describes the search for the Standard Model Higgs decaying into a Z boson and a photon, where the Z boson decays either to an electron or muon pair.

Personal contribution

Research programmes conducted in the field of elementary particle physics are carried out in collaborations in present day. Therefore, the work, presented in the thesis is the result of the collaboration of many people from different areas of expertise. Several chapters of the thesis include leading personal contributions to the analyses carried out by the ATLAS collaboration, and they are presented below.

Chapter 3: TRT performance studies. The results presented in the following chapter are obtained by me as the main analyser for my qualification task. For the first part of the chapter (Sec. 3.2) I performed tuning of the TRT digitisation to improve data to simulation agreement for several run periods and detector configurations. The second part of the chapter (Sec. 3.3) presents my studies on dE/dx performance, where I validated the choice of the algorithm for dE/dx estimator in low pile-up conditions and provided checks for high pile-up conditions.

Chapter 4: Object reconstruction algorithms. For the following chapter, I participated as one of many analysers, working on object reconstruction. My notable contribution is presented in Sec. 4.1.8, 4.1.9 and includes optimisation of the photon identification criteria for low energy scale photons for the analysis $H \to Z\gamma$ and studies of photon isolation variables.

Chapter 5: Photon performance studies with Radiative Z decays. I was providing the performance studies of low energy photons as the sole analyser during the whole time of my PhD. The chapter presents my latest results, published in [1], on the photon efficiency measurements, obtained for two different methods of photon identification - identification based on calorimeter shower shape variables, and isolation. I developed a new method of background estimation necessary to obtain a clean sample of photons and performed the comparison of data to simulation predictions. I provided the corrections of the simulated data for low energy photons, which are currently used as part of the official recommendations on systematic uncertainties on photon identification and isolation for all of the physical analyses involving photons in ATLAS collaboration.

Chapter 6: Search for the Higgs boson in the $H \to Z\gamma$ channel. I contributed to the analysis as one of the two main analysers. I proposed and validated a new strategy for the photon selection criteria, performed optimisation of the lepton selection criteria (Sec. 6.3). Next, I refined the strategy for the event categorisation and developed a new one, based on several methods of neural network (Sec. 6.4). I performed the calculation of the background contamination in the $H \to Z\gamma$ process (Sec. 6.5.2), signal modelling used in the final results (Sec. 6.5.1) and calculation of the theoretical uncertainties (Sec. 6.6.3). Finally, I contributed to the writing and editing process of the paper, published in [2].

1 Theory and motivation

The following chapter provides the theoretical background necessary for the understanding of the search presented in the thesis. The main focus will be on the Electroweak sector and Higgs boson physics in the framework of the Standard Model. Prospects of a search for the rare Higgs boson decay mode $H \rightarrow Z\gamma$ are presented. The additional motivation of this search comes from the possibility of finding hints of physics beyond the Standard Model. Several models describing this are presented.

1.1 The Standard Model of particle physics

The Standard Model (SM) of particle physics describes the basic structure of matter and its interactions through the fundamental forces. All of the predictions of the theory have been confirmed with the high precision by numerous experiments. In general, the SM describes the fundamental forces as the electromagnetic interaction (this theory is called quantum electrodynamics, QED), the strong interaction (quantum chromodynamics, QCD), and the weak interaction, which unifies with electrodynamics at higher energies. Matter in the SM is described in terms of fermions, which obey Fermi-Dirac statistics. The SM describes mediators (force carriers) of all of the interactions, which are called bosons and which obey Bose-Einstein statistics.

The quarks and leptons (fermions) are classified into three by structure identical generations of particles with different masses. Particles with integer electric charge include the electron (e), which is the lightest charged particle, followed by the muon (μ) and tau (τ) leptons. These leptons interact under weak and electromagnetic forces, and are paired with a chargeless lepton of the same flavour called a neutrino (ν_e, ν_μ and ν_τ). Quarks are particles with fractional electric charges (+2/3e or -1/3e) and have an additional colour charge, related to their strong interaction (they also experience weak and electromagnetic interactions), which binds them together inside colourless particles (hadrons). In addition, an anti-particle with the opposite quantum numbers corresponds to each fermion.

All of the fundamental interactions have one or more associated mediators:

- The electromagnetic interaction is carried by the photon (γ), a massless particle with no electrical charge.
- The strong interaction, which binds quarks together to form protons, neutrons or other particles, is mediated by gluons (g). Quarks are the only fermions carrying colour charge (so-called "red, green and blue") [3], and gluons carry

a colour charge too with at the same time an anti-colour. Gluons are massless and electrically neutral.

- The weak interaction is responsible for some nuclear decays such as β decay, and is mediated by the massive, electrically charged $W^{\pm}$ and electrically neutral Z bosons.

- The gravitational interaction currently is not included in the Standard Model. It is the weakest of all the fundamental forces ($\sim 10^{38}$ times weaker than the electromagnetic force).

It is important to note that the Higgs boson, which was recently discovered, is not considered as the mediator of any fundamental force. The Higgs boson however, corresponds to an excitation of the Higgs field, which is responsible for all the masses of the particles.

The Standard model is described as a quantum field theory based on the principle that physics is invariant under local symmetry transformations (so-called gauge symmetry). The combination of local gauge symmetry groups provides the framework for the description of the electromagnetic, weak and strong interactions: $SU(2)_L \otimes U(1)_Y \otimes SU(3)_C$ [4, 5, 6]. The transformation properties with respect to these symmetries determine the interactions of the particles. The conserved properties of each transformation are weak isospin (I), weak hyper-charge (Y) and colour (C).

The Electroweak theory (EW) (proposed by Glashow, Salam and Weinberg [7, 8]) describes the electromagnetic and weak interactions between quarks and leptons. It is based on the gauge symmetry group $SU(2)_L \otimes U(1)_Y$ and involves four massless mediating bosons: three bosons belong to the non-abelian group SU(2) and one isoscalar (I = 0) which belongs to the abelian U(1) group of weak hypercharge.

The spontaneous breaking of the electroweak symmetry (EWSB) is generated with an additional scalar SU(2) doublet. Through this EWSB mechanism, three of the gauge bosons acquire masses; the remaining neutral scalar field is called the Higgs field.

The Quantum Chromodynamic theory (QCD) is based on the gauge symmetry group $SU(3)_C$ and describes the strong interaction between the coloured quarks with gluons being the generators of the $SU(3)_C$ group [9, 10].

Fig. 1.1 gives a scheme of the particles with their properties, such as their charge, mass and spin.

1.2 Gauge symmetries in Quantum Electrodynamics

Quantum electrodynamics (QED) is the field theory which describes the interaction between spin 1 particles and charged particles (fermions), based on the local gauge symmetry. The QED symmetry group is the abelian $U(1)$ group, and a gauge transformation ($U(1)$ transformation) is an arbitrary phase applied to the state function of the system

$$\psi(x) \rightarrow e^{ie\phi(x)}\psi(x), \tag{1.1}$$

where ψ is a Dirac spinor, which can represent the fermion excitation of its field. Since ϕ phase depends on a space time coordinate, the transformation is defined as local. The Lagrangian describes the theory for a free spinor ψ

$$\mathcal{L}_{Dirac} = \bar{\psi}(i\gamma_\mu \partial^\mu - m)\psi, \tag{1.2}$$

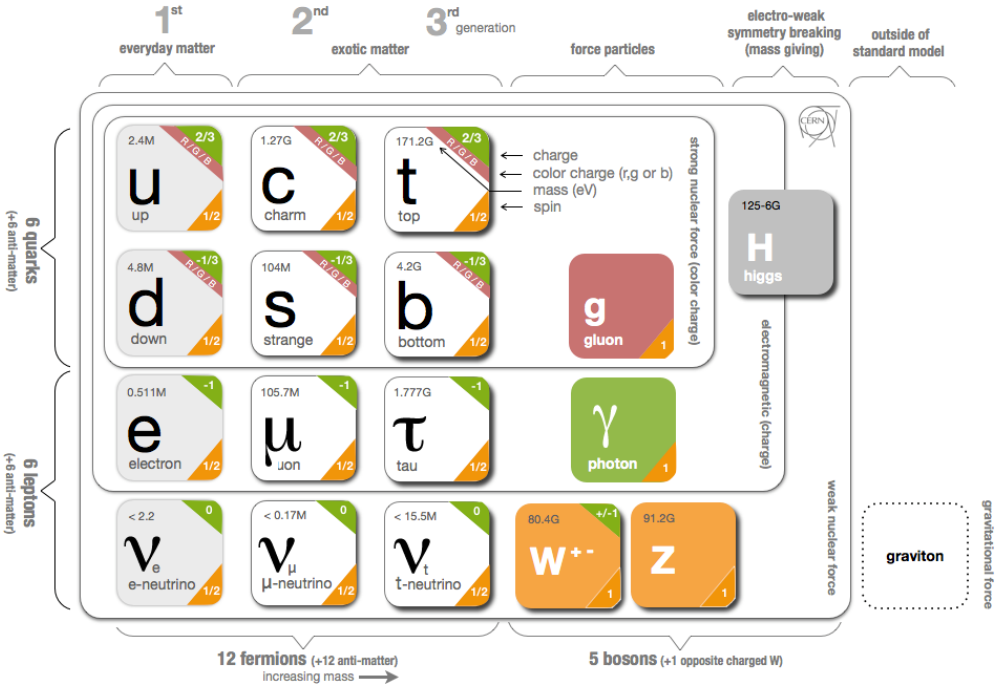

FIGURE 1.1: Standard Model particles scheme, divided into the three generations of fermions: leptons and quarks; and the gauge bosons. The properties of the particles are shown, such as electrical charge, colour, mass and spin [11].

where γ^μ are the Dirac matrices and m is the mass of the Dirac fermion with spin 1/2. The Lagrangian would be invariant under a global $U(1)$ transformation with ϕ phase being an arbitrary real constant. However, considering the locality of the gauge transformation, the Lagrangian in Eq. 1.2 is not invariant under the transformation, as shown below

$$\partial_\mu \psi \rightarrow e^{ie\phi(x)}(\partial_\mu + ie\partial_\mu)\psi. \tag{1.3}$$

In order to restore the gauge invariance under the local $U(1)$ transformation, it is necessary to introduce a vector field A^μ, which is an element of the $U(1)$ algebra. This field transforms as

$$A_\mu(x) \rightarrow A'_\mu(x) = A_\mu(x) + \frac{1}{e}\partial_\mu \phi. \tag{1.4}$$

Next the covariant derivative is defined as

$$D_\mu = \partial_\mu - ieA_\mu, \tag{1.5}$$

which transforms as

$$D_\mu \psi \rightarrow D'_\mu \psi = e^{ie\phi} D_\mu \psi. \tag{1.6}$$

The Lagrangian for a vector field A^μ associated with a spin 1 particle is

$$\mathcal{L} = -\frac{1}{4}F^{\mu\nu}F_{\mu\nu} + \frac{1}{2}m_A^2 A^\mu A_\mu, \tag{1.7}$$

where $F^{\mu\nu} = \partial^\mu A^\mu - \partial^\nu A^\nu$ is the field kinetic term. The fist term of the Lagrangian is invariant under local $U(1)$, the second term is not invariant. In order to keep the local gauge invariance the vector field has to be massless ($m_A = 0$). The new gauge-invariant Lagrangian is the following

$$\mathcal{L}_{QED} = \bar{\psi}(i\gamma_\mu \partial^\mu - m)\psi + e\bar{\psi}\gamma^\mu \psi A_\mu - \frac{1}{4}F^{\mu\nu}F_{\mu\nu}. \tag{1.8}$$

The new Lagrangian describes the interaction between Dirac (fermion) fields and the photon field (represented by the vector field A^μ), for which a mass term is not allowed.

1.3 Electroweak theory and the Higgs mechanism

1.3.1 Electroweak theory

Electroweak theory provides the unification for the weak and electromagnetic interaction. It is based on the gauge symmetry group $SU(2)_L \otimes U(1)_Y$, where the conserved quantities are the weak isospin (I) associated with the $SU(2)_L$ group and the weak hypercharge (Y) in the $U(1)_Y$ group. These quantities are connected to the electric charge Q by the Gell-Mann–Nishijima formula

$$Q = I_3 + Y/2, \tag{1.9}$$

where I_3 is the third component of the weak isospin.

Electroweak theory is a gauge invariant theory with three W^i_μ guage fields associated to the $SU(2)_L$ symmetry and one gauge field B_μ associated to the $U(1)_Y$ symmetry. The B_μ gauge field couples to left and right-handed components of the fermion fields (ψ_L and ψ_R) and W^i_μ field couples only to the left-handed components.

The covariant derivates $D_{\mu L}$ and $D_{\mu R}$ are introduced, which allow to check the electroweak Lagrangian invariance

$$D_{\mu L}\psi_L = (\partial_\mu + ig\frac{\sigma_i}{2}W_\mu^i + ig'\frac{Y_L}{2}B_\mu)\psi_L, \tag{1.10}$$

$$D_{\mu R}\psi_R = (\partial_\mu + ig'\frac{Y_R}{2}B_\mu)\psi_R, \tag{1.11}$$

where g and g' are the coupling constants of $SU(2)_L$ and $U(1)_Y$ groups, σ_i are the Pauli matrices, and Y_R, Y_L are the weak hypercharge for the left and right-handed components of the fermion fields.

The gauge invariant Lagrangian of electroweak theory is

$$\mathcal{L}_{EW} = i\bar{\psi}_L\gamma^\mu D_{\mu L}\psi_L + i\bar{\psi}_R\gamma^\mu D_{\mu R}\psi_R - \frac{1}{4}W_{\mu\nu}^i W_i^{\mu\nu} - \frac{1}{4}B_{\mu\nu}^i B_i^{\mu\nu}, \tag{1.12}$$

where the fist two terms are used for the description of the kinetic terms of the interaction between fermion and gauge fields, last two terms are the gauge field terms with the following

$$W_{\mu\nu}^i = \partial_\mu W_\nu^i - \partial_\nu W_\mu^i - g\varepsilon^{ijk}W_\mu^j W_\nu^k, \tag{1.13}$$

$$B_{\mu\nu}^i = \partial_\mu B_\nu^i - \partial_\nu B_\mu^i, \tag{1.14}$$

where ε^{ijk} are the structure constants of $SU(2)_L$ group. The electroweak gauge bosons γ, Z and $W^\pm$ are linear combinations of the four gauge fields

$$A_\mu = B_\mu cos\theta_W + W_\mu^3 sin\theta_W, \tag{1.15}$$

$$Z_\mu = -B_\mu sin\theta_W + W_\mu^3 cos\theta_W, \tag{1.16}$$

$$W_\mu^\pm = \frac{W_\mu^1 \mp W_\mu^2}{\sqrt{2}}, \tag{1.17}$$

with θ_W which is known as Weinberg's angle or weak mixing angle defined as

$$cos\theta_W = \frac{g'}{\sqrt{g^2 + g'^2}}, \tag{1.18}$$

$$sin\theta_W = \frac{g}{\sqrt{g^2 + g'^2}}. \tag{1.19}$$

The Lagrangian of electroweak theory in Eq. 1.12 does not allow mass terms for either the fermions or the gauge bosons as it would break gauge invariance. However the $W^\pm$ and Z^0 bosons, which are mediators of the weak interaction, are known to have masses. The values of their masses were first measured at the LEP and SLC colliders and were found to be approximately 80 and 90 GeV [12, 13]. The explanation of the masses of the $W^\pm$ and Z bosons was provided by Higgs, Brout and Englert in 1964 with the mechanism of spontaneous symmetry breaking (the Higgs mechanism) [14, 15, 16, 17].

1.3.2 Spontaneous Symmetry Breaking and the Higgs boson

The Higgs mechanism introduces masses and the resulting electroweak symmetry breaking. A doublet of complex scalar fields is introduced

$$\Phi_H = \frac{1}{\sqrt{2}}\begin{pmatrix}\Phi^+\\ \Phi^0\end{pmatrix} = \frac{1}{\sqrt{2}}\begin{pmatrix}\phi_1 + i\phi_2\\ \phi_3 + i\phi_4\end{pmatrix} \tag{1.20}$$

where Φ^+ and Φ^0 are a charged and a neutral field. The scalar field Φ_H is included to the electroweak Lagrangian as

$$\mathcal{L}_H = (D^\mu \Phi_H)^+ (D_\mu \Phi_H) - V(\Phi_H). \tag{1.21}$$

The covariant derivative has the form

$$D_\mu \Phi_H = (\partial_\mu + ig\frac{\sigma_i}{2}W_\mu^i + ig'\frac{Y_{\Phi_H}}{2}B_\mu)\Phi_H, \tag{1.22}$$

and $V(\Phi_H)$ is a potential term defined as

$$V(\Phi_H) = -\mu^2 \Phi_H^+ \Phi_H + \lambda(\Phi_H^+ \Phi_H)^2. \tag{1.23}$$

Fig. 1.2 shows the form of this potential for $\mu^2 < 0$ and $\lambda > 0$, where Φ_H takes a non-vanishing vacuum expectation value. The ground state of the Higgs field is given by the minimum of the potential

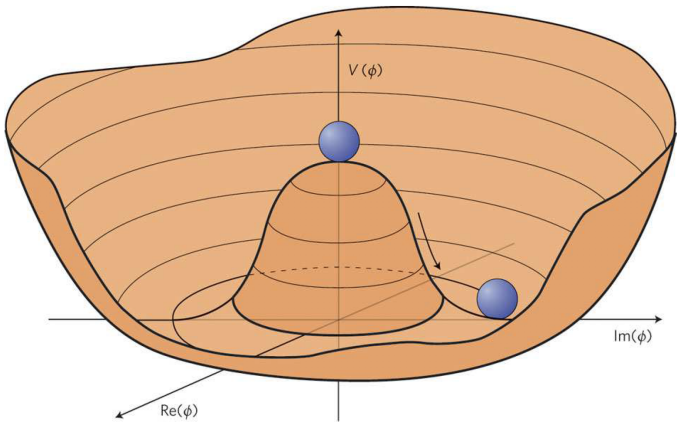

FIGURE 1.2: Higgs potential $V(\Phi_H)$ in the plane $Re(\Phi_H) - Im(\Phi_H)$ [18]

$$\Phi_{min} = \frac{1}{\sqrt{2}}\begin{pmatrix}0\\ \nu\end{pmatrix}, (\phi_1 = \phi_2 = \phi_4 = 0, \phi_3 = \nu) \tag{1.24}$$

where $\nu = \sqrt{\mu^2/\lambda}$ is the vacuum expectation value of the Higgs field.

The Higgs field can be parametrized in polar coordinates using the scalar fields θ_a (a = 1,2,3) and H, with $\langle H \rangle = 0$

$$\Phi_H = \frac{1}{\sqrt{2}} e^{i\sigma^a \theta_a(x)} \begin{pmatrix}0\\ \nu + H(x)\end{pmatrix} \tag{1.25}$$

where θ_i are called Goldstone bosons. These can be absorbed by an opposite gauge

transformation, choosing the so-called unitary gauge. As the three θ_i fields are absorbed by the gauge fields, they form the longitudinal components of $W^{\pm}$ and Z boson, giving them masses.

The Higgs Lagrangian becomes

$$\mathcal{L}_H = \frac{1}{2}\partial^\mu H \partial_\mu H + \left(\frac{g\nu}{2}\right)^2 \frac{W_\mu^+ W^{+\mu} + W_\mu^- W^{-\mu}}{2} + \left(\frac{g\nu}{2cos\theta_W}\right)^2 \frac{Z^\mu Z_\mu}{2} - V(\Phi_H), \tag{1.26}$$

which shows a massless photon and massive Z and $W^{\pm}$ bosons, with the mass terms provided by the symmetry breaking. The Z and $W^{\pm}$ boson masses are related via the Weinberg angle (weak-mixing angle) θ_W and with the coupling constants g and g'

$$m_W = cos\theta_W m_Z = g\nu/2. \tag{1.27}$$

The Higgs mass is not predicted by the theory, given that it depends on λ, which is a free parameter

$$m_H = \sqrt{-2\mu^2} = \sqrt{2\lambda\nu^2}. \tag{1.28}$$

Fermions acquire mass through the interaction with the Higgs field in the Yukawa interactions. Considering the measured mass of the fermions it is easy to define the coupling λ_f of the Higgs boson to the fermions by

$$m_f = \frac{\lambda_f \nu}{\sqrt{2}}. \tag{1.29}$$

1.3.3 The Higgs boson mass measurements

One of the free parameters of the theory was the mass of the Higgs boson. There were several attempts to find the Higgs boson and measure its mass, with the last attempt being successful.

The first attempt was performed by the Large Electron-Positron collider (LEP), operating from 1989 to 2000 with a centre-of-mass energy of 91-210 GeV. The Higgs boson was expected to be produced from the radiation by a vector boson. It was excluded with a mass below 114.4 GeV at the 95% confidence level [19].

The second attempt was performed by the Tevatron accelerator, which collided protons and antiprotons at a centre-of-mass energy of 1.96 TeV. The Higgs boson was excluded in 2011 with a mass between 145 and 177 GeV at the 95% confidence level [20].

The most recent results were obtained using the LHC (proton-proton collider), and on July 4th 2012 the Higgs boson discovery was announced by the ATLAS and CMS Collaborations [21, 22]. Fig. 1.3 shows latest results obtained by the ATLAS in 2020 and CMS collaborations in 2021 respectively at $\sqrt{s}$ = 13 TeV.

The most recent result on the combination of measurements of the Higgs boson mass from the ATLAS and CMS collaborations were presented in 2015 for the $H \to \gamma\gamma$ and $H \to ZZ \to 4\ell$ decay channels [25]. These were obtained from a simultaneous fit to the reconstructed invariant mass peaks, with the combined measured mass of the Higgs boson $m_H = 125.09 \pm 0.21(\text{stat.}) \pm 0.11(\text{syst.})$ GeV. Fig. 1.4 shows the summary of the Higgs boson mass measurements from both collaborations.

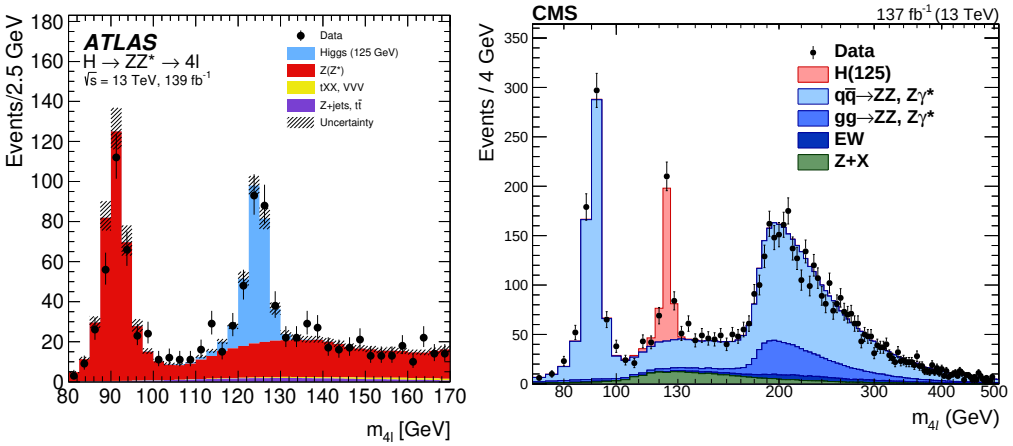

FIGURE 1.3: Left: results obtained by the ATLAS collaboration for the measurement of the four-lepton invariant mass, m_{4l}, shown for data (black dots) for an integrated luminosity of 139 fb^{-1} and at $\sqrt{s}$ = 13 TeV, and compared to the background expectation (filled red, yellow and violet area) in the 80 to 170 GeV mass range. The signal expectation for a SM Higgs with m_H = 125 GeV is also shown (blue) [23]. Right: results obtained by the CMS collaboration for the measurement of the four-lepton invariant mass, m_{4l}, shown for data (black dots) for an integrated luminosity of 137 fb^{-1} and at $\sqrt{s}$ = 13 TeV. The blue and green histograms represent the background, and the red histogram shows the signal expectation for a Higgs boson of mass, added to the background expectation [24].

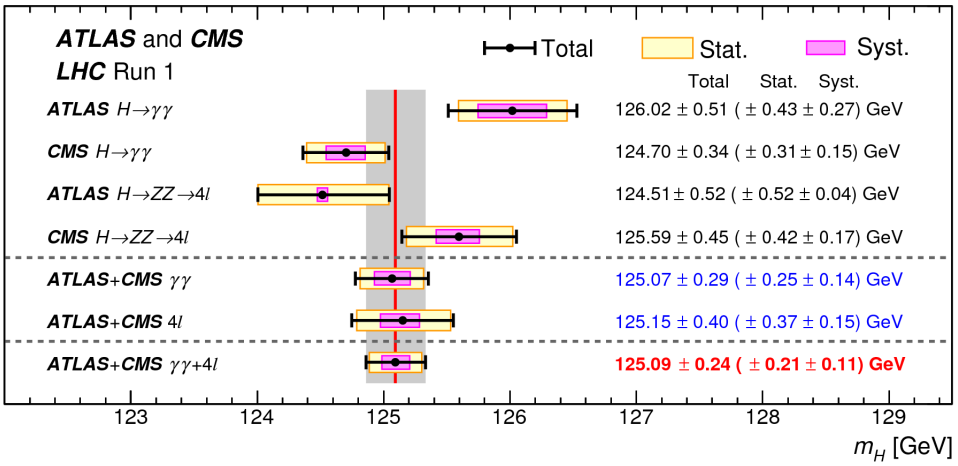

FIGURE 1.4: ATLAS and CMS summary of Higgs boson mass measurements from the individual analyses and from the combined ones. The systematic (narrower, magenta-shaded bands), statistical (wider, yellow-shaded bands), and total uncertainties (black error bars) are indicated. The (red) vertical line and corresponding (gray) shaded column indicate the central value and the total uncertainty of the combined measurement respectively [25].

1.4 The SM Higgs boson at the LHC

The following sections describe properties of the Standard Model Higgs boson at the LHC, such as production modes and main decay channels, with the focus on the $H \to Z\gamma$ decay channel.

1.4.1 Higgs production

The SM Higgs boson mostly couples to heavy particles, such as top and bottom quarks, or to the Z and W bosons. Fig. 1.5 shows the Feynman diagrams of the four main production modes of the Higgs boson in proton collisions.

- Gluon-gluon fusion (ggF) is the dominant production mode where the Higgs boson couples indirectly to gluons via a triangular loop of quarks dominated by the top or bottom quarks.
- Vector-boson fusion (VBF) is the production mode where the Higgs boson is produced by the fusion of two weak vector bosons (W or Z) radiated from quarks. The main contribution comes from the W bosons due to enhanced coupling to quarks comparing to the Z bosons. The two final energetic quarks fragment into two jets, located mostly in the forward and backward regions of the detector, with the Higgs boson decaying in the central region. Between the two jets no additional hadron activity is expected, thus leaving a special signature in the detector that can be used to suppress additional background coming from jets.
- Higgsstrahlung (WH or ZH) is the production mode where the Higgs boson is produced in the associated production with W or Z vector bosons. Since W or Z bosons are part of the final state event, it is normally possible to easily separate this type of the event from the background.
- Associated production with top quarks (ttH) is the production mode where the Higgs boson is produced in association with top quark pairs. It is the smallest contribution to the LHC Higgs production due to it having the lowest cross-section, but is an important process for the direct measurement of the Higgs coupling to the top quark.

Fig. 1.6 shows the Higgs cross-sections in different production modes for different centre-of-mass energies and for the fixed centre-of-mass energy of 13 TeV in a window around the Higgs mass. As can be seen, all the production modes are rising with the centre-of-mass energy, in particular between 8 and 13 TeV which are the LHC Run-1 and Run-2 periods.

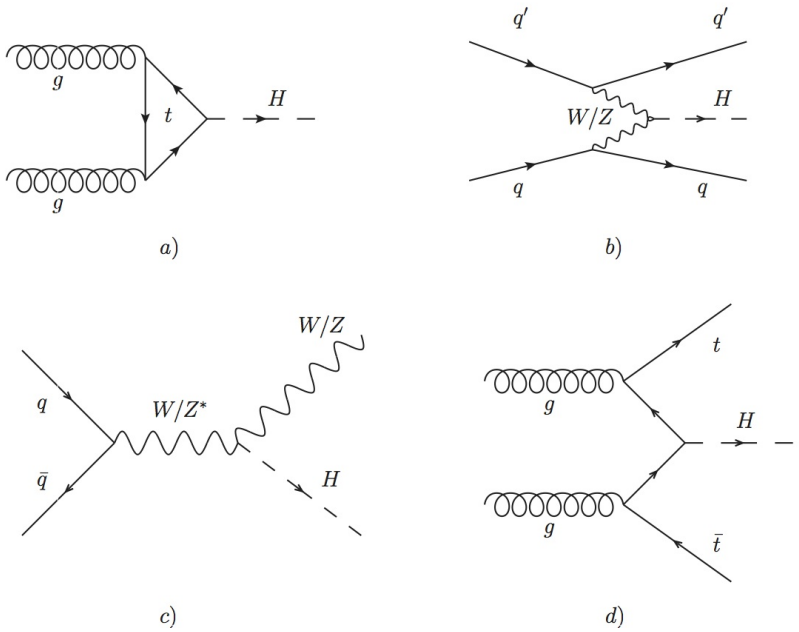

FIGURE 1.5: The main SM Higgs boson production modes in proton collisions. The gluon-gluon fusion (a), the vector boson fusion (b), the associated production with electroweak vector bosons W or Z (c) and the production in association with top pairs (d).

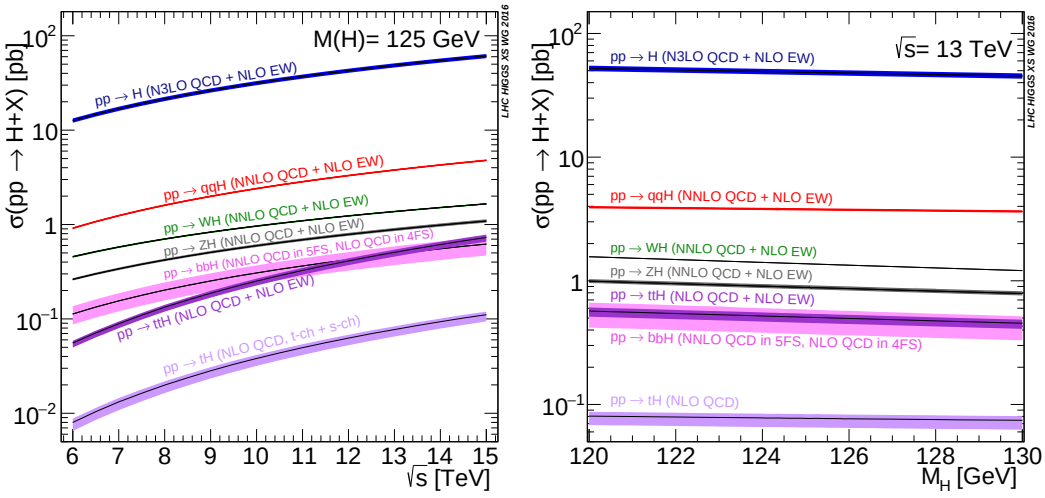

FIGURE 1.6: Left: Higgs cross-section for the main production modes as a function different centre-of-mass energies. Right: Higgs cross-section for the main production modes as a function of the Higgs mass for the centre-of-mass energy of 13 TeV [26]

1.4.2 The Higgs decay modes

The Higgs boson decays into fermions or bosons, and only by the measurement of its products it is possible to recover the information about the presence of a Higgs boson in the detector. The probability of the decay is proportional to the product's mass, meaning that heavier particles decay more quickly. Fig. 1.7 shows the Higgs branching ratios (BR) as a function of its mass [26]. The following probabilities of certain decays are:

- The highest number of decays can be seen with the Higgs boson decay into a $b\bar{b}$ pair in 57% of cases, due to the fact that decay into a pair of top quarks is kinematically forbidden (the mass of the top quark is higher than mass of the Higgs boson). This channel has low sensitivity at the LHC due to the production of the two jets from bottom quarks and overlapping large QCD background coming from pp collisions;
- The decay into WW pair happens in 22% of cases. Another decay into bosons being ZZ pair happens in around 2.7% of cases. This decay gives excellent resolution - the presence of four electrons or muons in one event creates a unique signature in the detector;
- The decay into a $\tau^+\tau^-$ pair has high BR as well (around 6% of cases), but it has a high background due to the $Z \to \tau^+\tau^-$ decay process. Nevertheless it is important channel as it allows to test the coupling with leptons;
- Both decays into a pair of photons or Z boson and a photon have BRs of the same order (10^{-3}). They both can be reconstructed with high resolution and have strong background suppression. $Z\gamma$ decays are described in more details below.

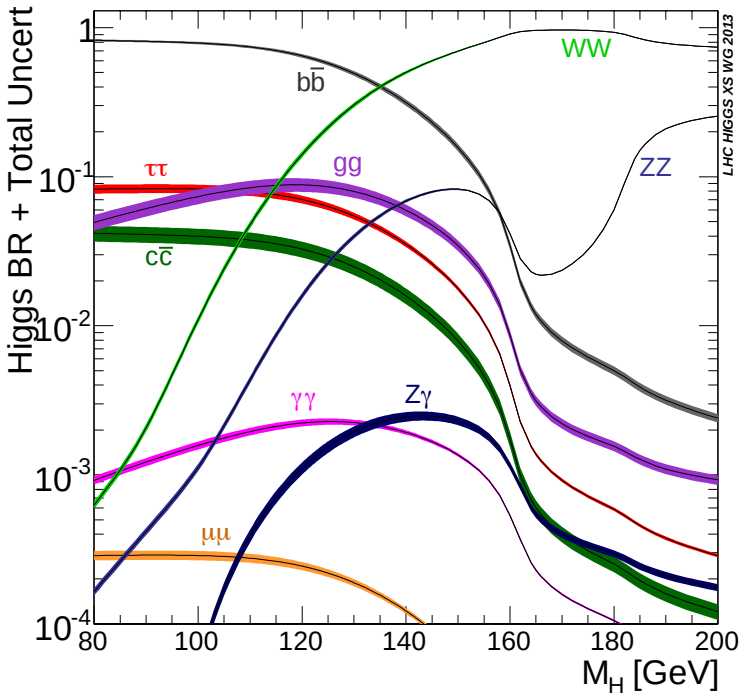

FIGURE 1.7: Higgs boson decay branching ratios as a function of the Higgs boson mass hypothesis [26].

The $H \to Z\gamma$ decay channel

The main topic of this thesis is the search for the rare decay $H \to Z\gamma$ in the ATLAS detector. This decay is mediated by loops via W bosons in most of the cases, and can also proceed via fermion loops dominated by top quarks, as is shown in Fig. 1.8.

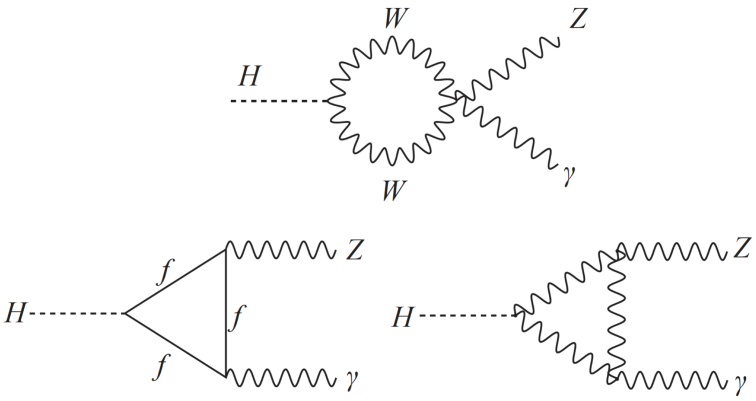

FIGURE 1.8: Feynman diagrams for the $H \to Z\gamma$ decays.

Higgs boson decays to both $\gamma\gamma$ and $Z\gamma$ have similar BR - 0.23% in case of the photon pair and 0.16% in case of the Z boson and photon decay. However, in order to have the clean signature required by the analysis, only the Z boson decays into a pair of electrons and muons are selected. The Z boson decay into a pair of tau leptons is not considered for the analysis since tau lepton decays mostly hadronically and this channel is dominated by large backgrounds. The choice of Z boson decays only into electrons or muons gives a lower branching ratio of the order of 10^{-4}, but can be reconstructed in the ATLAS detector with good energy resolution and high efficiency. In addition, the invariant mass can provide excellent way of signal to background separation - in case of Higgs boson it is expected to be distributed as narrow peak, while the background should be presented as smoothly falling distribution. The main background consists of the irreducible $Z\gamma$ background, which has the same final states as the signal, and reducible $Z + jets$ background, caused by jets misidentified as photons in the detector material. The dominant $Z\gamma$ background final states are shown in Fig. 6.2.

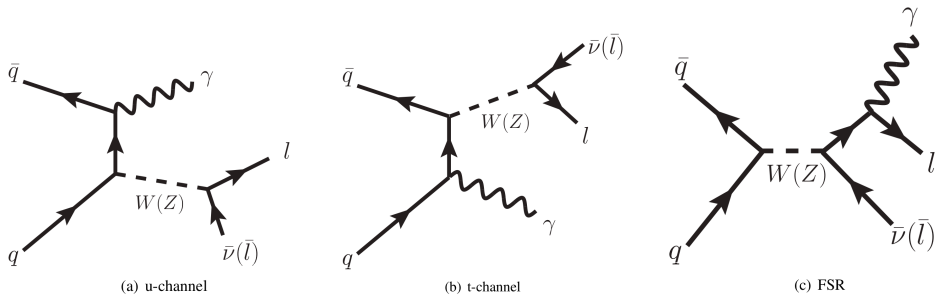

FIGURE 1.9: Feynman diagrams for the Z boson and photon production.

As was mentioned, in the Standard Model the $H \to Z\gamma$ decay is a rare decay induced by loop diagrams. Due to this fact, the channel is considered as sensitive to the new physics, as any new charged particle coupling to the Higgs boson could contribute to the loops and lead to changes in the decays rates. One model is described in

more detail in the next section, as well as some additional models which can provide hints to physics beyond the Standard Model.

1.5 Physics beyond the Standard Model

Currently, the Standard Model is a well developed model which effectively describes the phenomena at the electroweak scale. It provides an excellent description of the results observed by the experiments. However it has several problems and does not give answers to some questions, among which there are:

- The gravitational force is not described by the SM, whereas it becomes very important at high energies;
- The matching number of three generations of quarks and leptons with very different mass scales is not explained by the SM;
- The problem of the the neutrinos masses: in the SM model they are massless, however numerous experiments have confirmed the observation of neutrino oscillations, which implies that they have a mass [27, 28];
- The SM does not provide an explanation for the large amount of the Dark Matter and Dark Energy, nor candidates for them;
- The CP violation, responsible for the matter-antimatter observed asymmetry in the universe is not sufficiently explained [29];

These questions imply that the Standard Model is a low energy limit of a more fundamental theory, which could provide the unification of all four interactions. A set of "Beyond the Standard Model" theories (BSM) propose to extend the SM for that purpose. One of the LHC programs is search for new physics predicted by the BSM theories. The $H \rightarrow Z\gamma$ channel, which is considered in this thesis, can be affected by a few of such BSM theories - it is rare channel, which is highly sensitive to any changes in the decay rates. A brief overview of some of these theories is presented below.

1.5.1 New charged particles at the electroweak scale

The $Z\gamma$ rate could possibly be enhanced due to loop effects from new particles, which are described in some BSM models, in the Higgs decay. One of these thoeries assumes the presence of new colourless charged particles with couplings to the Higgs boson that will add to the dominant SM contribution from the $W^{\pm}$ boson loop [30]. The theory assumes that Higgs boson mass is at 125 GeV, and that the Higgs boson production rate stays the same. The theory considers new particles carrying no colour charge of spin zero, spin one-half and spin one. With the current experimental limits, the existence of additional new particles is possible at the TeV scale. For example, one of the proposed particles is a W' boson, which interferes constructively with the W boson loop and can lead to the enhancement of the width. Fig. 1.10 shows the enhancement in the $Z\gamma$ partial width of the Higgs boson in the case of an additional W' boson. At the LHC it can be search for directly through the pair-production of the W' bosons decaying into four jets plus missing transverse energy. In the case of extra fermions they can be pair-produced via electroweak processes, much like superpartners (for example charginos in supersymmetric theries).

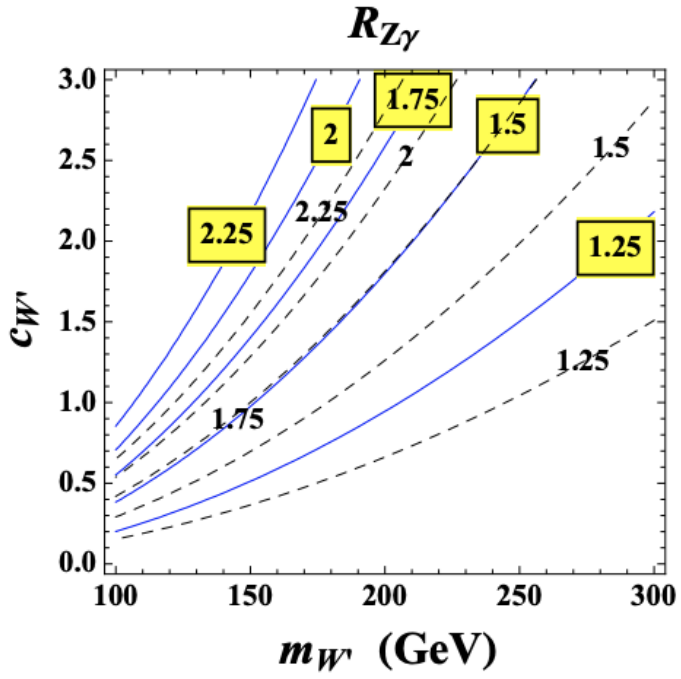

FIGURE 1.10: $Z\gamma$ partial width changes due to a new particle W' boson, normalised to the SM value, shown as a function of coupling strength to the Higgs and the new W' boson mass [30].

One more interesting model with exotic hypercharges is described in [31], where a set of new light vector-like leptons carrying large electric charges, transforming as electro-weak doublets and singlets, is considered. It allows modification of the $Z\gamma$ decay rate without modifying the main production process via gluon fusion, as vector-like leptons can interfere with the W loop contribution. In general, the maximum modification of the rate does not exceed 10%. At the LHC the new vector leptons could be found as mostly pair produced in Drell–Yan processes due to their large hypercharges, with sub-dominant channels being Higgs mediated pair production or through a W boson.

1.5.2 Models with Higgs extensions

There are currently many models with an extended Higgs sector, which often contain charged Higgs bosons that can contribute to the $h \to Z\gamma$ decays through the loop effect. For example, one can assume three classes of extended Higgs sectors: models with one singly-charged scalar boson (Class I), models with one singly-charged and one doubly-charged scalar boson (Class II), and models with two singly-charged scalar (Class III) bosons [32]. Models in Class I include the two Higgs doublet model [33, 34] and the minimal supersymmetric SM. Models in Class II include the Higgs triplet model [35, 36] And, models in Class III can include tiny Majorana neutrino masses that are generated via higher-loop processes [37]. Depending on the chosen model, $Z\gamma$ modes can be modified by a few to a few tens of percent.

The other type of model is described in [38], where a composite Nambu-Goldstone boson Higgs can modify the $h \to Z\gamma$ decay rate.

2 The Large Hadron Collider and the ATLAS detector

2.1 The Large Hadron Collider

The Large Hadron Collider (LHC) [39] is the most powerful and largest particle accelerator in the world at time of writing, located at the European Organisation for Nuclear Research (CERN[1]). It consists of the particle accelerator and collider, located in a tunnel of 27 km in circumference (Fig. 2.1). The LHC was designed for a particle collision energy in the centre-of-mass system of 14 TeV. For the period 2015-2018 the energy was fixed at a value of 13 TeV. It is mainly a high rate proton-proton accelerator, but some part of the program is dedicated to the heavy-ion collision studies. The LHC has four main experiments:

- The ATLAS [40, 41] and CMS [42] experiments, which were developed for high-rate collision studies necessary for the Higgs boson searches, for Standard Model (SM) precision measurements and for searches of physics beyond the Standard Model.
- The LHCb [43, 44] experiment, developed mainly for the study of B physics.
- The ALICE [45] experiment, dedicated to different types of research with lead-lead collisions at the LHC to study the quark gluon plasma.

2.1.1 Running conditions and performance

In the LHC, two beams of protons (or ions) travel in opposite directions in vacuum in two separate beam pipes. Protons are obtained from hydrogen atoms, ionised by an electric field. Before entering the collider, protons are accelerated in four steps: first the linear accelerator Linac2 accelerates protons to an energy of 50 MeV, then the Proton Synchrotron Booster (PSB) is used to increase the energy to 1 GeV, after that Proton Synchrotron (PS) accelerates to an energy of 26 GeV and at the last step Super Proton Synchrotron (SPS) is used to reach the energy of 450 GeV. In the Proton Synchrotron protons are arranged in bunches, with a number of protons around 1.15×10^{11}.

Beams, injected by the SPS, circulate in the two separate vacuum pipes. They are surrounded by 1232 superconducting dipole magnets which bend the beams while a

[1]The acronym derives from the original French denomination, Conseil Européen pour la Recherche Nucléaire

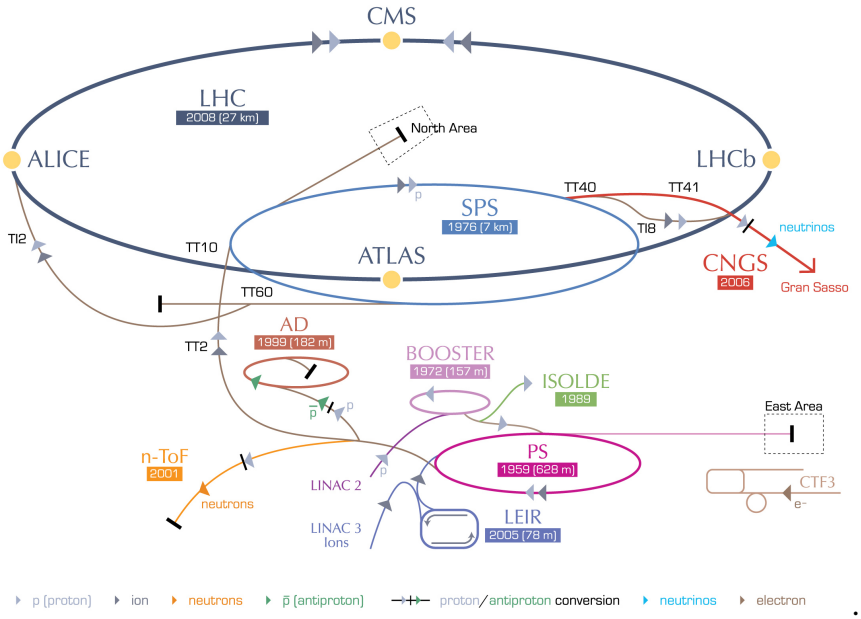

FIGURE 2.1: The CERN accelerator complex

few accelerator elements ramp up the energy until they reach the nominal energy of 14 TeV. The dipoles use niobium-titanium wires cooled to 1.9 K with liquid helium. In addition, the LHC also has 392 quadrupole magnets, which are used for focusing the beams.

Experiments start to collect data as soon as the beams are accelerated to the desired energy. The beam intensity decreases in time, and the expected beam lifetime is about 15 hours. When the intensity has become low, the beams are dumped away from the accelerator into a graphite block to be absorbed. The number of events per second during the LHC collisions is calculated as

$$N_{event} = \mathcal{L} \times \sigma_{event}, \tag{2.1}$$

where σ_{event} is the cross-section of the event and $\mathcal{L}$ - is the machine instant luminosity. The luminosity depends on the beam parameters, such as number of particles per bunch, the number of bunches per beam, the revolution frequency, and the transverse beam emittance. Integration of the luminosity over one run yields

$$L_{int} = L_0 \tau_L [1 - e^{-T_{run}/\tau_L}], \tag{2.2}$$

where T_{run} is the total duration of the luminosity run and τ_L the luminosity lifetime. The total collider efficiency depends on the ratio of the length of the run to the average turnaround time (the time taken to do all the filling, cycling, ramping, accelerating and further aborting process), which can have the minimum of 1.15 hours and a real average of 7 hours. Therefore, the maximum designed integrated luminosity is expected to be from 80 fb^{-1} to 120 fb^{-1} per year with the expected operation period of 200 days and the optimum run time of 12 hours. Fig. 2.2 shows the integrated luminosity per year delivered to ATLAS (starting from 2011 to 2019) and Fig. 2.3 shows the total recorded luminosity for the period of Run-2 of the LHC (starting from 2015 to 2019), which was 139 fb^{-1}.

There is a high probability during high luminosity collisions that one bunch crossing will produce several separate events, so-called pile-up events. For the description

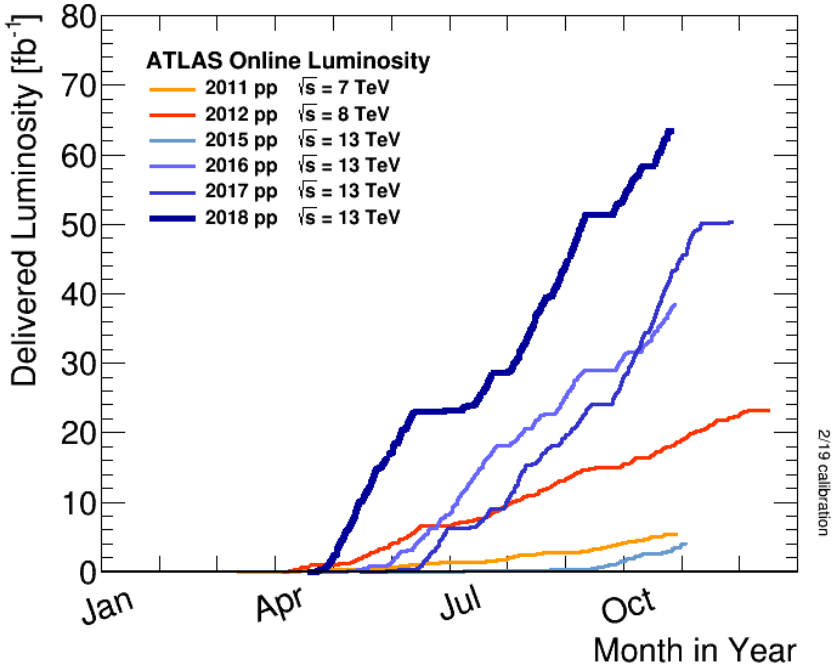

FIGURE 2.2: Cumulative luminosity delivered to ATLAS during stable beams and proton-proton collisions versus time for different years

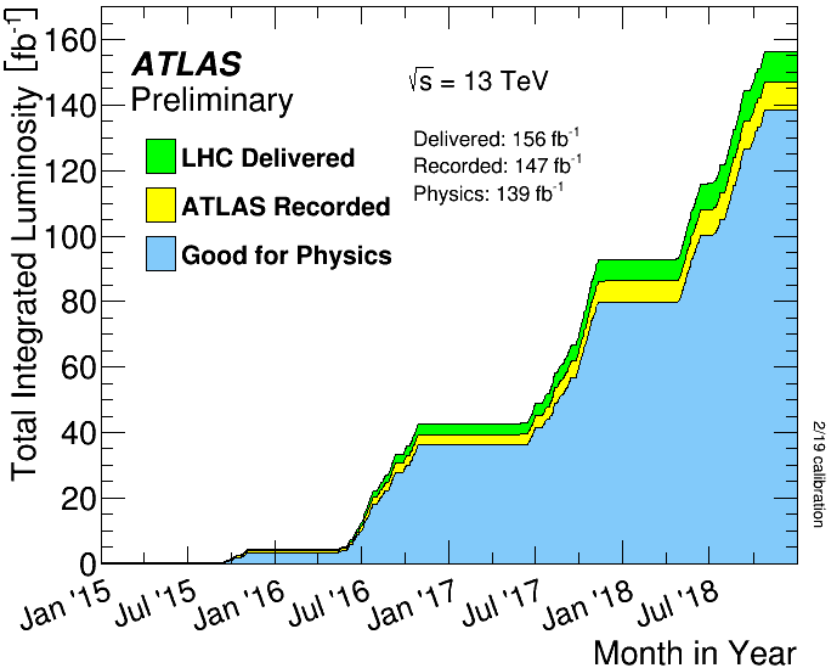

FIGURE 2.3: Cumulative luminosity versus time delivered to ATLAS during stable beams for proton-proton collisions. The green area shows the delivered LHC luminosity, the yellow area shows the recorded luminosity by ATLAS detector, the blue area shows the luminosity used in the physics analysis.

of the "pile-up" the observable of $< \mu >$ is used, which can be derived as the average number of collisions per bunch-crossing at the time of the recorded event

$$< \mu >= \frac{L \times \sigma_{inel}}{N_{bunch} \times f_{LHC}}, \tag{2.3}$$

where L is the average instantaneous luminosity over a large time period Δt ($\Delta t_{pile-up} >> 600$ ns), σ_{inel} is the total inelastic cross section, N_{bunch} is the number of colliding bunches in the LHC and f_{LHC} is the revolution frequency. Fig. 2.4 shows the average number of collisions, $< \mu >$, per recorded integrated luminosity, depending on year of data taking, and averaged $< \mu >$ value for the total recorded luminosity.

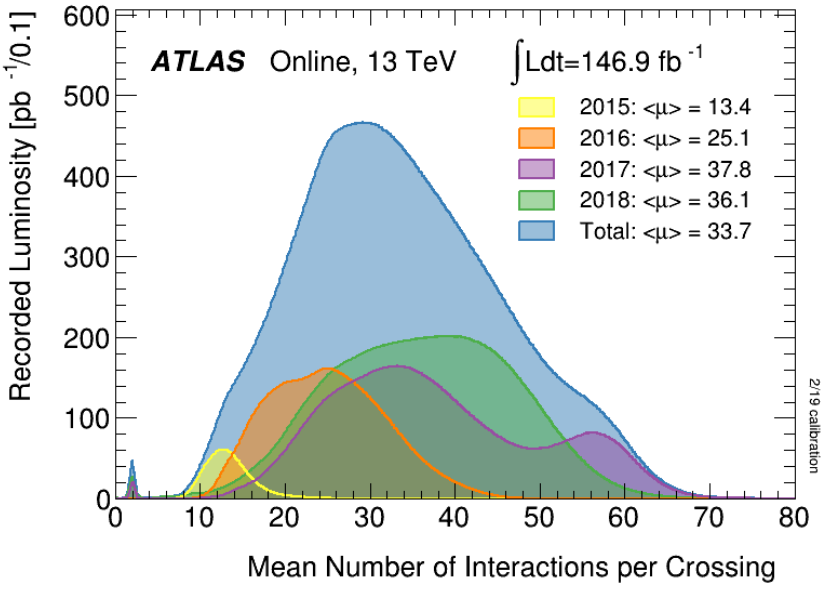

FIGURE 2.4: The average number of collisions $< \mu >$ for 2015-2019 years over integrated luminosity.

2.2 The ATLAS detector

The ATLAS detector is a multipurpose detector constructed for the measurements of proton-proton and heavy ion collisions, obtained from the LHC. It was designed to respond to the high rate of collisions, radiation level and energies at which the LHC works. ATLAS is designed to be able to perform searches for the Higgs boson and new physics, test QCD and provide precision measurements of the electroweak interactions. It is forward-backward and radially symmetric and composed of different sub-detectors in concentric layers in the central (Barrel) and forward regions (Endcaps) (Fig. 2.5)

The Inner Detector (ID) consists of tracking detectors, surrounded by a 2 T solenoidal field. It measures the position and momentum of charged particles, such as electrons and muons, and can also provide information on their identity. The next layers are the electromagnetic and the hadronic calorimeters [46] [47], where the first measures particle energies and position, especially for photons and electrons, and the second is used for measurements of hadrons that were not absorbed

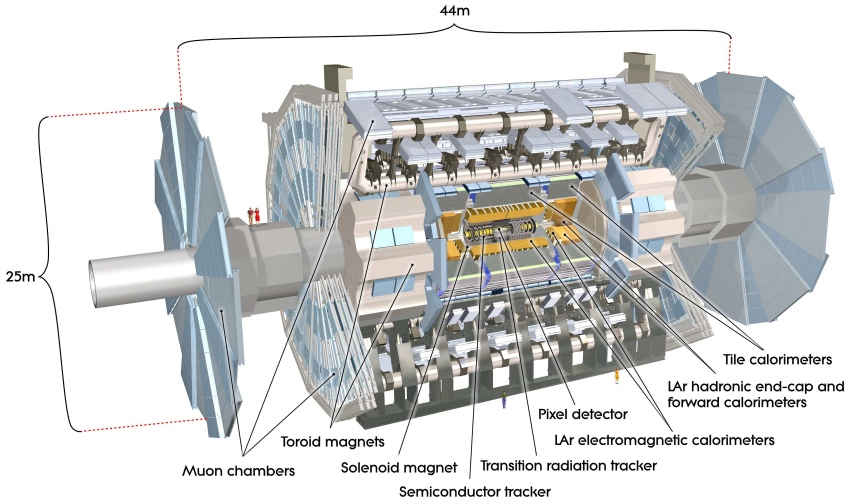

FIGURE 2.5: Image of the ATLAS detector and its sub-systems.

by the electromagnetic calorimeter. The muon spectrometer (MS) [48] surrounds the calorimeter and provides identification of muons and a high precision measurement of their momentum.

The performance of the sub-detectors was optimised to fulfil several goals:

- All electronics and sensors had to be radiation-hard and to respond to the high collision rate
- To estimate particle fluxes and to reduce the probability of pile-up in events, it was necessary to have high granularity
- The ID had to have a good momentum resolution and high reconstruction efficiency
- Muon identification and good muon momentum resolution is necessary in a large acceptance region. In addition, the charge of the muons with high transverse momentum has to be resolved by the detector unambiguously.
- The detector had to be able to operate with a high trigger rate

2.2.1 The ATLAS Coordinate System

The origin of the right-handed Cartesian coordinate system is set at the nominal interaction point. The z-axis goes along the beam pipe, the positive x-axis points towards the centre of the LHC ring, and the y-axis points upwards. Two spherical angles are defined: the polar angle θ is the angle from the beam axis, and the azimuthal angle ϕ is measured around the beam axis. Pseudorapidity η is defined as

$$\eta = -\ln(\tan(\theta/2)). \tag{2.4}$$

The distance between two particles in the pseudo-azimuthal angle space is defined as

$$\Delta R = \sqrt{(\Delta\eta^2 + \Delta\phi^2)}. \tag{2.5}$$

The projection of a particle's momentum vector on the traverse plane, referred to as the transverse momentum, is defined as

$$p_{\mathrm{T}} = \sqrt{p_x^2 + p_y^2}, \tag{2.6}$$

The transverse energy is then defined as $E_{\mathrm{T}}^2 = p_{\mathrm{T}}^2 + m^2$.

2.2.2 Inner Detector

The Inner Detector (ID) of the ATLAS detector was developed in order to provide an efficient tool for the measurement of the position and momentum of charged particles and contribute to particle identification. It also provides measurements of the primary and secondary vertex. It was designed as a high granularity detector to have ability to separate a large number of tracks left by charged particles emerging from the interaction point within a pseudo-rapidity range of $|\eta|$<2.5. Three sub-detectors allow ATLAS to achieve the designed performance: the Pixel Detector [49], the Silicon Microstrip Tracker (SCT) [50] and the Transition Radiation Tracker (TRT) [51] (Fig. 2.6).

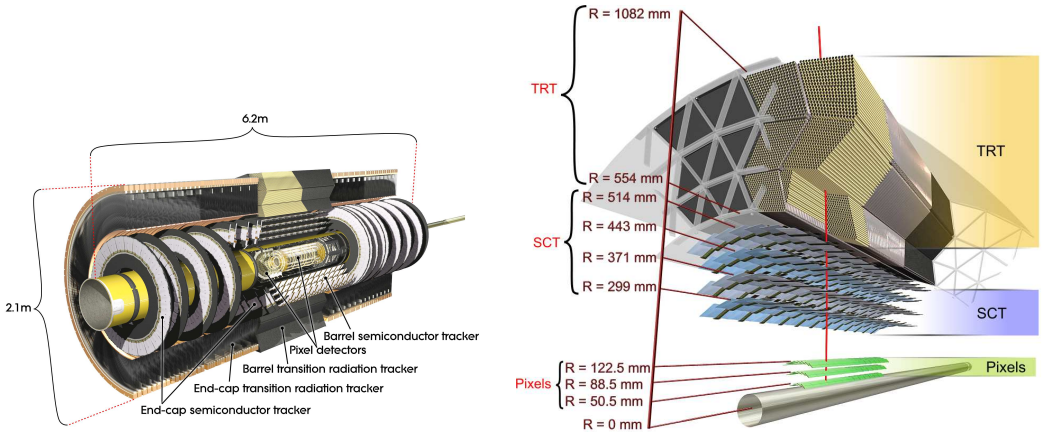

FIGURE 2.6: Left: cut-away view of the ID. Right: different sub-detectors of the ID

The Inner Detector is immersed inside a 2 T magnetic field, which is provided by the surrounding superconducting solenoid of a length and diameter of 5.3 and 2.5 m respectively. Sub-detectors, which provide precision track measurements (Pixel and SCT) cover an acceptance of $|\eta|$<2.5. In the barrel these detectors are organised in concentric regions around the beam, and they have a radial configuration in the endcaps. The pixel detector (which is closest to the beam pipe) has a high granularity and specially arranged lay-out, so that each track can cross at least three pixel layers. The innermost layer, the Insertable b-layer (IBL), was installed in 2014 to increase the tracking resolution [52] and is capable of withstanding 250 Mrad of ionising dose. Its pixels are 50 x 250 μm^2 in r - ϕ x z (where r - ϕ is a lateral plane). The other pixels are located in three outer layers and three endcap discs and have a minimum size R - ϕ x z 50 x 400 μm^2

The SCT detector is located outside the pixel detector, at the distance of 299 mm from the beam axis, containing eight silicon strip layers. It consists of four barrel and nine endcap layers. In the barrel part, small angle stereo strips are used for the second coordinate measurement, which requires use of two lines of sensors with a distance of 80 μm between those sets. The spatial resolution of the SCT is 17μm in

the $r-\phi$ plane and 580 μm in the $z(r)$ direction for the central (endcap) region. The total number of read-out channels is around 6.3 million.

The TRT detector is the outermost of the inner sub-detectors, and consists of 52544 144 cm long straw tubes collected in 73 concentric layers. These straw tubes are proportional drift tubes used for measurements in the TRT, each of a diameter of 4 mm. Each straw tube consists of polyimide multylayers bounded by polyurethane, with aluminium coating located on 25μm Kapton film. In addition, all of the straws are reinforced with carbon fiber filaments on the outer straw walls. Each straw has a centrally placed gold-plated tungsten anode wire from which the signal is read out. The straws are filled either with Xe-based or with Ar-based gas. The straw tubes have polypropylene fibres for barrel or polypropylene foil for endcap which act as a transition radiation material. The TRT covers the region $|\eta|<2.0$, and provides R - ϕ information with a precision of 130μm per straw. In the barrel part, the straws are parallel to the beam axis. In the endcaps, straws are radially configured in wheels. The total number of read-out channels is around 351000. More details about TRT construction and performance are provided in Sec. 3 as the TRT plays crucial role in the reconstruction of electrons and photons, used in the analysis.
Fig. 2.7 shows detailed cross-section of one of the Inner Detector parts. Combined use of the three independent sub-detectors allows to have a high-precision momentum measurement along with an excellent vertex measurement.

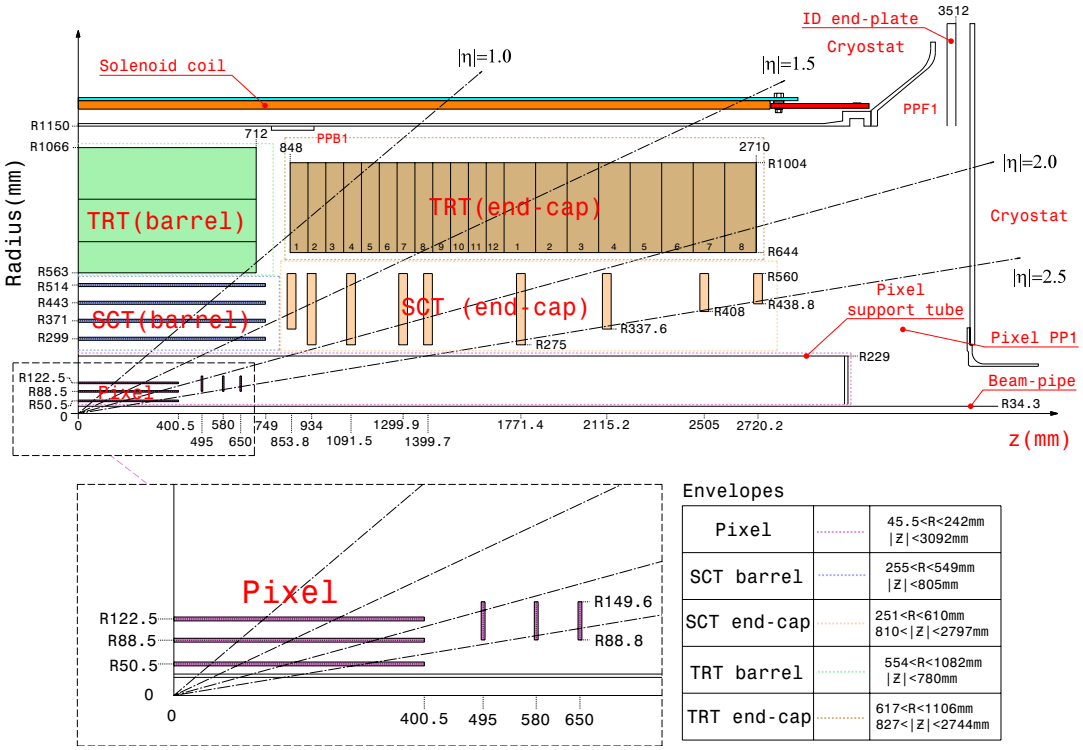

FIGURE 2.7: Detailed cross-section image of one of the Inner Detector parts

2.2.3 Calorimeters

The ATLAS calorimeter system consists of a number of detectors symmetric in ϕ, covering the $|\eta| < 4.9$ range. Photons and electrons are precisely reconstructed in the highly granulated electromagnetic calorimeter (EMCAL). By passing through the material of the detector they are absorbed and shower electromagnetically. For photons this process results in production of e^+e^- pairs which together with electrons emit bremsstrahlung photon radiation. EMCAL calorimeter is complimented by the hadronic calorimeter which allows jet reconstruction and provides measurements of the missing energy. Three cryostats (one barrel and two endcaps) are used to house these calorimeters which are the closest to the beam-line and next to the inner detector. The barrel cryostat contains the electromagnetic calorimeter. The endcap cryostats have an electromagnetic calorimeter followed by a hadronic calorimeter and a Forward Calorimeter (FCal) covering the region closest to the beam (Fig. 2.8).

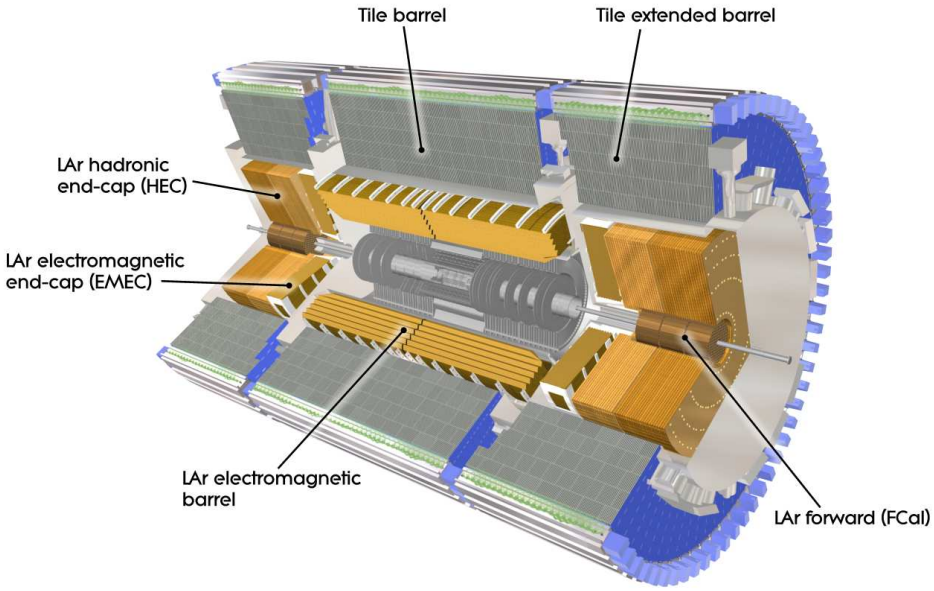

FIGURE 2.8: Cut-away view of the ATLAS calorimeter system

All calorimeters have to absorb electromagnetic and hadronic showers, which leads to several requirements for the depth of the whole system. For the electromagnetic calorimeter in the barrel, the thickness is over 22 radiation lengths (X_0) and it is more than $24X_0$ in the endcap. The interaction length (λ) of the active part of the calorimeter is defined as the mean distance travelled by a hadron before undergoing an inelastic nuclear interaction. The barrel part is about 9.7 λ, the endcaps are about 10 λ thick and the total interaction length is about 11λ at $\eta = 0$.

LAr electromagnetic calorimeter

The Liquid Argon (LAr) calorimeter is an electromagnetic calorimeter constructed with liquid argon volumes, which are interleaved with passive lead+steel absorbers ranging from 1.1-2.2 mm and copper-polyimide readout boards arranged in an accordion geometry. Use of such geometry allows to identify photons and reconstruct their direction with good precision. LAr calorimeter encased in a cryostat held at around 90K. Total compact calorimeter design is achieved with use of the lead absorber, which has a small X_0 of 0.5 cm. The barrel part of the electromagnetic calorimeter consists of two half-barrels, separated by a small gap (4mm at z=0) covering the $|\eta| < 1.475$ region [53]. Fig. 2.9 (left) shows scheme of the central barrel module. It is segmented into three layers and has total thickness of at least 22 radiation lengths. The first layer has a high granularity for a better position resolution of the particles in the calorimeter, the second layer is the thickest one to collect the major part of the energy deposit and the third layer collects only the tail of the electromagnetic shower. The separate presampler detector is a thin liquid-argon layer and is located in front of inner surface of the barrel. It allows to recover energy lost in the cryostat and provides shower sampling. The endcap parts have thickness of 24 radiation lengths. These cover the region of $1.375 < |\eta| < 3.2$ and are divided into two inner and outer coaxial wheels. The boundary between inner and outer wheels is filled mostly with low-density material. The transition between barrel and endcaps is located in the $1.37 < |\eta| < 1.52$ region and has space for the detector services. The electrodes, which are placed at the centre of the LAr gap, are used to collect the electrons drift proportional to the energy of the traversing particles. The energy resolution in the electromagnetic calorimeter can be described by the following relation

$$\frac{\sigma_E}{E} = \frac{a}{\sqrt{E}} \oplus \frac{b}{E} \oplus c, \tag{2.7}$$

where a is the sampling term related to shower fluctuations in the calorimeter and depends on the material in front of the calorimeters with the design value of $10\%/\sqrt{E[GeV]}$ at low $|\eta|$. b is associated to the electronic noise and is about cosh $\eta \times 350$ MeV. c is a constant term and the design value of it is 0.7%.

Hadronic calorimeters

The hadronic calorimeter (HCAL) consists of three sub-detectors: the barrel hadronic calorimeter (Tile), the LAr hadronic endcap calorimeter (HEC) and the LAr forward calorimeter (FCal). They provide measurements of the jet energy and position and of the missing energy.

Tile Calorimeter

The tile calorimeter [54] is a sampling calorimeter, which uses steel as the absorber and scintillating tiles as the active material. It is located in the region $|\eta| < 1.6$ behind the EMCAL, and is segmented into three layers (central barrel and two extended barrels) with 64 modules each of $0.1|\Delta\phi|$ size. Modules embed optic fibres, the tiles, photomultipliers, absorbers and front-end electronics. The front-end electronics provide analogue sums of channels, forming the trigger towers, passed to the trigger system. Example of barrel module is shown in Fig. 2.9 (right). The scintillator tiles are oriented radially to the beam line, which allows for almost full azimuthal coverage. The gap between the central and extended barrels is filled with

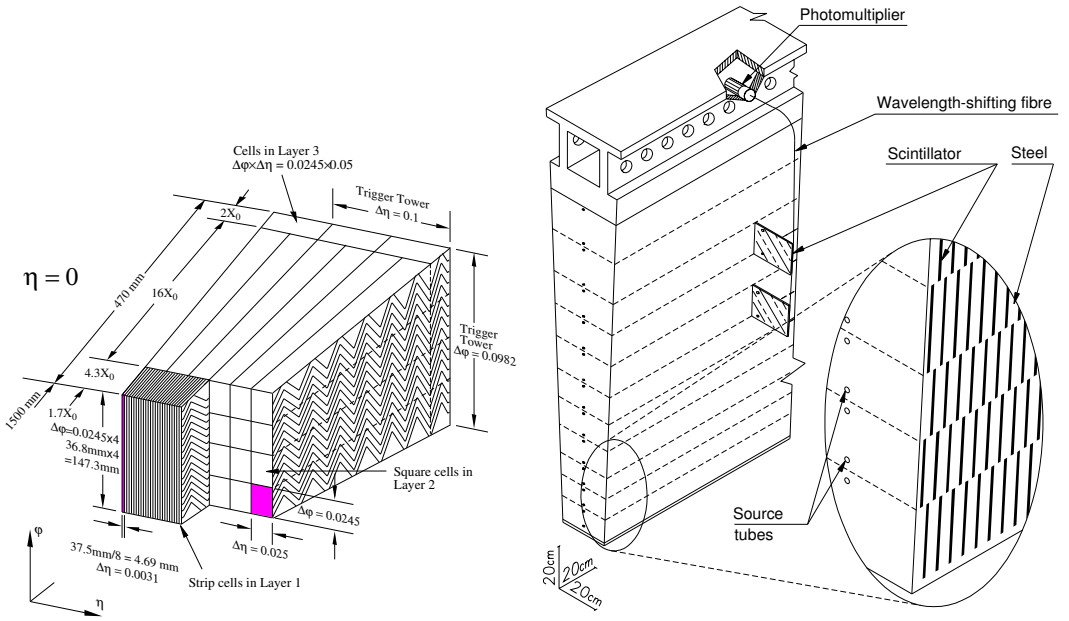

FIGURE 2.9: Left: Sketch of an electromagnetic calorimeter barrel module showing the segmentation in three layers. The granularity of the cells and trigger towers is also shown. Right: Schematic of a single barrel module in the hadronic tile calorimeter, showing the integration of the tiles, fibres, and photomultipliers [44].

modules organised in steel-scintillator layers, which allows to partially recover the energy loss in the crack regions.

LAr Hadronic End-Cap Calorimeters

The HEC calorimeter is a copper/LAr sampling calorimeter, which covers the region $1.5 < |\eta| < 3.2$. It is located directly behind the electromagnetic endcap calorimeter and shares the same LAr cryostats with the FCal calorimeters (Fig. 2.10). The HEC calorimeter consists of two wheels in each cryostat, a front wheel (HEC1) and a posterior wheel (HEC2). Both wheels are divided into two segments, with a total of four layers in each end-cap. The front wheels modules are made of 24 copper plates. For the rear wheels the modules are made of 16 copper plates. The resolution of the Tile calorimeter described earlier and the HEC calorimeter, as provided in [55], is

$$\frac{\sigma_E}{E} = \frac{50\%}{\sqrt{E[\text{GeV}]}} \oplus 3.0\% \oplus \frac{1.6\ \text{GeV}}{E}. \tag{2.8}$$

In addition, the HEC calorimeter has an important ability to detect muons and measure any radiative energy loss.

LAr Forward Calorimeter

The Forward calorimeters complete the EMCAL and HCAL at $3.1 < |\eta| < 4.9$, and they are located in the same cryostat. They are exposed to high particle fluxes as they are placed at high η with a distance of 4.7m from the interaction point, which

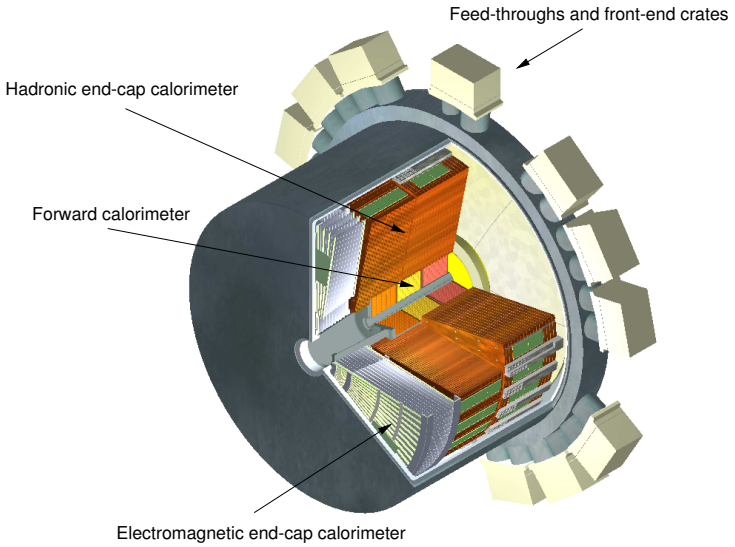

FIGURE 2.10: Cut-away view of an endcap cryostat with the three endcap calorimeters.

resulted in design with small liquid-argon gaps. The overall hermetic design of the calorimeters allows to reduce the possible background which can reach the muons system and minimise energy losses in cracks between the systems. The FCal has three modules for each endcap: the first one consists of a LAr sampling calorimeter with copper used for the absorber plates, and it is optimised for electromagnetic measurements. The second and third layers use tungsten instead of copper to contain the lateral spread of hadronic showers and are used for hadronic measurements. The FCal is about 10 interaction lengths thick and the resolution is derived [55] to be

$$\frac{\sigma_E}{E} = \frac{94\%}{\sqrt{E[\text{GeV}]}} \oplus 7.5\%. \tag{2.9}$$

2.2.4 Muon Spectrometer

Muons leave only a small amount of energy in the calorimeters ($\lesssim 5$ GeV) and reach the Muon Spectrometer, which is the outermost detector of ATLAS. It is designed to detect charged particles and measure their momentum in the range $|\eta| < 2.7$ (Fig. 2.11). The momentum measurement is based on the bending of the muon trajectory in the magnetic fields of the large superconducting toroid magnets. In the region $|\eta| < 1.4$ muon tracks are bent by the large barrel toroid, and by two smaller endcap toroids, which are inserted at the ends of the barrel toroids, provide the magnetic bending in the range $1.6 < |\eta| < 2.7$. In the region $1.4 < |\eta| < 1.6$ (transition region) the bending power is provided by both barrel and endcap system, but it is reduced. The created magnetic field is mostly orthogonal to the muon trajectories, it reduces multiple scattering and minimises the degradation of resolution.

In the barrel, the tracks are measured in chambers in three cylindrical layers around the beam axis. For the transition region and end-caps, the chambers are

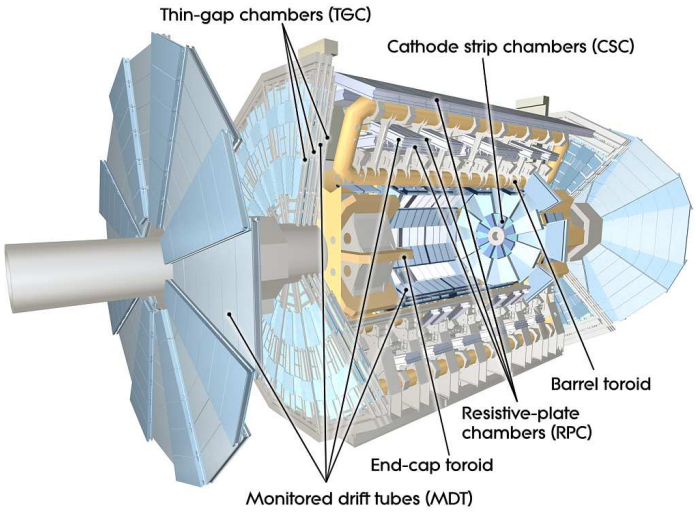

FIGURE 2.11: Computer generated image of the ATLAS detector highlighting the muon spectrometer components.

installed in three layers perpendicular to the beam. The tracking chambers can determine the coordinate of the track in the bending plane.

The Muon Spectrometer is equipped with Monitored Drift Tubes (MDT) and Cathode-Strip Chambers (CSC). The MDT cover the pseudorapidity region $|\eta| < 2.7$ (except the innermost endcap layer). They consist of three to eight layers of drift tubes operating at 3 bar of absolute pressure with an average resolution of $80\,\mu$m per tube. The MDT combines simplicity of construction, high measurement accuracy and provides predictability of mechanical deformations.

CSCs are located in the endcap region of $2.0 < |\eta| < 2.7$, and are multi-wire proportional chambers with cathode planes segmented into strips in the orthogonal direction. They are used to perform the innermost tracking, providing the higher rate capability and time resolution. Their resolution is $40\,\mu$m in the bending plane and about 5 mm in the transverse plane. The difference in resolution is due to the fact that the azimuthal readout runs parallel to the anode wires and due to the different readout pitch.

A high-precision optical alignment system is implemented to monitor the positions and internal deformations of the MDT chambers and CSC strips which allows to know their position along a muon trajectory better than $30\,\mu$m.

The additional trigger capabilities for the MS are provided by the extra detectors, with the response times below 25 ns. Resistive Plate Chambers (RPC) are used in the barrel region at $|\eta| < 1.05$ and consist of small gas volumes with two sets of orthogonal cathode strips. Their resolution is about 10 mm in both the bending and non-bending directions. Different solution is used for the endcap due to the much higher radiation level. Thin-Gap Chambers (TGC) are designed for that purpose and are located in the region $1.05 < |\eta| < 2.4$. They are multi-wire proportional chambers with the wire-to-cathode distance smaller than the wire separation. The muon track information is provided with a precision of 2 mm to 7 mm in the η coordinate and 3 mm to 7 mm in the ϕ coordinate.

The design goal for standalone transverse momentum resolution for muons momenta $p_T = 1$ TeV is $\sigma_{p_T}/p_T = 10\%$.

2.2.5 Trigger system

The ATLAS trigger system has several different sub-systems or levels [56]. They are a hardware-based first level trigger (L1) and a software-based high-level trigger (HLT). The bunch-crossing rate of the LHC is 40 MHz, with an average around 40 interactions per bunch-crossing. The trigger system has to reduce the high event rate to an output rate of about 1 kHz by selecting only interesting events.

The first level trigger (L1) uses coarser-granularity signals from the calorimeters and the muon chambers to reduce the event rate from the 40 MHz bunch crossing rate to below 100 kHz; it has 2.5 μs to decide which events to keep. It consists of L1Calo, L1Muon, L1Topo and Central Trigger Processor (CPT) modules. The last one also forms the trigger decision. They define regions-of-interest (RoIs) which have calorimeter clusters with high transverse energy, E_{T} or muon tracks in the muon chambers.

The events are sent to the Read-Out System (ROS) and processed by the HLT after they pass through the L1 trigger acceptance. The HLT also receives RoI information from L1. It has to further reduce the number of events recorded to disk to an average rate of about 1 kHz within a few seconds. The HLT uses tracking information from the ID, finer-granularity calorimeter information and precision measurements from the MS. The criteria of the reconstruction and object identification become similar to the offline level. The HLT selection is performed at each step and subsequent steps are not executed if it fails at a certain step - this requirement is essential in order to reduce the time needed by the HLT to make a decision.

The so-called 'trigger menu' is the configuration of the trigger which define a full list of the L1 and HLT triggers and their configurations. It is composed and optimised depending on the LHC running conditions, such as beam type, luminosity, etc. Such configurations are necessary to fit within the event acceptance rate and the bandwidth constraints of the data acquisition (DAQ) system of the ATLAS detector as well as within the offline storage constraints.

2.2.6 Data processing

The raw data recorded by the ATLAS DAQ system are further transferred to the CERN computing centre. It is later processed and encoded in the Event Summary Data (ESD) format, which can be distributed to the major sites of the LHC Computing Grid [55], a world-wide network of computer clusters, the heart of which is the CERN computing centre. The ESD files have a very large size and have to be processed into smaller Analysis Object Data files (xAOD) - they contain only specific physics objects information needed for the analysis, such as electrons, muons, jets and photons. This standard is used for both data and simulated events and retains a large fraction of the event information. Simulated xAOD datasets commonly used in analyses are as large as tens of TB. Therefore, a further reduction step, called derivation, is performed by large analyses groups. The derivation format files can be used for both performance and calibrations studies in which case they contain detector-specific information and non-calibrated objects, or for physics analysis where they contain information about calibrated objects only, which helps to reduce their size on the disk. The resulting files are finally processed by the analysers into ROOT [57] ntuples, which can be handled by any personal computer equipped with the ROOT analysis framework.

3 The ATLAS Transition Radiation Tracker

The search for the Higgs boson decay to a Z boson and a photon, which is the main topic of this thesis, relies on precise measurements of many parameters. All of them require excellent performance of all sub-detector systems in the ATLAS detector and their description in the software. Studies in this chapter concern improvements of performance of the ATLAS experiment - in particular the ATLAS Transition Radiation Tracker (TRT), and particle identification provided by it. The particle identification with the TRT [58] is performed by accounting the energy deposited in the straws, which is defined as the sum of the energy deposits due to transition radiation (TR) and ionisation losses of the charged particle crossing the straw. In general, the TR yield is proportional to the Lorentz factor γ of the particle. This effect can be used for separation of light particles (electrons) from particles with higher masses (pions) which have the same momentum. In addition to the TR, the measurement of specific energy losses (dE/dx) of charged particles passing through the detector volume enhances the electron-pion separation, particularly at low momentum (below $p \leq 10$ GeV). It also can be used for identification of highly ionising particles such as protons at low momenta, or hypothetical exotic objects such as highly ionising stable massive particles [59]. The best electron-pion separation is achieved with the combination of TR and dE/dx-based measurements in a single likelihood function. Correct electron identification is critical for multiple physics analyses, including the Higgs boson decay analysis. Dedicated studies were performed to improve the simulation of the TR response of the detector. Due to the fact that the TRT detector configurations were changing in different run periods the TRT response has to be constantly tuned to reach the best agreement between data and simulations. In this chapter the results of the optimisation studies related to transition radiation and dE/dx measurements are described. The TR response tuning was done using data collected during the 2015 run period and in addition it was performed for the changing gas composition of that run period. The dE/dx studies were carried out for low and high pileup conditions for two different TRT gas geometries, related to 2015 and 2016 run periods. During these periods the detector was mainly filled with xenon but few TRT layers (in the barrel and endcaps) were filled with an argon gas mixture.

3.1 Particle identification with the TRT

3.1.1 Transition radiation

In the ATLAS experiment the TRT detector plays a role of the tracking and particle identification device. It is constructed from straw drift tubes filled with a Xe-mixture interleaved with the multi-layer radiator made from polypropylene foils (TRT end-caps) or polypropylene fibres (TRT barrel). Such design allows to provide many coordinate measurements of the particle track based on time needed for ionisation electrons to reach the anode wire and also effectively produce and absorb transition radiation. Transition Radiation (TR) x-rays are produced when highly relativistic charged particle with a high Lorentz factor (γ) traverses boundaries between detector materials of different dielectric constants. Since the TR yield is about a few % per boundary crossing, in order to exploit and maximise emission rate the TR radiator is constructed to have many sequential transitions on the particle trajectory. The TR X-rays, ranging from a few keV to a few dozen keV or more, are emitted in a forward direction at small angles (within few mrad) to the particle trajectory. In this energy range it the TR yield has a threshold dependence on γ and for the TRT the effective production starts at $\gamma \gtrsim 5 \cdot 10^2$. The TR intensity for a single boundary crossing always increases with γ, but, for multiple boundary crossings, interference leads to saturation above a Lorentz factor which is defined by radiator parameters and for the TRT it practically saturates above $\gamma \gtrsim 3 \cdot 10^3$. This feature allows to distinguish between different types of particles such as electrons and pions in the momentum range from 1 to 150 GeV. The soft part of the TR is absorbed in the radiator itself or in the straw walls and only photons above 4 keV are detected in the active gas. An average energy deposition of the ionising particle in the straw is about 2.5 keV. The combination of these two values defines the threshold of about 6.5 keV used in the TRT to detect TR.

In the TRT the gas mixtures based either on xenon or on argon are used. The xenon is a TRT base line mixture. It is used because of its high X-absorption efficiency. However, starting from 2012, some TRT modules developed large leaks which could not be tolerated because of high price of the xenon gas. To mitigate this problem these modules were feed with less expensive Ar-mixture. This mixture preserves very good TRT tracking properties but it has significantly lower absorption efficiency of the TR photons.

A gold-plated tungsten wire is located at the centre of the straw (anode). The strong electric field appeared between the wire and the straw wall can be expressed as follows

$$E = \frac{1}{r} \frac{V_0}{ln(b/a)}, \tag{3.1}$$

where r is the radial distance, V_0 is the wire voltage, a and b are radii for the anode wire and the tube.

When a charged particle traverses the straw, it creates electromagnetic interaction between gas atoms of the tube, which leads to the gas ionisation. Ionisation electrons drift towards the wire and cascade in the high electric field (more than 100 keV/cm) very close to the wire. Schematically it is shown in Fig. 3.1. The amplitude of the induced signal depends on the path length in the straw and the ionisation density.

Two electronics thresholds are used to discriminate the signal - the low threshold (LT) at 300 eV and the high threshold (HT) at 6-7 keV [60]. The LT separates the signal from noise and is used for coordinate and dE/dx measurements. The HT is

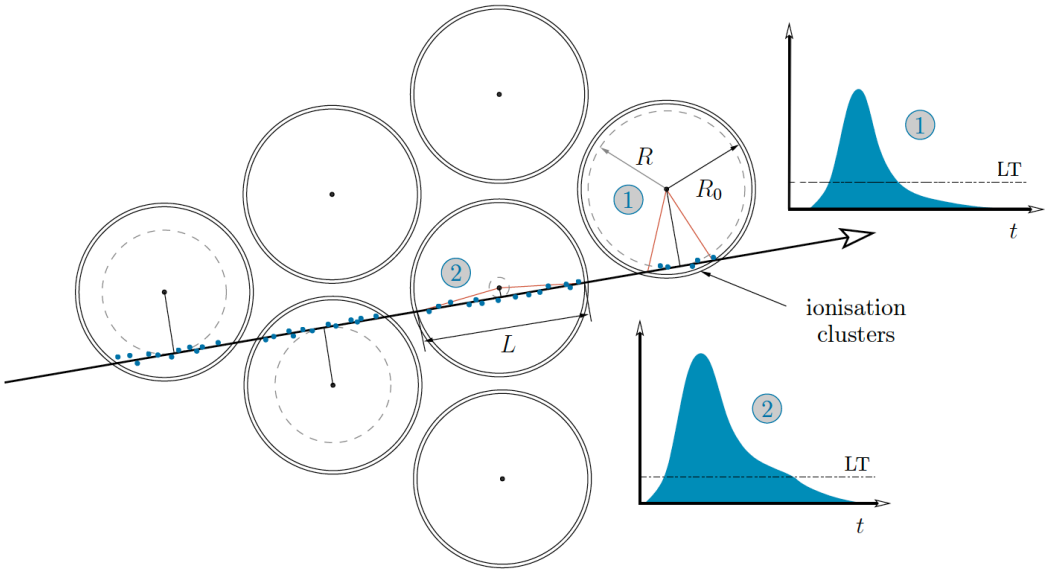

FIGURE 3.1: Scheme of a particle traversing the TRT detector. The gas is ionised along the way of passing particle, the ionisation electrons drift towards the anode wire and a signal proportional to the ionisation is induced at the wire.

used for TR measurements. The counting number of straws with HT hits allows to separate electrons which produce TR and pions for which HT hits originate from rear cases of large ionisation energy deposits. When the signal exceeds the thresholds a bit pattern is created. A bit is set either to 1 when signal is present or to 0 otherwise, as shown in Fig. 3.2. The LT is readout in 24 bins with 8 bins per 25 ns, the HT has only three single bits stored per 25 ns. For bit pattern from the low threshold there are defined the leading edge (LE) and the trailing edge (TE). The LE corresponds to the first bit set in the bit pattern and is defined during the first LT transition 0→1. It represents the time of arrival of the ionisation electrons produced at the point of the closet approach to the readout wire. The TE corresponds to the last bit set in the bit pattern and is defined during the last transition 1→0. It represents the time of arrival of the ionisation electrons which are produced close to the straw walls. TE also depends the signal shape and its amplitude at the output of the amplifier-shaper and thus reflects on the energy deposited in the straw. A difference TE-LE is used for dE/dx measurements. In general, TR hit is defined a if any of the three HT bits is high. Later, in order to reduce effect of pile-up bunches, only middle HT bit information was used.

The fraction of HT hits on particle track (High Threshold Fraction, $F_{HT} = N_H L/N_L L$), is interpreted as a HT probability. Fig. 3.3 illustrates the probability to find the HT hit in straw as a function of the particle γ factor. One sees that for pions below 100 GeV the averaged probability is at the level of 4% where as for electrons above 3 GeV it is at the level of 23 %. For particle which crosses about 32 straws in the barrel TRT the averaged number of high level hits for pion is about 1.3 and for the electrons it is about 7.4. This is illustrated in Fig. 3.4, where example of the event display for B^0_D decay is shown. Blue dots represent straws which have LT hit and red dots are straws with LT and HT hits. Bottom plots show distribution of the number of HT hits on track for pions and electrons. In order to obtain separation between pions

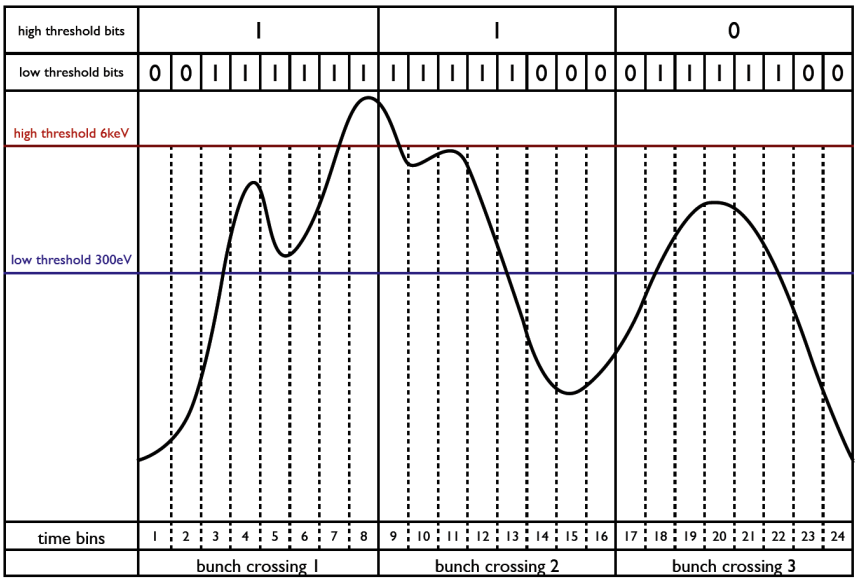

FIGURE 3.2: Scheme of the TRT bit pattern. The ionisation signal is discriminated between two thresholds and readout in 24 time bin in a period of 75 ns.

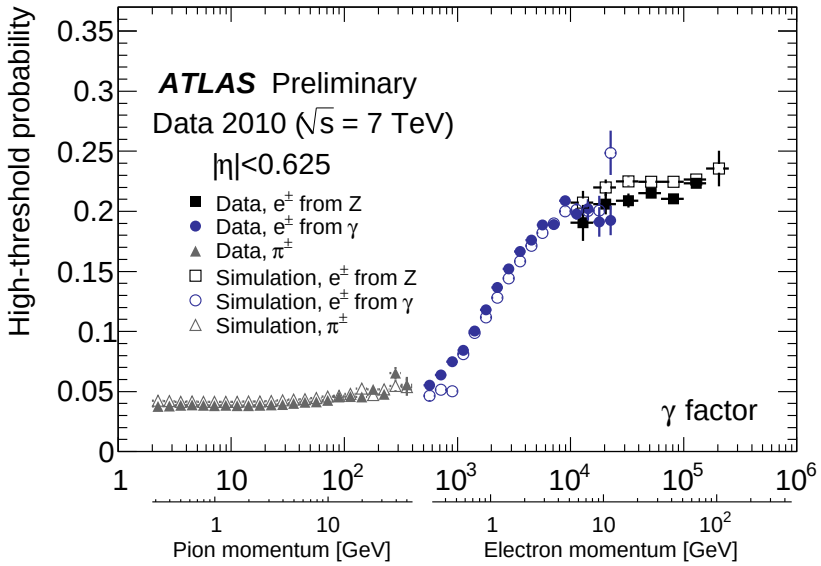

FIGURE 3.3: The high-threshold hit probability as a function of the Lorentz gamma factor for the barrel part of the TRT. Particle energy scale is calculated assuming a mass of the candidate (electron or pion) [58].

and electrons the threshold has to be set for the number of HT hits on the particle track. This number depends on many parameters and, in practice, for particle identification likelihood approach is used. For the TRT this approach is described later in this section. For a final particle identification in the ATLAS experiment a global likelihood variable is built using information from all relevant detectors. Detailed description of particle identification variables for the physics analysis is presented in Sec. 4.1.4.

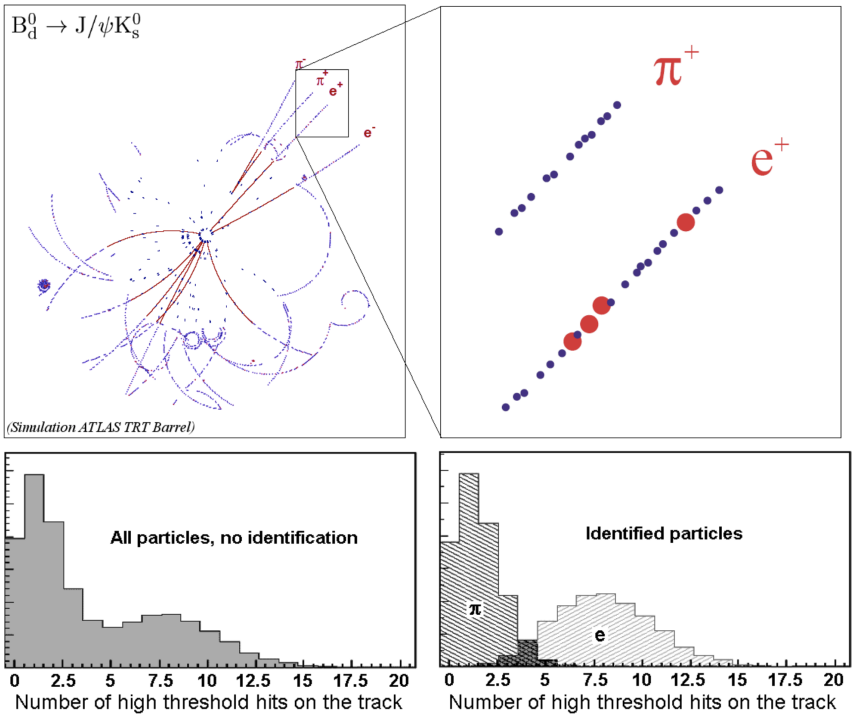

FIGURE 3.4: Event display for one event with B^0_D decay in the barrel TRT. Blue dots are the straws with LL hit and read ones the straws with low level (LL) and high level (HL) hits. Bottom plots show distribution of the number of HL hits on track for pions and electrons. [61].

3.1.2 Identification with dE/dx

As signal width depends on its amplitude the measurement of the Time-over-Threshold (ToT=TE-LE) also brings a valuable information about the energy loss of particles. This information can be used to estimate the specific energy loss per track length (dE/dx) of a charged particle which could enhance TRT PID performance when particles have different ionisation losses. Ionisation is the dominant energy loss process for low energy whereas at high energies bremsstrahlung becomes the dominant energy loss process, Fig. 3.5:

The theoretical prediction of the average energy loss per path length of a charged particle in matter below bremsstrahlung limit is given by the Bethe-Bloch formula [62] and shown in Fig. 3.5:

$$\frac{dE}{dx} = \frac{4\pi N e^4}{mc^2\beta^2} z^2 \left(ln\frac{2mc^2\beta^2\gamma^2}{I} - \beta^2 - \frac{\delta(\beta)}{2} \right), \tag{3.2}$$

where N is the number density of electrons in the matter, e is the elementary charge, z is the charge of the particle, mc^2 is the electron's rest energy, β is the velocity of the travelling particle in terms of the velocity of light c, $\gamma^2 = \frac{1}{\sqrt{1-\beta^2}}$, and I is the mean excitation energy of the atom.

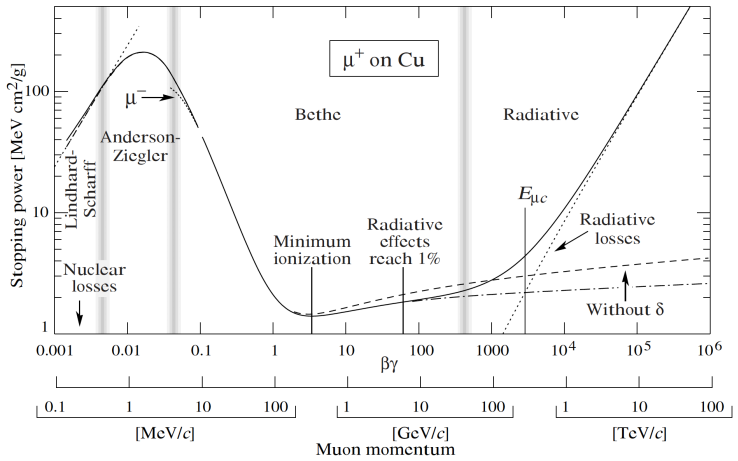

FIGURE 3.5: The energy loss of particles in matter as a function of $\beta\gamma$

In the TRT detector dE/dx can be used to help electron-pion separation for momenta $p \leq 10$ GeV, and for identification of any highly ionising particles, for example heavy ionising stable massive particles (SMP) and multi-charged particles (as dE/dx is proportional to the square of the particle charge) [63].

As all of the parameters except $\beta\gamma$ are material dependent, the mean energy loss can be parametrised as a function of $\beta\gamma$. The physical motivation of such parametrisation is given by Blum-Rolandi function [64]:

$$\frac{dE}{dx}(\beta\gamma) = \frac{p1}{\beta^{p4}}\left(p2 - \beta^{p4} - log\left(p3 + \frac{1}{(\beta\gamma)^{p5}}\right)\right), \tag{3.3}$$

where free parameters p1,...p5 represent the material dependence and can be determined from a fit to the measured dE/dx. In addition, $\beta\gamma$ can be expressed as a function of the momentum p and mass m of the particle:

$$\beta\gamma = \frac{p}{m}. \tag{3.4}$$

Fig. 3.6 shows the predictions for the TRT dE/dx variable of different particles as a function of momentum, extracted from the fit in Eq. 3.3. Details on dE/dx measurements with the TRT ToT are presented in Sec. 3.3.1

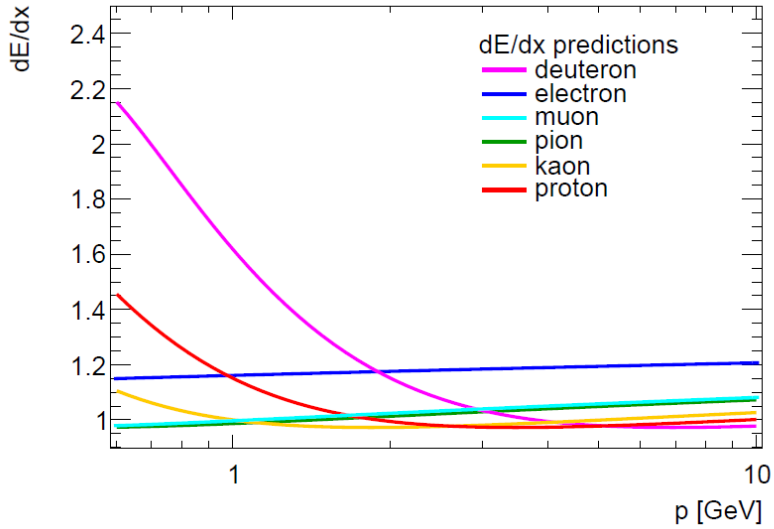

FIGURE 3.6: Predictions for dE/dx of different particles [63].

3.1.3 Combination of TRT identification techniques

The electron identification can be performed with use of the set of discriminating variables, provided by the ATLAS inner detector and calorimeter reconstruction software. The final discriminant is formed from the likelihoods of an electron to originate from signal or background (more details are provided in Sec. 4.1.6). A general likelihood hypothesis L can be expressed as follows:

$$L(\mathbf{x}) = \prod_{i=1}^{n} P_i(x_i).$$

where P_i is a probability extracted from a variable x for a given hypothesis i. In the TRT detector, in order to achieve the best electron-pion separation the combination of the HT fraction and ToT measurements is used in the final discriminant. The corresponding likelihood is then formed by multiplying two likelihood function: one for HT and one for ToT, which are considered as independent. The electrons are then selected by applying a cut on a combined likelihood. Fig. 3.7 shows pion misidentification probability at 90% electron efficiency as a function of momentum for the ToT-based, HT fraction based selections and their combination. As is seen, ToT-based measurements improve pion rejection at low momentum $p < 10$ GeV.

3.2 Tuning studies of the TRT digitisation

The TRT straw produces the information about the time-structure and amount of the energy in it and can be used for both tracking and particle identification. In the TRT detector, as is mentioned in Sec. 3.1.1, two thresholds, low (LT) and high (HT) are used. LT to separates the signal from noise and also provides information for coordinate and dE/dx measurements. The HT is used is for TR measurements. The TRT reads out data over a period of 75 ns for each triggered event. The information about whether the low threshold is exceeded or not is measured separately in time

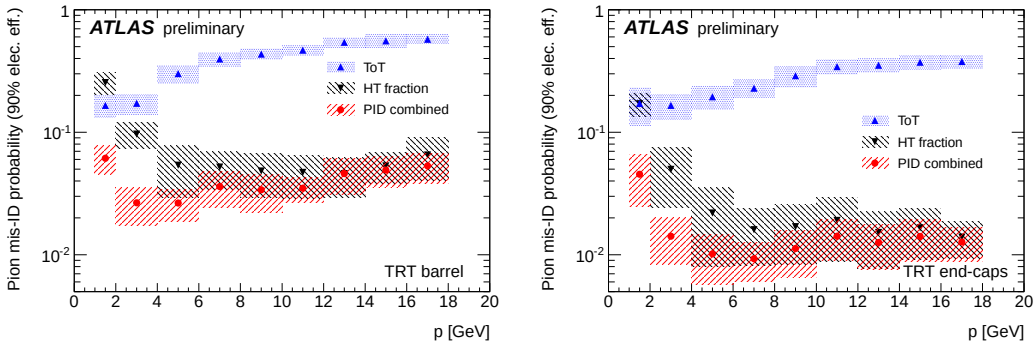

FIGURE 3.7: The pion misidentification probability that gives 90% electron efficiency, as a function of momentum for the barrel (left) and endcap (right) [58].

intervals of 24 time bins of 3.125 ns. In case of HT only three HT bits of 25 ns make up the 75 ns readout window.

Due to the effect of high pile-up during the Run2 period, only the middle of the three TRT HT bits is used. The HT middle bit fraction ($f_{middleHTbit}$) is defined by

$$f_{middleHTbit}(\text{region}) = \frac{N_{\text{HT hits with middle HT bit high}}}{N^{total}_{HThits}}(\text{region}), \tag{3.5}$$

where 'region' is straw layer, barrel or endcap.

Currently particle identification in the TRT is based on using the HT middle bit. Good agreement between data and simulation is required for the physics analysis. As detector configuration (for instance, gas geometry) is changing over the time the simulation model needs to be tuned. Studies presented below show the tune of the TRT digitisation in order to reach good the agreement between data and simulations.

3.2.1 Data samples and event selection

The TRT tuning studies are based on several runs taken from 2015 pp collisions collected at $\sqrt{s}$ = 13 TeV by the ATLAS detector. Samples with electrons and muons originating from Z boson decays are used. The results observed in data were compared to Monte Carlo (MC) simulations. Pythia $Z \to ee$ and $Z \to \mu\mu$ MC samples were produced with different HT settings for tuning studies.

During the 2015 run period, the TRT operated with the *baseline scenario* shown in Fig. 3.8 below - one innermost barrel layer and two layers in endcap wheels are filled with an argon gas mixture, the other layers are filled with a xenon gas mixture.

For the selection of high purity control samples from $Z \to \mu\mu$ and $Z \to ee$ decays the following requirements are applied to both electrons and muons: the transverse energy has to be more than 20 GeV and loose quality working point is required. An additional requirement is set on muon momentum to be less than 60 GeV since above this momentum muons start to produce significant transition radiation. Pairs of electrons or muons from Z decays require an angular separation of δR > 0.3 and an invariant mass window of $75 < m_{\ell\ell} < 105$ GeV.
The selection of TRT hits requires an association with tracks of at least 2 Pixel hits, at least 6 SCT hits and a minimum of 15 TRT hits.
Only events with $<\mu>$ between 8 and 14 are considered in order to have overlapping

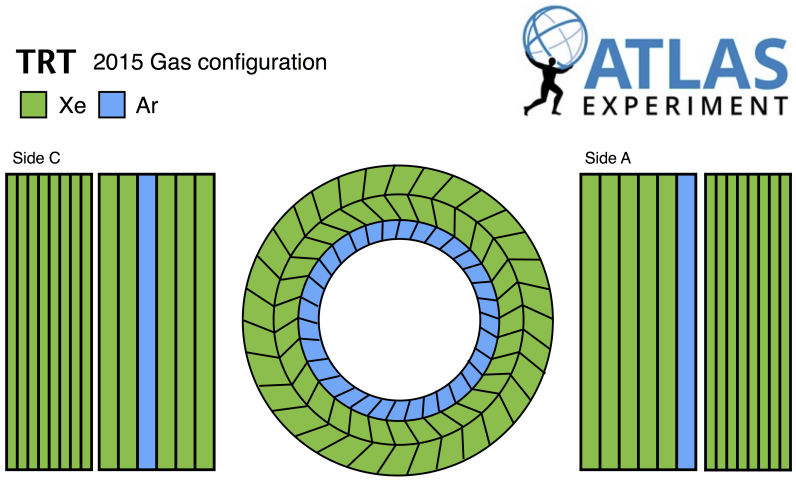

FIGURE 3.8: Barrel layer 0 (B0), endcap side C wheel 3 (EC3), endcap side A wheel 5 (EA5) are filled by argon gas mixture, all other layers are filled with xenon-based gas mixture.

regions in both data and simulation.
After applying the above criteria Fig. 3.9 shows good agreement between data and simulation for two basic kinematic distributions in the muon channel, similarly good agreement is seen for the electron channel.

3.2.2 HT middle-bit tuning

During the process of TRT digitisation four parameters are normally tuned to improve the agreement of the HT middle bit fraction between data and simulation:

1. High threshold signal shaping function: three different shaping properties (model rising, falling and undershoot)
2. High threshold setting: discrimination of the TRT hit between ionisation and transition radiation.
3. TR efficiency: reduction of the amount of TR (which is over-estimated in the simulation step).
4. High threshold T0 shift.

More details on 1. and 4. can be found in [65], the remaining points 2 and 3 were studied by me and presented here.

Fig. 3.10 compares the HT middle bit probability [66] as a dependence on straw layer for the barrel and endcap before the retune, separately for argon- and xenon-based gas mixtures, for case of the $Z \to \mu\mu$ and $Z \to ee$ channels. As it is seen, the initial modelling of HT middle bit probability shows some discrepancies and has to

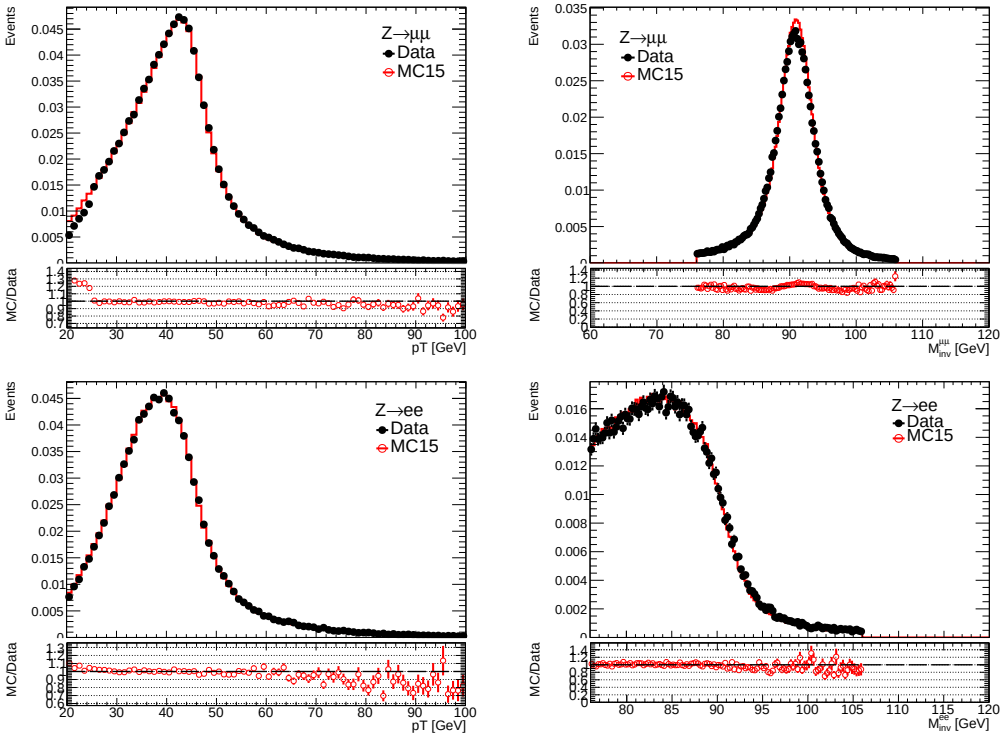

FIGURE 3.9: Transverse momentum distribution of muon candidates after muon selection (left top), and in case of electron channel after electron selection (left bottom). $\mu\mu$ invariant mass after all $Z \to \mu\mu$ selection (right top), ee invariant mass after all $Z \to ee$ selection (right bottom). Data is in good agreement with simulation. The bottom part of the plots show the ratio between data and simulation.

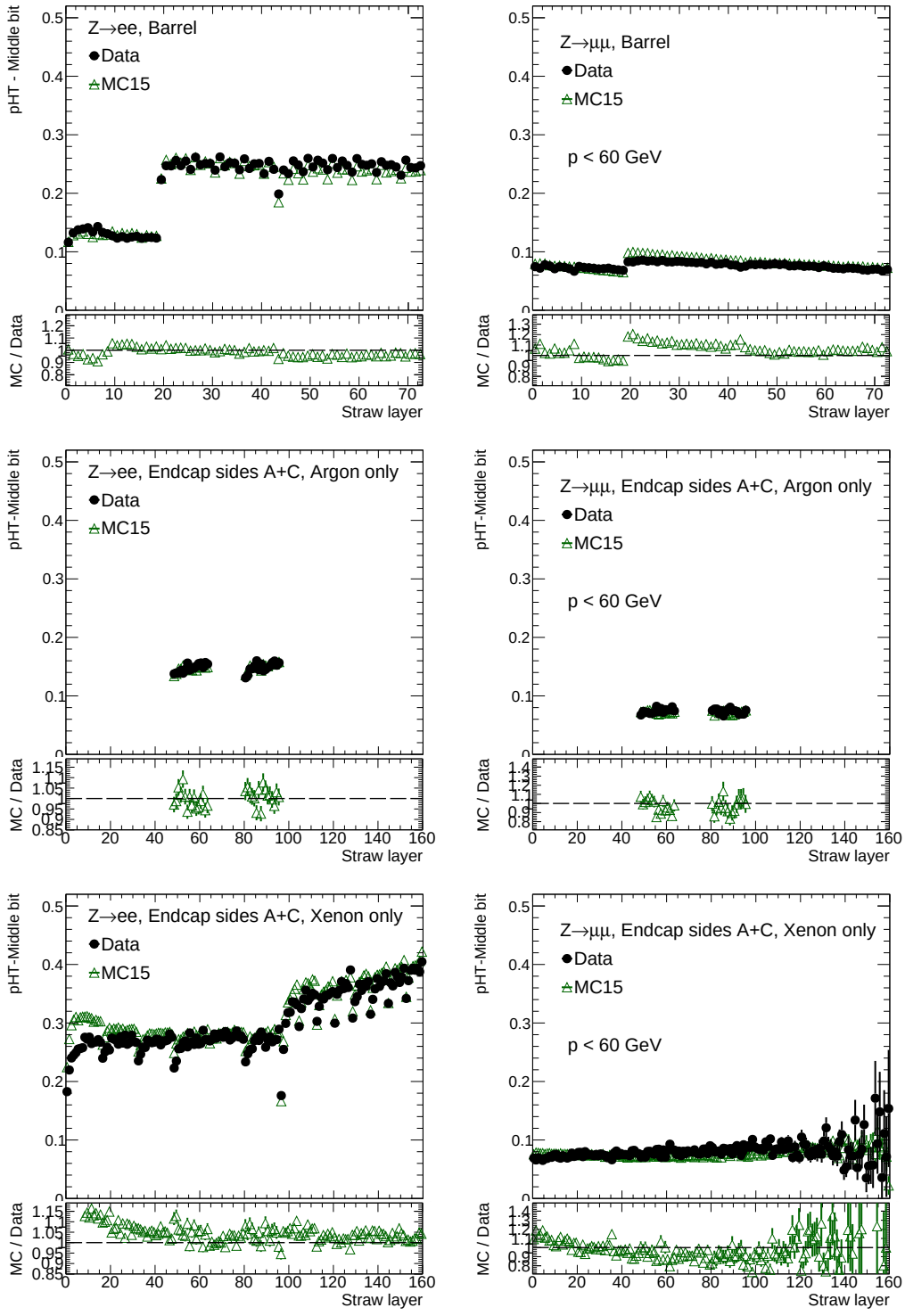

FIGURE 3.10: HT middle bit probability vs. straw layer for data (black dots) and simulation before any tune (green dots) for the barrel and end-cap, in case of $Z \to ee$ (left) and $Z \to \mu\mu$ (right) channels. The bottom part of the plots show the ratio between simulation and data.

be tuned separately for each gas mixture and for each TRT region, i.e. as a function of straw layer. Two sets of corrections are provided in the following order:

- Tune of high threshold value based on $Z \rightarrow \mu\mu$ sample
- additional tune of transition radiation efficiency for electrons

Tables 3.1, 3.2 show the original high threshold and transition radiation efficiency settings and the new high threshold settings.

	Original high threshold [eV]	New high threshold [eV]
Argon Barrel short	2660	2607
Xenon Barrel short	5412	5195
Argon Barrel long	2352	2540
Xenon Barrel long	4949	4751
Argon Endcap A side wheel	2414	2414
Xenon Endcap A side wheel	5251	5513
Xenon Endcap B side wheel	5072	5326

TABLE 3.1: Original and tuned high threshold level settings

	Original TR efficiency	New TR efficiency
Argon Barrel	0.550	0.610
Xenon Barrel	0.774	0.774
Argon Endcap A side wheel	0.800	0.800
Xenon Endcap A side wheel	0.932	0.909
Xenon Endcap B side wheel	0.830	0.809

TABLE 3.2: Original and tuned transition radiation efficiency level settings

3.2.3 Results

New results are obtained for electron and muon channels after tuning the high threshold and transition radiation efficiency levels; the discrepancy between data and simulation have improved in most of TRT regions. Fig. 3.11 shows a comparison of two HT middle bit probabilities for the old simulation sample (green) and simulation sample with tuned settings (red).

A weighted mean of the ratio of the simulation to the data is calculated as

$$\bar{x} = \frac{\sum (x_i \sigma_i^{-2})}{\sum \sigma_i^{-2}} \tag{3.6}$$

$$\sigma_{\bar{x}}^2 = \frac{1}{\sum_i \sigma_i^{-2}} \tag{3.7}$$

where $x = p^{MC}_{middleHTbit}(i) / p^{data}_{middleHTbit}(i)$ and i is the index referring to the straw layer. Tables 3.3 and 3.4 show the weighted mean for the simulation/Data ratio for each TRT region and gas mixture, in case of electron and muon channels. The results show

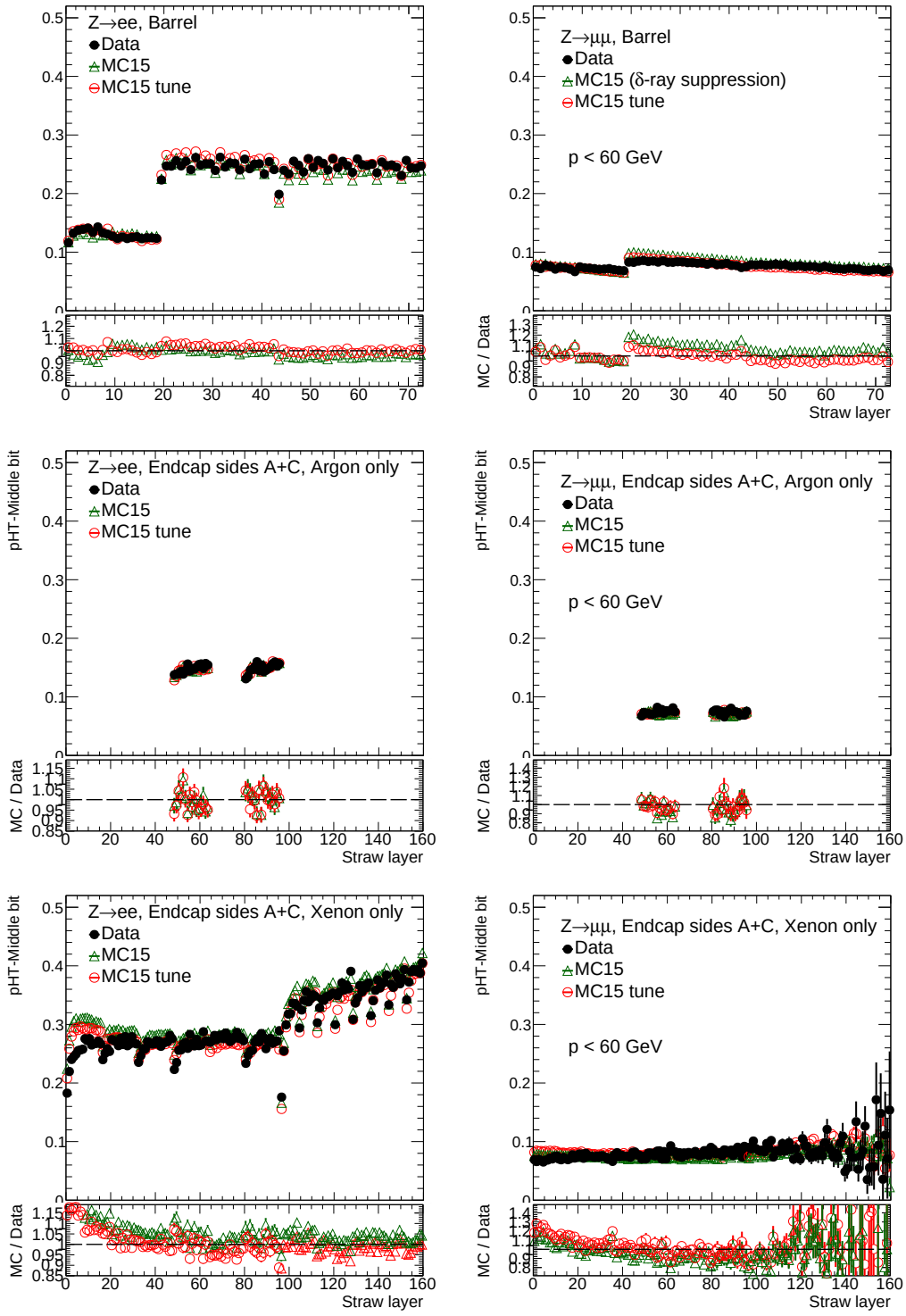

FIGURE 3.11: HT middle bit probability vs. straw layer for data (black) and simulation before any tune (green), after tuning procedure (red) for the barrel and end-cap, in case of Zee (left) and $Z\mu\mu$ (right) channels. The bottom part of the plots show the ratio between simulation and data.

that in general for electrons the HT probability is tuned to better than 2% while for muons the agreement is slightly worse.

	Original weighted mean	New weighted mean
Argon barrel short	0.959 ± 0.011	1.011 ± 0.009
Argon barrel long	1.010 ± 0.007	0.992 ± 0.005
Xenon barrel long	1.014 ± 0.002	1.014 ± 0.002
Argon endcap A side wheel	0.986 ± 0.009	0.986 ± 0.009
Xenon endcap A side wheel	1.019 ± 0.007	1.016 ± 0.003
Xenon endcap B side wheel	1.021 ± 0.008	0.983 ± 0.003

TABLE 3.3: The HT middle bit agreement in case of Zee channel

	Original weighted mean	New weighted mean
Argon barrel short	1.017 ± 0.006	1.015 ± 0.006
Argon barrel long	0.970 ± 0.003	0.974 ± 0.003
Xenon barrel long	0.954 ± 0.001	0.994 ± 0.002
Argon endcap A side wheel	0.968 ± 0.012	0.968 ± 0.012
Xenon endcap A side wheel	1.023 ± 0.005	1.060 ± 0.005
Xenon endcap B side wheel	0.929 ± 0.016	0.943 ± 0.016

TABLE 3.4: The HT middle bit agreement in case of $Z\mu\mu$ channel

The tuning of HT settings and TR efficiency shows significant improvement for the agreement between simulation and data for both electrons and muons in all TRT regions.

3.3 dE/dx studies

3.3.1 General concept of dE/dx estimator

The time of the closest (furthest) electron cluster drift to the wire located at the centre of the straw has a dependence on the time of leading (trailing) edge. Therefore it is possible to say that the leading edge time is related to the track- to-wire distance [67]. A particle will have a higher signal if it deposits more ionisation inside the straw. It will also have on average signal above threshold for longer time, having in addition earlier leading edge, later trailing edge and longer the time-over-threshold (ToT). Time-over-threshold can vary as a function of dE/dx in the straws, thus it is possible to obtain a ToT-based dE/dx estimate [58]. In general, dE/dx can be calculated by averaging and dividing the ToT by the track length in the straw over all good hits on the track.

An example of a formed bit pattern is show below with two groups of set bits or *islands*, which are separated by unset bits:

$$0000\boxed{1}111100000111111\boxed{1}000,$$

where first and last 1 represent leading edge and trailing edge. Fig. 3.12 shows an illustration of a track passing near the wire and corresponding signal islands.

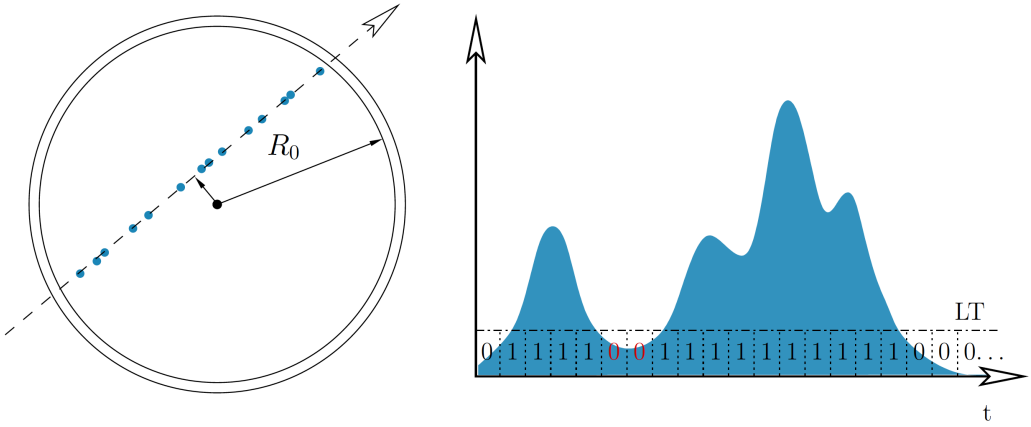

FIGURE 3.12: Formation of islands in the bit pattern.

Since ToT is extracted from the low threshold bit pattern various definitions can be used. The initial main approach **ToTLargerIsland** was developed in the period of Run1. However due to runs with high pile-up condition during the Run2 period it was required to develop new ways of definition of ToT from bit pattern. It is possible that due to high occupancy during Run2 more than one particle can pass the straw in an event, which can lead to bit pattern distortion. Three main approaches are considered:

- **ToTLargerIsland** defines the length of the largest signal island in the bit pattern as the Time-Over-Threshold (Fig. 3.13).

High threshold	0								0								0							
Low threshold	0	0	1	1	1	1	1	1	1	1	1	1	0	0	1	1	0	0	1	1	1	1	0	0
Time bins	1	2	3	4	5	6	7	8	9	10	11	12	13	14	15	16	17	18	19	20	21	22	23	24

FIGURE 3.13: ToTLargerIsland

- **ToTHighOccupancy** counts all bits between the LE and the TE, but for leading edge and trailing edge gates are defined in the bit pattern:
  For leading edge it is required to find a 0 to 1 transition in the range from second bit to the eighteenth, while search is going from the beginning.
  For trailing edge the gate is installed from the twentieth to the ninth bit and the search starts from the end of bit pattern. (Fig. 3.14).
- **ToTHighOccupancySmart** counts all bits as **ToTHighOccupancy**, but search for second TE has been added. (Fig. 3.15).

Several gas geometries are currently used in the TRT which leads to the additional task of ToT calculation when track crosses straws with different gas mixtures. Four scenarios have been considered and implemented, two main and perspective scenarios are selected for the further detailed study:

High threshold	0								0								0							
Low threshold	0	0	1	1	1	1	1	1	1	1	1	1	0	0	1	1	0	0	1	1	1	1	0	0
Time bins	1	2	3	4	5	6	7	8	9	10	11	12	13	14	15	16	17	18	19	20	21	22	23	24

FIGURE 3.14: ToTHighOccupancy

High threshold	0								0								0							
Low threshold	0	0	1	1	1	1	1	1	1	1	1	1	0	0	1	1	0	0	1	1	1	1	0	0
Time bins	1	2	3	4	5	6	7	8	9	10	11	12	13	14	15	16	17	18	19	20	21	22	23	24

FIGURE 3.15: ToTHighOccupancySmart

- ToT is calculated for each hit on track. For argon, the calculated ToT is normalised such that the mean value is equal to the mean value for xenon for each region of the TRT. The hit with the largest ToT is removed.
- Weighted average algorithm: the calculation of dE/dx estimator is performed for each gas mixture (Xe, Ar) track part and then a combined estimator is calculated. The algorithm removes the hit with the highest ToT for each gas part of the track (*kAlgReweightTrunkOne*).

Additional r-S and $<\mu>$ corrections are needed: the r-S calibration aims to make Time-Over-Threshold independent of the wire position (s) and the drift radius (r) (Fig. 3.16); $<\mu>$ corrections provide a shift of the dE/dx mean value which can occur in high occupancy conditions from pile-up effects. The following plan is required in order to provide best dE/dx estimator configuration and correct calibration parameters and values:

1. A decision has to be made on which ToT definition is to be used. Two approaches are chosen for consideration: **ToTHighOccupancySmart** and **TOTLargerIsland**.
2. Two scenarios have to be checked: *kAlgScalingToXe* and *kAlgReweightTrunkOne*. Due to additional layers filled with argon gas mixture in case of 2016 gas geometry it is possible that the argon ToT normalization will not work properly.
3. r-S corrections
4. corrections based on $<\mu>$ dependence

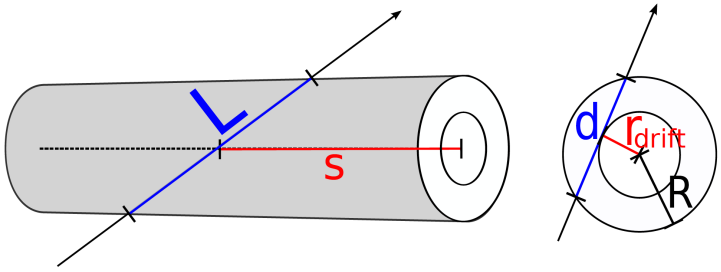

FIGURE 3.16: Sketch of a TRT straw with the track length in the straw L, the projection of the track length in the x-y-plane d, the straw radius R (2 mm), the drift radius r_{drift} and the position on the readout wire s.

3.3.2 Samples and event selection

Two run periods are considered for 2015 and 2016 years, collected at pp collisions at $\sqrt{s}$ = 13 TeV. Simulation samples are generated with two different gas geometries. For the 2015 run period for the baseline scenario one innermost barrel layer and two layers in endcap wheels are filled with an argon gas mixture, the other layers are filled with a xenon gas mixture, as it shown in Fig. 3.17. For the 2016 run period additional layers with argon gas mixture are added - one middle layer in barrel and three layers in endcaps as shown in Fig. 3.18

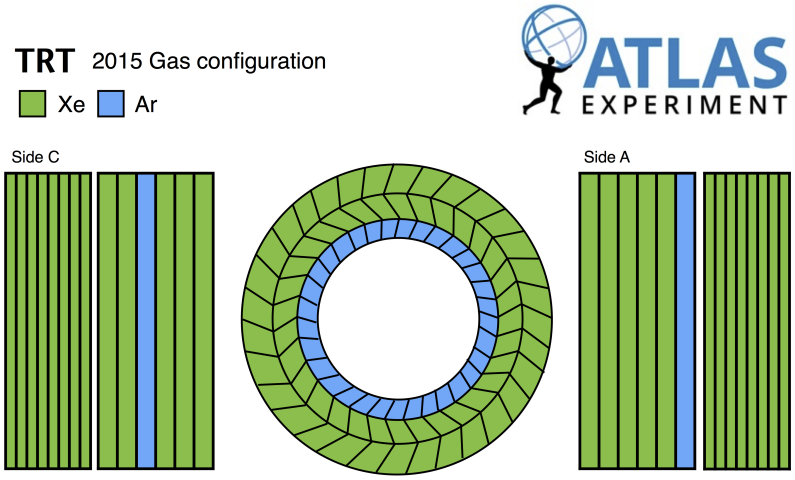

FIGURE 3.17: Barrel layer 0 (B0), endcap side C wheel 3 (EC3), endcap side A wheel 5 (EA5) are filled by an argon gas mixture, the rest layers are filled with a xenon gas mixture

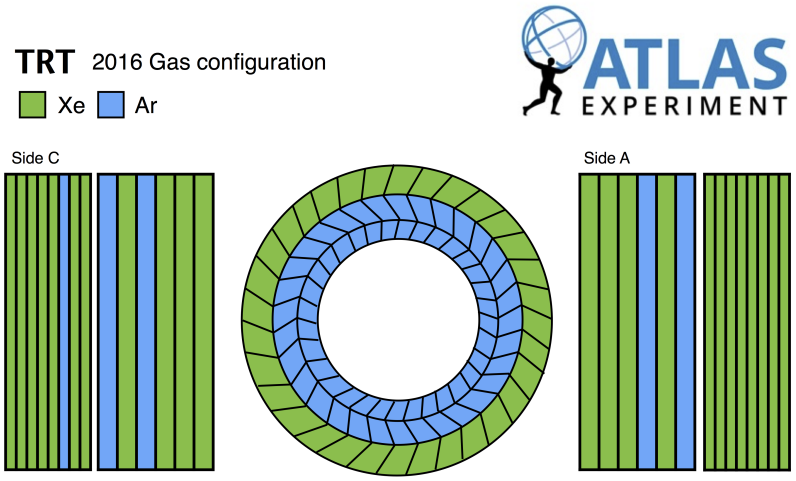

FIGURE 3.18: Barrel layers 0, 1 (B0, B1), endcap side C wheels 3, 5, 8 (EC3, EC5, EC8), endcap side A wheels 3 and 5 (EA3, EA5) are filled with an argon gas mixture, the rest layers are filled with a xenon gas mixture

Two types of samples are used for both data and simulation: Minimum Bias samples with $<\mu>$ less than one for studies of "pure" not distorted dE/dx without any pile-up conditions, and $Zee/Z\mu\mu$ samples with two different $<\mu>$ regions ($8 < <\mu> < 14$, and $28 < <\mu> < 36$ in case of the 2015 and 2016 run periods respectively) which allow a study of dE/dx performance under different pile-up conditions.

Tracks are selected using the standard minimum bias track selection which is applied in case of any $<\mu>$ value: at least one Pixel hit has to be selected with a minimum of 5 SCT hits. Two options of vertex selection are considered for these studies: selection of only primary vertices for all calibration studies and selection of secondary vertices, which is used only in case of particle separation power studies. The selection of primary vertices is the following:

- $|d_0| < 1.5$mm
- $|z_0 \sin(\theta)| < 1.5$mm

and for selection of secondary vertices both of the opposite requirements on $|d_0|$, $|z_0 \sin(\theta)|$ are used:

- $|d_0| > 1.5$mm
- $|z_0 \sin(\theta)| > 1.5$mm

Fig. 3.19 shows the dE/dx estimator distribution for simulation and data after all selection in case of primary vertices.

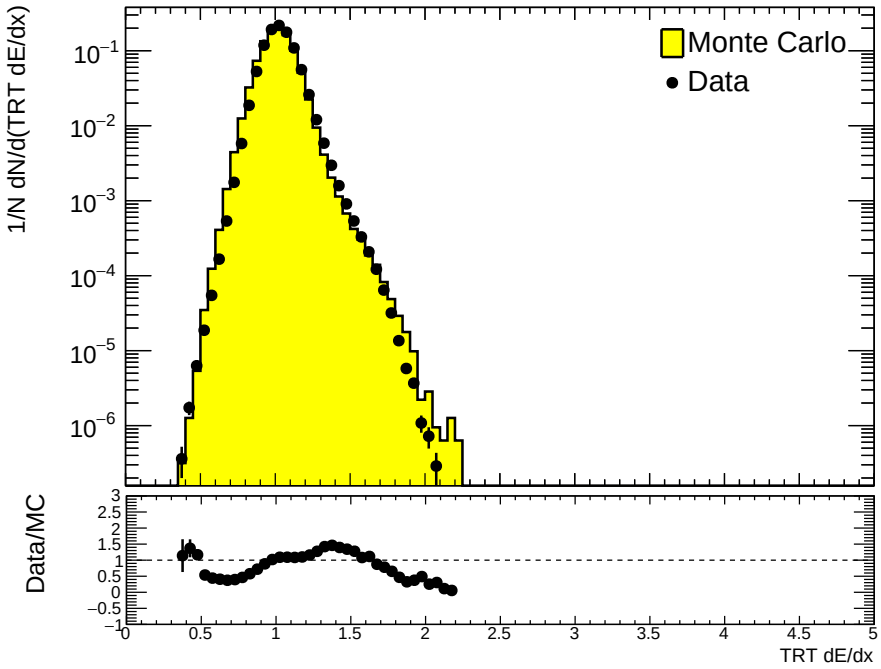

FIGURE 3.19: TRT dE/dx^{ToT} estimator distributions. The bottom part of the plots show the ratio between data and simulation.

3.3.3 dE/dx performance with low pileup conditions

In order not to bias dE/dx estimator results by pile-up effects only minimum bias samples with $<\mu>$ less than one are considered.
A dedicated study is provided to analyse which of the two approaches - **ToTHighOccupancySmart** and **TOTLargerIsland** - shows better results. The simplest way to understand this is to check which approach gives better results in particle separation. This can be done by selecting secondary vertices, as it allows to determine peaks coming from different particles in clear way. Fig 3.20 shows dE/dx estimator dependence on absolute track momentum p, for **TOTLargerIsland** (left) and **ToTHighOccupancySmart** (right). The dependencies are presented for data 2016 and simulation samples 2015, the choice of samples is made under their availability.

In order to finally define which approach shows better results, it is decided to use narrow p regions and study dE/dx estimator distribution in these p regions. Several momentum regions are chosen and it's possible to see the evolution of dE/dx estimator separation power over momentum value (Fig. 3.21). Both approaches show ability in particle separation, but as it is seen, for both data and simulation, **TOTLargerIsland** shows better results in separation power.

The check of two gas mixture scenarios *kAlgScalingToXe* and *kAlgReweightTrunkOne* is required as the next step. The same procedure of slicing in several momentum regions is performed; from Fig. 3.22 it is seen clearly that there is no significant difference between two scenarios, making it possible to further use any of them.

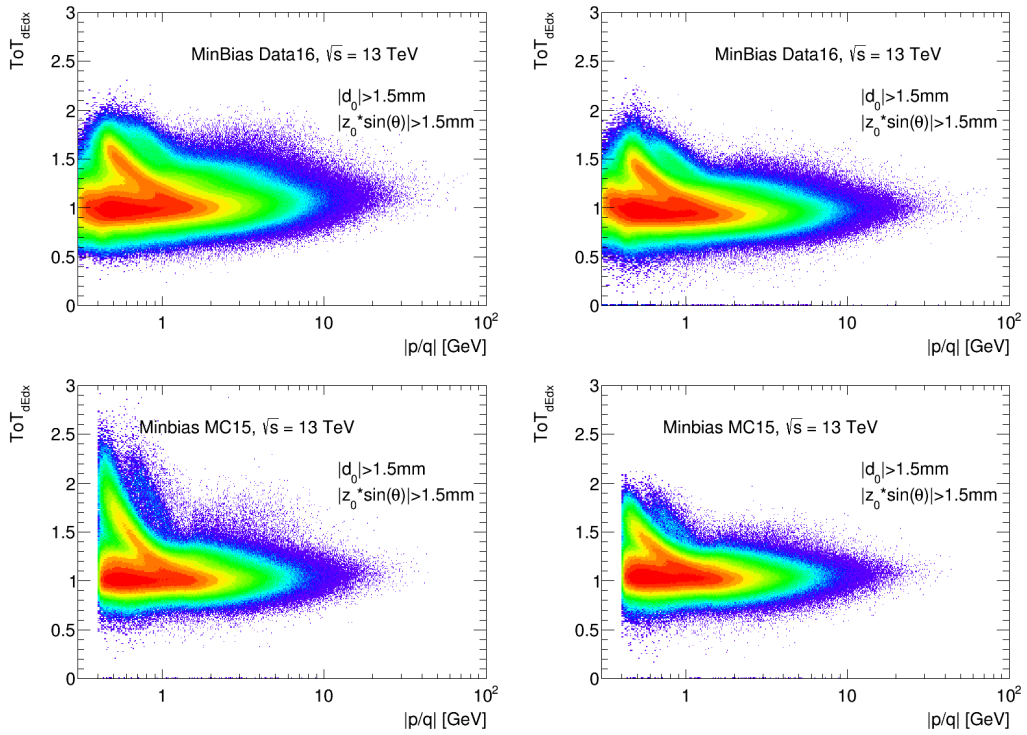

FIGURE 3.20: TRT dE/dx estimator vs absolute track momentum dependence for **ToTHighOccupancySmart** (left) and **TOTLargerIsland** (right), in case of data 2016 and simulation 2015

3.3.4 dE/dx performance with high pileup conditions

Due to runs with slow increase of $<\mu>$ during 2015 and 2016 periods it was possible to study dE/dx estimator under different pile-up conditions. For this purpose three different samples are chosen: minimum bias sample with $<\mu>$ value less than one which allows to see the dE/dx behavior with no distortion from pile-up, sample from 2015 run period with $<\mu>$ between 10 and 14 and sample with high pile-up with $<\mu>$ between 30 and 35. The same distributions as in section 3.3.3 are studied - dE/dx estimator distribution over absolute momentum (left) and the dE/dx estimator distribution in a given momentum range (right), which are presented on Fig. 3.23. It is clearly seen that separation power degrades over $<\mu>$ and for high pile-up almost no separation is observed. As it is expected that higher pile-up will be used in the following run periods (average $<\mu>$ value in 2018 was around 40-60), and the performance of the dE/dx measurements at this conditions will be very much limited.

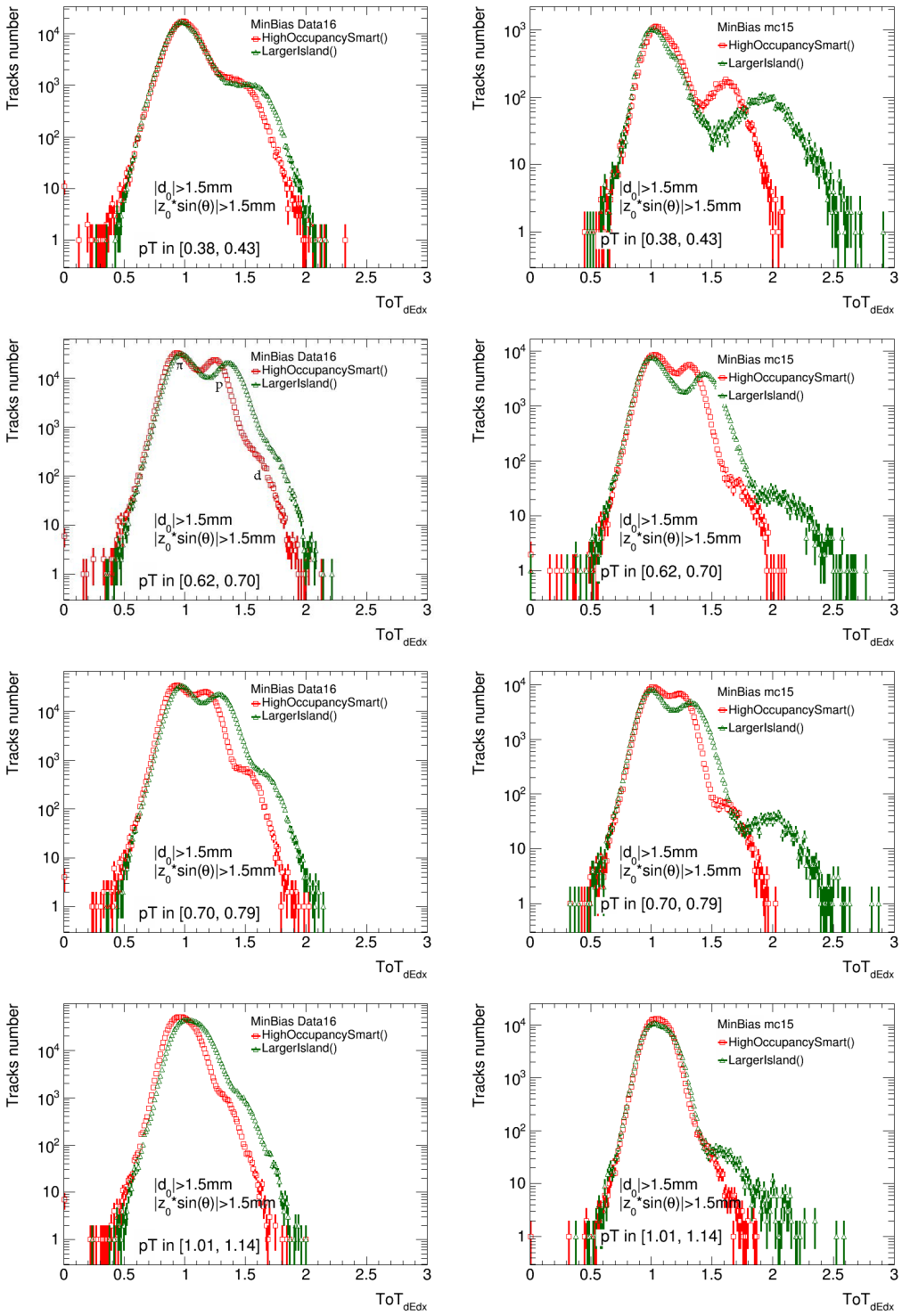

FIGURE 3.21: TRT dE/dx estimator in four momentum slices for **ToTHighOccupancySmart** (red square) and **TOTLargerIsland** (green triangle), in case of data 2015 (left) and simulation 2015 (right).

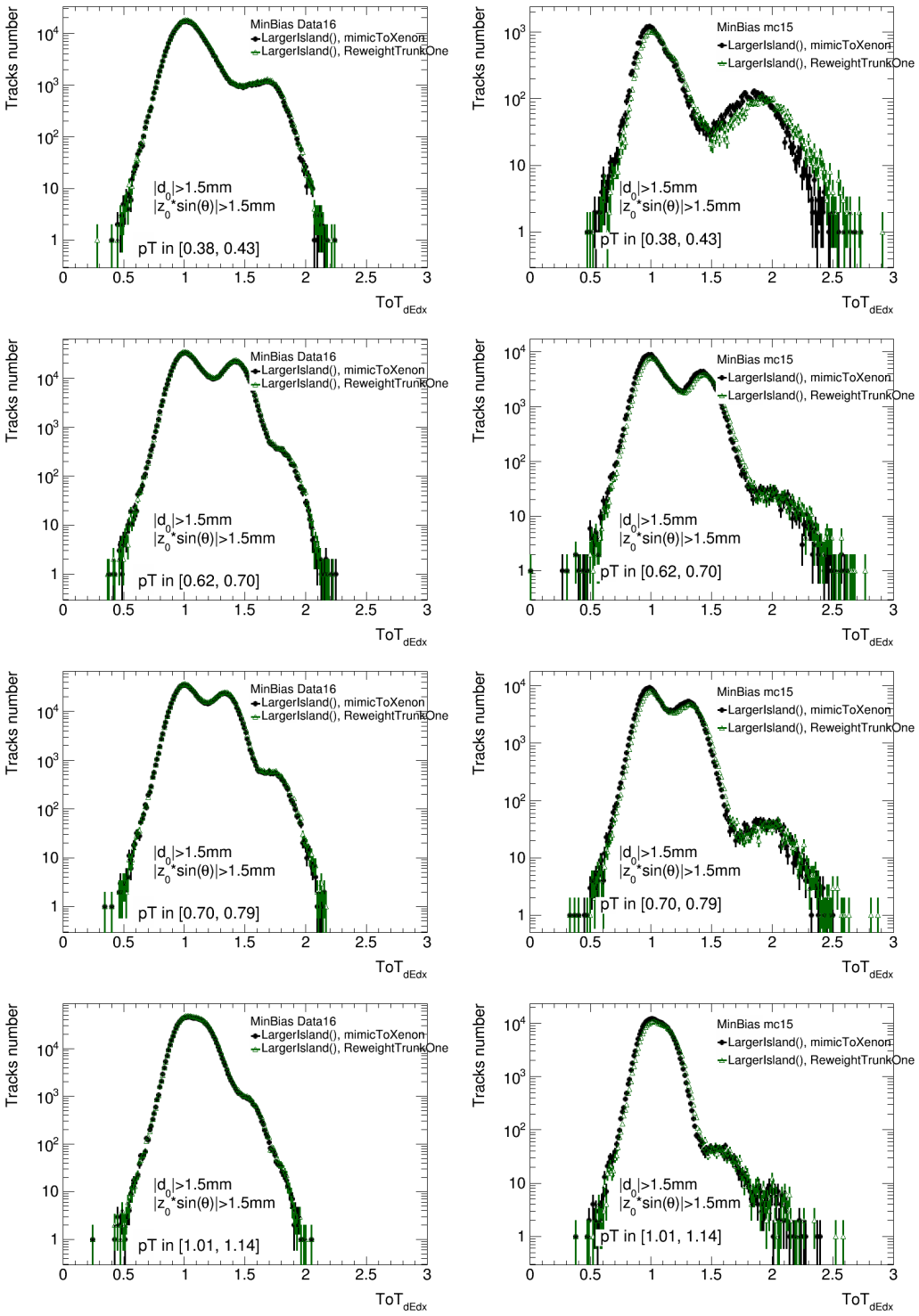

FIGURE 3.22: TRT dE/dx estimator in four momentum slices for *kAlgScalingToXe* (black circle) and *kAlgReweightTrunkOne* (green triangle), in case of data 2015 (left) and simulation samples 2015 (right)

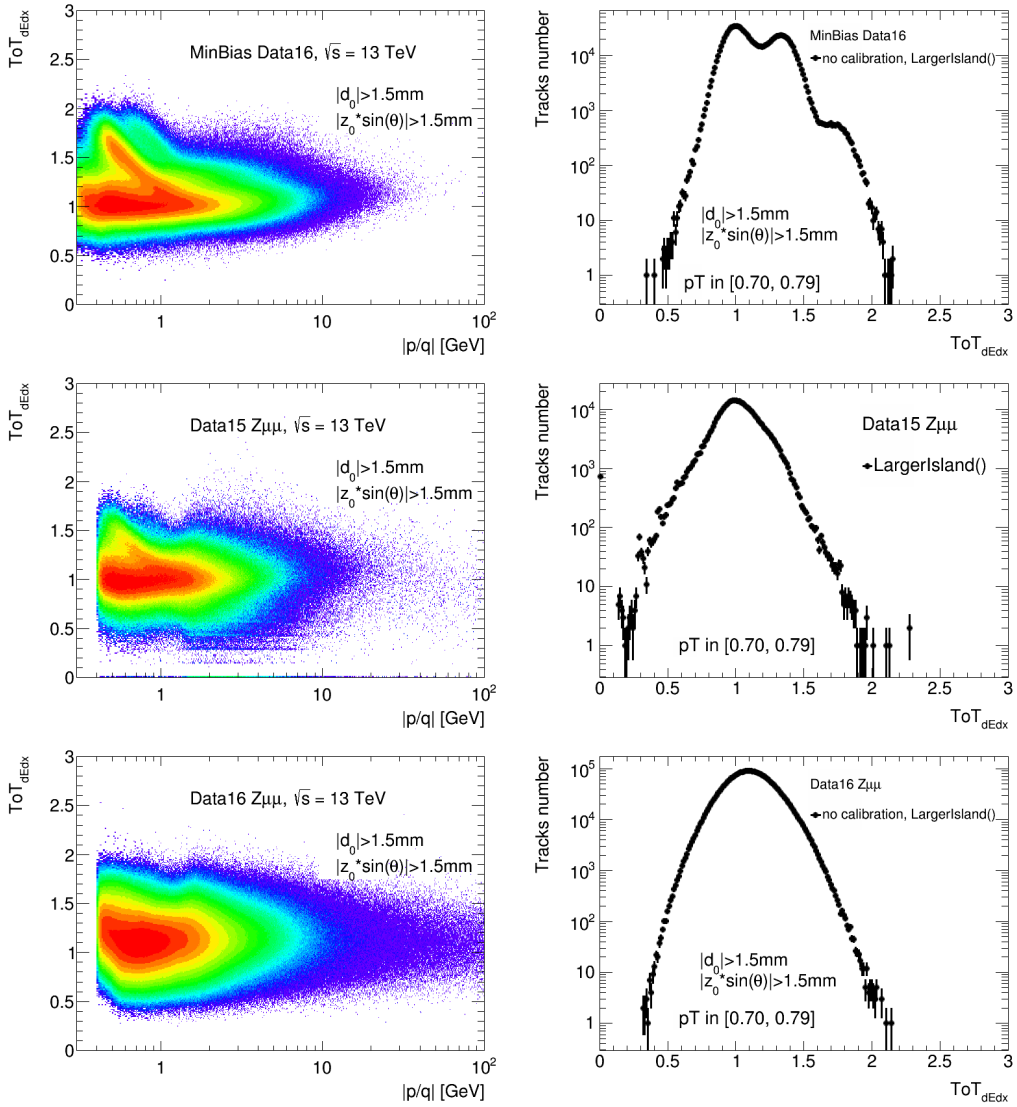

FIGURE 3.23: TRT dE/dx estimator versus $|p/q|$ (left) and dE/dx estimator distribution for $0.70 < p_T < 0.79$ (right) in case of $<\mu>$ < 1 (top), $<\mu>$ from 10 to 15 (middle) and $<\mu>$ from 30 to 35 (bottom).

3.4 Summary

This chapter describes performance studies of the TRT detector necessary for precision measurements in future physics analysis. Two studies related to improvements of performance and particle identification are presented. The first part is dedicated to the TRT digitisation tune. It is shown that tuning allows to improve the agreement for the TRT HT middle-bit fraction between data 2015 and simulation. The high threshold value and transition radiation efficiency are tuned to achieve good agreement of the TRT HT middle-bit fraction.

The second part is dedicated to the dE/dx estimator performance studies. A number of conditions have been checked, and they include update of the preferred Time-over-Threshold bit pattern calculation approach which shows good separation power and improved performance in comparison with previous default approach. dE/dx estimator performance under high occupancy is checked and it was shown that at high $<\mu>$ particle separation with this method will be very much limited.

Results of both of the studies were implemented in the main ATLAS software releases, and used further in the particle reconstruction for Run-2 of the LHC.

4 Object reconstruction algorithms

Successful reconstruction of electrons, photons, muons and jets is necessary for most of the physics analyses performed at ATLAS. A dedicated set of algorithms (so-called event reconstruction) has been developed to reconstruct objects from raw detector data and provide tools for the efficient measurement of various kinematic properties of such objects.

The main focus of this chapter will be on photon reconstruction. The optimal performance in their measurement plays a crucial role in the precise measurement of the properties of particles such as the Higgs (particularly $H \to Z\gamma$) and W/Z bosons, in searches for new particles and in measurements of Standard Model properties. For the $H \to Z\gamma$ analysis the invariant mass is computed with use of reconstructed particles in their final states, therefore it is important to have a good understanding of kinematic properties of photons.

Electrons are used in a large number of searches as well, such as the Higgs boson $H \to Z\gamma$, $H \to WW^*$ and $H \to ZZ^*$ decay channels, and they are also a signature of the W and Z bosons decays. The electron and photon reconstructions procedures use similar algorithms. The description of these algorithms is provided in Sec. 4.1. The method is based on information from inner tracking detectors and the cluster reconstruction in the electromagnetic (EM) calorimeter with energy calibration corrections. Sec. 4.1.8, 4.1.9 and 4.1.6 provide overview of photon and electron identification methods.

A brief description of the muon object reconstruction is provided in Sec. 4.2, and the jet object reconstruction is provided in Sec. 4.3. The latter two parts do not describe my personal contribution as they mostly aim to provide background for the following sections and chapters.

4.1 Electron and photon reconstruction

The photon and electron reconstruction is performed through several algorithms. These algorithms include the object trajectory (or track) reconstruction from hits in the inner detector and topological clusters construction from energy deposits in the calorimeters. Fig. 4.1 shows an example of such an event with an electron traversing the ATLAS detector. It typically hits the IBL pixel layer, 3 pixel layers, 4 silicon strips and in average 30 straw hits in the TRT. Next it crosses the solenoid and deposits its energy in electromagnetic calorimeter layers, with only small amount of energy reaching the hadronic calorimeter.

The basic reconstruction level in the EM calorimeter for photons and electrons relies on a so-called "sliding window algorithm" [68], which determines local energy deposits in the EM calorimeter, using fixed-size clusters of calorimeter cells. This has been recently improved with use of dynamic, variable-size clusters called superclusters [69, 70, 71]. The optimisation became possible with the use of improved calibration techniques and it allows energy to be recovered from bremsstrahlung photons or from electrons from photon conversions with high efficiency.

An object is reconstructed as an electron when a track (or tracks) is matched to a cluster, built from energy deposits in the calorimeter (supercluster). For the photon reconstruction, it is necessary to define two possible types: converted and unconverted. A converted photon is defined as an object consisting of a cluster matched to a conversion vertex (or vertices), and an unconverted photon is defined as a cluster matched to neither an electron track nor a conversion vertex.

Clusters for the object reconstruction are selected from energy deposits measured in topologically connected EM and hadronic calorimeter cells (topo-clusters), which are described in Sec. 4.1.2. The superclusters are formed separately for electron and photon objects using the seed clusters - primary clusters formed from the electron shower, and the satellite clusters - nearby secondary clusters which are formed from the photon showers. The matching between electron tracks or conversion vertices to the resulting superclusters (electron and photon, respectively) happens after applying energy calibration, described in Sec. 4.1.5. The final selection of the fully reconstructed objects for analysis happens after the setup of specially defined discriminating variables, which are used to separate electrons and photons from background (Sec. 4.1.4)

4.1.1 Track and photon conversion reconstruction

Track reconstruction begins with hits in the inner detector tracking layers. Clusters from these hits are assembled in the Pixel and SCT detectors in order to create three three-dimensional measurements used for track seeds forming. The tracking reconstruction steps are as follows: first, with the basic p_T and spatial requirements, segments of 3 silicon hits are found. Second, a pattern recognition algorithm based on a Kalman filter [72] is used. It models energy loss of a particle through the interactions with the detector material. Track seeds with $p_{\mathrm{T}} > 400$ MeV are fit using the ATLAS Global χ^2 Track Fitter [73] following the hypothesis used in the pattern recognition. Third, the track reconstruction proceeds with an ambiguity step where track candidates sharing same hits are resolved. Additionally, tracks are re-fitted using a Gaussian sum filter (GSF) algorithm [74] with the condition of the track to have at least four silicon hits and a loose match to EM clusters. The GSF method allows to better account for radiative energy losses in detector material. When such losses happen they lead to a decrease in electron's momentum, resulting in increased curvature of the trajectory in the magnetic field. The GSF method improves all track parameters relevant to the bending-plane, such as the transverse impact parameter significance: d_0 divided by its estimated uncertainty $\sigma(d_0)$.

As the final step GSF-track candidates are matched to the candidate EM calorimeter seed cluster and the final cluster size is determined. In case of several tracks the primary electron track is chosen considering the number of hits in the SCT, the number of hits in the innermost silicon layer and the distance in ϕ and η between the tracks and the cluster barycentres in the second layer of the calorimeter. However, if the primary track does not have pixel hits and can be matched to a secondary vertex, it is classified as a photon conversion.

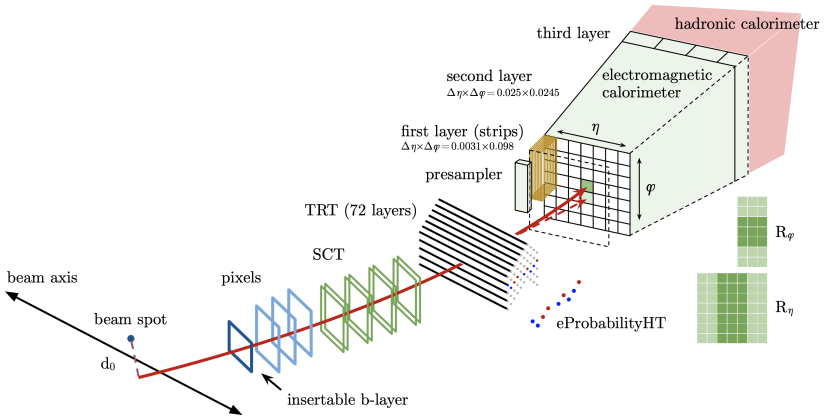

FIGURE 4.1: Example of an electron traversing the ATLAS detector.

For the photon conversion reconstruction [70], standard track reconstruction is first performed everywhere in the inner detector, part of which includes use of TRT detector and is described in Chapter. 3. Generally tracks with silicon hits (Si tracks) and tracks reconstructed only in the TRT detector (TRT tracks) are used for the conversion-vertex reconstruction. Two opposite-charge tracks pointing to the reconstruction of a two-track conversion vertex which is consistent with a massless particle. Single-track vertices are tracks without hits in the innermost sensitive layers. Only the tracks that have a high probability to be electron tracks as determined by the TRT detector are used to build conversion vertices in order to have increased converted-photon purity [58]. It is possible to reconstruct both double-track (single-track) Si conversions, where conversions are reconstructed with two (one) Si tracks and to have reconstructions of single or double-track TRT conversions, where one or two TRT tracks are used for reconstruction of conversions. The newly optimised tracking ambiguity processor is used to improve the efficiency for double-track Si conversions in the case where the two tracks are expected to be close to each other or to have shared hits.

The conversion vertices are matched to the EM topo-clusters, where the vertex with the smallest conversion radius is preferred. In the case of multiple conversion vertices matched to a cluster, double-track Si track conversions are preferred over other double-track conversions, followed by single-track conversions.

4.1.2 Topo-cluster reconstruction

The reconstruction algorithm for topo-clusters [69, 75] begins by following spatial signal-significance patterns generated by particle showers. The initial proto-clusters are formed in the electromagnetic calorimeter and hadronic calorimeters by the use of a set of noise thresholds. Noise thresholds are necessary for the suppression of the known electronic noise and pile-up noise, where the latest is estimated from the average instantaneous luminosity for Run2 in the period 2015-2018. The proto-clusters then collect neighbouring cells. Each neighbour cell passing the threshold of significance becomes a seed cell in the next iteration, collecting each of its neighbours into the proto-cluster.

Both electron and photon reconstruction starts from the topo-clusters using only the energy from cells in the electromagnetic calorimeter. The transition region of

$1.37 < |\eta| < 1.63$ is excluded since the energy measured in the presampler and the scintillator between the calorimeter cryostats is also added. The energy of the clusters is used to define fraction f_{EM} as the ratio of the EM energy to the total cluster energy.

4.1.3 Supercluster reconstruction

The seed cluster with its associated satellite clusters is called a supercluster. Photon and electron supercluster reconstruction proceeds independently in two steps: first, topo-clusters have to pass a requirement to be used as seed cluster candidates (in order to form the basis of superclusters); second, topo-clusters near the seeds, which can emerge from bremsstrahlung radiation or topo-cluster splitting are identified as satellite clusters. The final superclusters are formed when satellite clusters are added to the seed candidates. Later to fully form a supercluster, the initial list of EM topo-clusters is sorted according in descending E_T. The cluster transverse energy, E_T, must be greater than 1.5 GeV to be defined as a supercluster seed for the case of photon reconstruction, with no requirement made on any track or conversion vertex matching. For the electron reconstruction a cluster becomes a supercluster seed if it has a minimum energy E_T of 1 GeV and is matched to a track with at least four hits in the silicon tracking detectors. A cluster cannot be used as a seed cluster if it has already been added as a satellite cluster to another seed cluster.

Fig. 4.2 shows a summary of a process of finding satellite clusters for photon and electron objects. The steps described below rely on tracking information in order to be able to discriminate either conversion electrons or radiative photons from pile-up noise or other unrelated clusters. The current method of finding a secondary EM shower from an object is to consider a satellite cluster within a window of $\Delta\eta \times \Delta\phi = 0.075 \times 0.125$ around the seed cluster barycentre. If photon conversion vertices only have Si tracks, a cluster is added as a satellite if its best-matched (electron) track belongs to the conversion vertex matched to the seed cluster. In order to build a supercluster the algorithm has to assign cells to a provided supercluster. The size of each topo-cluster is restricted to a maximal width of 0.075 (0.125) in the η direction in the barrel (endcap) region, respectively, to have a limit on the supercluster's sensitivity to pile-up noise. Interactions between the photon (or electron) and detector material cause the electromagnetic shower to spread in the ϕ direction since the magnetic field in the inner detector is parallel to the beam-line, and the restriction in η direction generally allows the photon (electron) energy to be captured.

4.1.4 Creation of electrons and photons for analysis

For the electron reconstruction, tracks have to match to electron superclusters. An electron is defined and created for analysis if a cluster with a good track attached can be found with no good photon conversion verticies.

For the photon reconstruction, an initial energy calibration and position correction has to be applied to photon superclusters with tracks matching conversion vertices. For the creation of the analysis-level photons the next step is required: a seed cluster can produce both an electron and a photon, since electron and photon superclusters are built independently. Next, it's necessary to provide an ambiguity resolution mechanism, which works in the following way: if a chosen object can be identified in a simple way as only a photon (for example, a cluster exists with no track attached) or only as an electron (i.e. a cluster with a good track attached, with no photon conversion vertex attached), then no ambiguity resolution is necessary; otherwise, both an electron and a photon object are created and marked as ambiguous.

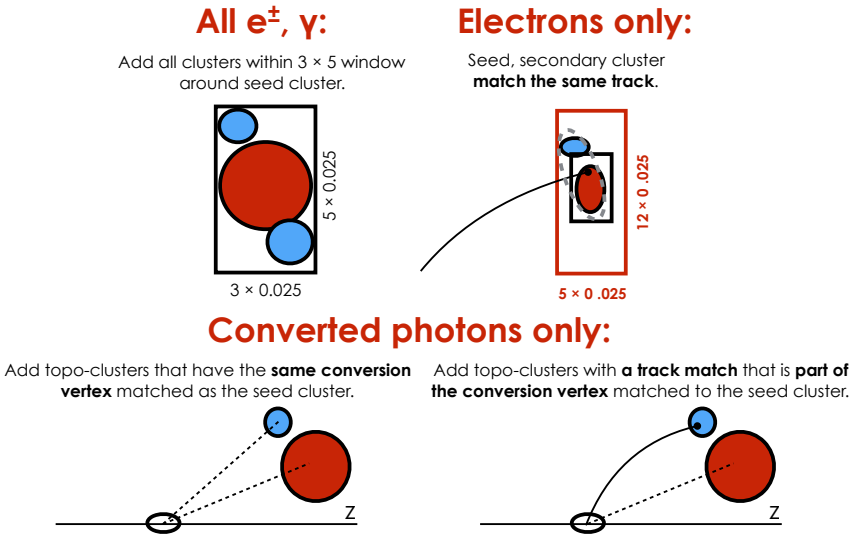

FIGURE 4.2: Diagram of the superclustering algorithm for electrons and photons. Seed clusters are shown in red, satellite clusters in blue.

The initial supercluster calibration is performed before the final track and conversion matching, followed by the recalibration of the energies of the photons (electrons) since the energy calibration depends on matched tracks and conversion vertices. More information about the calibration methodology is given in Sec. 4.1.5.

At the final step, shower shape and other discriminating variables [70, 71] are calculated to provide a powerful tool for electron and photon identification. A list is given in Table 4.1 for calorimeter-based variables and in Table 4.2 for tracking variables. The lateral shower shapes are based on the position of the most energetic cell, so they are independent of the clustering used, provided the same most energetic cell is included in the clusters.

The calorimeter-based variables, listed in Table 4.1, can capture differences in shower shapes of different particles (electrons, photons and hadronic jets). They are mostly based on measurements of energy ratios and shower widths in different layers of the EM and hadronic calorimeters, which allows to distinguish electrons and photons from hadrons.

The track-based variables, listed in Table 4.2 describe the number of hits associated with the track for the pixel, SCT, and TRT detectors, the track fit, and the track-calorimeter matching. Variables related to different track parameters can help to distinguish electrons from hadronic activity, and variables describing quality of matching between the track and the cluster can be used for both distinguishing electrons from photon converted tracks or hadrons.

The transition radiation effect, provided by the TRT (described in Sec. 3.1.1), provides an additional way of discrimination between electrons and heavier particles. Light particles (such as electrons) have larger γ factor and they radiate more photons than heavy particles (such as pions and muons) with lower γ factor. The radiated photons originating from electrons then produce larger number of high threshold (HT) hits in the TRT detector compared to heavier particles. This number is later used to define the High Threshold Fraction, F_{HT}, which is calculated as the ratio of HT hits to the total number of TRT hits along the reconstructed track. Next, a likelihood probability can be used as a discriminating variable for separation of electrons from pions. It is based on the HT hit information and is defined as per hit as a function of

the location of the straw in the detector and the track-to-wire distance of the hit. It is then calculated as a ratio of probabilities between for electron and pion hypotheses.

A description of the electron identification methods is given in Sec. 4.1.6 and Sec. 4.1.7. More information about the photon variables and the identification methods is given in Sec. 4.1.8 and Sec. 4.1.9.

ATLAS simulations do not always predict the photon (or electron) shower developments in the EM calorimeter with high accuracy [76]. In particular, the shower profiles in η are broader in data than in simulation. The disagreements which are currently observed can arise due to several potential effects: the mismodeling of the electric field in the LAr gaps, or the mismodeling of the energy sharing between calorimeter cells due to electronics failures possible in η direction, etc. It is possible to reduce the observed disagreement between data and simulation with the corrections applied as simple shifts to each of the shower shape distributions in Monte-Carlo simulation. These shifts, so-called *fudge factors*, are obtained by the minimisation of the χ^2 comparisons between data and simulated shower shapes. The fudge factor approach is effective for first order corrections of the shower shape distributions, and the residual differences between data and simulation are accounted through identification efficiency corrections, described in case of photons later in Sec. 5.2

4.1.5 Energy calibration

The energy calibration is required to correct the energy response of electrons and photons from the energy of a cluster of cells in the EM calorimeter, and it is described in ref. [77]. Several steps follow:

- the energy resolution of electrons or photons is optimised, and the impact of material in front of the calorimeter is minimised with use of the multivariate regression algorithm.
- a correction to the data is applied before the estimation of the energy of the electron or photon to adjust the relative energy scales of the different layers of the EM calorimeter. That correction is required for the correct extrapolation of the energy calibration to the full energy range of electrons and photons.
- the correction of the geometric effects is applied at the boundaries between calorimeter modules, using electrons from Z boson decays, with the improvements of the corrections for non-nominal HV settings in some parts of the calorimeter.
- the following corrections are similar for both electrons and photons, and are done with use of a sample of Z boson decays to electrons: the full energy scale is corrected in data and an additional correction is applied to simulation to account for the differences in energy resolution between data and simulation.
- the final step of the calibration is to check of the results using the comparison between data and simulation with independent samples: $J/\psi \to ee$ decays are used probe the energy response for electrons, while radiative Z boson decays are used to check the energy response for photons.

For the final step of the photon calibration, the energy scale corrections are performed to correct the photon energy scale. Radiative Z boson decays to both electrons and muons, covering mainly the low-energy region, are used for the data-driven correction validation. Residual energy scale factors for photons, $\Delta\alpha$, are derived by

Category	Description	Name	Usage
Hadronic leakage	Ratio of E_{T} in the first layer of the hadronic calorimeter to E_{T} of the EM cluster (used over the ranges $\lvert\eta\rvert < 0.8$ and $\lvert\eta\rvert > 1.37$)	R_{had1}	e/γ
	Ratio of E_{T} in the hadronic calorimeter to E_{T} of the EM cluster (used over the range $0.8 < \lvert\eta\rvert < 1.37$)	R_{had}	e/γ
EM third layer	Ratio of the energy in the third layer to the total energy in the EM calorimeter	f_3	e
EM second layer	Ratio of the sum of the energies of the cells contained in a 3×7 $\eta \times \phi$ rectangle (measured in cell units) to the sum of the cell energies in a 7×7 rectangle, both centred around the most energetic cell	R_η	e/γ
	Lateral shower width, $\sqrt{(\Sigma E_i \eta_i^2)/(\Sigma E_i) - ((\Sigma E_i \eta_i)/(\Sigma E_i))^2}$ where E_i is the energy and η_i is the pseudorapidity of cell i and the sum is calculated within a window of 3×5 cells	$w_{\eta 2}$	e/γ
	Ratio of the sum of the energies of the cells contained in a 3×3 $\eta \times \phi$ rectangle (measured in cell units) to the sum of the cell energies in a 3×7 rectangle, both centred around the most energetic cell	R_ϕ	e/γ
EM first layer	Total lateral shower width, $\sqrt{(\Sigma E_i (i - i_{\max})^2)/(\Sigma E_i)}$, where i runs over all cells in a window of $\Delta\eta \approx 0.0625$ and $i_{\max}$ is the index of the highest-energy cell	w_{stot}	e/γ
	Lateral shower width, $\sqrt{(\Sigma E_i (i - i_{\max})^2)/(\Sigma E_i)}$, where i runs over all cells in a window of 3 cells around the highest-energy cell	w_{s3}	γ
	Energy fraction outside core of three central cells, within seven cells	f_{side}	γ
	Difference between the energy of the cell associated with the second maximum, and the energy reconstructed in the cell with the smallest value found between the first and second maxima	ΔE_s	γ
	Ratio of the energy difference between the maximum energy deposit and the energy deposit in a secondary maximum in the cluster to the sum of these energies	E_{ratio}	e/γ
	Ratio of the energy measured in the first layer of the electromagnetic calorimeter to the total energy of the EM cluster	f_1	e/γ

TABLE 4.1: Discriminating calorimeter variables used for electron and photon identification.

Category	Description	Name	Usage
Track conditions	Number of hits in the innermost pixel layer	$n_{\text{innermost}}$	e
	Number of hits in the B-Layer	n_{Blayer}	γ
	Number of hits in the pixel detector	n_{Pixel}	e
	Total number of hits in the pixel and SCT detectors	n_{Si}	e
	Total number of hits in the TRT detector	n_{TRT}	
	Ratio of the number of high-threshold hits to the total number of hits in the TRT	F_{HT}	e
	Likelihood probability based on transition radiation in the TRT	eProbabilityHT	e
Track parameters	Transverse impact parameter relative to the beam-line	d_0	e/γ
	Significance of transverse impact parameter defined as the ratio of d_0 to its uncertainty	$\lvert d_0/\sigma(d_0)\rvert$	e/γ
	Momentum lost by the GSF track between the perigee and the last measurement point divided by the momentum at perigee	$\Delta p/p$	e
Track–cluster matching	$\Delta\eta$ between the cluster position in the first layer of the EM calorimeter and the extrapolated track	$\Delta\eta_1$	e
	$\Delta\phi$ between the cluster position in the second layer of the EM calorimeter and the momentum-rescaled track, extrapolated from the perigee, times the charge q	$\Delta\phi_{res}$	e
	Ratio of the cluster energy to the measured track momentum	E/p	e

TABLE 4.2: Discriminating tracking variables used for electron and photon identification.

comparing the mass distribution of the $\ell\ell\gamma$ system in data and simulation. If $\Delta\alpha$ is consistent with zero within the uncertainties the energy calibration is correct. Fig. 4.3 shows the measured within the uncertainties as a function of E_{T}, separately for converted and unconverted photons.

4.1.6 Electron identification

Both ATLAS inner detector and calorimeter provide sets of software reconstruction algorithms which allow to discriminate electrons from their possible background - hadronic jets and photon conversions. Different types of hadronic jets can be typically distinguished from electrons by their hadronic shower as they leave more diffused electromagnetic response. Hadronic showers also deposit energy in both EM and hadronic calorimeters, while electron's energy deposit is typically contained only inside the EM calorimeter. Background, coming from photon conversions, can be distinguished from electrons by slightly different shower signatures, larger impact parameter and sometimes poor track-calorimeter matching. A set of variables, described in Sec. 4.1.4, are used in the electron identification according to their discriminating power, necessary for the separation of prompt isolated electrons from energy deposits from the background. The electron candidate is required to pass set of quality requirements, such as a number of hits in the SCT and in the two inner tracking layers closest to the beam line. The discriminant is formed from the likelihoods of a reconstructed electron to either originate from signal, L_S, or background, L_B using transverse impact parameter of the track and its significance. In addition, particle identification in the TRT and $\Delta p/p$ are used. The discriminant is calculated

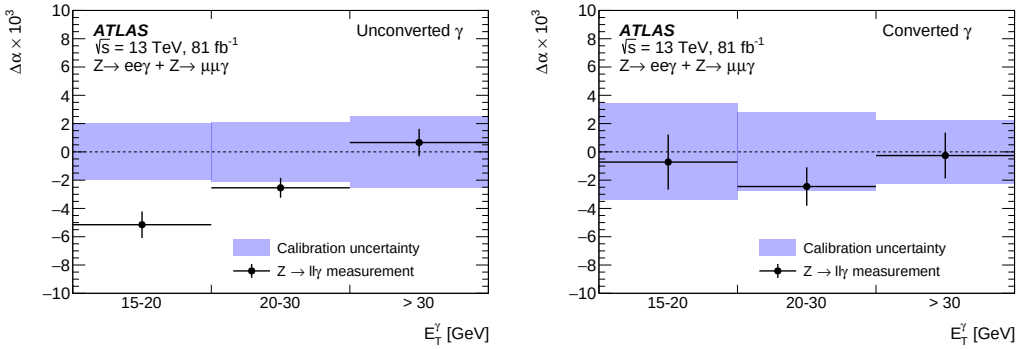

FIGURE 4.3: Residual photon energy scale factors, within the uncertainties, for unconverted (left) and converted (right) photons as a function of the photon transverse energy E_{T}. The points show the measurement with its total uncertainty and the band represents the full energy calibration uncertainty for photons from $Z \to \ell\ell\gamma$ decays.

from probability density functions (pdfs), P, which are created by smoothing histograms of the n discriminating variables with an adaptive kernel density estimator, separately for signal and background:

$$L_{S(B)}(\mathbf{x}) = \prod_{i=1}^{n} P_{S(B),i}(x_i).$$

Signal and background the pdfs take the values $P_{S,i}(x_i)$ and $P_{B,i}(x_i)$, respectively, for the quantity i at value x_i. The likelihood discriminant d_L is defined as the natural logarithm of the ratio of L_S and L_B. The electron identification working points are defined as a selection on the likelihood discriminant, which gives better background rejection than a "cut-based" approach. The pdfs are derived from data for all of eta/E_{T} bins for both the offline and trigger likelihood discriminants. There are three identification points defined, these are Loose ID, Medium ID and Tight ID, in order of the increasing background rejection. The requirements on likelihood discriminant are designed to meet the predefined efficiencies, which are 93%, 88% and 80% for the Loose, Medium, and Tight points respectively and they gradually increase from low to high E_{T}. For the Medium and Tight ID at low E_{T} ($20 < E_{\mathrm{T}} < 50$ GeV) the high background rejection is obtained. In addition, rejection of background electrons is tuned to be stable over pile-up level. Fig. 4.4 shows the efficiencies in data as a function of E_{T} and η, compared to the simulated data.

4.1.7 Electron isolation

In addition to the identification requirement, isolation criteria are also used, which is necessary to further discriminate signal from background. Electron isolation provides a good rejection of prompt electrons from heavy-flavour decays or light hadrons misidentified as electrons, or electrons from photon conversions and electrons from heavy flavour hadron decays. Electron isolation is constructed from several steps: first the candidate and its direction has to be identified. Second, it is followed by its contribution to the activity within the cone, together with all other activity around the cone (pile-up and underlying event). There are two classes of isolation variables defined:

- Calorimeter isolation [70] ($E^{\mathrm{isol}}_{\mathrm{T,raw}}$) is constructed as a sum of the transverse energy of topological clusters, whose barycentre is within a cone located around

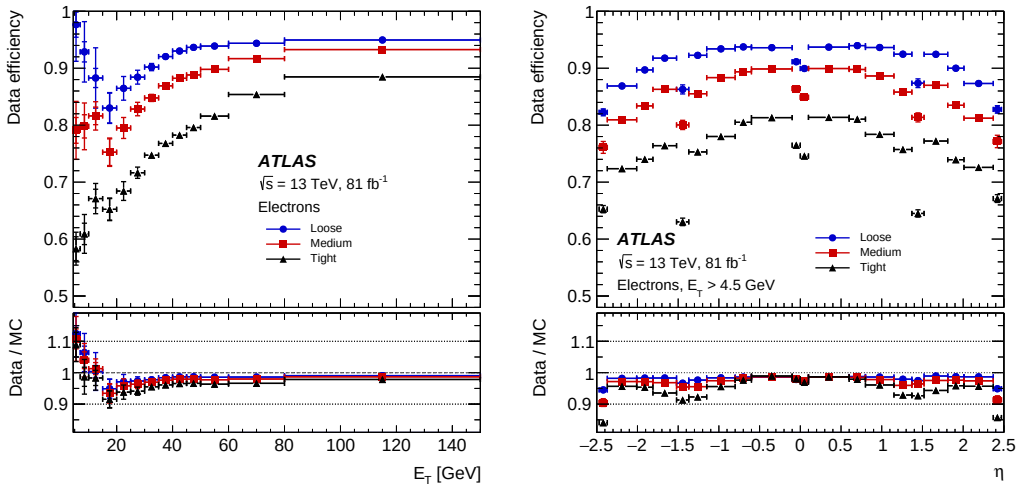

FIGURE 4.4: The electron identification efficiency in $Z \to ee$ events in data as a function of E_{T} (left) and as a function of η (right) for the Loose, Medium and Tight operating points. The inner uncertainties are statistical and the total uncertainties are the statistical and systematic uncertainties in the data-to-simulation efficiency ratio added in quadrature. For both plots, the bottom panel shows the data-to-simulation ratios.

the photon cluster barycentre. The EM energy ($E_{\mathrm{T,core}}$) which is included in the isolation, has to be subtracted by removing the energy of the calorimeter cells in a $\Delta\eta \times \Delta\phi = 5 \times 7$ rectangular cluster around the barycentre of the EM particle cluster. However, despite its simplicity and possibility of subtraction of any real or fake object, this method cannot subtract all the EM particle energy. Therefore, an additional leakage correction is needed, which can be parameterised as a function of E_{T} and $|\eta|$. In addition, a correction for the pile-up contribution to the isolation cone is also needed.

The full correction of the calorimeter isolation variable is defined as

$$E_{\mathrm{T}}^{coneXX} = E_{\mathrm{T,raw}}^{\mathrm{isolXX}} - E_{\mathrm{T,core}} - E_{\mathrm{T,leakage}}(E_{\mathrm{T}}, \eta, \Delta R) - E_{\mathrm{T,pile\text{-}up}}(\eta, \Delta R),$$

where XX is a size of the cone defined as $\Delta R = \mathrm{XX}/100$.

- Track isolation ($p_{\mathrm{T}}^{varconeXX}$) is computed as the sum of the transverse momentum of selected tracks within a varied cone size centred around the cluster direction. The cone size gets smaller with larger momentum - this is necessary to separate electrons produced in decays of high-momentum heavy particles, which can be very close to the other products of decays. Tracks matched to the electron are excluded.

The electron isolation working points include combinations of calorimeter and track isolation, and are presented in Table 4.3. The HighPtCaloOnly, Loose and Tight working points have a fixed requirement on the calorimeter and the track isolation variables. The Gradient working point is designed in a different way - it provides a fixed efficiency of 90% at $p_{\mathrm{T}} = 25$ GeV and 99% at $p_{\mathrm{T}} = 60$ GeV. Fig. 4.5 shows the electron isolation efficiency measured in data as a function of the electron E_{T} and η, compared to the simulated data, for the case of the Medium identification.

Working point	Calorimeter isolation	Track isolation
Gradient	$\epsilon = 0.1143 \times p_{\mathrm{T}} + 92.14\%$ (with $E_{\mathrm{T}}^{\mathrm{cone20}}$)	$\epsilon = 0.1143 \times p_{\mathrm{T}} + 92.14\%$ (with $p_{\mathrm{T}}^{varcone20}$)
HighPtCaloOnly	$E_{\mathrm{T}}^{\mathrm{cone20}} < \max(0.015 \times p_{\mathrm{T}}, 3.5)$ GeV	-
Loose	$E_{\mathrm{T}}^{\mathrm{cone20}}/p_{\mathrm{T}} < 0.20$	$p_{\mathrm{T}}^{varcone20}/p_{\mathrm{T}} < 0.15$
Tight	$E_{\mathrm{T}}^{\mathrm{cone20}}/p_{\mathrm{T}} < 0.06$	$p_{\mathrm{T}}^{varcone20}/p_{\mathrm{T}} < 0.06$

TABLE 4.3: Definition of the electron isolation working points and isolation efficiency ϵ.

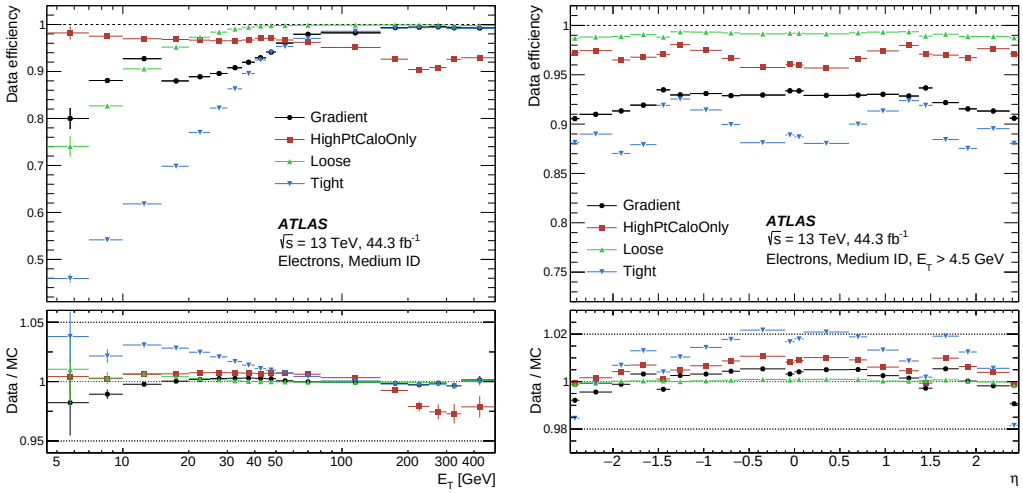

FIGURE 4.5: Efficiency of the different isolation working points for electrons from inclusive $Z \rightarrow ee$ events as a function of the electron E_{T} (left) and electron η (right). The lower panel shows the ratio of the efficiencies measured in data and in MC simulations. The total uncertainties are shown, including the statistical and systematic components.

4.1.8 Photon identification

The purpose of the photon identification criteria are primarily to reject hadronic jet activity and select prompt photons with a specified efficiency. The photon ID is constructed from cut-based selection, using the shower shape variables described in Table 4.1. The variables using the EM first layer play a particularly important role in rejecting π^0 decays into two highly collimated photons.

There are three main possible points of identification selection, the choice of which depends on the purposes of the analysis: Loose and Medium, with selection criteria close to the online level of trigger algorithms and Tight. The Loose identification criteria generally provides a very loose level of background rejection along with a high signal efficiency. It is mostly used for background estimation methods in physics analyses. Only the R_{had}, R_{had1}, R_{η} and $w_{\eta 2}$ shower shape variables are used. The Medium ID has an additional loose cut on E_{ratio} compared with the Loose ID and is used as the main trigger selection. Both Loose and Medium identification criteria are the same for converted and unconverted photons since the reconstruction of photons in the ATLAS trigger system does not differentiate between converted and unconverted photons. The Tight identification criteria are designed to provide a high level of background rejection with a high level of ID efficiency. It is constructed as a subset of the Medium ID. Alternative identification criteria, called Loose'2-5, are also defined and used mostly for background estimation methods. They are obtained from the nominal Tight ID criteria by reverting the requirements on two to five shower

shape variables (w_{s3}, w_{tots1}, F_{side}, ΔE, E_{ratio}). The definition of all identification requirements is summarised in Table 4.4.

Category	Variable	Loose	Loose'2	Loose'3	Loose'4	Loose'5	Tight
Acceptance		+	+	+	+	+	+
Hadronic leakage	R_{had1}	+	+	+	+	+	+
	R_{had}	+	+	+	+	+	+
EM Middle layer	R_{η}	+	+	+	+	+	+
	$w_{\eta 2}$	+	+	+	+	+	+
	R_{ϕ}		+	+	+	+	+
EM Strip layer	w_{s3}						+
	w_{tots1}		+	+	+		+
	F_{side}						+
	ΔE		+				+
	E_{ratio}		+	+			+

TABLE 4.4: Discriminative shower shape variables used for Loose and Tight photon identification.

All of the identification criteria are optimised separately in bins of $|\eta|$ due to the fact that the shower shapes vary with the geometry of the calorimeter. In addition, the Tight identification cut-based selection was optimised as an E_{T}-dependent ID in 2017 (compared to its earlier version with E_{T}-independent selection) using TMVA [78]. The optimisation of ID was required in the $H \to Z\gamma$ analysis in order to have an increased photon efficiency at low E_{T}, and was additionally tuned to have a higher efficiency with the same level of background rejection at high E_{T}. The cut-based selection for the ID is performed separately for unconverted and converted photons. The shower shapes of converted photons differ from unconverted photons due to the opening angle of the e^+e^- conversion pair, which is amplified by the magnetic field, and from the additional interaction of the conversion pair with the material upstream of the calorimeters. The Tight identification is optimised using a different set of Monte-Carlo samples that provide prompt photons and representative backgrounds at different transverse momenta. For photons with $10 < E_{\mathrm{T}} < 25$ GeV, the sample with $Z \to \ell\ell\gamma$ following the description in Sec. 5.1 is used as a signal, and the data sample enriched with Z+jets events is used as a corresponding background sample. Above $E_{\mathrm{T}} = 25$ GeV, the inclusive-photon production Monte-Carlo sample is used for the optimisation with a dijet background Monte-Carlo sample that is enriched in high-E_{T} energy deposits using a generator-level filter.

Fig. 4.6 shows the result of the optimisation for the updated version of Tight ID, compared to its previous version, in terms of the efficiencies as a function of E_{T} for the signal and background Monte-Carlo training samples. The optimised type of selection (labelled as E_{T}-dependent) is compared with a selection that uses criteria that do not change with E_{T} (E_{T}-independent). The E_{T}-dependent Tight identification allows the efficiencies of low- and high-E_{T} photon regions to be tuned separately. Corresponding efficiency numbers of the new E_{T}-dependent Tigh ID for $H \to Z\gamma$ analysis are shown in Sec. 6

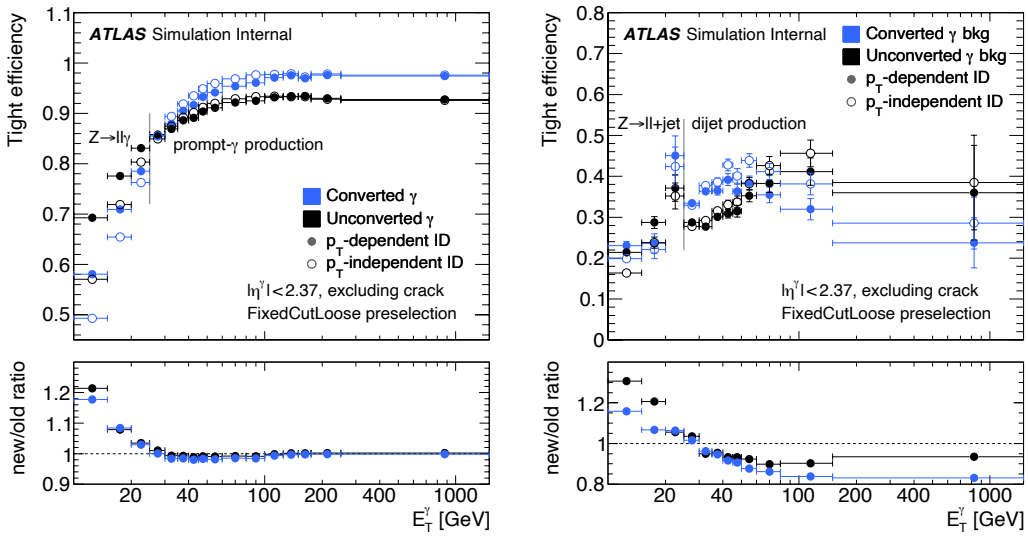

FIGURE 4.6: Efficiencies of the Tight photon identification for signal photons (left) and for background photons from jets, plotted as a function of photon E_{T}.

4.1.9 Photon isolation

Photon isolation is a powerful instrument necessary for precise photon identification that can be defined as the activity near photon objects coming either from energy deposits in the calorimeters or from the tracks of nearby charged particles.

Calorimeter isolation (E_{T}^{coneXX}, where XX is a size of the cone) is defined as a sum of the transverse energy of topological clusters, and described in detail in Sec. 4.1.7.

An example of calorimeter isolation variable distribution is shown below in Fig. 4.7 and 4.8, for $E_T^{cone40} - 0.022 \times p_{\mathrm{T}}$ and $E_T^{cone20} - 0.065 \times p_{\mathrm{T}}$, respectively, in data 2017 and simulation, for unconverted and converted photons, for $E_{\mathrm{T}} > 20$ GeV, using photons obtained from radiative Z decays.

The track isolation variable, p_{T}^{coneXX}, is defined as the sum of the transverse momentum of selected tracks within a cone around the photon cluster. Those tracks which are matched to the converted photon are excluded.

The selected tracks are required to have $p_{\mathrm{T}} > 1$ GeV and $|\eta| < 2.5$, at least seven silicon hits, at most one shared hit (defined as $n_{\mathrm{Pixel}}^{\mathrm{sh}} + n_{\mathrm{SCT}}^{\mathrm{sh}}/2$, where $n_{\mathrm{Pixel}}^{\mathrm{sh}}$ and $n_{\mathrm{SCT}}^{\mathrm{sh}}$ are the numbers of hits assigned to several tracks in the Pixel and SCT detectors), at most two silicon holes (i.e. missing hits in the pixel and SCT detectors) and at most one pixel hole. In addition the requirement $|\Delta z_0| \sin\theta < 3$ mm is applied. Track based isolation $p_{\mathrm{T}}^{cone20}/p_{\mathrm{T}}$ distributions are shown in Fig. 4.9 in data and simulated events for unconverted and converted photons with $E_{\mathrm{T}} > 20$ GeV, using photons from $Z \to \ell\ell\gamma$. A disagreement is seen for unconverted photons. Fig. 4.10 shows $p_{\mathrm{T}}^{cone20}/p_{\mathrm{T}}$ in Monte-Carlo for reconstructed unconverted and converted photons, with overlaid truth unconverted and converted photons for each case. The differences seen in 4.9 arise due to failed reconstruction of conversion tracks.

The photon isolation criteria are defined as follows:

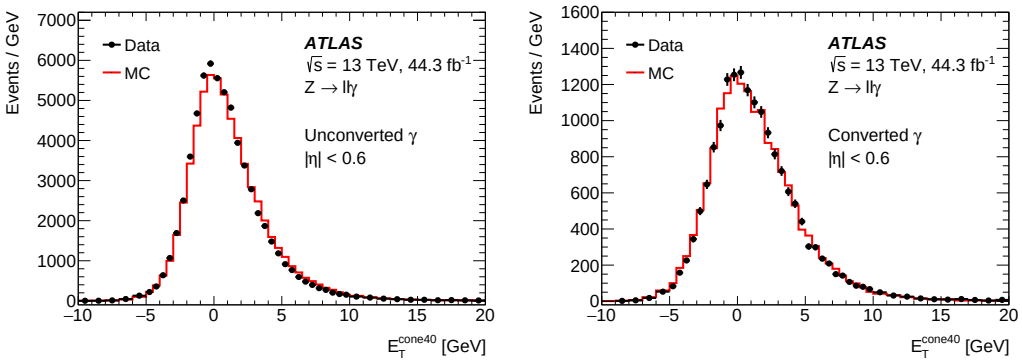

FIGURE 4.7: Distribution of $E_T^{cone40} - 0.022 \times p_T$ in data and simulation using $Z \to \ell\ell\gamma$ events, in the central region of the detector ($|eta|$ < 0.6), separately for unconverted (left) and converted (right) photons.

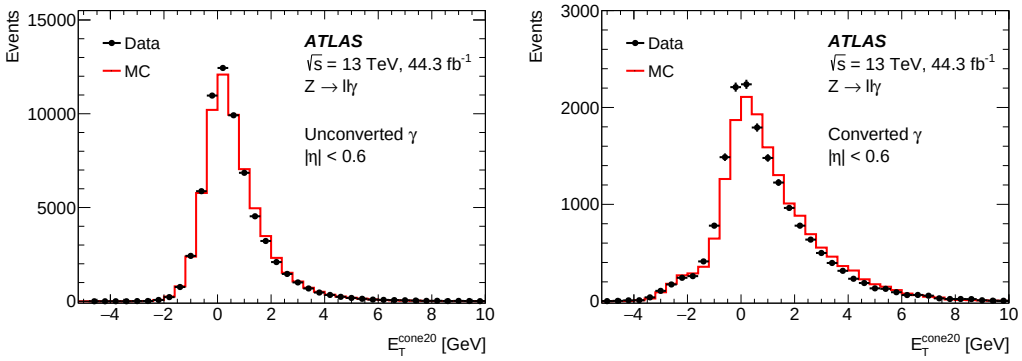

FIGURE 4.8: Distribution of $E_T^{cone20} - 0.065 \times p_T$ in data and simulation using $Z \to \ell\ell\gamma$ events, in the central region of the detector ($|eta|$ < 0.6), separately for unconverted (left) and converted (right) photons.

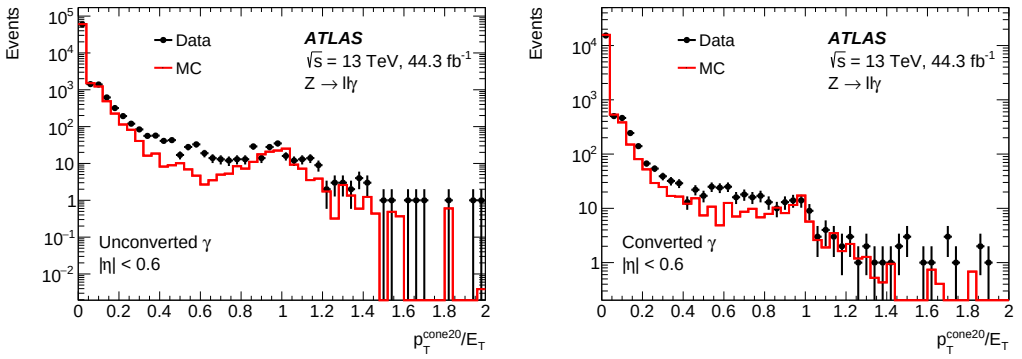

FIGURE 4.9: $p_{\mathrm{T}}^{cone20}/p_{\mathrm{T}}$ distributions for data and simulation for unconverted (left) and converted (right) photons, in the central region of the detector ($|eta|$ < 0.6).

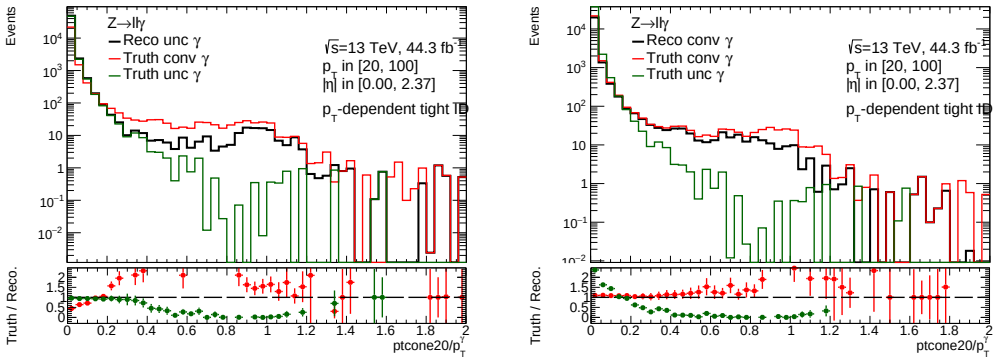

FIGURE 4.10: $p_{\mathrm{T}}^{cone20}/p_{\mathrm{T}}$ distributions for signal MC simulated Sherpa, reconstructed photons (black line), for true converted (red line) and true unconverted (green line), in the case of reconstructed unconverted (left) and reconstructed converted (right) photons, in signal photon region for $E_{\mathrm{T}} > 20$ GeV.

The `Loose` photon isolation working point was optimised primarily for the purpose of the diphoton channel of the 125 GeV Higgs boson search. An isolation cone of $\Delta R = 0.2$ for both calorimeter and track isolation has been chosen to reduce the dependence on pileup. The smaller cone also helps greatly to reduce inefficiencies in busy environments such as those occurring from $t\bar{t}H$ production.

Relative isolation cuts which scale with the transverse energy of the photon were chosen as opposed to the absolute isolation cuts used in Run 1. The main motivation of changing from fixed to relative cuts is that more rejection is needed at lower E_{T}, where the rate of background is higher. Working points were chosen by optimising the Higgs boson signal (from the $gg \to H \to \gamma\gamma$ Monte-Carlo simulated sample) efficiency against the continuum background (from the Sherpa $\gamma\gamma$ and γj MC simulated sample) rejection. The photon calorimeter and track isolations (E_T^{cone20} and p_T^{cone20}) are chosen to not exceed $0.065 \times p_{\mathrm{T}}$ and $0.05 \times p_{\mathrm{T}}$ respectively (tab. 4.5).

The `Tight` and `TightCaloOnly` photon isolation working points were optimised for high and very high E_{T} photons. For the `Tight` working point, a selection is applied both on calorimetric isolation (E_T^{cone40}, cone $\Delta R = 0.4$) and on track isolation (p_T^{cone20}), while for the `TightCaloOnly` a selection is applied only on the calorimetric isolation (E_T^{cone40}, cone $\Delta R = 0.4$). The main motivation to use relative cuts is that more rejection is needed at lower E_{T}, where the rate of background is higher, while at high E_{T} the selection is loose enough to have an efficiency on signal samples greater than 98%. The selection on calorimetric and track isolation is of the form $< X \times E_{\mathrm{T}} + Y$. The values of X and Y, given in tab. 4.5, were optimised by looking at the signal efficiency of Higgs boson samples in the diphoton channel and the rejection of background modelled using Sherpa diphoton and photon jet samples. The fraction of diphoton and photon jet used in this study was chosen to emulate Run 1 purity. These two working points were used in analyses requesting high E_{T} photons such the Higgs *low high* mass search, gamma-jet and mono-photon analyses.

TABLE 4.5: Isolation working points

WP	Calorimeter selection	Track selection
`Loose`	$E_T^{cone20} < 0.065 \times p_T$	$p_T^{cone20}/p_T < 0.05$
`Tight`	$E_T^{cone40} < 0.022 \times p_T + 2.45$ GeV	$p_T^{cone20}/p_T < 0.05$
`TightCaloOnly`	$E_T^{cone40} < 0.022 \times p_T + 2.45$ GeV	-

4.2 Muon reconstruction

Muons are reconstructed in the following way [48]: a track in the muon spectrometer (MS) is matched to a reconstructed track in the inner detector (ID), and the measurements of the momenta are combined. The reconstruction in the ID is performed in the same way as for all of the charged particles. The reconstruction in the MS starts with a search algorithm which looks for segments in each Monitored Drift Tube (MDT) and trigger chamber. Track candidates are built by simultaneously fitting hits belonging to different segments. Next, if they are compatible with the primary vertex and with χ^2 passing the selection criteria, they are accepted [79]. The MS track is then extrapolated and matched with an inner detector track and a global fit is performed. There are four types of muons which can be defined, depending on which sub-detector information was used in reconstruction:

- *Combined (CB)* muons are the most common type of the muon for physics analyses. They are reconstructed independently using measurements from both the inner detector and the muon spectrometer, with the tracks being extrapolated from the MS to the ID. The final muon track candidate is obtained through a global fit, which combines hits from both sub-detectors;

- *Segment-tagged (ST)* muons are reconstructed if an ID track matches at least one track segment in the MS chambers. ST muons are used for the cases when muons cross only one layer of MS chambers due to their low p_T or in cases when muons fall in regions with reduced MS acceptance;

- *Extrapolated (ME)* muons are reconstructed based only on the MS track extrapolated to the interaction point (IP). The parameters of the muon track are defined at the IP, with the estimated energy loss of the muon in the calorimeters. ME muons are used in general to extend the acceptance for muon reconstruction into the regions not covered by the ID ($2.5 < |\eta| < 2.7$);

- *Calorimeter-tagged (CT)* muons have a track in the inner detector that can be matched to an energy deposit in the calorimeter compatible with a minimum-ionizing particle. This type of muon is used to recover acceptance in uninstrumented regions of the MS, used for cabling and services to the calorimeters and inner detector ($|\eta| < 0.1$), although it has the lowest purity of all muon types. Therefore the identification criteria for such muons are optimised for that η region and a momentum range of $15 < p_T < 100$ GeV.

Cases of overlap between different muon types are resolved in the following way: when two muon types share the same ID track, preference first is given to CB muons, then to ST, and finally to CT muons.

Two main quality criteria are defined for the discrimination of prompt muons and rejection of background muons: the standard identification and isolation requirements.

4.2.1 Muon identification and isolation

Muon identification is defined as a set of quality requirements that can suppress background, coming mainly from pion and kaon decays. Background muons often can be separated by the presence of a special "kink" topology in the reconstructed track, which results in the poor fit quality of the resulting combined track, accompanied with the not compatible momentum measured in the ID and MS. The variables, which provide good discrimination power between signal and background muons (such as the ratio of the charge and momentum of the muons measured in the ID and MS, χ^2 of the combined track fit, etc) form a set of identification working points: Medium ID, Loose ID, Tight ID, and High-pT ID. Medium identification is the default selection for muons in ATLAS, and only CB and ME tracks are used. Loose identification maximises the reconstruction efficiency and it provides good-quality muon tracks, with all muon types used. Tight identification is designed to provide maximal purity of muons, and only CB muons are used. The High-pT identification is used to maximise the momentum resolution for tracks with transverse momentum above 100 GeV, and it uses CB muons. Fig. 4.11 shows the reconstruction efficiency for muons with Medium identification as a function of the η (left) and p_{T} (right) of the muon, for the data and simulated events.

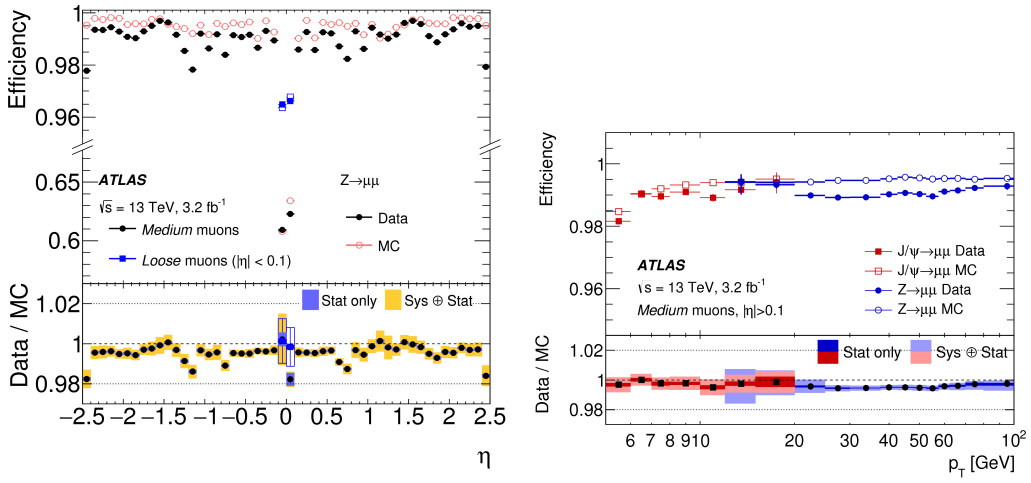

FIGURE 4.11: Left: Muon reconstruction efficiency as a function of η measured in $Z \to \mu\mu$ events for muons with p_{T} >10 GeV shown for the Medium muon selection. Right: Muon reconstruction efficiency for the Medium muon selection as a function of the p_{T} of the muon, obtained with $Z \to \mu\mu$ and $J/\psi \to \mu\mu$ events. The error bars on the efficiencies indicate the statistical uncertainty. Panels at the bottom show the ratio of the measured to predicted efficiencies, with statistical and systematic uncertainties.

Similar to electrons, muon isolation is used to separate prompt muons from fake muons originating from semileptonic decays, which are often embeded in jets or from muons coming from light mesons. The variables $p_{\mathrm{T}}^{varconeXX}$ and $E_{\mathrm{T}}^{\mathrm{isol}}$, described in Sec. 4.1.6, are used to define track and calorimeter isolation respectively. $p_{\mathrm{T}}^{varcone}$ is

defined in a cone of size $\Delta R = \min(10\ \text{GeV}/p_{\text{T}}^{\mu}, 0.3)$ around a muon of transverse momentum p_{T}^{μ}. The calorimeter isolation is defined in a cone of size $\Delta R = 0.2$ around the muon, after correction for pile-up effects. There are seven isolation selection working points defined (Table. 4.6), which use the combination of track and calorimeter isolation. Fig. 4.12 shows the muon isolation efficiency measured for Medium muons in data and simulated events as a function of the muon p_{T} for Loose and FixedCutLoose isolation working points.

Working point	Calorimeter isolation	Track isolation
LooseTrackOnly	$\epsilon = 99\%$ in all η and p_{T}	
Loose	$\epsilon = 99\%$ in all η and p_{T}	
Tight	$\epsilon = 96\%$ in all η and p_{T}	
Gradient	$\geq 90(99)\%$ ϵ at 25 (60) GeV	
GradientLoose	$\geq 95(99)\%$ ϵ at 25 (60) GeV	
FixedCutTightTrackOnly	-	$p_{\text{T}}^{varcone30}/p_{\text{T}}^{\mu} < 0.06$
FixedCutTight	$E_{\text{T}}^{\text{cone20}}/p_{\text{T}}^{\mu} < 0.30$	$p_{\text{T}}^{varcone30}/p_{\text{T}}^{\mu} < 0.15$

TABLE 4.6: Definition of the muon isolation working points and isolation efficiency ϵ.

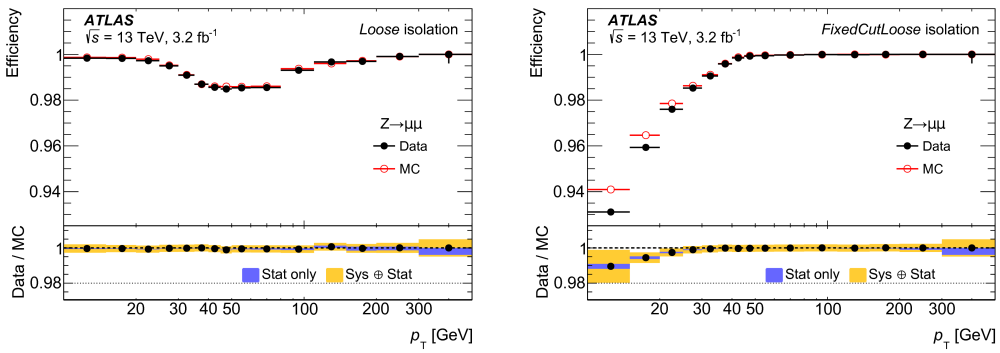

FIGURE 4.12: Isolation efficiency for the Loose (left) and FixedCutLoose (right) muon isolation working points. The efficiency is shown as a function of the muon transverse momentum p_{T} and is measured in $Z \to \mu\mu$ events. The full (empty) markers indicate the efficiency measured in data (MC) samples. The errors shown on the efficiency are statistical only. The bottom panel shows the ratio of the efficiency measured in data and simulation, as well as the statistical uncertainties and combination of statistical and systematic uncertainties.

4.3 Jet reconstruction

Jets are defined when the hadronization and fragmentation of quarks or gluons from the hard scattering process produces large showers of particles in the detector material (both the ECAL and HCAL). The jet object reconstruction [75] starts from the formation of the topo-clusters, which are initially reconstructed from the electromagnetic component of the jet, and later adds iteratively neighbouring cells with an energy above the expected noise threshold. The *anti-k_t* algorithm [80] is used as the main jet reconstruction algorithm, and it iteratively merges pairs of particle candidates until the distance between nearby jets is greater than some value. The distance can be defined, for two candidates i and j, as

$$d_{ij} = min(p_{Ti}^{2\kappa}, p_{Tj}^{2\kappa}) \frac{\Delta R_{ij}^2}{R^2}, \tag{4.1}$$

where ΔR is the distance in the $r - \phi$ plane, R and κ are arbitrary parameters. In the anti-k_t algorithm, the distance d_{ij} between a soft and a hard particle is dominated by p_{T} of the hard particle and $\kappa = -1$. In the case of two soft particles considered with a similar separation ΔR_{ij}, the distance d_{ij} becomes larger. The typical radius parameter is set to $R = 0.4$. The results of the anti-k_t algorithm are not significantly affected by small-angle or low-energy gluon emission.

4.3.1 Jet calibration

Reconstructed jets are calibrated to the jet energy scale (JES) derived from simulation and in-situ corrections, where calibration goes in several steps [81]:

- Origin correction is firstly used to recompute the four-momentum of the jet to point it towards the primary vertex instead of the centre of the detector;
- Pileup correction is necessary to remove the excess energy due to the pile-up. It consists of two components: an area-based pile-up subtraction applied event by event and a residual correction derived from MC simulations. Fig. 4.14 shows the effect of the pile-up corrections;
- Jet energy scale (JES) calibration is obtained from simulation, and is correcting the reconstructed jet energy to the truth level. It is performed due to biases in the jet *eta* reconstruction, coming mostly from undetected jets in transition regions between different sub-detectors.
- Global sequential calibration is necessary to further improve energy reconstruction and to reduce the effects that lead to a different calorimeter response. It uses jet shower shape information from calorimeter, MS and track-based variables (such as jet p_{T});
- Residual in-situ calibration is defined to correct remaining jet mismodelings between data and simulation. These data to simulation disagreements may typically arise from the imprecise simulation of the detector response or from disagreement in the hard scatter, underlying event and showering.

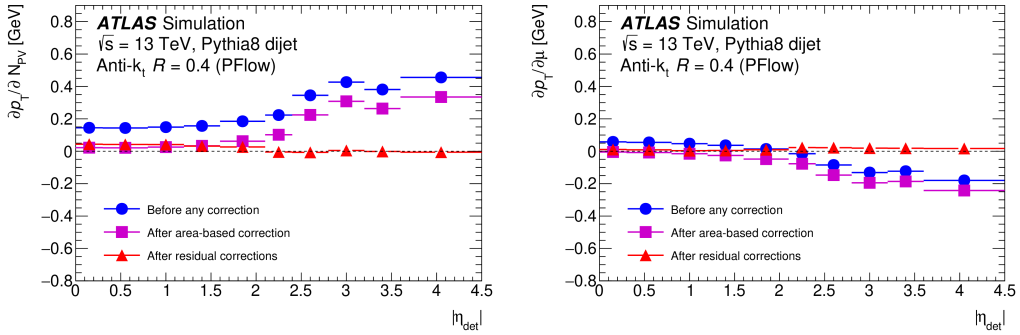

FIGURE 4.13: Jet pile-up corrections for p_T dependence on the number of primary vertices, N_{PV} as a function of η (left) and p_T dependence on the number of interactions per bunchcrossing μ as a function of η (right).

4.3.2 Jet identification

In order to select jet candidates originating only from pp collisions, several selection identification criteria can be applied, which allow rejection of background jets coming from processes such as cosmic ray showers, calorimeter noises or proton losses upstream the interaction point. The identification requirements [82] are typically rather loose. They are based on use of several variables: variables based on signal pulse shape in the LAr calorimeters, which provide good discrimination against noise; energy ratio variables and track-based variables, which provide rejection of calorimeter noise in the LAr and Tile calorimeters and beam-induced background with cosmic muon showers. There are two main identification quality requirements: Loose and Tight. The Loose selection is defined to provide high jet efficiency, with keeping high fake jet rejection. The efficiency of designed to be about 99.5% (99.9%) for $p_T > 20$ (100) GeV. The Tight selection is used to provide a higher fake jet rejection with a smaller efficiency for good jets. The designed efficiency is above 95% (99.5%) for $p_T > 20$ (100) GeV. An additional algorithm called Jet Vertex Tagger (JVT) is used to discriminate jets coming from pileup vertices from those coming from primary vertex [83] and is applied on jets with $p_T < 60\,\text{GeV}$ and $|\eta| < 2.4$. It uses a multivariate approach with a two-dimensional likelihood, where the discriminating variables are based on the p_T of the tracks associated with the jet, the jet p_T, the scalar sum of the p_T of all the associated tracks originating from any of the pile-up interactions, corrected for the number of the primary vertices.

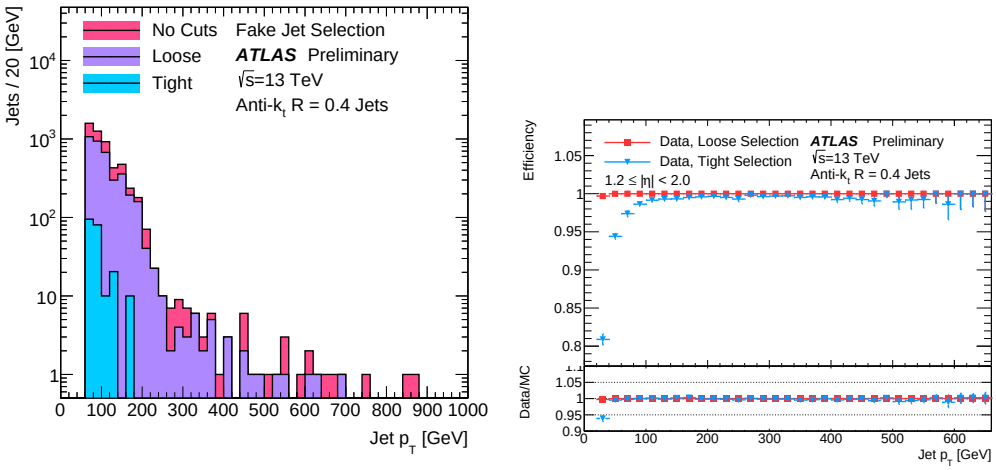

FIGURE 4.14: Jet transverse momentum distributions for the fake jets enriched sample before and after the jet quality selection (left) and jet quality selection efficiency as a function of p_{T} for the Loose and Tight selection criteria (right).

5 Photon identification techniques with radiative Z decays

The ATLAS detector provides powerful instruments for photon identification, using the information from the tracking detector and calorimeters. A precise definition of photon objects is necessary for all of the analysis involving photons, such diphoton decays of the Higgs boson and decays of Higgs boson to a Z boson and photon, as well as for BSM searches with the resonant photon pairs from graviton decays or from decays of supersymmetric particles, etc. However, the selection of prompt photons in proton-proton collisions can be challenging due to the presence of jets which can be misidentified as photons in the calorimeter. Several sets of designed variables and software algorithms provide the possibility to discriminate photons from the background. One of the major algorithms (denoted as identification) relies on the use of shower shape variables, which allow to effectively distinguish photons from the multijet background using the fine granularity of the EM calorimeter, and is described in detail in Sec. 4.1.8. Another one (denoted as isolation) can quantify the activity around photons from either the tracks of nearby charged particles, or from energy deposits in the calorimeter, and is described in Sec. 4.1.9. Efficiencies of both of the algorithms are studies in two main signatures: with radiative Z decays, which cover the region of $10 < E_{\mathrm{T}} < 100$ GeV, and with inclusive photons used in the region 25 GeV $< E_{\mathrm{T}} <$ 1.5 TeV. In addition, electrons from $Z \to ee$ decays are used in studies of identification efficiency in a method which transforms the electron shower shapes to resemble the photon shower shapes. All of the signatures and methods are combined to provide unified results on identification and isolation efficiencies studies on the full spectrum of photon energies. The precise measurement of the efficiencies is necessary to reduce the uncertainty on the mentioned physics analysis. This chapter presents my personal studies on photon identification and isolation obtained with radiative Z decays, developed based on both Monte Carlo simulations and using collision data. Results of in-depth studies of low energy photons coming from $Z(l^+l^-)\gamma$ are applied later in the searches of the Higgs boson decay to a Z boson and a photon and described in Sec. 6. Sec. 5.1 gives an introduction to the method which provides a clean sample of photons from radiative Z decays, necessary for the performance studies. Sec. 5.2 presents measurements of photon identification efficiency, and Sec. 5.3 provides measurements of photon isolation efficiency. Finally, Sec. 5.4 provides summary of the studies.

5.1 Z boson production in Initial and Final State Radiation

The performance measurements, described in the following sections, are conducted with a clean source of relatively low-energy photons from radiative Z decays. There are two main production modes possible for the SM $pp \to Z(l^+l^-)\gamma$ processes, where l is either an electron or a muon, as shown in Fig. 5.1. These are: Final State Radiation (radiative Z decays or FSR), which happens when the photon is radiated from one of the leptons in the final state through bremsstrahlung, and Initial State Radiation (ISR), where the Z boson is created together with a radiated photon.

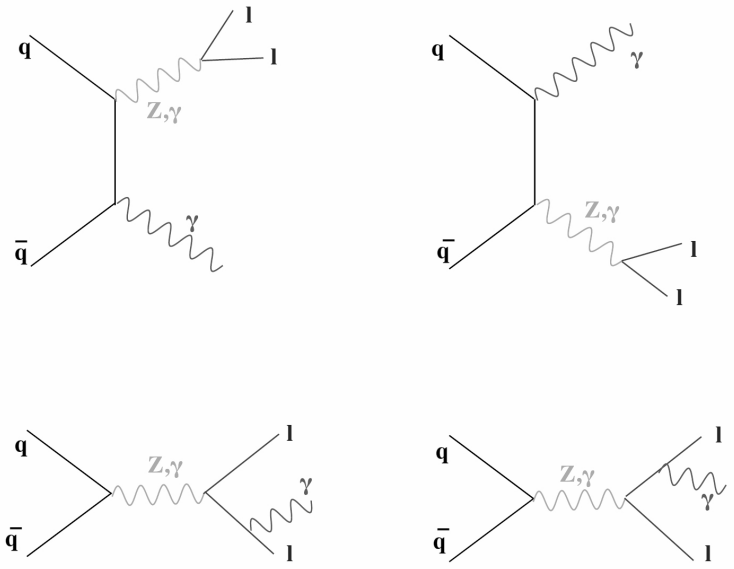

FIGURE 5.1: Feynman diagrams for the SM $pp \to Z\gamma$ productions. The two top diagrams are Initial State Radiation (ISR). The two bottom diagrams are Final State Radiation (FSR).

Both the FSR and ISR processes can be easily identified by comparing the two-body invariant mass m_{ll} distribution to the three-body invariant mass $m_{ll\gamma}$ distribution. The simple separation is possible since the ISR process m_{ll} is described just by the Z line-shape. The additional contribution of the photon energy to the lepton pair for the ISR process makes the total invariant mass larger than 91 GeV. The opposite case occurs for the FSR process: $m_{ll\gamma}$ follows the Z line-shape. The visible separation of two processes is shown in Fig 5.2 on the Dalitz diagram for $m_{ll\gamma}$ versus m_{ll} in the electron and muon decay channels. Only photons from Z radiative decays (FSR) into electrons and muons are considered for the photon identification and isolation studies. As it is possible to select events only by kinematic requirements on m_{ll} and $m_{ll\gamma}$ invariant masses, the reconstruction and selection of the photon probe are not biased. The choice of FSR photons over ISR photons is driven mostly by the following: the FSR process provides a sample of photons which is very clean from background contamination, while the choice of ISR process leads to a mixed sample of ISR photons and jet contributions, where the jet was misidentified as a photon (the cross-section for Z+jets is about three orders of magnitudes higher than for $Z+\gamma$, and a non-negligible fraction of jets contain high-momentum π^0's decaying to the collimated

photon pairs). The ISR process will be considered later in Chapter 6, given that it is the main background for the $H \to Z\gamma$ search.

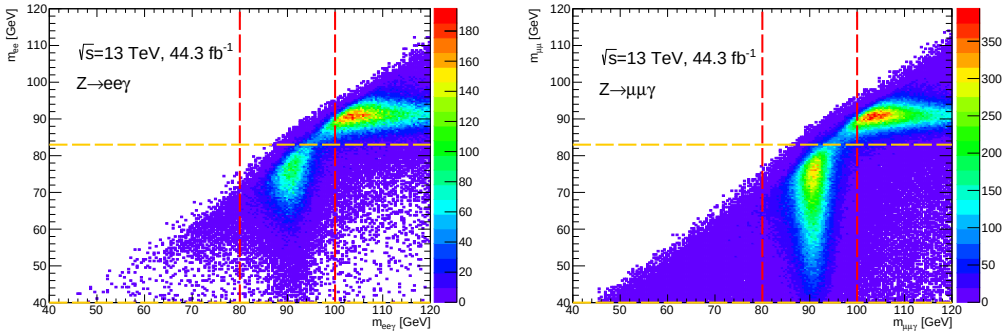

FIGURE 5.2: The Dalitz diagram of three-body invariant mass $m_{ll\gamma}$ as a function of the two-body invariant mass m_{ll} for $Z\gamma$ decays in the electron (left) and muon (right) channels. The vertical and horizontal lines show possible selection cuts on separation of the FSR contribution (where $m_{ll\gamma} \sim m_Z$) from the ISR contribution (where $m_{ll} \sim m_Z$).

5.1.1 Data and simulated samples

Monte-Carlo simulations are compared to collision data. The Monte-Carlo samples are re-weighted to reproduce the distribution of the mean number of interactions per bunch crossing observed in data.

The studies are based on the full 2015, 2016 and 2017 pp collisions dataset, collected at $\sqrt{s} = 13$ TeV, with corresponding integrated luminosity 80.4 fb^{-1}.

The simulated radiative Z events are generated with SHERPA, with the $ee\gamma$ and $\mu\mu\gamma$ final states being produced in separate samples. For each of those final states, three samples are produced, with different values of the true p_T of the generated photon. The slices of true p_{T} are [10, 35], [35, 70] and [70, 140] GeV. They are used to study the properties of the signal and to compute the photon ID efficiency in the simulation. Samples generated using Powheg and interfaced to Pythia8 for hadronization and showering were used for evaluating systematic uncertainties.

The properties of the background are studied using Z+jets samples generated with Sherpa. They are generated in slices of the Matrix Element (ME) partons and the photon transverse momentum. A truth level $m_{\ell\ell}$ cut at 40 GeV is applied.

5.1.2 Event selection

The following criteria are used for selection of the photon control sample from $Z \to ee\gamma$ decays and $Z \to \mu\mu\gamma$: both the electron and muon from Z boson are reconstructed, requiring that the leptons have a E_{T} greater than 10 GeV, the absolute pseudorapidity for electrons should be $|\eta(e)| < 1.37$ or $1.52 < |\eta| < 2.47$, and for muons $|\eta(\mu)| < 2.5$. The leptons are required to fulfil the Loose isolation requirements (yielding a 99% efficiency) and to pass a medium identification.

The photons are required to have transverse energy $E_{\mathrm{T}} > 10$ GeV with a pseudorapidity selection of $|\eta| < 1.37$ or $1.52 < |\eta| < 2.37$ excluding the crack region; the e/γ object quality and "photon cleaning" requirements are applied. A ΔR_{min} cut between the photon and its closest lepton is applied to eliminate contamination of the

photon cluster that might be produced by the lepton. For the electron channel it has to be $\Delta R_{min}(e,\gamma) > 0.4$ and $\Delta R_{min}(\mu,\gamma) > 0.2$ in case of the muon channel. In addition, the selection on the `Loose` isolation working point is required when performing photon identification efficiency studies in Sec. 5.2. For the photon isolation efficiency studies, described in Sec. 5.3, an additional Tight identification requirement is applied.

The $Z \to ll\gamma$ candidates are selected by applying the requirement to have two opposite-sign charged leptons of the same flavour. Selection of the FSR photons is performed by requiring $80 < m_{\ell\ell\gamma} < 100$ GeV and $40 < m_{\ell\ell} < 83$ GeV. Events in the $Z \to \mu\mu\gamma$ and $Z \to ee\gamma$ channels are analysed separately. The consistency of results in both channels allows having a combination into a single measurement.

5.2 Photon identification efficiency measurements with radiative Z decays

The measurements of the photon identification efficiency described in this section rely on a method which uses signatures from the radiative Z decays, and can be applied to probe low E_{T} photons in a very clean environment. It uses photons with energies from $E_{\mathrm{T}} = 10$ GeV, below which photons are not reconstructed, to $E_{\mathrm{T}} = 100$ GeV, beyond which event yields are insufficient.

The efficiency of photon identification is measured as a fraction of selected photons (probes) that pass the identification criteria

$$\varepsilon_{ID} = \frac{N_{probes,ID}}{N_{probes}}. \tag{5.1}$$

5.2.1 Photon Tight ID efficiency estimation

Eq. 5.1 is used for the Tight identification efficiency estimation. Due to a small contamination from Z+jets, where the jets are mis-identified as photons, the equation described above is not entirely correct and is affected by a systematic uncertainty. The fraction of background contamination in the sample depends on the reconstructed photon transverse energy, varying between $\approx$ 15% for $10 < E_{\mathrm{T}} < 25$ GeV and $\leq$ 1% for higher E_{T} regions. The background contamination is also affected by the presence of the isolation requirement - fake photons coming from hadron decay or mis-identified electrons are usually not isolated in comparison to non-fake leptons/photons. For isolated photons the background is estimated in data with a template fit method (more details provided below) and subtracted in the three E_{T} bins (10-15, 15-20 and 20-25 GeV), while for higher E_{T}, the computed efficiency assumes that the background is completely negligible and a systematic uncertainty is assigned. The obtained purity in a data sample allows calculation of the number of background events to be subtracted from the sample. The PID efficiency in the $10 < E_{\mathrm{T}} < 25$ GeV region is corrected as follows

$$\varepsilon_{ID} = \frac{N_{probes,Tight} - N_{B,Tight}}{N_{probes} - N_B}, \tag{5.2}$$

which is equivalent to:

$$\varepsilon_{ID} = \frac{N_{S,Tight}}{N_S}. \tag{5.3}$$

With B standing for background and S for signal. A template fit to the $m_{\ell\ell\gamma}$ invariant mass distribution is used to evaluate the signal purities (P) and yields (S) before and after the photon Tight ID selection. To perform the fit, the $m_{\ell\ell\gamma}$ requirement is removed from the selection and the probability density functions (PDFs) of $m_{\ell\ell\gamma}$ are extracted for signal ($Z \to \ell\ell\gamma$) and background ($Z \to \ell\ell$ + jets) from Monte Carlo samples. The sum of the signal and background PDFs, with floating normalisations, is fitted to the data distribution.
Two fits are performed: one for all the events after the nominal selection, and one for the events in which the photon candidate also passes the Tight ID requirements, shown in Fig. 5.3. The fitted shape is always in good agreement with the data distribution. The fit range is chosen as [65, 105] GeV for both the muon and electron channels. From the fit, the signal purity is determined in the signal region 80 GeV$< m_{\ell\ell\gamma} <$ 100 GeV: the purity for the region 10$<p_{\mathrm{T}}<$25 GeV before the Tight ID requirements for $ee\gamma$ is 91.6% for unconverted photons and 89.4% for converted photons; for $\mu\mu\gamma$ it is 91.2% for unconverted photons and 88.9% for converted photons. After applying the Tight identification criteria, the photon purity for $ee\gamma$ is 97.7% for unconverted photons and 97.3% for converted photons; for $\mu\mu\gamma$ it is 97.3% for unconverted photons and 97.1% for converted photons.
The difference

$$\Delta\varepsilon_{ID} = N_S^{Tight}/N_S - N_{probes,Tight}/N_{probes}, \tag{5.4}$$

is taken as a systematic uncertainty on the efficiency estimated for $E_{\mathrm{T}} > 25$ GeV. It is thus found to be 0.4% for unconverted photons and 3.3% for converted photons in the $Z \to \mu\mu\gamma$ sample and 2.8% for unconverted photons and 1.6% for converted photons in the $Z \to ee\gamma$ case, which is caused by residual background.

The average purity over 25-100 GeV is essentially dominated by the purity in the 25-30 GeV bin. This is shown in Table 5.1, where the fitted purity in the 25-30 GeV bin is compared to the purity in the $>$ 25 GeV bin.

channel	Purity [%] $25 < E_{\mathrm{T}} < 30$ GeV	Purity [%] $E_{\mathrm{T}} > 25$ GeV
ee	97.5 ± 7.1	97.9 ± 6.9
$\mu\mu$	96.6 ± 3.4	97.4 ± 2.7

TABLE 5.1: Fitted photon purity of all probes (converted+unconverted), before Tight ID, for region $25 < E_T < 30$ GeV and for $E_T > 25$ GeV. The uncertainty are only statistical.

The efficiencies measured in the two different channels are found to be in agreement within their uncertainties. They are therefore combined, the central value is evaluated as the weighted average of the two efficiencies

$$\varepsilon = \frac{\frac{\varepsilon_e}{\sigma_e^2} + \frac{\varepsilon_\mu}{\sigma_\mu^2}}{\frac{1}{\sigma_e^2} + \frac{1}{\sigma_\mu^2}}, \tag{5.5}$$

and for the total uncertainty the square root of its variance

$$\sigma_\varepsilon = \frac{1}{\sqrt{\frac{1}{\sigma_e^2} + \frac{1}{\sigma_\mu^2}}}. \tag{5.6}$$

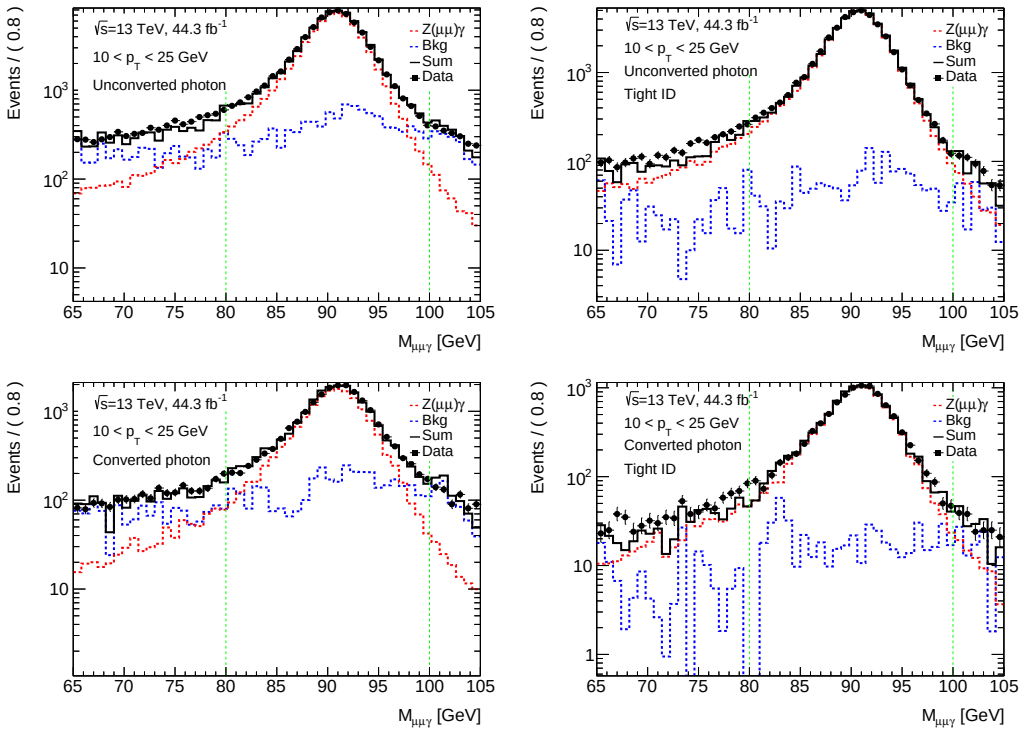

FIGURE 5.3: Invariant mass ($m_{\ell\ell\gamma}$) distribution of events selected in data after applying all the $Z \to \ell\ell\gamma$ selection criteria except that on $m_{\ell\ell\gamma}$ (black dots). Only the muon channel is shown. The solid black line represents the result of the fit of the data distribution with the sum of the signal (red dashed line) and background (blue dotted line) invariant mass distributions obtained from the simulation. Top: photons are reconstructed as unconverted. Bottom: photons are reconstructed as converted. Left: no ID requirement is applied. Right: The photon candidates are required to pass Tight identification criteria.

The total statistical uncertainty is

$$\sigma_{\varepsilon,stat} = \frac{1}{\sqrt{\frac{1}{\sigma^2_{e,stat}} + \frac{1}{\sigma^2_{\mu,stat}}}}, \tag{5.7}$$

and the total systematic is:

$$\sigma_{\varepsilon,syst} = \sqrt{\sigma^2_{\varepsilon} - \sigma^2_{\varepsilon,stat}}. \tag{5.8}$$

The comparison between the data-driven photon identification efficiency and the efficiency obtained from simulated Z sample as a function of E_{T} is shown in Fig. 5.4. The total uncertainties include statistical and systematic uncertainties.

The next step would be to evaluate the scale factors (SF) binned in eleven E_{T} bins and four $|\eta|$ bins, which are needed to correct the simulation for differences with the measured efficiency on data. These are applied as weights in simulated samples.
The scale factors are defined as

$$SF = \frac{\varepsilon_{data}}{\varepsilon_{MC}}, \tag{5.9}$$

then the statistical and systematic uncertainties are computed as

$$\frac{\sigma_{SF,stat}}{SF} = \sqrt{\left(\frac{\sigma_{\varepsilon_{data,stat}}}{\varepsilon_{data}}\right)^2 + \left(\frac{\sigma_{\varepsilon_{MC,stat}}}{\varepsilon_{MC}}\right)^2}, \tag{5.10}$$

$$\frac{\sigma_{SF,syst}}{SF} = \frac{\sigma_{\varepsilon_{data,syst}}}{\varepsilon_{data}}. \tag{5.11}$$

5.2.2 Systematic uncertainties

Several sources of systematic uncertainty contribute to the total systematic uncertainty on the measurement of the photon. Tight identification efficiency. For the most part, these come from background estimation method:

- **Closure test**
  The results of photon identification efficiency on reconstructed photons are matched to true photons and compared to the results of the template fit method. Simulated background was added to the signal truth photons, coming from radiative Z decays. Results coming from template fit method are also presented in the fit as a sum of background and signal events. A closure test is provided only for E_{T} region [10, 25] GeV due to lack of statistics in higher regions. The maximum difference between signal efficiency on reconstructed photons and efficiency corrected with the template fit method with true photon matching is about 2% for converted photons and 1% for unconverted photons.

- **Background uncertainty**
  The results of the template fit are redone with a different fit range. Instead of using the nominal fit range of [65, 105] GeV an extended range of [45, 120] GeV is chosen; the signal region thus is changed and varied to [45, 95] GeV and to [80, 120] GeV to cover the mismodeling effects on the low mass range. An example of such fitting is presented in Fig. 5.5. The background uncertainty is provided only for the E_{T} region [10, 25] GeV due to lack of statistics in higher regions.

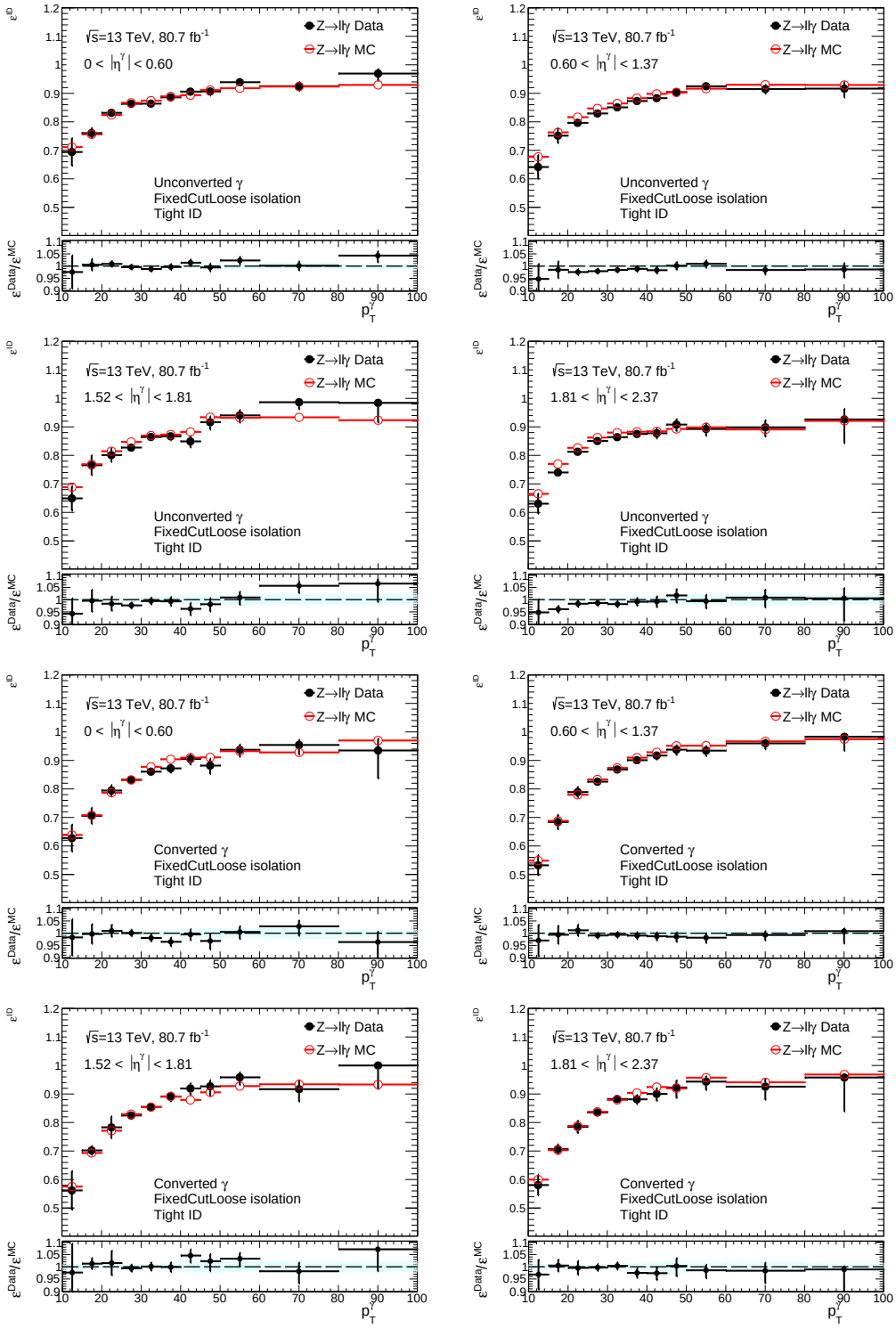

FIGURE 5.4: Comparison of the Tight photon identification efficiency results measured using $Z \to \ell\ell\gamma$ from data and simulated samples in four different pseudorapidity regions. The uncertainties include both statistical and systematic ones. Yellow band corresponds to statistical uncertainty of simulated sample, shaded green one - to photon efficiency pre-recommendation uncertainty.

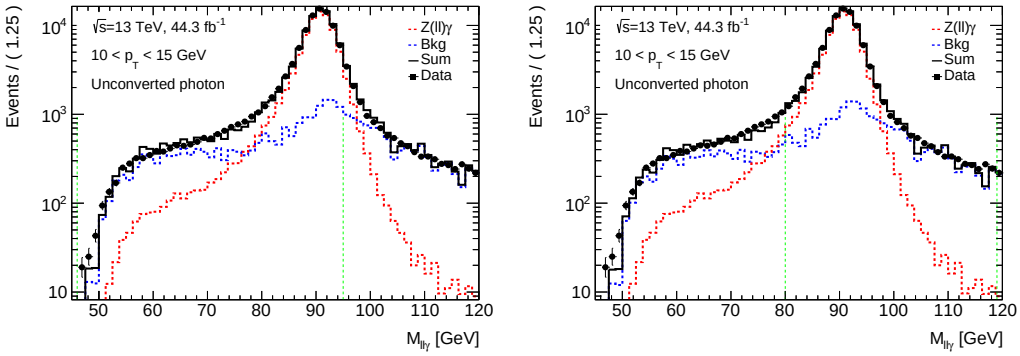

FIGURE 5.5: Invariant mass ($m_{\ell\ell\gamma}$) distribution of events selected in data after applying all the $Z \to \ell\ell\gamma$ selection criteria except that on $m_{\ell\ell\gamma}$ (black dots). The solid black line represents the result of the fit of the data distribution with the sum of the signal (red dashed line) and background (blue dotted line) invariant mass distributions obtained from MC simulation. The signal fitting region is chosen as [45, 95] GeV (left) and [80, 120] GeV (right). Photons are reconstructed as unconverted

- **Fudge-factor uncertainty**
  Systematic uncertainty is calculated from variations of the fudge factors, which are used to correct the shower shape variables in Monte Carlo. There are four different sets of variations, applied on the following discriminating calorimeter variables (detailed description is listed in Table 4.1):

  - R_{had};
  - R_{Φ};
  - R_{η}, ω_{η_2};
  - $\omega_{s,3}$, $\omega_{s,tot}$, F_{side};

  The variations are applied only in the E_{T} region of the background estimation method of [10, 25] GeV. Each of the sets of values is subtracted from the corresponding values of the Tight ID menu and four new Tight ID menus are obtained. The template fit is redone for each of the varied Tight ID menus. The uncertainty is evaluated from the difference of the nominal data efficiency and the varied data efficiency, where the varied data efficiency is corrected with use of templates extracted with the varied Tight ID menu. The final uncertainty is calculated as four different sets of variations added in quadrature. For unconverted photons, the maximum difference arising from the difference between the varied Tight ID menu and the nominal one is below 5%. The largest observed difference for converted photons is approximately 6%.

- **Monte-Carlo-generator uncertainty**
  The systematic uncertainty arising from an alternative MC simulation event generator is taken into account. The alternative MC simulation event generator sample is chosen, where the uncertainty comes from the deviation in the MC simulation predictions of the background. The subtraction of background events with the templated fit method is obtained with use of templates extracted from the alternative MC simulation event generator Powheg+PYTHIA instead of nominal one (SHERPA). The final uncertainty is evaluated from the difference

between the nominal scale factors and systematic scale factors, where the numerator is data efficiency corrected with use of templates extracted from the alternative MC simulation event generator, and the denominator is the efficiency from the nominal MC simulated sample. For unconverted photons, the maximum difference arising from simulation-related uncertainties between alternatively obtained scale factors and the nominal ones is below 2%, for converted photons it is approximately 5%.

5.2.3 Pile-up dependence of the photon Tight identification efficiency

It is possible that the photon identification efficiency is be affected by the (in-time) pile-up since the photon shower shapes become broader from the additional energy deposited in the calorimeter. According to the pile-up recommendations for Run 2, MC simulated samples should be reweighted to match the actual μ distribution in data. However, there might be residual differences between data and MC simulated efficiencies due to incorrect simulation of the detector response to pile-up. Therefore, one more general source of uncertainty arises from pile-up dependence: the pile-up dependence of the Tight photon identification efficiency is evaluated as a function of μ. The photon probes are used only for data from 2017 and the probe sample is divided in smaller subsets according to the μ to which the photon belongs.

In Fig. 5.6 the in-time pile-up dependence of the Tight photon identification efficiencies obtained with radiative $Z \to \ell\ell\gamma$ decays in data sample are compared to the same quantities obtained from simulated $Z \to \ell\ell\gamma$ samples. Only photons with $20 < E_{\mathrm{T}} < 40$ GeV are used to avoid background contamination in the data sample. The pile-up dependence is presented for unconverted and converted photons in two selected η regions. The distributions show a decrease of the photon identification efficiency with higher pile-up, having however a similar dependence for both data and simulated samples.

The dependence of the scale factors on μ provides a good estimate of the pile-up dependence. The slope of data to simulation ratio is expected to be zero. The ratios between data and simulated efficiencies as a function of μ are fitted with a linear distribution. The slopes are listed in Table 5.2. Those slopes are compatible with 0 within uncertainties, meaning that it is not possible to conclude on a pile-up dependence of the scale factors with the current statistical uncertainties. The pile-up uncertainty is not taken into account.

$\lvert\eta\rvert$	$0.00 < \lvert\eta\rvert < 0.60$	$0.60 < \lvert\eta\rvert < 1.37$	$1.52 < \lvert\eta\rvert < 1.81$	$1.81 < \lvert\eta\rvert < 2.37$
unconverted	0.0004 ± 0.0003	-0.0001 ± 0.0003	-0.0012 ± 0.0006	0.0009 ± 0.0005
converted	0.0009 ± 0.0007	-0.0013 ± 0.0005	0.0007 ± 0.0007	0.0009 ± 0.0008

TABLE 5.2: Slope of the fit of the scale factors as a function of $<\mu>$ with a linear distribution.

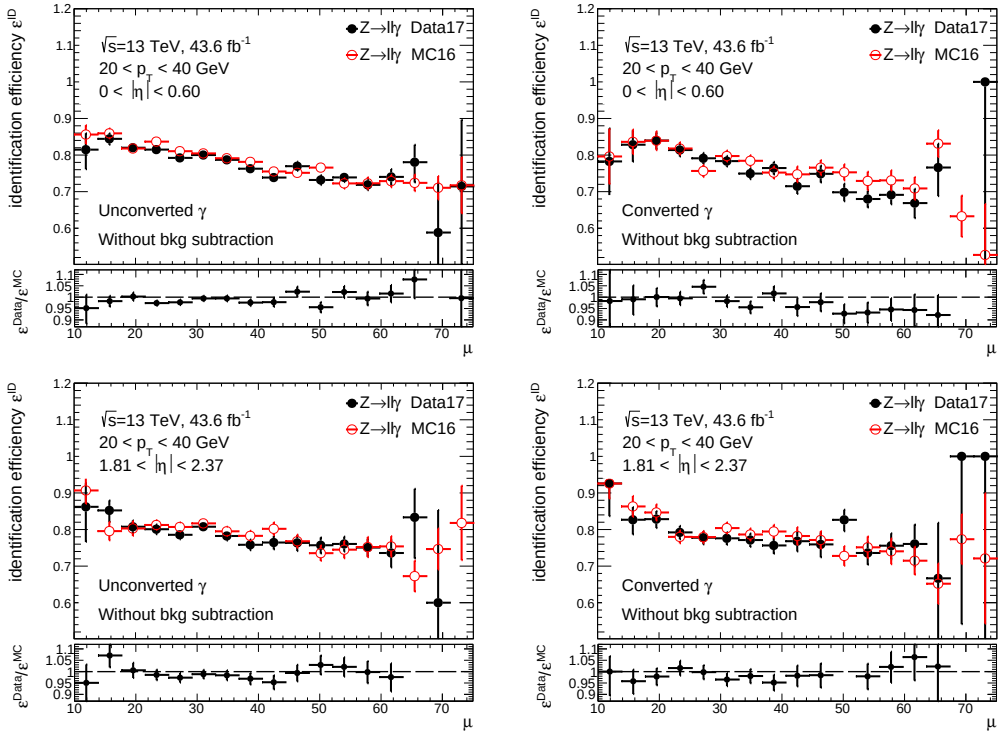

FIGURE 5.6: Photon identification efficiencies versus μ for reconstructed unconverted photons (left) and converted photons (right), in two selected different pseudorapidity regions. Solid black dots represent data and hollow red dots represent the simulated sample.

5.2.4 Results

The final photon Tight identification efficiency for radiative $Z \to \ell\ell\gamma$ decays and total uncertainties are computed in data using equations 5.3, 5.5, 5.7 and 5.8. These are shown in Fig. 5.4. Total systematic uncertainties include uncertainties such as uncertainty from the non-closure in simulation, the template fit background estimation method, the alternative MC simulation event generator and fudge-factor uncertainty. The effect from pile-up dependence is compatible with zero and is not taken into account. Individual and total uncertainties are shown in Fig. 5.7 for both unconverted and converted photons in two selected $|\eta|$ bins.

5.3 Photon isolation efficiency with radiative Z decays

The studies of the photon isolation efficiency shown below are performed with FSR photons from Z decays in an E_{T} range of 10 GeV up to 100 GeV. Data and simulation samples, as well as the main procedure for the event selection, are the same as described in Sec. 5.2. The following additional criteria are applied to study photon isolation efficiency: photon objects are required to pass the Tight ID requirement and there is no requirement being made on the isolation.

The efficiency of photon isolation is measured as a fraction of selected photons (probes) that pass isolation requirement

$$\varepsilon_{iso} = \frac{N_{probes,iso}}{N_{probes}}. \tag{5.12}$$

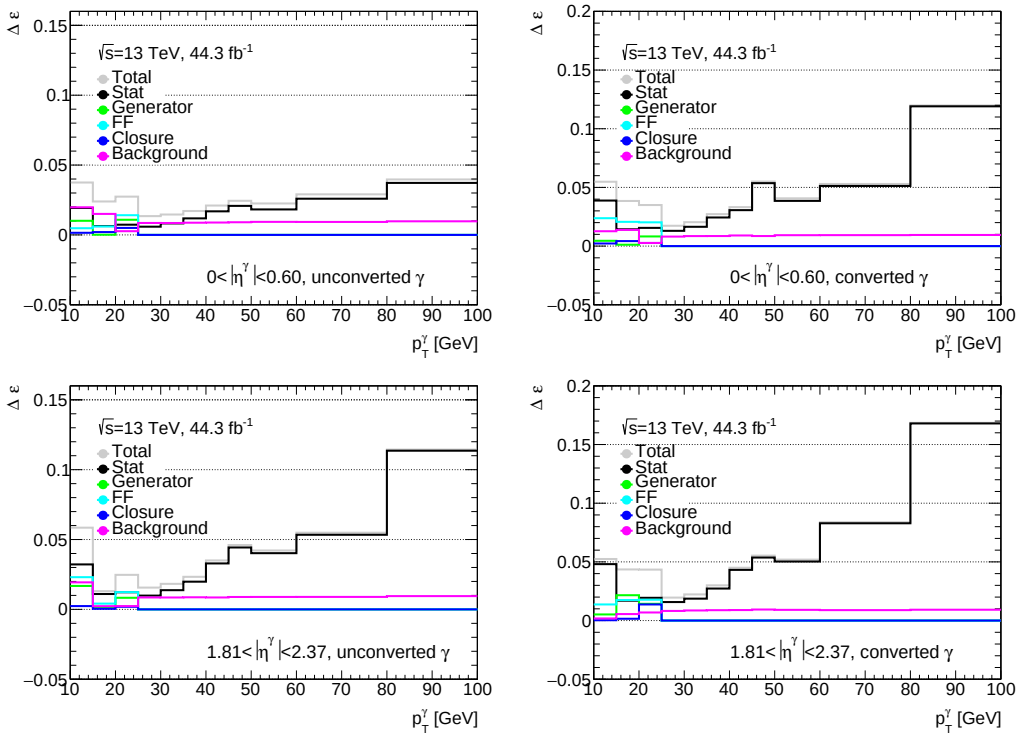

FIGURE 5.7: Uncertainties measured using $Z \to \ell\ell\gamma$ from data and MC simulated samples in two different pseudorapidity regions.

5.3.1 Photon isolation efficiency estimation

As described in Sec. 5.2.1, the low E_{T} region is contaminated with background from Z+jets events which needs to be subtracted. A template fit to the three body invariant mass ($m_{\ell\ell\gamma}$) distribution is performed, where the templates are extracted from signal ($Z \to \ell\ell\gamma$) and background (Z+jets) simulated events (more details on the procedure are provided in Sec. 5.2.1). The purity obtained in the data sample allows the calculation of the number of background events to be subtracted from the number of probes to get the estimate of the number of true photons. The isolation efficiency in the $10 < E_{\mathrm{T}} < 20$ GeV region is corrected as follows

$$\varepsilon_{iso} = \frac{N_{probes,iso} - N_{B,iso}}{N_{probes} - N_B}, \tag{5.13}$$

which is equivalent to:

$$\varepsilon_{iso} = \frac{N_{S,iso}}{N_S}. \tag{5.14}$$

The purity reached is $> 95\%$ when the photon E_{T} is between 10-20 GeV and $> 99\%$ otherwise. Given the negligible background contamination above 20 GeV, no background subtraction is performed (see [71]).

The evolution of the isolation efficiency measured in 2017 data as a function of η and E_{T} is illustrated in Fig. 5.8, for three isolation working points (defined in Table 4.5), together with the data-to-simulation efficiency ratio, separated for unconverted and converted photons. The overall differences between data and simulation are less than approximately 5%.

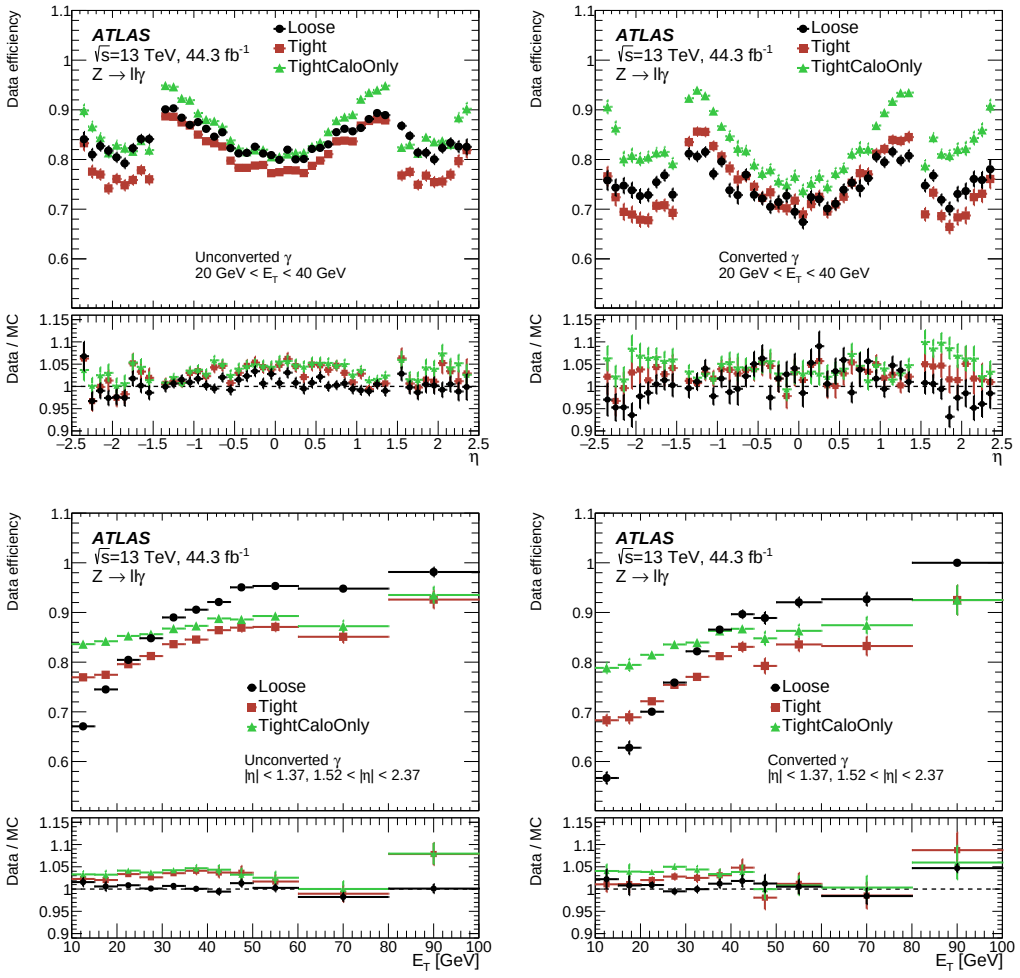

FIGURE 5.8: Efficiency of the isolation working points, using $Z \to \ell\ell\gamma$ events, for unconverted (left) and converted (right) photons as a function of photon η, E_{T}. The lower panel shows the ratio of the efficiencies measured in data and in simulation.

5.3.2 Pile-up dependence of the photon isolation efficiency

Pile-up can affect the photon isolation efficiency due to the additional energy deposited in the calorimeter by the products of the pile-up collisions. Therefore, the pile-up dependence of the photon isolation efficiency is evaluated, as a function of μ. In Figure 5.9, the pile-up dependence of the efficiency obtained in data with radiative $Z \to \ell\ell\gamma$ decays for all of the isolation working points, and is compared to the same obtained in simulated $Z \to \ell\ell$ MC samples in the lower panel of the plots. Only photons with $20 < E_{\mathrm{T}} < 40$ GeV are used to avoid background contamination in the data sample. The pile-up dependence is presented for unconverted and converted photons in inclusive η region. As is seen, efficiency decreases by 10% when μ is increasing from 15 to 60. This loss is only well described by the simulation for the `Loose` isolation working point, and some mismodelling is seen for other working points.

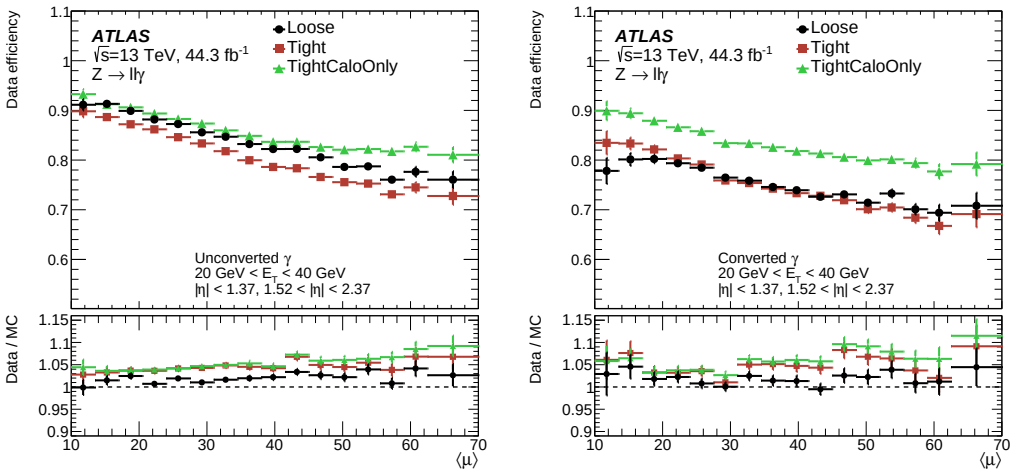

FIGURE 5.9: Efficiency of the photon isolation working points for unconverted (left) and converted (right) photons as a function of μ. The lower panel shows the ratio of the efficiencies measured in data and in simulation. The total uncertainty is shown, including the statistical and systematic components.

5.3.3 Systematic uncertainties

Several sources of systematic uncertainties contribute to the total systematic uncertainty on the measurement of photon isolation efficiency. The dominant ones come from the template fit method.

Closure test

The photon isolation efficiencies estimated from photon candidates matched to true photons are compared to the results of the template fit method. Simulated background was added to the signal for truth photons from $Z \to \ell\ell\gamma$. The closure test was provided only for the E_{T} region [10, 20] GeV due to lack of statistics at higher E_{T}. The maximum difference between the two estimates is less than 0.1% for all isolation working points.

Background uncertainty

The template fit is performed with different fit ranges - instead of the nominal fit range [65, 105] GeV, an extended range [45, 120] GeV is chosen. The signal region is also changed and varied to [45, 95] GeV and to [80, 120] GeV to cover mismodeling

effects on the low mass range. The maximum value is 0.4% for converted and and 0.2% for unconverted photons.

Simulation-related uncertainty

An alternative MC simulation event generator sample was chosen, where the uncertainty comes from the deviation in the simulated predictions of the background. Subtraction of background events (for E_{T} in [10, 20] GeV) with the template fit method was performed using templates extracted from the alternative generator POWHEG+PYTHIA instead of the nominal one (SHERPA). The final uncertainty is evaluated from the difference between the nominal scale factors and then scale factors where the numerator is the data efficiency which was corrected with the varied templates and the denominator is the efficiency from the nominal MC simulated sample. The maximum value is 0.4% for both unconverted and converted photons.

Alternative background estimation method

An alternative background estimation method based on two different photon identification requirements was developed. It gives results consistent with the template fit method and is mainly used as a cross-check.

The method is defined as a 2D-sideband method and it is based on the identification (ID) of the photon candidate and the two-body invariant mass $m_{\ell\ell}$ requirement. One region is defined as the signal region (A) with $Z \to \ell\ell\gamma$ events and the other three regions are enriched with Z+jet events.

The Tight ID requirement is used in signal region A since it provides good background rejection while retaining a photon efficiency above 95% for photons with transverse energy above 20 GeV [84]. Regions C and D use looser or "not-Tight" photon identification requirements ("Loose Prime4").

The two-body invariant mass requirement is good to be used on both selection of Z boson and background sample. By reversing the $m_{\ell\ell}$ from 40 GeV $< m_{\ell\ell} <$ 83 GeV to $m_{\ell\ell} >$ 85 GeV, almost all photon candidates should be jets since the minimal photon energy is $E_{\mathrm{T}} >$ 10 GeV.

The four method regions are defined as follows:

- Tight and direct mass cut region (A): the photon candidates are required to pass the Tight ID criteria and $40 < m_{\ell\ell} < 83$ GeV;
- Tight, reversed mass cut region (B): the photon candidates are required to have two-body invariant mass $m_{\ell\ell} > 85$ GeV but pass Tight ID criteria;
- Not-Tight, direct mass cut region (C): the photon candidates have mass requirement $40 < m_{\ell\ell} < 83$ GeV, fail the Tight ID criteria but pass "Loose Prime4" ID criteria;
- Not-Tight, reversed mass cut region (D): the photon candidates are required to have two-body invariant mass $m_{\ell\ell} > 85$ GeV, fail the Tight ID criteria but pass "Loose Prime4" ID criteria.

The 2 GeV-wide two-body invariant mass gap between the signal and background regions helps reducing the signal leakage into the background region.

The difference between the alternative background subtraction method and the template fit method is measured; the maximum difference is 2% for unconverted photons and 4% for converted photons.

5.3.4 Results

Total systematic uncertainties include uncertainties from the non-closure in simulation, the template fit method, the difference in data efficiencies from the template fit method and the data-driven method and the alternative MC simulation event generator. Individual and total uncertainties are shown in Figure 5.10 for both unconverted and converted photons, for $|\eta| < 0.6$.

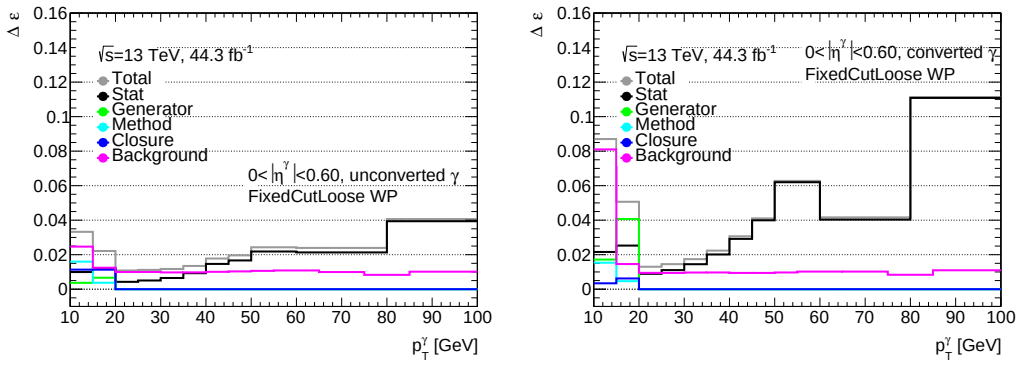

FIGURE 5.10: Systematic uncertainties for the `Loose` isolation working point, measured using $Z \to \ell\ell\gamma$ events from data and simulated samples, for $|\eta| < 0.6$ and unconverted (left) and converted (right) photons.

5.4 Summary

In this chapter two sets of studies are presented, on photon identification and photon isolation efficiencies, which are described in details and documented in [1]. Both of them use pure sample of photons from radiative Z decays in the range of low energies from 10 to 100 GeV. The analysis is performed using 2015, 2016 and 2017 data with collected integrated luminosity 80.4 fb^{-1}.

For the photon identification measurements the efficiency of the Tight ID is provided, and computed ratio of data to simulation is very close to one. Additionally, study of pile-up dependence of the Tight ID is presented, and even though both simulation and data show matching results, a decrease of the efficiency is observed of approximately 15%. Considering that the average number of collisions per bunch-crossing is going to increase in future runs at the LHC, development of a new pile-up robust version of the photon identification is a necessary step.

For the isolation measurements the efficiency of the `Loose`, `Tight` and `TightCaloOnly` working points is provided with the corresponding Scale Factors. A new, fully data-driven method is developed to estimate the possible $Z + jets$ background in the non-isolated region, and it gives compatible results with the template fit method, which was initially developed for the photon identification measurements and later adapted for the isolation measurements. Next, pile-up dependence is studied, and it shows that the isolation working points efficiencies decrease with the higher pile-up. In addition, a mismodelling is observed at high values of μ, which can be explained by not correctly modelled shapes of the isolation variables. Both the development of pile-up robust working points and correction of isolation in high pile-up is required in the future.

6 Search for the SM Higgs boson in the $H \to Z\gamma$ decay channel

In 2012 the Higgs boson was discovered by the ATLAS and CMS Collaborations and some of its measured properties, such as spin and parity, were found to be consistent with the SM predictions. Its mass has been determined to be $m_H = 125.09 \pm 0.21(\text{stat}) \pm 0.11(\text{syst})$ GeV [85, 86, 87, 88]. However, it is still important to determine precisely the remaining properties, such as to observe the missing decay modes, their branching ratios and measure the Higgs boson mass in these modes. The branching ratio of the Higgs boson decay to $Z\gamma$ is predicted to be $B(H \to Z\gamma) = (1.54 \pm 0.09) \times 10^{-3}$ at $m_H = 125.09$ GeV. Considering that the Higgs boson decays to $Z\gamma$ through loop diagrams, its branching ratio can, as was described in Sec. 1.5, differ from the SM value in several BSM theories.

This chapter presents the search for the Standard Model Higgs boson decay to the $Z\gamma$ channel. The focus of the search is on the leptonic final states of the Z boson decay only, despite the small branching ratio (6.7% to electrons or muons). This allows a good invariant mass resolution, a relatively small background, and a high signal efficiency compared to Z boson decays to hadrons, to τ pairs or to neutrinos. This chapter describes the final version of the analysis, published in [2]. A summary is presented in the sections below.

6.1 Analysis strategy

The search for the Higgs boson to $Z\gamma$ uses data recorded at $\sqrt{s} = 13$ TeV at the LHC in the years from 2015 to 2018, with a total integrated luminosity of 139 fb^{-1}. Fig. 6.1 shows a Feynman diagram of the $H \to Z\gamma$ process.

The main backgrounds for this analysis are expected to be from the SM $Z\gamma$ initial state radiation (ISR) events, from final-state radiation (FSR) in radiative Z boson decays ($Z \to \ell\ell\gamma$) and from the production of a Z boson in association with jets, followed by a $Z \to \ell\ell$ decay, where the jet is misidentified by the detector as a photon. Fig. 6.2 shows Feynman diagrams of the dominant $Z\gamma$ background final states. Other contributions include the background from $t\bar{t}$, which is evaluated from the simulation to be much smaller and is neglected, and the contribution from WZ which is expected (from Run-1 studies [89]) to be even smaller and thus also neglected.

The first attempt at the search for the $Z\gamma$ decay of the Higgs boson was performed by ATLAS with 25 fb^{-1} at $\sqrt{s} = 7$ and 8 TeV during Run-1 [89]. No significant deviation from the background was observed, and an observed (expected) upper limit on the Higgs boson production cross section times its branching ratio to $Z\gamma$ was

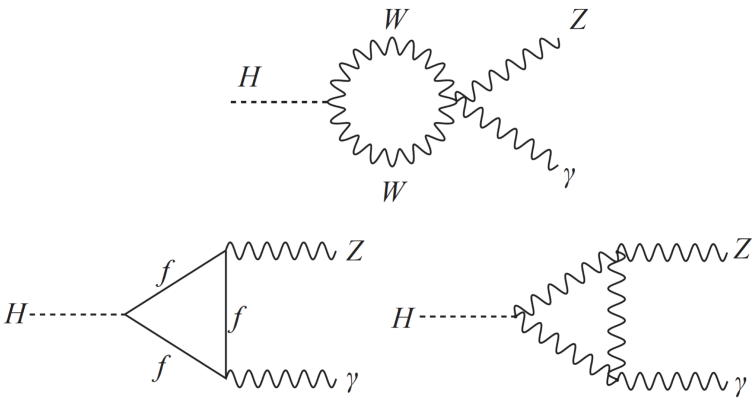

FIGURE 6.1: Feynman diagrams for the $H \to Z\gamma$ decays.

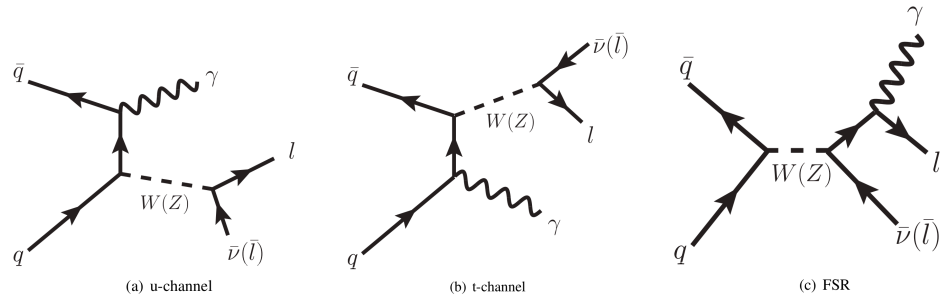

FIGURE 6.2: Feynman diagrams for the Z boson and photon production.

set at the level of 11 (9) times the SM expectation, at 95% confidence level. In Run-2, this search was performed by ATLAS with the partial dataset of 36.1 fb^{-1} collected at $\sqrt{s} = 13$ [90]. Again, no significant excess was observed an an observed (expected) upper limit of 5.21 (4.41) was set at 95% CL for $m_H = 125.09$ GeV.

The updated search includes, as previously, the increased integrated luminosity (about 350% larger than in Run-1). Next there are several major improvements in the analysis technique. The object selection requires the presence of a photon and two same-flavour, opposite-sign leptons consistent with a Z boson decay. Identification and isolation requirements are applied to the photon and the leptons to suppress background events. Both the photon and lepton requirements have been optimised for the LHC conditions during the data-taking period. Details are provided in Sec. 6.3. After the selection, events are classified into categories with either different signal-to-background ratios or signal invariant mass resolutions of the dilepton-plus-photon triplet. The categories were designed and optimised using multivariate techniques to maximise the sensitivity to the SM Higgs boson and are given in Sec. 6.4. After applying a Z-boson mass constraint to the dilepton pair to improve the signal resolution, a maximum likelihood fit to the distribution of the $Z\gamma$ invariant mass is performed in all the categories to determine the $H \to Z\gamma$ signal yield.

6.2 Monte Carlo modelling

Simulated Monte Carlo (MC) samples with various event generators are produced to study the characteristics of signal and background events and to optimise the search strategy. The MC events, which describe interactions of particles with the detector material, are generated with the ATLAS detector simulation [91] based on GEANT4 [92]. In order to have a matching description to the experimental data, all of the simulated samples contain bunch-train pile-up, modelled by overlaying simulated inelastic pp events over the original hard-scattering event. The Monte Carlo events are weighted to reproduce the experimental data distribution of the number of interactions per bunch crossing. Simulated events are reconstructed using the same software and the same algorithms used for experimental data. The Higgs boson mass value for all simulated samples is chosen to be $m_H = 125$ GeV.

6.2.1 Signal samples

Signal samples have been generated and passed through the full ATLAS detector simulation and event reconstruction in order to study the efficiency of the final selection.

Signal simulated events are generated using the following programs: events produced in gluon fusion (ggF) or vector-boson fusion (VBF) have been generated using POWHEG [93, 94, 95, 96, 97] interfaced with PYTHIA8 [98] for parton showering, hadronization and the underlying event. Events produced in association with a vector boson (WH or ZH) or with a $t\bar{t}$ pair (ttH) have been generated with POWHEG+PYTHIA8. In all Higgs signal MC samples, the Z boson is forced to decay to charged lepton pairs including electrons, muons, and taus with a branching ratio of 3.36%. In addition, as was mentioned, only 125 GeV samples are used, with the shift of the signal shape to 125.09 GeV.

The signal samples used for the SM Higgs boson search include all the 5 main production modes (ggF, VBF, WH, ZH, ttH) for $m_H = 125$ GeV. All of these contribute to the signal and their relative yields are fixed to the SM predictions.

An additional sample with multiple parton interactions disabled is used to study the theoretical uncertainties related to the modelling of non-perturbative quantum chromodynamics (QCD) effects. The gluon fusion production mode of the Higgs boson is used. It is generated with MADGRAPH5_aMC@NLO [99] using the NNPDF30 PDF [100, 101] set, which includes up to two jets at next-to-leading-order (NLO) accuracy in QCD using the FxFx merging scheme [99, 102].

6.2.2 Background samples

There are potential background contributions from other Higgs decay modes. They include the evaluated contribution from $H \to \mu\mu$, where the reconstructed photon originates from QED final-state radiation. One more contribution is from the interference between Higgs boson decays with the same final-state signature ($H \to \gamma^*\gamma$, $\gamma^* \to e^+e^-/\mu^+\mu^-$ and $H \to \mu\mu$) which is expected to be negligible in the Standard Model [103] and is neglected.

The main background sources are mainly from non-resonant production of a Z boson and a photon ($Z\gamma$), and from the production of Z bosons in association with jets (Z+jets), where the jet is misidentified as a photon.

Fully simulated $Z\gamma$ events are generated with Sherpa 2.2 [104]. The matrix element for real emission of up to three partons is included. The leading-order (LO) accuracy in QCD and the NN30NNLO PDF set are used. The samples are generated

separately for the electron and the muon final states in slices of the photon transverse momentum. The fully simulated samples are used for the categorisation optimisations and background composition studies.

To perform systematic uncertainty studies related to the choice of the functional form of the background $\ell\ell\gamma$ invariant mass distribution, a large sample of $Z\gamma$ events with an invariant mass between 95 GeV - 3 TeV has been generated with Sherpa 2.2 using the fast simulation of the calorimeter response [105]. The matrix elements used for the generation include real emissions of up to two partons. A dedicated study of the matrix elements for the production of up to 0, 1, 2, or 3 partons together with the two leptons and the photon showed that this configuration provides the best generation speed with sufficient accuracy of the predicted invariant mass shape. The samples are generated separately for the electron and the muon final states, in slices of the three-body invariant mass. However, the statistics of these samples are not sufficient for the background modelling study (described in Sec. 6.5.4) in a VBF-enriched category with 2 or more partons with a very tight selection. Hence, a special 2 parton fast simulation $Z\gamma$ sample is used for studying the cases where it is necessary to have events with 2 or more partons N_{par}>=2, a large distance between leading and sub-leading partons $\Delta\eta_{pp}$>2, and large transverse momentum of the leading parton.

The Z+jets background is estimated using a data-driven technique. $Z \to ll$ samples, simulated with POWHEG generator and interfaced to PYTHIA8 at NLO accuracy in QCD are used in addition to validate Z+jets data-driven background.

6.3 Object and event selection

The $H \to Z\gamma$ analysis uses events recorded in the years 2015-2018 during pp-collisions of the LHC. The data is required to pass a combination of the lowest-p_{T} threshold unprescaled single-lepton or di-lepton triggers (Table 6.1). In addition, these events are required to contain at least one primary vertex (PV) candidate, determined from a fit to the tracks reconstructed in the inner detector with transverse momentum $p_{\mathrm{T}} > 500$ MeV. The primary vertex candidate is defined as the one with the largest sum of the squared transverse momenta of the tracks associated with it. The total integrated luminosity after trigger selection and quality criteria is 139 fb^{-1}.

Candidates	Channel	Single/Di-lepton	Trigger name
2015 data	$Z(\to ee)\gamma$	single electron	HLT_e24_lhmedium_L1EM20VH
			HLT_e60_lhmedium, HLT_e120_lhloose
2015 data	$Z(\to ee)\gamma$	di-electron	HLT_2e12_lhloose_L12EM10VH
2016 data	$Z(\to ee)\gamma$	single electron	HLT_e26_lhtight_nod0_ivarloose
			HLT_e60_lhmedium_nod0, HLT_e140_lhloose_nod0
2016 data	$Z(\to ee)\gamma$	di-electron	HLT_2e17_lhvloose_nod0
2017-2018 data	$Z(\to ee)\gamma$	single electron	HLT_e26_lhtight_nod0_ivarloose
			HLT_e60_lhmedium_nod0, HLT_e140_lhloose_nod0
2017-2018 data	$Z(\to ee)\gamma$	di-electron	HLT_2e24_lhvloose_nod0
2015 data	$Z(\to \mu\mu)\gamma$	single muon	HLT_mu26_imedium, HLT_mu50
2015 data	$Z(\to \mu\mu)\gamma$	di-muon	HLT_mu22_mu8noL1
2016 data	$Z(\to \mu\mu)\gamma$	single muon	HLT_mu26_imedium
			HLT_mu26_ivarmedium, HLT_mu50
2016 data	$Z(\to \mu\mu)\gamma$	di-muon	HLT_mu22_mu8noL1
2017-2018 data	$Z(\to \mu\mu)\gamma$	single muon	HLT_mu26_ivarmedium, HLT_mu50
2017-2018 data	$Z(\to \mu\mu)\gamma$	di-muon	HLT_mu22_mu8noL1

TABLE 6.1: Triggers used to select data in 2015 - 2018.

6.3.1 Object selection

For the analysis, it is necessary to reconstruct photon, jet, electron and muon candidates (described in details in Ch. 4). Next, two levels of selection are applied: first, a "preselection" applied to define the objects used as inputs to the overlap removal procedure (Sec. 6.3.1). Second, a set of final selection criteria are applied to the object candidates in addition to the preselection. The final selection criteria are applied after overlap removal and after a Z-boson candidate is chosen in an event. Events with photon candidates passing the preselection but satisfying a looser criteria will be used to estimate the background composition of the selected sample in terms of $Z\gamma$ and Z+jet contributions.

Preselected photons are required to have transverse momentum above 10 GeV and pseudorapidity within the region $|\eta| < 1.37$ or $1.52 < |\eta| < 2.37$. Photons reconstructed in or near regions of the calorimeter affected by read-out or high-voltage failures are not accepted. Photons are preselected with a "Loose ID" identification requirement, described in Sec. 4.1.8. No isolation requirement is applied at preselection stage, to allow for background composition studies described later.

The final photons are selected using a requirement on $p_T^{\gamma}/m_{\ell\ell\gamma}$, found by maximising the expected sensitivity as described later in Sec. 6.3.3. The final photons use the optimised "Tight ID" definition, which allows maximisation of the expected sensitivity and photon efficiency for transverse momentum above 10 GeV for the current analysis. The final photon isolation requirements are described in Section 6.3.3.

Preselection electrons are required to have a transverse momentum $p_{\mathrm{T}} > 10$ GeV and a pseudorapidity of $|\eta| < 2.47$. Electron candidates in the transition region between the barrel and the end-cap sections of the electromagnetic calorimeter ($1.37 < |\eta| < 1.52$) are excluded. For preselection muons, the required transverse momentum is $p_{\mathrm{T}} > 10$ GeV and the allowed rapidity range is $|\eta| < 2.7$. The transverse impact parameter significance d_0/σ_{d_0} of the ID track associated with a lepton within the acceptance of the inner detector is required to be less than 3 for muons (except for standalone muon candidates) and less than 5 for electrons. This requirement suppresses secondary leptons produced in the decay chains of heavy-flavor hadrons. The electron impact parameter is affected by bremsstrahlung and it thus has a broader distribution. Furthermore, both electrons and muons have to satisfy the criterion $|z_0 \sin\theta| < 0.5$ mm, as well as the lepton identification requirements. The Loose likelihood ID is required for electrons, and the Medium muon ID is required for muons.

Preselected leptons are required to be isolated from hadronic activity in order to suppress background from leptons produced in decays of hadrons inside jets as well as lepton fakes from hadronic jets. The "FCLoose" relative isolation criteria are applied to electrons as well as muons. It also employs tracking information from the inner detector, using isolation cones of $\Delta R = 0.2$ for electrons and $\Delta R = 0.3$ for muons, requiring for both to contain in total less than 0.15 of the lepton p_T. The "FCLoose" isolation criteria provide a signal efficiency of 90% to 99% depending on the lepton p_T.

The final electrons and muons are defined by applying stricter p_{T} thresholds, which are partially based on which trigger collected the event in order to avoid trigger turn-on inefficiencies. The requirement is mostly

$$p_{\mathrm{T}} > p_{\mathrm{T}}(\text{trigger threshold}) + 1 \text{ GeV}, \tag{6.1}$$

for the matching lepton, and the two matching leptons in the case of di-lepton triggers. The requirements described above are imposed after overlap removal (sec. 6.3.1) and after selecting the Z boson candidate as described in Section 6.3.2.

The p_{T} threshold of the final electrons was optimised using MC, always respecting the trigger threshold requirement stated above.

The default jet selection criteria uses the EMTopo jet collection with the anti-k_t algorithm [80] with a distance parameter of $R = 0.4$. Jets are required to have an absolute rapidity of less than 4.4, a transverse momentum of at least 25 GeV and to fulfil the "LooseBad" jet quality requirements. The default JVT calibration working point is used which has an average efficiency of 92% and requires jets that have $p_{\mathrm{T}} < 60$ GeV and $|\eta_{\mathrm{det}}|$ <2.4 to satisfy JVT > 0.59. Jets outside of this p_{T} and η region are accepted without any cut on JVT.

Overlap removal

The overlap removal procedure allows the resolution of ambiguities between reconstructed objects and its application is described below.

The *ee* overlap removal criteria are defined as follows: If two electron candidates have identical track parameters, only the candidate with the highest p_{T} is retained. If the two electron clusters are closer than $|\Delta\eta| < 0.075$ and $|\Delta\phi| < 0.125$, the electron cluster with highest p_{T} one is kept. If the track associated to an electron candidate is within a distance at the interaction point of $\Delta R < 0.02$ from the track associated to a muon candidate passing all the muon selection criteria, the electron candidate is rejected.

The $\mu\mu$ overlap removal is applied at the reconstruction level, and it allows the resolution of close by muons within an angular resolution of the order 0.01-0.02.

The overlap removal procedure for photons and jets has been optimised to account for the possible impact of the loose electron identification on the number of fakes. It is applied after the $Z \to \ell\ell$ selection, described in sec. 6.3.2. Photon candidates are rejected within $\Delta R < 0.3$ of a selected pair of electron or muon candidates with an invariant mass closest to the Z pole, thus suppressing background from final-state-radiation (FSR) $Z+\gamma$ events and an additional possible contribution from photons faking electrons. Likewise, jets that are within $\Delta R < 0.2$ of photons, pairs of electrons or muons are removed.

6.3.2 $Z \to \ell\ell$ reconstruction and selection

Z boson candidates are reconstructed from pairs of same flavor, opposite sign leptons passing the preselection. In the case of multiple Z candidates in the same event, the candidate with the constrained invariant mass closest to the Z pole is chosen, with the FSR corrections implemented before the Z-mass constraint.

After selecting one Z-boson candidate, depending on whether single or di-lepton triggers were passed, either one or both of the leptons used to form the Z boson candidate are required to satisfy the signal lepton requirements described previously, to match the trigger object(s) and to satisfy the corresponding thresholds of the triggers used to select the event. For the trigger matching, an angular matching between the offline lepton and the trigger-level lepton is performed. If these requirements are not met then the event is discarded.

To improve the Higgs boson mass resolution, a Z-mass constraint [106] is applied to the Z boson candidates after applying FSR corrections [107] for muons. The FSR correction contributes very little to the improvement of the mass resolution and is only applied in the $Z \to \mu\mu$ channel since for electrons, soft photons almost collinear to the muon are reconstructed in the same cluster as the electron and are thus already accounted for when estimating the electron energy. Fig. 6.3 shows corrections applied

on $Z \to \ell\ell$ mass distribution for the ggH signal Monte Carlo. The resolution improves by 11% in both the $Z \to ee$ channel and $Z \to \mu\mu$ channels. An invariant mass (without corrections) requirement $m_{\ell\ell} > 45$ GeV is applied in order to remove biases from the generator-level filter ($m_{\ell\ell} > 40$ GeV) of the simulated Z+jet samples. The default final selection for the Higgs Boson search requires the corrected (Final-State-Radiation and Z mass constraint corrections) di-lepton mass, $|m_{\ell\ell} - m_Z|$, to be less than 10 GeV.

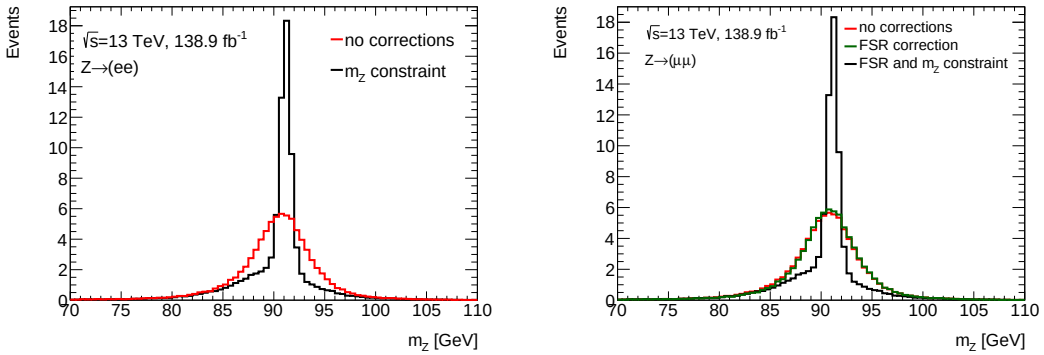

(a) $Z \to ee$ (b) $Z \to \mu\mu$

FIGURE 6.3: $Z \to \ell\ell$ mass distribution at 125 GeV with or without the Z mass constraint (for electrons and muons) and the FSR correction (only for the muons).

6.3.3 $H \to Z\gamma$ reconstruction and selection

Signal candidates are reconstructed from the combination of the Z candidate with an invariant mass closest to the Z pole and the photon with the largest transverse energy.

Photon candidates are required to pass a stricter selection than that applied at the pre-selection stage:

- They must pass the Tight identification criteria, based on their shower shapes in the electromagnetic calorimeter. The criteria has been redefined for the search of the SM Higgs Boson decay to $Z\gamma$ [1] at the end of Run-2. The optimised, p_{T}-dependent Tight identification allows for the efficiencies of low- and high-p_{T} photon regions to be tuned separately. The new version of the Tight ID is tuned to have a ∼20% higher efficiency at low-p_{T} w.r.t the previous version, and an improved background rejection at high-p_{T}, with the estimated improvement of the sensitivity around 4%. Figure 6.4 shows a comparison of the Tight ID requirement used in the old analysis, which is p_{T}-independent, to the new p_{T}-dependent ID as a function of their efficiency and background rejection. Fig. 6.5 shows the photon p_{T} distribution for signal ($m_H = 125$ GeV) Monte-Carlo and for background ($Z\gamma$ and Z+jets) events, with impact of the Tight ID requirement applied.

- They must be isolated from hadronic activity. For the search of the SM Higgs boson decay to $Z\gamma$, the "`Loose`" working point is used which is based firstly on the energy in a cone of radius 0.2 around the photon and requires $E_{\mathrm{T}}^{\mathrm{iso}}$ to be less than $0.065 \times p_{\mathrm{T}}$ GeV, and secondly on $E_{\mathrm{T}}^{\mathrm{iso}}$ in a cone with radius 0.2 around the photon and requires $E_{\mathrm{T}}^{\mathrm{iso}}$ to be less than $0.05 \times p_{\mathrm{T}}$.

- In the Higgs boson search the ratio between the photon transverse momentum and the three-body invariant mass $p_T/m_{\ell\ell\gamma}$ must be larger than 0.12.

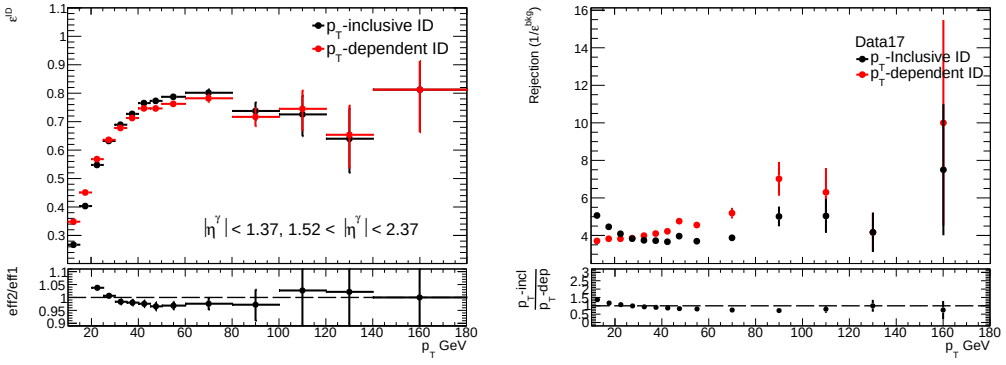

FIGURE 6.4: The Tight photon ID efficiency vs photon p_T, the p_T-dependent ID (red dots) and p_T-independent ID (black dots).

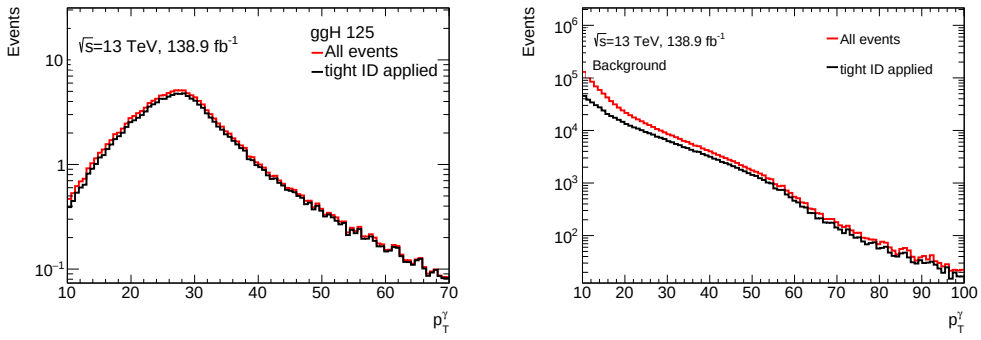

(a) Signal (b) Background

FIGURE 6.5: Photon p_T distribution without the Tight ID applied (red line) and with the Tight ID applied (black line), for the signal (ggH 125) and for the background $Z\gamma$ and Z+jets events.

The standard choice of higher photon transverse momentum p_T threshold, applied after the initial photon p_T threshold, is replaced by the requirement on the ratio between the photon transverse momentum and the three-body invariant mass $p_T/m_{\ell\ell\gamma}$. The final value of the minimum photon relative transverse momentum ($p_T/m_{\ell\ell\gamma} > 0.12$) was chosen by taking the value that maximises the expected sensitivity. Figure 6.6 shows the comparison of the distributions of the three-body invariant mass $p_T/m_{\ell\ell\gamma}$ with the photon p_T and $p_T/m_{\ell\ell\gamma}$ requirements applied. As is seen, both distributions have similar shapes, with $p_T/m_{\ell\ell\gamma}$ having no turn-on effect present in the $m_{\ell\ell\gamma}$ spectrum. Further details of the study can be found in Sec. 6.5.4.

After the final event selection, 99.94% of the reconstructed photons from the gluon fusion signal MC sample match truth photons within a cone of $\Delta R = 0.4$, which confirms that the contribution from pile-up jets faking photons is negligible.

The invariant mass $m_{Z\gamma}$ of the selected $H \to Z\gamma$ candidates is calculated from the reconstructed lepton and photon four-momenta applying the lepton corrections to improve the resolution for signal events and thus improve discrimination against non-resonant background events. In particular, muon momenta are corrected for collinear final state radiation effects and lepton (both electron and muon) four-momenta are finally corrected using a Z-boson mass constraint. The latter estimates the most

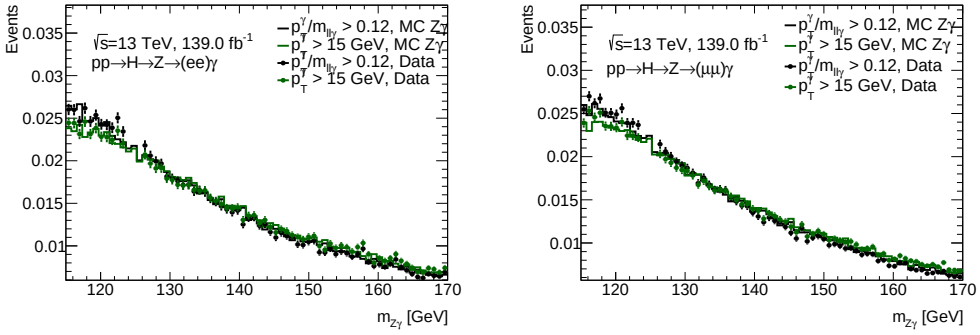

(a) Electron channel (b) Muon channel

FIGURE 6.6: 3-body mass distribution of data between 100 and 170 GeV (data is blinded for 123-127 GeV), Zgamma (full-sim MC), with photon $p_{\mathrm{T}} > 15$ GeV and $p_{\mathrm{T}}/m_{\ell\ell\gamma} > 0.12$.

probable values for the lepton momenta from their measured values by maximizing a likelihood function that contains a Breit-Wigner function describing the Z boson lineshape and Gaussian functions describing the resolution of the measurements of the lepton momenta. These estimated most probable values are then used to correct the measured lepton momenta.

The Z-boson mass constraint has large impact on Z mass resolution but does not influence the angular distributions. Table 6.2 shows the improvement of the $Z\gamma$ mass resolution from the Z mass constraint and the FSR (Final-State-Radiation) correction. The mass resolution is defined here as the RMS of the $Z\gamma$ mass distribution.

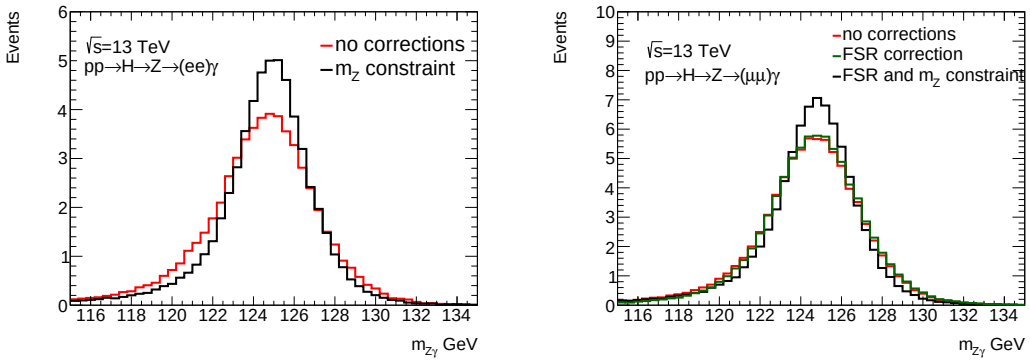

(a) $Z\gamma \to ee\gamma$ (b) $Z\gamma \to \mu\mu\gamma$

FIGURE 6.7: $Z\gamma$ mass distribution at 125 GeV with or without the Z mass constraint (for electrons and muons) and the FSR correction (only for the muons).

For the SM Higgs boson search ($m_H = 125$ GeV), the resolution is improved by

RMS(GeV)	$Z \to ee$	$Z \to \mu\mu$
no corrections	2.75	2.61
FSR correction only	2.75 (no FSR on e)	2.53
FSR + Z mass constraint	2.36	2.34

TABLE 6.2: $Z\gamma$ mass resolution (RMS of 3-body mass spectrum) with/without the Z mass constraint and the FSR correction, at 125GeV.

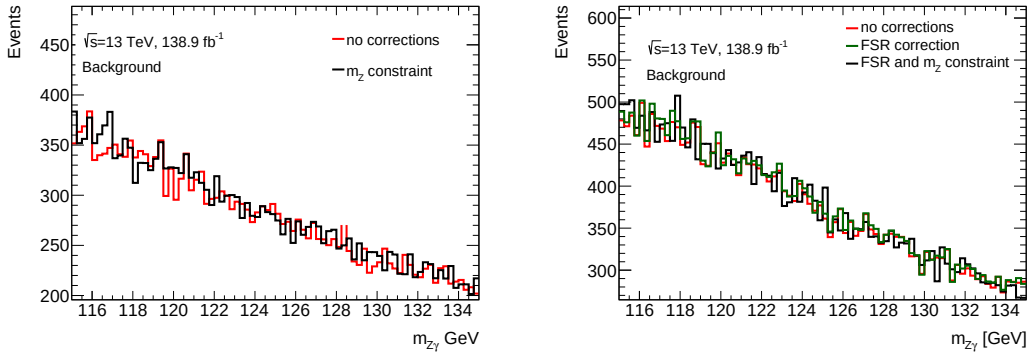

(a) Electron channel (b) Muon channel

FIGURE 6.8: $Z\gamma$ mass distribution with or without the Z mass constraint (for electrons and muons) and the FSR correction (only for the muons), for the background $Z\gamma$ and Z+jets events.

14% in the $Z \to ee$ channel and by 10% in the $Z \to \mu\mu$ channel. Fig. 6.7 shows corrections applied on $Z\gamma$ mass distribution for the ggH signal Monte Carlo with $m_H = 125$ GeV with a clear improvement on the mass resolution. Fig. 6.8 shows the corrections applied for the background $Z\gamma$ and Z+jets events, with no impact observed.

For the search of the SM Higgs Boson decay to $Z\gamma$, candidates with 115 GeV $< m_{\ell\ell\gamma} <$ 170 GeV are retained.

The effect of the contribution of other Higgs processes, such as $H \to \gamma^*\gamma$ and $H \to \mu\mu$, has been estimated. The additional condition on truth invariant mass $m_{\ell\ell}$ to be more than 50 GeV is required in order to remove contamination from $H \to \gamma^*\gamma$ process, with the remaining contribution found to be negligible. The contamination of the $H \to \mu\mu$ process can be reduced with use of the requirement on raw reconstructed invariant mass $m_{\ell\ell}$, without any FSR and Z mass constraint, to be less than 101 GeV. The largest contribution over all event categories of the $H \to \mu\mu$ process to the signal $H \to Z\gamma$ process after the $m_{\ell\ell}$ requirement was found to be 3.3%.

The final reconstruction and selection efficiency for $H \to Z(\to \ell\ell)\gamma$ events is 18.4-22.4% varying depending on the production mode.

6.4 Event categorisation

To improve the sensitivity of the $H \to Z(\to \ell\ell)\gamma$ signal, events can be filtered into mutually exclusive categories, each carry their own signal-to-background ratio, expected signal efficiencies and invariant mass resolution. The sensitivity (z) can be expressed as the following equation 6.2

$$z = \frac{N_S}{\sqrt{N_S + N_B}}, \tag{6.2}$$

where N_S is the yield of the SM prediction and N_B is the yield of the total ($Z\gamma$ and $Z + jet$) non-resonant background. The background yield is normalised to the data with 139.0 fb^{-1} in the mass range 115 - 170 GeV.

For the signal yield prediction of Higgs search, all of the Higgs processes are used, such as ggF, VBF, WH, ZH and ttH production modes.

The background is defined as the sum of the $Z\gamma$ component from the full simulation $Z\gamma$ sample (defined in Sec. 6.2) and the Z+jet component from a Z+jet enriched data control sample obtained by inverting the photon ID requirement. The sum of the two components is normalised to the data and their relative fraction is set to 80% (as it is measured in Sec. 6.5.2).

Several strategies of categorisation are tried and described below, where categorisation methods are based on use of kinematic variables and on specific features of different Higgs production processes.

6.4.1 Kinematic cut-based categorisation

In the search for the $Z\gamma$ decay of a SM Higgs boson, event categories can be defined based on the various kinematic properties of the Higgs boson decay to a Z boson and photon. Among all of them two quantities were selected based on their background to signal separation power:

- the relative p_T, $p_T^\gamma/m_{\ell\ell\gamma}$;
- the component of the Higgs candidate p_{T} that is orthogonal to the axis defined by the difference between the photon and the Z boson momenta, p_{Tt} (see Eq 6.3 and Fig. 6.9), where $p_{\mathrm{T}}^{Z-\gamma}$ is the p_T of the 3-vector subtraction of Z and γ.

$$p_{\mathrm{Tt}} = 2\frac{|p_x^Z p_y^\gamma - p_x^\gamma p_y^Z|}{p_{\mathrm{T}}^{Z-\gamma}} \tag{6.3}$$

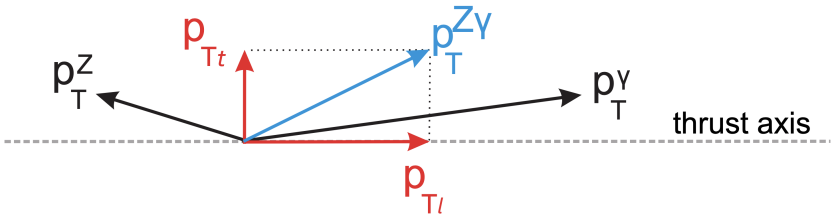

FIGURE 6.9: Diagram of the Higgs p_{Tt} variable.

The estimated sensitivity is calculated to be 1.20 for an SM Higgs boson of 125 GeV, as shown in Table 6.3. In addition to two of the described quantities, separation to the lepton flavour is used as it shows improvement in achieved sensitivity.

number	Category	N_S	N_B	N_S 68% SR	N_B 68% SR	$\frac{S}{\sqrt{(S+B)}}$	Mass range (GeV)
1	$p_T^\gamma/m_{\ell\ell\gamma} > 0.4$	12.85	2930.00	8.99	131.13	0.76	123.5-127.5
2	$ee\gamma$, $p_T^\gamma/m_{\ell\ell\gamma} < 0.4$, $p_{\mathrm{Tt}} > 40$ GeV	15.20	5383.00	10.22	488.58	0.46	123.5-127.5
3	$ee\gamma$, $p_T^\gamma/m_{\ell\ell\gamma} < 0.4$, $p_{\mathrm{Tt}} < 40$ GeV	50.90	55226.00	33.20	6085.17	0.42	123.5-127.5
4	$\mu\mu\gamma$, $p_T^\gamma/m_{\ell\ell\gamma} < 0.4$, $p_{\mathrm{Tt}} > 40$ GeV	18.45	6678.00	12.34	627.41	0.49	123.5-127.5
5	$\mu\mu\gamma$, $p_T^\gamma/m_{\ell\ell\gamma} < 0.4$, $p_{\mathrm{Tt}} < 40$ GeV	64.13	73008.00	49.28	10376.64	0.48	122.5-127.5
	combined sensitivity	161.53	143225.00			1.20	

TABLE 6.3: The signal sensitivity at 125 GeV at 139.0 fb^{-1}, with cut-based categories.

The cut points of $p_T^\gamma / m_{\ell\ell\gamma}$ and p_{Tt} are chosen based on their individual maximum sensitivity through the scans of all possible cut values applied on the criteria. Figure 6.10 shows the 2D sensitivity as a function of $p_T^\gamma / m_{\ell\ell\gamma}$ and p_{Tt}. The combined sensitivity at the cut point with $p_T^\gamma / m_{\ell\ell\gamma} > 0.4$ and $p_{\mathrm{Tt}} > 40$ GeV gives the value of 1.11.

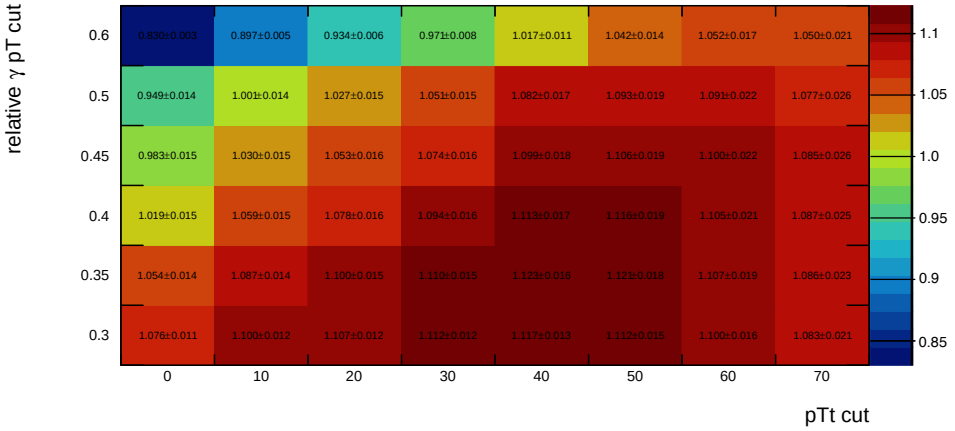

FIGURE 6.10: 2D combined sensitivity as a function of $p_T^\gamma / m_{\ell\ell\gamma}$ and p_{Tt} of the 5 cut-based categories.

6.4.2 VBF-enriched categorisation

Vector boson fusion (Fig. 6.11) is the second-most prominent Higgs production process. Its signature, characterised by two extra jets with large invariant mass and rapidity separation, permits defining a category of events with a better signal-to-background ratio.

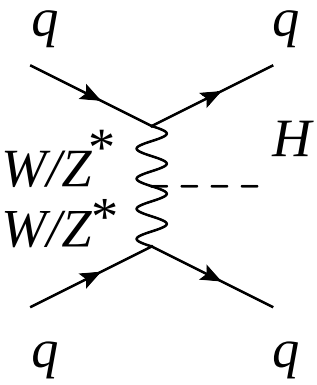

FIGURE 6.11: Leading order Feynman diagram for VBF process.

The main non-resonant backgrounds to VBF events in $H \to Z\gamma$ analysis are from Standard Model QCD processes:

- direct $Z\gamma$ pairs produced in association with at least two jets,
- direct single Z boson events with at least three jets where one of the jets fakes a photon.

Additional small background contamination to the VBF production process can come from VBS Zγ + two jets. Hence the mixed non-VBS Zγ, VBS Zγ+jets, and Z+jets events passing the $N_{jet} >= 2$ requirement ($N_{jet} >= 2$, $\Delta\eta_{j,j} > 2$) are used as background. The three background components are mixed according to the background fraction of 0.77 for non-resonant Zγ, 0.02 for VBS Zγ+jets and 0.21 for Z+jets.

The variables used to define a VBF-enriched category are chosen to have the best possible performance in signal-to-background separation among all of the kinematic variables. The definition of these variables is shown in Table 6.4, and their distributions for signal, background and data are shown in Fig 6.12. These variables are used in the Gradient Boosted Decision Tree (BDTG) method using TMVA (Toolkit for Multivariate Data Analysis) [108] to do the training and testing of the BDTG discriminant. A VBF-enriched preselection, which requires at least two jets ($N_{jet} >= 2$) and $\Delta\eta_{jj} > 2$, is applied before training and testing. Fig. 6.13 shows the BDTG response distribution between signal and background. Since the VBS Zγ+jets component is small, its presence does not impact the BDTG training and performance.

Variables	Definition
$\Delta\Phi_{Z,\gamma}$	Azimuthal angle between di-lepton system and photon
$\Delta\eta_{jj}$	Pseudo-rapidity separation of dijet
$\Delta R^{min}_{\gamma or Z,j}$	Minimum ΔR between one object of the Zgamma and jets
m_{jj}	Invariant mass of dijet
p_{Tt}	Zgamma p_{T} projected perpendicular to the Zgamma thrust axis
$\eta^{Zeppenfeld}$	$\lvert\eta_{Z\gamma} - 0.5 * (\eta_{j1} + \eta_{j2})\rvert$
$\Delta\Phi_{Z\gamma,jj}$	Azimuthal angle between Zgamma and dijet system

TABLE 6.4: Variables used for VBF-enriched selection and their definitions.

It is possible to determine from the response the optimal cut point, which would allow the best possible signal to background separation with the highest sensitivity of the category to be achieved. Fig. 6.14 shows the sensitivity obtained for the VBF production mode (regarding VBF production mode as signal and ggH+WH+ZH+Zγ+Zjet as background) (a) and for all of the Higgs production modes ggH+VBF+WH+ZH (b). From this, it is possible to select the response point BDTG > 0.87 with the maximum sensitivity (0.67 ± 0.05).

The estimated combined sensitivity with use of VBF-enriched category with cut on BDTG of 0.87 is measured to be 1.04 for a SM Higgs boson of 125 GeV and is shown in Table 6.5.

Number	Category	N_S	N_B	N_S 68% SR	N_B 68% SR	$\frac{S}{\sqrt{(S+B)}}$	Mass range (GeV)
1	BDTG > 0.87	3.91	169.00	2.34	11.56	0.63	123.5-126.5
2	BDTG < 0.87	157.62	143056.00	103.79	15550.60	0.83	123.5-127.5
	combined sensitivity	161.53	143225.00			1.04	

TABLE 6.5: The signal sensitivity = $N_S/\sqrt{N_S + N_B}$ at 125 GeV at 139.0 fb^{-1}, with use of VBF-enriched only category.

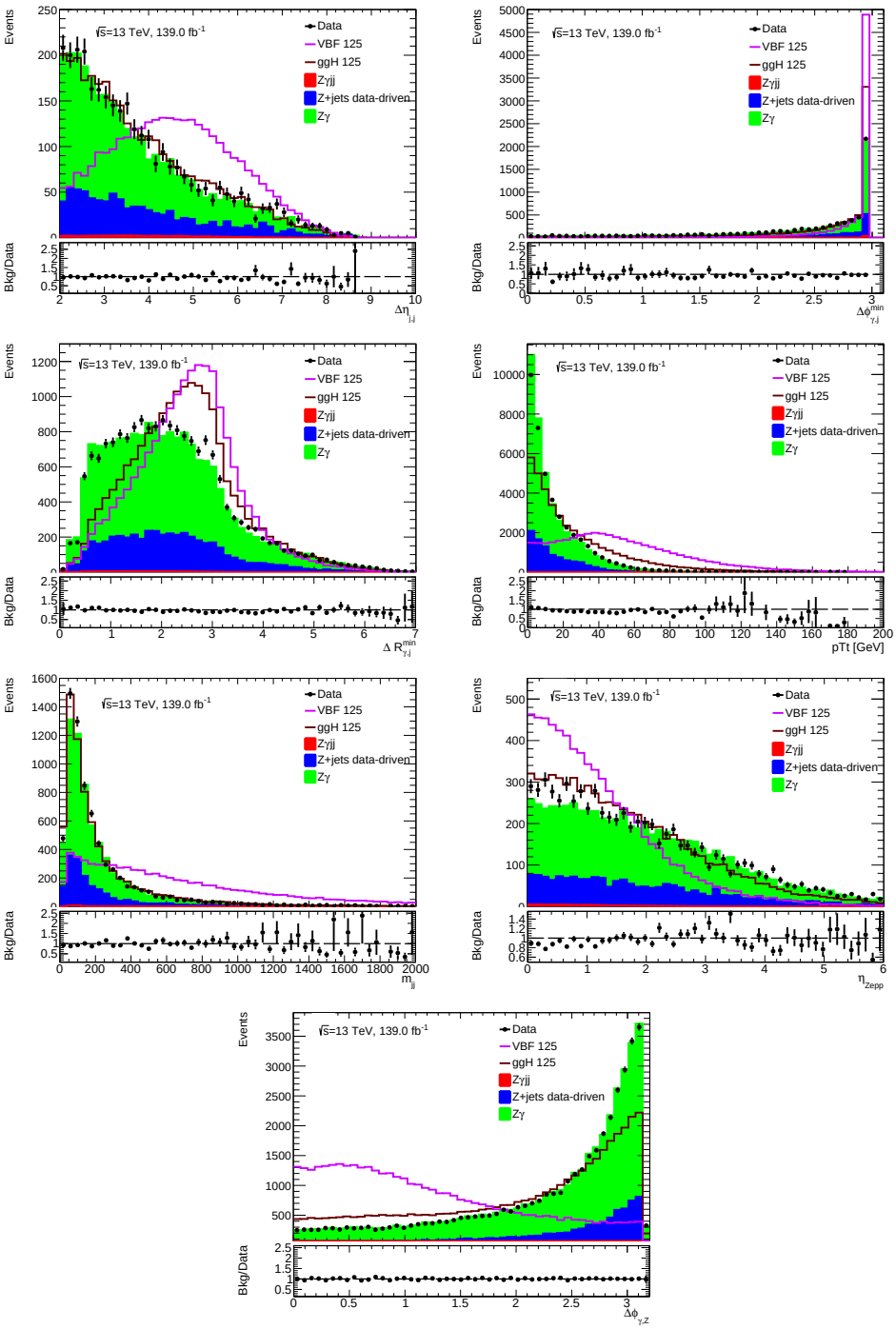

FIGURE 6.12: Variables distribution used in the MVA. The shapes of MC are normalised to the number of events in data. In the lower pad, the ratio shows background samples over data.

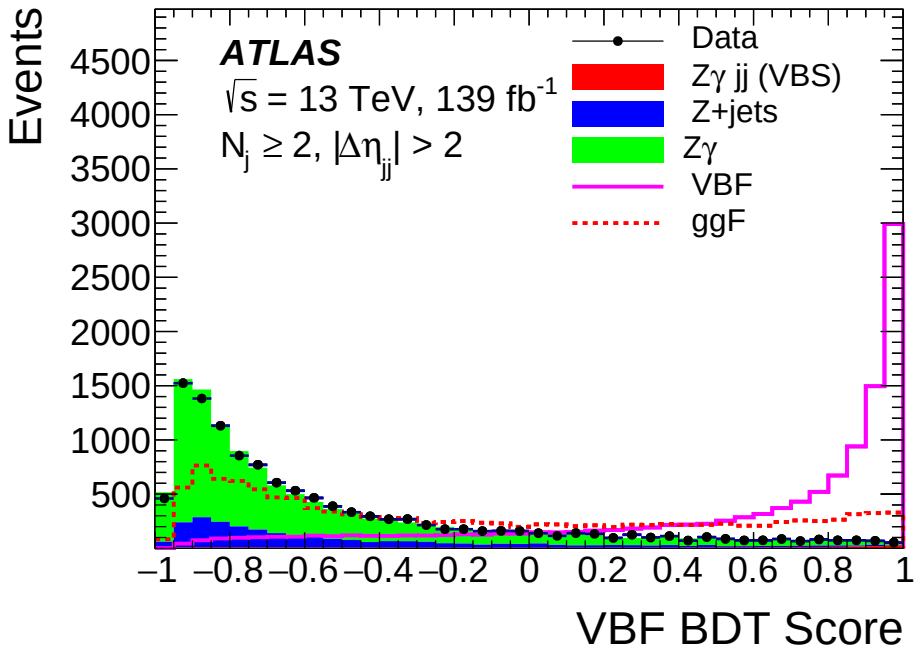

FIGURE 6.13: Distribution of the BDTG variable as a result of the MVA training. The shapes of MC are normalized to the number of events in data. In the lower pad, the "ratio" means background samples over data.

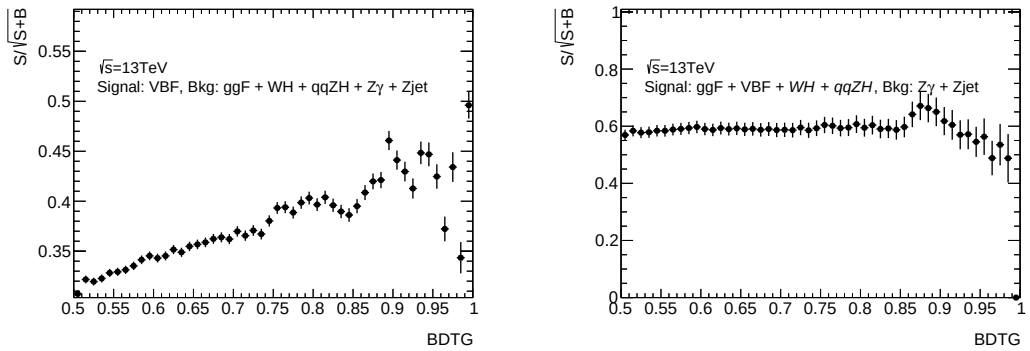

(a) (b)

FIGURE 6.14: (a) The VBF sensitivity (regarding VBF production mode as signal and ggH+WH+ZH+Zγ+Zjet as background) in the VBF-enriched category as a function of the new BDTG cut. (b) Sensitivity of the Higgs boson signal (regarding ggH+VBF+WH+ZH as signal and Zγ+Zjet as background) in the VBF-enriched category as a function of the BDTG cut. In (b), the $Z\gamma + Zjet$ yield are normalized to the data in the inclusive BDTG region.

6.4.3 Full Higgs signal categorisation

The gluon-gluon fusion (ggF) production mode is the dominant mode, where the Higgs boson couples indirectly to gluons via a triangular loop of quarks dominated by the top quark. This process is generally characterised either by no presence of jets, or by presence of one extra jet from gluon radiation. Vector boson fusion, as was described in 6.4.2, is the second Higgs production process and characterised by two extra jets. Additionally, events with two extra jets can also come from the associated production with vector bosons (WH or ZH, fig. 6.15), where W(jj) or Z(jj) are characterised by two extra jets with their invariant mass equal to the invariant mass of W or Z bosons. WH and ZH processes can also be characterised by absence of any jets in case of leptonic decays ($Z(\ell\ell)H$) or in case of decays with the presence of missing energy ($Z(\nu\nu)H$, $W(\nu\ell)H$).

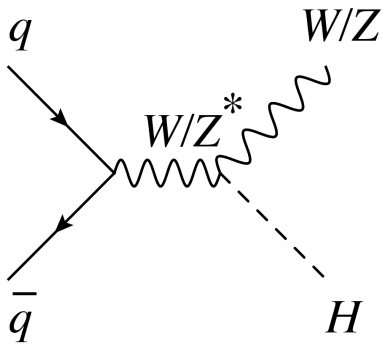

FIGURE 6.15: Leading order Feynman diagram for WH+ZH process.

Therefore it is possible to define three event categories based on number of jets with separation on Higgs production modes:

- Category with absence of jets: $N_{jet} = 0$,
- Category with one jet: $N_{jet} = 1$,
- Category with at least two jets: $N_{jet} >= 2$.

The main non-resonant backgrounds to Higgs signal processes are from SM QCD processes:

- direct Zγ pairs produced in association with either at least two jets, one jet or produced without any association to jets.
- direct single Z events with either with one jet, two jets, or with at least three jets, where one of the jets fakes a photon.

The mixture of the Zγ and Z+jet events is taken with the background fraction measured in Sec 6.5.2.

Three sets of variables are introduced, each of them defining its own category based on number of jets. The definition of these variables is shown in Table 6.6, and their distributions for signal, background and data are shown in Fig. 6.16.

Each of the variables sets, which defines its own category, was used with its own classification method in order to obtain a signal-background discriminant. The choice of classification method was done with use of TMVA, based on the following principles: ROC-curve (Receiver Operating Characteristic curve) for the chosen method

Variables	Definition
	$N_{jet} = 0$
$p_T^{\gamma}/m_{\ell\ell\gamma}$	Ratio of p_T to mass $\ell\ell\gamma$
$p_{Tt}^{\ell\ell\gamma}$	p_{Tt} of $ll\gamma$ system
$\Delta\phi_{Z,\gamma}$	Azimuthal angle between Z and γ
$\Delta\eta_{Z,\gamma}$	Pseudo-rapidity between Z and γ
$m_{\ell\ell}$	Mass of the di-lepton system
	$N_{jet} = 1$
$\Delta\phi_{Z,\gamma}$	Azimuthal angle between Z and γ
$p_{Tt}^{\ell\ell\gamma}$	p_{Tt} of the system $\ell\ell\gamma$
$p_T^{\gamma}/m_{\ell\ell\gamma}$	Ratio of p_T to mass $\ell\ell\gamma$
$\Delta R_{Z/\gamma,jet}^{min}$	Min.ΔR between Z/γ and leading jet
$\Delta\eta_{Z,\gamma}$	Pseudo-rapidity between Z and γ
	$N_{jet} >= 2$
$\Delta\phi_{Z,\gamma}$	Azimuthal angle between Z and γ
$p_{Tt}^{\ell\ell\gamma}$	p_{Tt} of the system $\ell\ell\gamma$
$\Delta R_{Z/\gamma,jet}^{min}$	Min.ΔR between Z/γ and leading jet
$p_T^{\ell\ell\gamma}$	p_T of the system $ll\gamma$
$\Delta\eta_{Z,\gamma}$	Pseudo-rapidity between Z and γ
$\Delta\phi_{Z\gamma,jj}$	Azimuthal angle between $Z\gamma$ and dijet system

TABLE 6.6: Variables used for full Higgs selection and their definitions.

has to be higher than for other checked methods and the corresponding sensitivity for the chosen method (considering VBF+ggH+WH+ZH as signal and Zγ+Zjet as background) for the method parameters has to give higher values than for other methods.

For the category with $N_{jet} = 0$, no additional preselection is applied before training and testing. The input variables are used in a DNN method (Deep Neural Network) to do the training and testing of the DNN discriminant. The DNN method is a class of artificial neural network with several hidden layers and large amount of neurons for each hidden layer. The variable ranking is performed by using the sum of the weights-squared of the connections between the variable's neuron in the input layer and the first hidden layer. It is noteworthy that in addition the DNN method can distinguish data that is not linearly separable.

The performance of the DNN method is shown in Fig. 6.17 with the DNN response distribution between signal and background.

For the category with $N_{jet} = 1$ the preselection, which requires one jet ($N_{jet} = 1$), is applied before training and testing. The input variables are used in an MLP method (Multilayer Perceptron) to do the training and testing of the MLP discriminant. The MLP method is a class of artificial neural network which consists of at least three layers of nodes (an input layer, a hidden layer and an output layer) and which uses backpropagation technique for training. The method relies on the same principle of variable ranking based on Separation Power, as DNN method.

The performance of the MLP method is shown in Fig. 6.18 with the MLP response distribution between signal and background.

For the category with $N_{jet} >= 2$ the preselection, which requires at least two jets ($N_{jet} >= 2$), is applied before training and testing. The input variables are used in

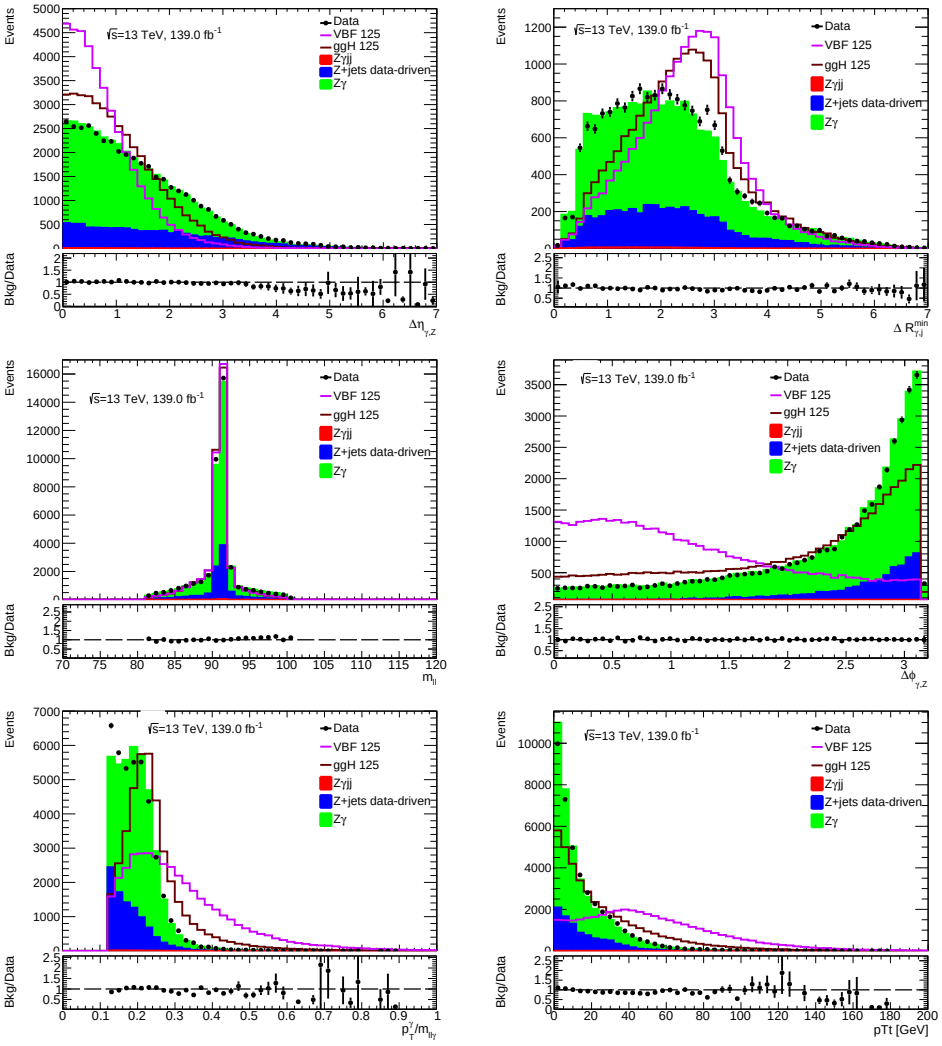

FIGURE 6.16: Variables used in MVA.

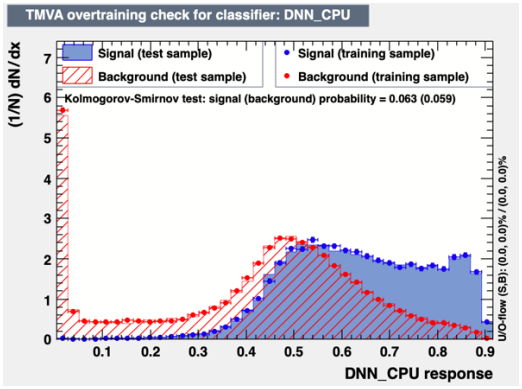

FIGURE 6.17: Distribution of the DNN variable for the category with $N_{jet} = 0$, as a result of the MVA training with the over-training test.

the DNN method. The performance of the method is shown in Fig. 6.19 with the DNN response distribution between signal and background.

Events with a DNN response > 0.51 are assigned to the category with $N_{jet} = 0$. Events with MLP response > 0.79 are assigned to the category with $N_{jet} = 1$. Events with DNN response > 0.85 are assigned to the category with $N_{jet} >= 2$. Each of the

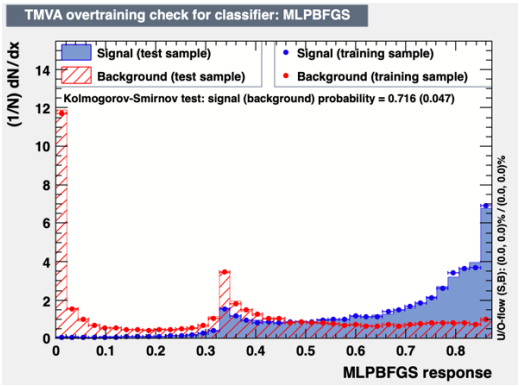

FIGURE 6.18: Distribution of the MLP variable for the category with $N_{jet} = 1$, as a result of the MVA training with the over-training test.

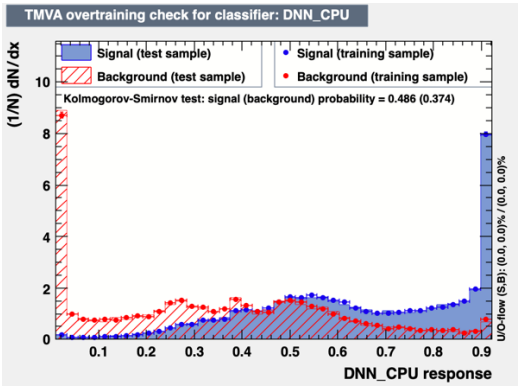

FIGURE 6.19: Distribution of the DNN variable for the category with $N_{jet} >= 2$, as a result of the MVA training with the over-training test.

category thresholds are chosen by scanning the values that give the highest Higgs sensitivity (considering VBF+ggH+WH+ZH+ttH as signal and Zγ+Zjet as background when calculating $S/\sqrt{S+B}$ (Fig. 6.20). The combined sensitivity is calculated in 6 categories, based on number of jets and 3 MVA discriminants (Tab. 6.7), with the resulting sensitivity = 1.31.

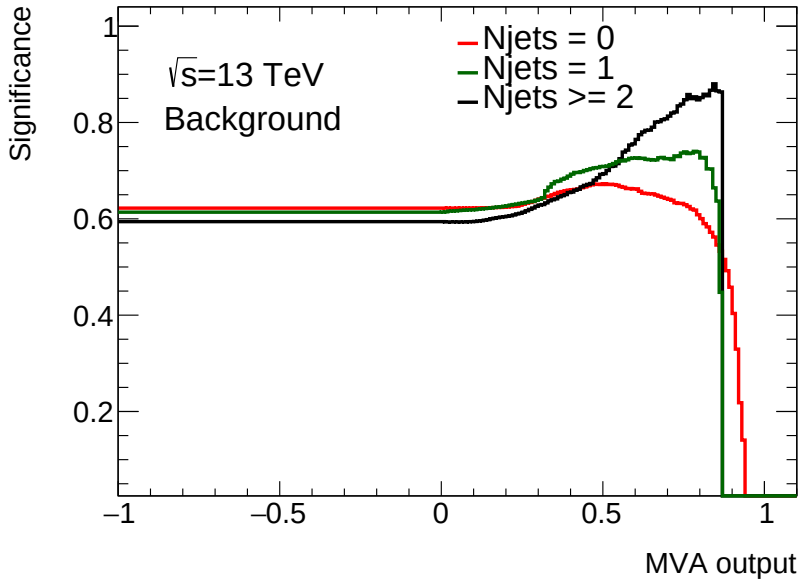

FIGURE 6.20: Sensitivity of the Higgs boson signal (VBF+ggH+WH+ZH as signal and Zγ+Zjet) in categories, based on number of jets, as a function of the method (MLP, DNN, BDTG) discriminant.

N_{jet}	Category	N_S	N_B	N_S 68% SR	N_B 68% SR	$\frac{S}{\sqrt{(S+B)}}$ 68% SR	N_{jet}/All events
N_{jet} = 0	DNN > 0.51	49.55	21978.5	28.62	3341.44	0.49	26.7%
N_{jet} = 0	DNN < 0.51	14.16	47322	6.87	2685.12	0.13	
N_{jet} = 1	MLP > 0.79	18.19	1837.25	11.07	316.73	0.61	55.8%
N_{jet} = 1	MLP < 0.79	31.67	34854.8	16.95	2709.49	0.32	
N_{jet} >= 2	DNN > 0.85	12.13	542.17	7.32	61.85	0.88	17.5%
N_{jet} >= 2	DNN < 0.85	34.03	25137.1	19.14	1895.9	0.44	
combined sensitivity		159.73	131671.82			1.31	

TABLE 6.7: Signal and background yield, and combined signal sensitivity (normalised to 139.0 fb^{-1}), in the mass range expecting 68% of signal yields, in categories based on number of jets.

6.4.4 Final analysis categorisation

It is possible to consider the case of no categorisation employed at all. In that case the inclusive total sensitivity is measured to be 0.85.

The use of additional categories allows to enhance sensitivity, and, as it is shown above, both cut-based and MLP-based categories show good results in improving analysis sensitivity. In the end, the final event categorisation includes six mutually exclusive, non-overlapping categories sketched in Figure 6.21. The names of categories are defined as follows:

- "VBF-enriched" for the category with BDT score > 0.87,
- "Relative pT" for relative $p_T^{\gamma}/m_{\ell\ell\gamma} > 0.4$,
- "High pTt ee" for electron channel with applied high $p_{\mathrm{Tt}} > 40$ GeV and $p_T^{\gamma}/m_{\ell\ell\gamma} < 0.4$,
- "Low pTt ee" for electron channel with applied low $p_T^{\gamma}/m_{\ell\ell\gamma} < 0.4$ and $p_{\mathrm{Tt}} < 40$ GeV,
- "High pTt $\mu\mu$" for muon channel with applied high $p_{\mathrm{Tt}} > 40$ GeV and $p_T^{\gamma}/m_{\ell\ell\gamma} < 0.4$,
- "Low pTt $\mu\mu$" for muon channel with applied low $p_T^{\gamma}/m_{\ell\ell\gamma} < 0.4$ and $p_{\mathrm{Tt}} < 40$ GeV.

The choice of VBF-enriched categorisation over full Higgs categorisation is made based on the simplicity of the proposed categorisation and clear background to signal separation.

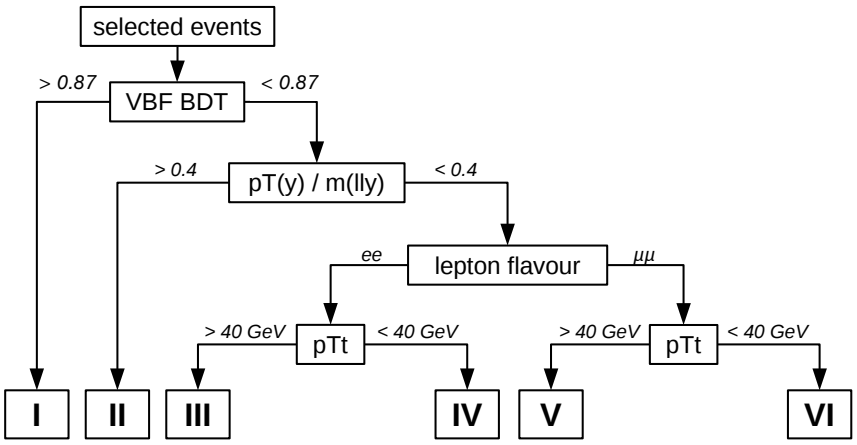

FIGURE 6.21: Schematic of the categorisation for the SM Higgs boson based on the discriminant of the BDT described in Section 6.4.2, the relative transverse momentum $p_{\mathrm{T}}(\gamma)/m_{ll\gamma}$, the lepton flavour and p_{Tt}.

The expected signal yield is defined as following, for each of the production decay modes i, categories j and lepton flavour ℓ

$$N^{SM}_{i,j,\ell}(m_H) = \int Ldt \times \sigma_i(m_H) \times B(H \to Z\gamma)(m_H) \times B(Z \to \ell\ell) \times \varepsilon_{i,j,\ell}(m_H), \quad (6.4)$$

where $\int Ldt$ is the integrated luminosity of the data sample. $\sigma_i(m_H)$ is the SM Higgs boson production cross section in the production process i (gg, VBF, WH, ZH, ttH), $B(H \to Z\gamma)(m_H)$ is the branching fraction for the SM Higgs boson decay to $Z\gamma$, $B(Z \to \ell\ell)$ is the Z decay to two leptons branching fraction [26].

The signal yield and sensitivity in the mass range expecting 68% of all the signal yields is shown in Tab. 6.8 (the mass window is defined as the region between the 16% and the 84%). In each category, the background yield is normalised to the data. Table 6.9 shows signal yields and efficiencies with different production modes in each category with respect to all leptonic decays from the Z boson. Figure 6.22 gives the illustration for the signal fractions of signal production processes in each category. The signal in the VBF-enriched category is mostly populated by events from VBF production mode (72%).

Therefore, the categorisation improves the expected sensitivity by over 40% compared to the case of no categorisation at all.

Category	N_S	N_B	N_S	N_B	$\frac{S}{\sqrt{(S+B)}}$	mass range (GeV)
			68% SR	68% SR	68% SR	68% SR + 0.09GeV shift
VBF-topo	3.91	169.00	2.34	11.56	0.63	123.59-126.59
Rel. pT	11.05	2886.00	7.72	127.87	0.66	123.59-127.59
High pTt ee	14.44	5337.00	9.69	483.10	0.44	123.59-127.59
Low pTt ee	50.66	55211.00	33.04	6082.53	0.42	123.59-127.59
High pTt $\mu\mu$	17.59	6631.00	11.77	622.95	0.47	123.59-127.59
Low pTt $\mu\mu$	63.86	72991.00	49.09	10374.03	0.48	122.59-127.59
total	161.53	143225.00			1.29	

TABLE 6.8: Signal, background yield and signal sensitivity (normalized to 139.0 fb^{-1}), in the mass range expecting 68% of signal yields, in six categories.

6.5 Signal and background modelling

In the analysis of $H \to Z\gamma$, the signal and background yields are determined through a maximum-likelihood fit to the $Z(\ell\ell)\gamma$ invariant mass spectrum, as described in Sec. 6.7. The choice of invariant mass $m_{Z\gamma}$ allows precise discrimination of signal from background, as both of the components have distinctly different shapes. Both the signal and background normalised distributions are parametrised with analytic functions. Their parameters are fixed from the simulation for the signal, or fitted to the data for the background. Section 6.5.1 describes procedure and parameters for signal shape modelling of the $H \to Z\gamma$ process. Section 6.5.2 provides details on composition of main backgrounds $Z\gamma$ and Z+jet for the $H \to Z\gamma$ process and describes method which allows to estimate their relative fractions. Section 6.5.4 contains the details of the choice of analytical functions for background modelling of the main backgrounds combination.

Production Mode	Category						Sum
	VBF-topo	Rel. pT	High pTt ee	Low pTt ee	High pTt $\mu\mu$	Low pTt $\mu\mu$	
ggH	1.075397 0.001025	7.852571 0.007483	11.588351 0.011043	47.458195 0.045225	14.081498 0.013419	59.850567 0.057034	141.906579 0.135229
VBFH	2.804247 0.034311	1.432273 0.017524	1.572991 0.019246	1.916353 0.023447	1.974043 0.024153	2.384109 0.029170	12.084016 0.147851
WmH	0.008856 0.000771	0.323200 0.028127	0.264950 0.023058	0.287211 0.024995	0.310913 0.027058	0.367298 0.031965	1.562429 0.135972
WpH	0.011718 0.000647	0.475405 0.026231	0.369751 0.020401	0.375325 0.020709	0.461354 0.025455	0.503873 0.027801	2.197425 0.121244
ZH	0.009666 0.000506	0.524706 0.027494	0.428365 0.022446	0.464782 0.024354	0.522845 0.027397	0.580942 0.030441	2.531306 0.132638
ttH	0.004987 0.000455	0.514156 0.046936	0.277847 0.025364	0.226774 0.020702	0.314422 0.028703	0.257834 0.023537	1.596019 0.145696
Sum	3.914870 0.003288	11.122311 0.009340	14.502256 0.012179	50.728639 0.042602	17.665075 0.014835	63.944622 0.053701	161.877774 0.135945

TABLE 6.9: Populations (as signal yields, top) and efficiencies (in %, bottom) for the different Higgs production modes with respect to all leptonic decays from the Z boson. The full low-mass event selection is applied before the categorisation and the Monte Carlo yields are normalised to an integrated luminosity of 139.0 fb^{-1}.

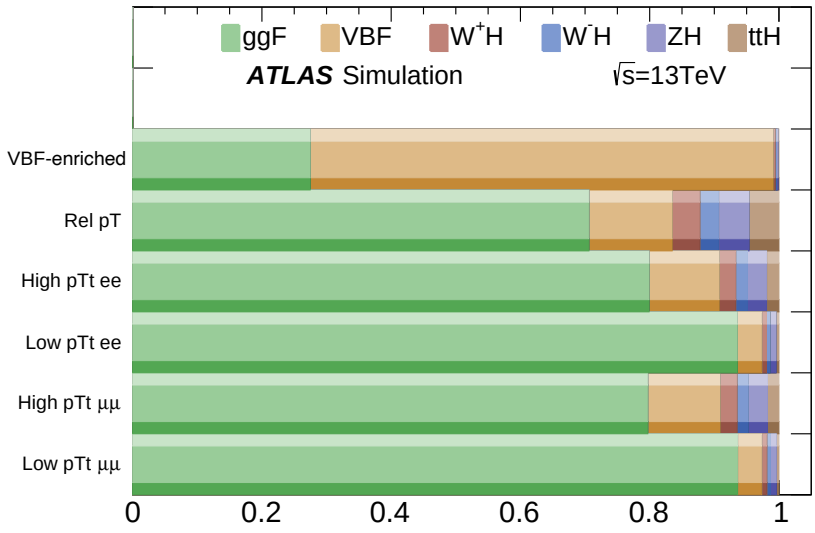

FIGURE 6.22: Illustration for the expected signal fractions in each category in terms of the various production processes.

6.5.1 Signal modelling

The signal-related parameters that enter the final fit for the $H \to Z\gamma$ process are:

- the signal invariant mass distribution, needed to extract the signal yield from the signal-plus-background fit
- the signal efficiency, needed to infer the signal cross section times branching ratio to $Z\gamma$ from the measured yield

From the full simulation signal samples (such as ggF, VBF, WH, ZH and ttH summed taking into account their relative SM cross-sections), the three body invariant mass distribution for a resonance of mass m_H is found to be well modelled by a Double-Sided Crystal Ball function (DSCB). The mass distribution takes as a sum all Higgs signal production modes with the corresponding normalisation based on their the cross section. The DCSB function consists of a Gaussian core with power-law tails on both sides of the mode of the distribution. It is defined as

$$N \cdot \begin{cases} e^{-t^2/2} & \text{if } -\alpha_{\text{Lo}} \leq t \leq \alpha_{\text{Hi}} \\ \frac{e^{-0.5\alpha_{\text{Lo}}^2}}{\left[\frac{\alpha_{\text{Lo}}}{n_{\text{Lo}}}\left(\frac{n_{\text{Lo}}}{\alpha_{\text{Lo}}} - \alpha_{\text{Lo}} - t\right)\right]^{n_{\text{Lo}}}} & \text{if } t < -\alpha_{\text{Lo}} \\ \frac{e^{-0.5\alpha_{\text{Hi}}^2}}{\left[\frac{\alpha_{\text{Hi}}}{n_{\text{Hi}}}\left(\frac{n_{\text{Hi}}}{\alpha_{\text{Hi}}} - \alpha_{\text{Hi}} + t\right)\right]^{n_{\text{Hi}}}} & \text{if } t > \alpha_{\text{Hi}}, \end{cases} \tag{6.5}$$

where $t = \Delta m_H/\sigma_{\text{CB}}$, $\Delta m_H = m_{Z\gamma} - \mu_{\text{CB}}$, N is a normalisation parameter, μ_{CB} is the peak of the Gaussian distribution, which is shifted by 0.09 GeV for the 125 GeV signal MC samples, σ_{CB} represents the width of the Gaussian part of the function, α_{Lo} (α_{Hi}) is the point where the Gaussian becomes a power law on the low (high) mass side, n_{Lo} (n_{Hi}) is the exponent of this power law.

The results of the fits for each category are shown in Fig. 6.23 and in Table 6.10. In addition, Fig. 6.24 shows an example of two selected categories (low p_{Tt} and high p_{Tt}) separately for the electron and the muon channels. As was described earlier, the $H \to \mu\mu$ process can contribute to the $H \to Z\gamma$ process. The details of the effect from the additional contribution of the $H \to \mu\mu$ process to the signal parametrisation can be found in App. A.

Category	Mean [GeV]	Resolution [GeV]
Inclusive	124.89	1.613
Inclusive ee	124.93	1.581
Inclusive $\mu\mu$	124.86	1.629
e or μ, $BDTG > 0.87$	124.87	1.519
e or μ, $BDTG < 0.87$, $p_{\text{T}}^{\gamma}/m_{ll\gamma} > 0.4$	125.01	1.417
e, BDTG < 0.87, $p_{\text{T}}^{\gamma}/m_{ll\gamma} < 0.4$, $p_{\text{Tt}} > 40$	124.93	1.439
e, BDTG < 0.87, $p_{\text{T}}^{\gamma}/m_{ll\gamma} < 0.4$, $p_{\text{Tt}} < 40$	124.92	1.685
μ, BDTG < 0.87, $p_{\text{T}}^{\gamma}/m_{ll\gamma} < 0.4$, $p_{\text{Tt}} > 40$	124.88	1.608
μ, BDTG < 0.87, $p_{\text{T}}^{\gamma}/m_{ll\gamma} < 0.4$, $p_{\text{Tt}} < 40$	124.85	1.662

TABLE 6.10: Mean and resolution for the PDF in each category.

The application of the pileup weights in signal MC samples could have the effect of reducing the statistics, as such it is worthwhile studying its impact on the signal model and efficiency. The $m_{Z\gamma}$ distributions in the signal MC ggH 125 sample with and without pileup weight applied are shown in Fig. 6.25 demonstrating that the pileup weight has a negligible impact on the shape of the distribution. As such for the purpose of modelling the signal shape the pileup weight does not necessary have to be applied.

Since there is visible effect from pileup weight on the signal efficiency, the pileup weight is kept for the signal efficiency parametrisation.

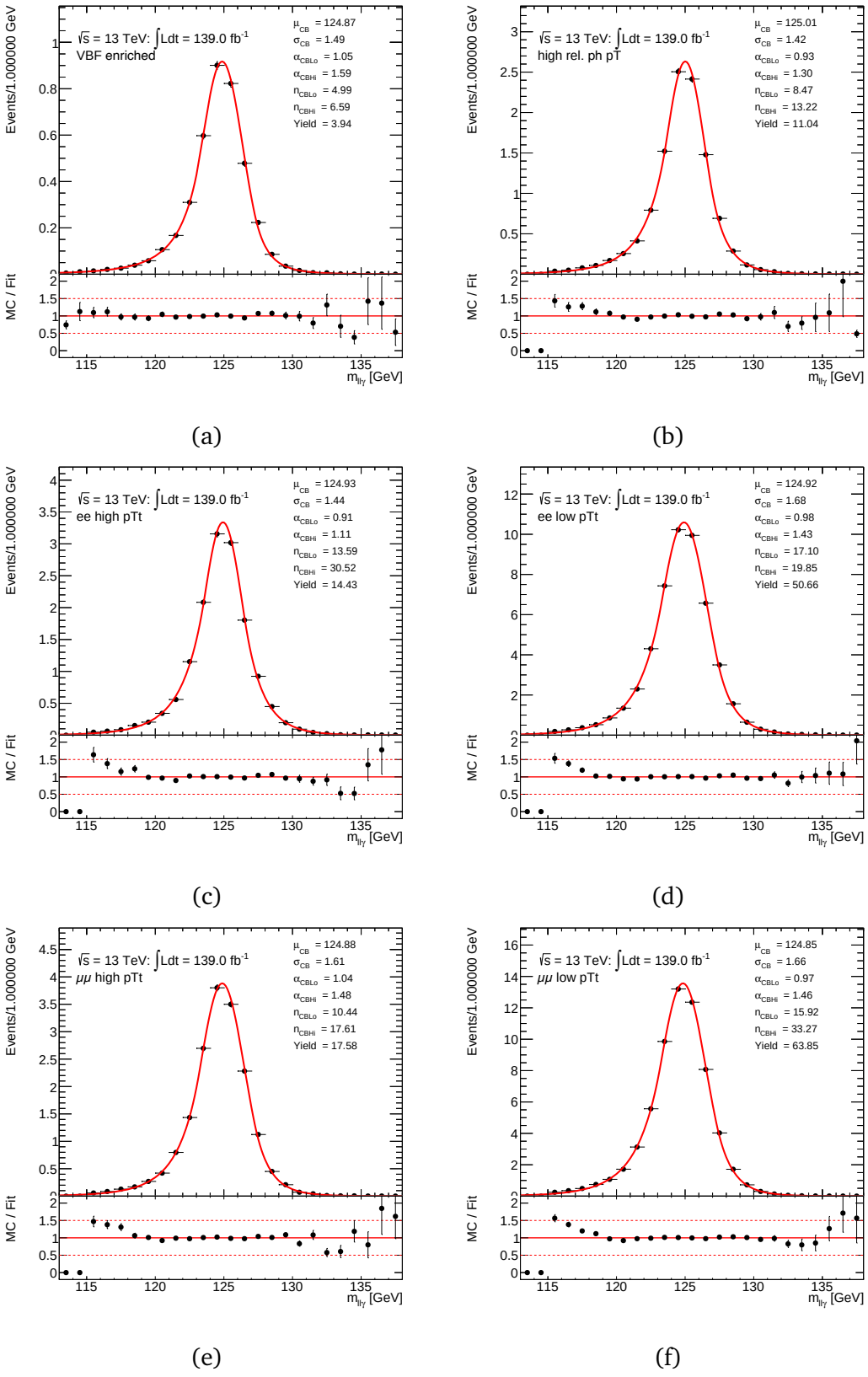

FIGURE 6.23: Results of simultaneous fits of DSCB parameters as a function of the invariant mass spectrum of $Z(\rightarrow ll)\gamma$ in data derived from all full simulation signal samples, in the (a) "VBF-enriched", (b) "high rel. pT", (c) "high pTt ee", (d) "low pTt ee", (e) "high pTt $\mu\mu$", and (f) "low pTt $\mu\mu$", categories for the Higgs Boson search (115-170 GeV).

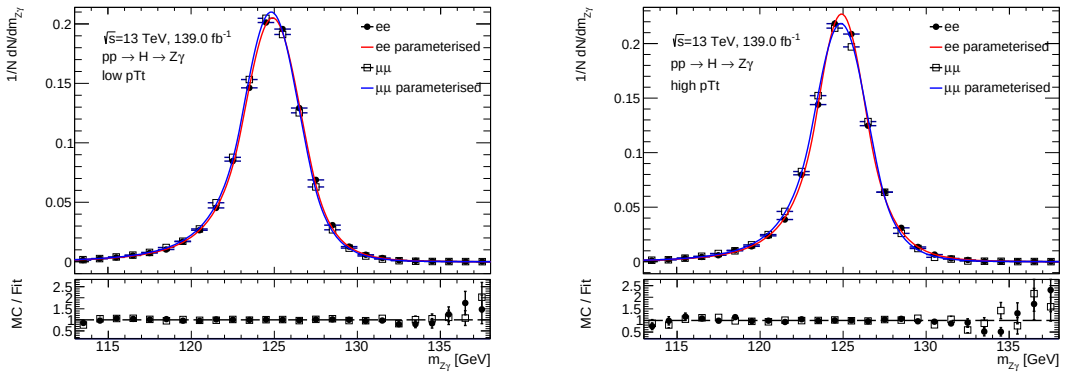

(a) (b)

FIGURE 6.24: Results of simultaneous fits of DCSB parameters as a function of the invariant mass spectrum of $Z(\to ll)\gamma$ in data derived from all full simulation signal samples, separately for electron (black dots, red line) and muon (hollow dots, blue line) channels, in the (a) "low pTt" , (b) "high pTt", categories for the Higgs Boson search.

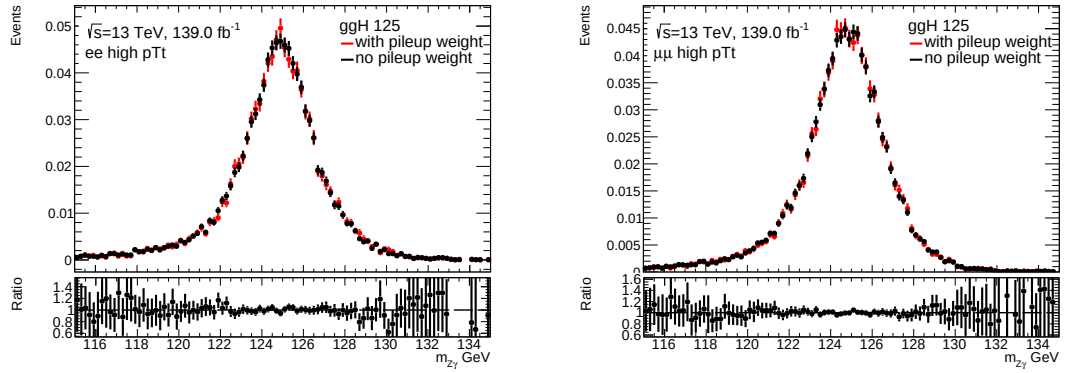

(a) (b)

FIGURE 6.25: Distribution of $m_{Z\gamma}$ in the signal ggH MC sample with and without the pileup weight applied for the cases of (a) high pTt ee and (b) high pTt $\mu\mu$.

6.5.2 Background composition

The dominant background mainly originates from non-resonant SM $Z\gamma$, with a smaller contribution from the Z+jets, with one jet misidentified as a photon. One more background is from the electroweak production of Zγjj, which contributes to the VBF-enriched category, with an estimated 2.4% fraction from Monte-Carlo to other sources of the background. The normalisation of the $Z\gamma jj$ background is done based on its cross-section.

The fraction (purity) of $Z\gamma$ events (including a possible signal) in the total selected sample is measured in data in the following way. In $Z\gamma$ events, the photon candidate is a prompt photon, which gives rise to a narrow energy cluster in the electromagnetic calorimeter and is usually isolated from hadronic activity, while in Z+jet events, the photon candidate is mainly from the decay of a neutral meson (typically a π^0) carrying a large fraction of the initial parton's energy and produces an energy cluster in the electromagnetic calorimeter which usually has non-negligible leakage in the hadronic calorimeter, and is not isolated from hadronic activity as the other

particles in the same jet deposit energy in the calorimeters near the photon candidate. Therefore, photon identification and isolation variables can be used to estimate the contributions of $Z\gamma$ and Z+jet events in data.

The composition of the selected dataset is measured using the following technique: a template-fit method with prompt photons in the final state with the 139.0 fb^{-1} SM $H \to Z\gamma$ search.

However, the background composition only plays a minor role in the final measurement, since the sum of both backgrounds yields a smooth three-body invariant mass distribution whose parameters are fitted directly from the data. The measured background fractions are only used when combining together $Z\gamma$ and Z+jet samples in the "spurious signal" (SS) studies described later.

Data-driven background estimation with the template-fit method

The purity is estimated with a binned template fit to the calorimeter isolation distribution of the selected photon candidate. A simultaneous fit is performed to the signal region, defined by the full selection described in the previous section, and to a control region, in which the events pass all the selection requirements except that the photon fails the Tight identification criteria but passes the looser ones as also exploited in the two-dimensional sideband method (Loose'4).

The fit extracts the yield and shape of $Z\gamma$ events in signal and control regions. As a consequence, the fit also determines the yield and shape of the Z+jet distribution in both regions. The parameters of the template fit are:

- signal ($Z\gamma$) yields in the signal region N_{SR}^{Sig}.
- background (Z+jet) yields in the signal region N_{SR}^{Bkg}.
- background (Z+jet) yields in every E_T^{cone20} bins of the control region N_{ibin}^{Bkg}.

assuming that the $Z\gamma$ shape in signal region ($Fraction_{ibin}$) as well as the $Z\gamma$ leakage between the two regions ($Leakage_{ibin}$) are those predicted by the $Z\gamma$ simulation (MC), and assuming Z+jet shape is the same in the two regions. It is possible to obtain the following equations in each E_T^{cone20} bin of signal and control region, in signal region

$$N_{ibin}^{SR} = N_{SR}^{Sig} * Fraction_{ibin} + N_{SR}^{Bkg} * \frac{N_{ibin}^{Bkg}}{\sum_{ibin=1}^{Nbins} N_{ibin}^{Bkg}}, \tag{6.6}$$

and the in background region

$$N_{ibin}^{CR} = N_{SR}^{Sig} * Fraction_{ibin} * Leakage_{ibin} + N_{ibin}^{Bkg}. \tag{6.7}$$

So when Nbins >= 2, a simutaneous fit can be perfromed to obtain all the parameters.

The statistical uncertainties of both signal and control regions are automatically propagated to the final estimations and systematic uncertainties associated to the assumptions above can be obtained with the variation of the different definitions of the control region (using Loose'2, '3, '5 as the looser ID criteria). An additional check of various isolation combinations, i.e. use of calorimeter variable with a larger cone size E_T^{cone40}, helps to refine template fit and get more precise results as well.

Fig. 6.26 shows the result of the template fit to the isolation distributions for photon candidates in the signal region (left) and in the jet control region (right).

In these plots "signal" corresponds to $Z\gamma$ events while "background" corresponds to Z+jet events.

According to the fit, the fraction of $Z\gamma$ events in the signal region of the Higgs boson search is 0.80 ± 0.01 for the inclusive case. Details can be found in Table 6.11. Variations of the $Z\gamma$ fraction were calculated with use of the Loose'2, '3, '5 identification criteria and alternative isolation working point (`Tight`), the obtained results are included as a range window and include nominal case as well.

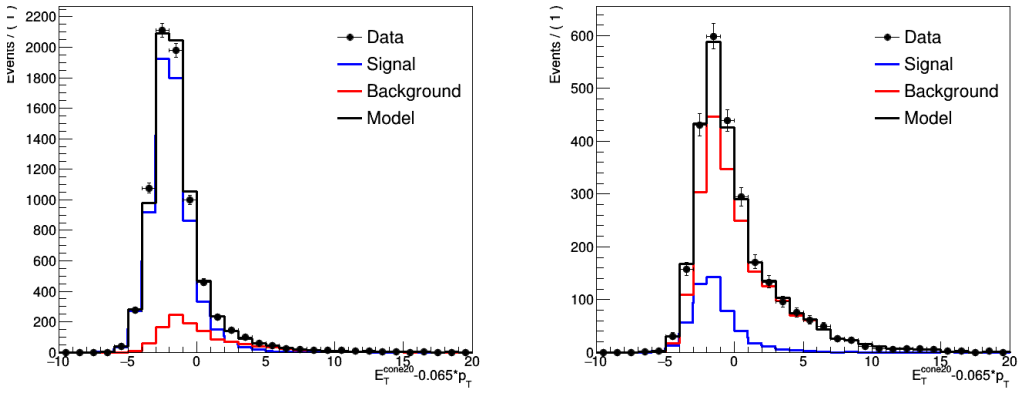

FIGURE 6.26: (115-170GeV) Template fit to the isolation distributions for photon candidates passing the Tight ID (left) and the Loose'4 (right) requirements in the Higgs boson search. The signal here is $Z\gamma$ events and the background is Z+jet events.

Category	Nominal purity	Range
Inclusive	0.80 ± 0.01	[0.79 , 0.81]
e or μ, $BDTG > 0.87$	0.87 ± 0.08	[0.79, 0.87]
e or μ, $BDTG < 0.87$, $p_{\mathrm{T}}^{\gamma}/m_{ll\gamma} > 0.4$	0.95 ± 0.02	[0.92, 0.97]
e, BDTG < 0.87, $p_{\mathrm{T}}^{\gamma}/m_{ll\gamma} < 0.4$, $p_{\mathrm{Tt}} > 40$	0.89 ± 0.02	[0.76, 0.90]
e, BDTG < 0.87, $p_{\mathrm{T}}^{\gamma}/m_{ll\gamma} < 0.4$, $p_{\mathrm{Tt}} < 40$	0.80 ± 0.01	[0.71, 0.81]
μ, BDTG < 0.87, $p_{\mathrm{T}}^{\gamma}/m_{ll\gamma} < 0.4$, $p_{\mathrm{Tt}} > 40$	0.89 ± 0.01	[0.83, 0.90]
μ, BDTG < 0.87, $p_{\mathrm{T}}^{\gamma}/m_{ll\gamma} < 0.4$, $p_{\mathrm{Tt}} < 40$	0.81 ± 0.01	[0.70, 0.81]

TABLE 6.11: $Z\gamma$ Nominal inclusive purity and purity variations with template fit method for the Higgs Boson (115-170GeV) search.

6.5.3 Comparison of data and background simulation

In the analysis, the envelope of the purity variation ranges from the template-fit method (Table 6.11) is taken as the uncertainty of the purity in each category. As is described below in the Sec. 6.5.4, the purity uncertainty, specifically the border of the ranges, is going to be taken into account in the background model studies in order to check the impact on the choice of the background function.

A mass shape comparison between data and the sum of the $Z\gamma$ and Z+jet background distribution, after normalising both to the yields measured in data, is shown in Fig. 6.27. The VBS $Z\gamma + jets$ events are taken into account only for the VBF-enriched category, since their impact to all of the other categories is negligible. The sum of non-VBS $Z\gamma$ and the VBS $Z\gamma + jets$ is normalised to the corresponding purity in the category. A good agreement between data and simulation is observed.

The shape of the background, as later described in Sec. 6.5.4, is formed from a combination of a $Z\gamma$ Monte Carlo sample and a Z+jets-dominated control region in data.

6.5.4 Background modelling

As mentioned above, the main backgrounds for the $H \to Z\gamma$ process are from Z bosons in association with a photon, from inclusive Z boson production in which a hadronic jet is misidentified as a photon and from VBS $Z\gamma$ production with two jets, which is seen mostly in the VBF production mode. The $Z\gamma$ and Z+jets background is normalised to the number of data events per category with the $Z\gamma jj$ subtracted. The relative normalisations of the sum of $Z\gamma$ and $Z\gamma jj$ to Z+jets background is done using the method described in Sec. 6.5.2. Due to limited statistics in the full simulation $Z\gamma$ Monte-Carlo samples, used in the previous sections, fast simulation $Z\gamma$ samples are used in the background modelling. For the Z+jets background, the Monte-Carlo sample has very limited statistics as well, so a data-driven shape is obtained instead by inversion of the photon identification. Fig 6.28 shows the data-driven shape and comparison with the shape obtained from the low statistics Z+jets Monte Carlo sample, both are in agreement.

The remaining statistical fluctuations of the Z+jets $m_{Z\gamma}$ distribution can be large in some of the categories with limited statistics. In order to smooth them, an analytical function can be fitted to the ratio of the $m_{Z\gamma}$ distributions for $Z\gamma$ and Z+jets events using the following procedure:

- $R_{Zj/Z\gamma} = B_{Zj}/B_{Z\gamma}$ where $B_{Z\gamma}$ and B_{Zj} are $Z\gamma$ and $Z + jet$ yields, respectively, in each mass bin
- FK1 function ($f(x) = (1 - x^{1/3})^b x^{a_0 + a_1 log(x)}$) is fitted to $R_{Zj/Z\gamma}$.
- Z+jets in the signal region and in each mass bin is determined as $B_{Zj} = FK1(m_{Z\gamma})B_{Z\gamma}$

Fig. 6.29 shows the effect of mimicking the Z+jets shape as an example for the "VBF-enriched" and "low pTt ee" categories. In the "VBF-enriched" category, the $Z\gamma$ legend in the plot is the summation of the non-VBS $Z\gamma$ and the VBS $Z\gamma + jets$ processes. In the ratio pad, the ratio of Z+jets divided by $Z\gamma$ is fitted by the following function

$$f_{k=1;d=1/3}(x; b, d, a_0, a_1) = (1 - x^{1/3})^b x^{a_0 + a_1 log(x)}. \quad (6.8)$$

Finally, after the smoothing procedure, the invariant mass distributions of the combined backgrounds have smoothly falling distributions and can be described with an analytical function. The parameters of such a function are fitted later directly to the data, thus avoiding reliance on the simulation and reducing systematic uncertainties related to the theoretical normalisations of the backgrounds and with their selection efficiencies. The functional form used to describe the background is selected based on several principles. The first one states that the form has to be chosen in a way to prevent the introduction of possible bias that can create either a false peak or reduce the actual signal. The second one states that the model has to have the fewest possible free parameters to reduce the uncertainty on the background modelling:

- The background model must give a small amount of bias in the extracted signal yield, denoted "spurious signal", compared to the expected uncertainty from the background fluctuations. The bias over its uncertainty $\frac{S}{\delta S}$ is required to be less than 50% of the expected statistical uncertainty in the signal yield, which

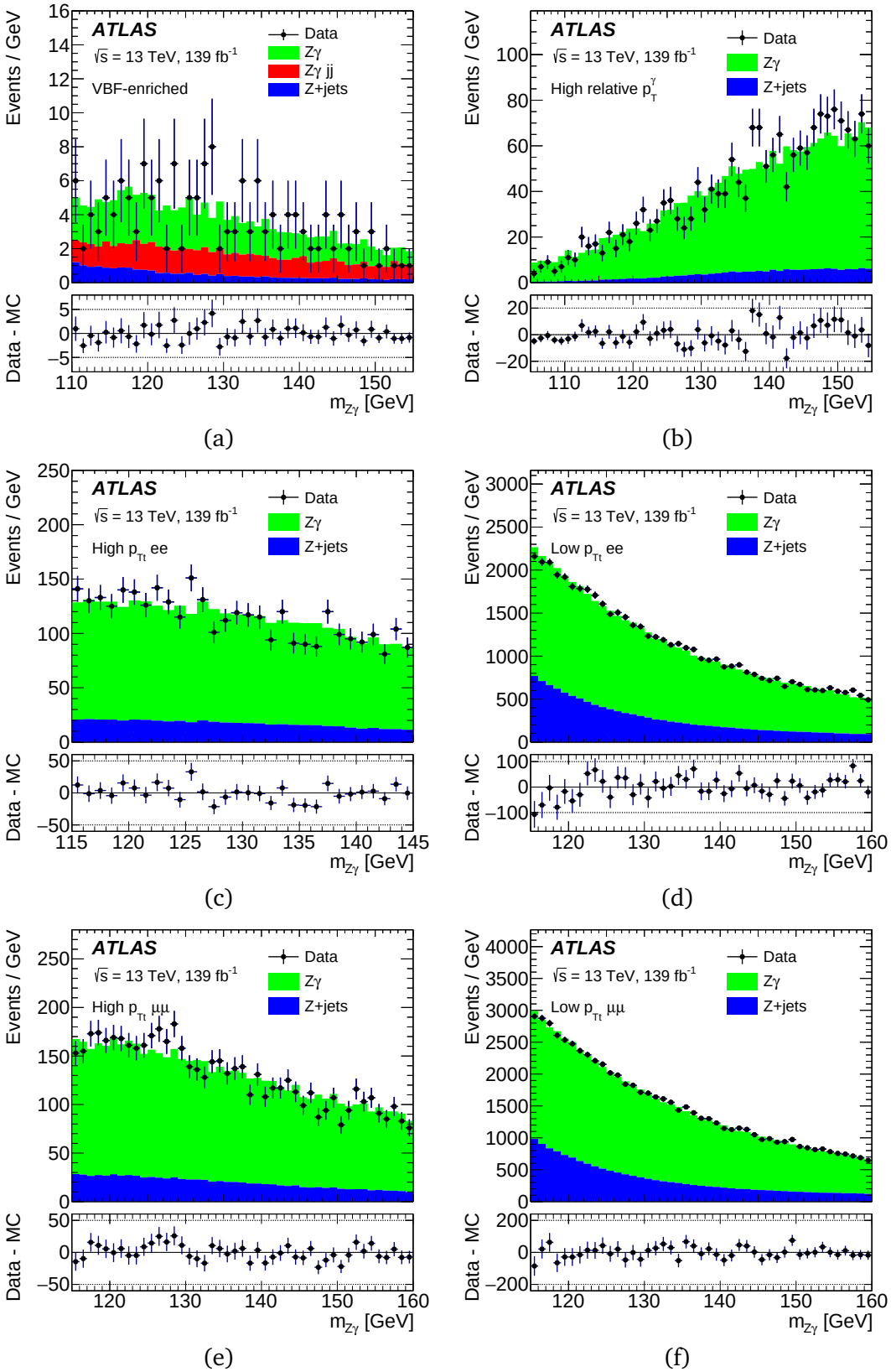

FIGURE 6.27: Background composition for: (a) "VBF-enriched" , (b) "high relative p_{T}" , (c) "high pTt ee" , (d) "low pTt ee" , (e) "high pTt mumu" , and (f) "low pTt mumu" , invariant mass distribution for data and estimated background ($Z\gamma$ and Z+jets).

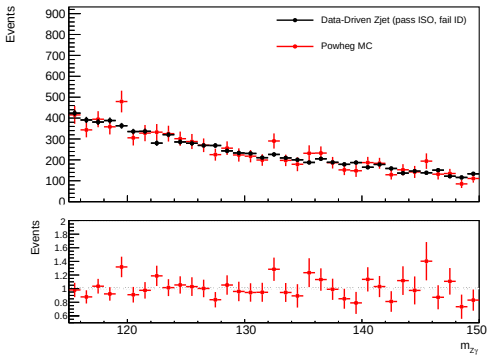

FIGURE 6.28: Comparison of the full simulation $Z + jet$ $m_{Z\gamma}$ distribution to the data-driven $Z + jet$ shape.

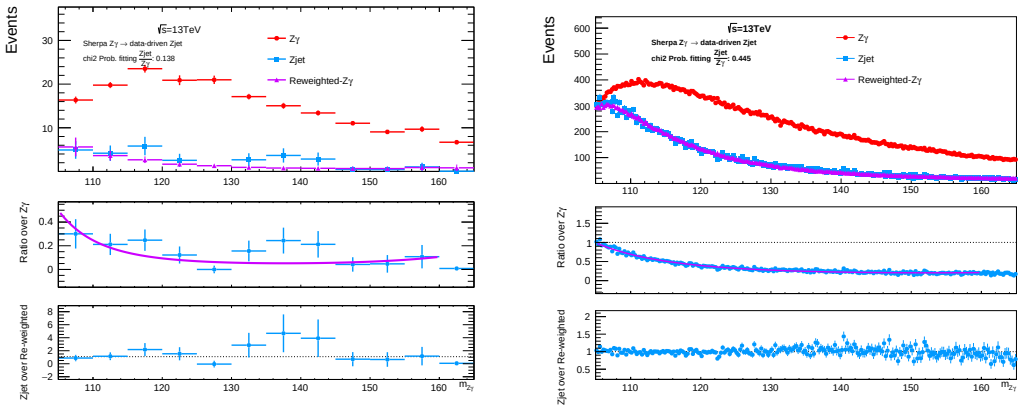

(a) (b)

FIGURE 6.29: Comparison and ratio on $m_{Z\gamma}$ between the data-driven Z+jets and fast simulation $Z\gamma$, for (a) "VBF-enriched", (b) "low pTt ee", categories in the Higgs search region. The ratio of $R_{Zj/Z\gamma} = B_{Zj}/B_{Z\gamma}$ is fitted by the purple line in the ratio pad using FK1 function, the χ^2 probability is shown in the legend.

means the spurious signal + statistic uncertainty has to be 12% larger than statistic only uncertainty if take the sum in quadrature. Stricter requirements on the spurious signal are not possible due to the statistical uncertainty of the $m_{Z\gamma}$ background template.

- The agreement of the fit to the background Monte Carlo has to be good with χ^2 probability bigger than 1%.

The spurious signal describes the bias on the signal yield caused by the choice of a particular background parameterisation. It is evaluated by fitting a high statistics background-only sample, normalised to the data yields, with a signal plus background model. Several functional forms to the background distribution are chosen for the test, for each of the categories separately. The bias on spurious signal is estimated by performing a signal+background fit to the $m_{Z\gamma}$ background only distribution (Asimov fit [109]) in a selected fit range. A requirement for the spurious signal to be less than 50% is applied during the selection of the background modelling function. The final choice of the fitting functions for background modelling was made from the following set:

- Exponential polynominal functions second to fourth order, $e^{x*f_{Poly}(a_0,a_1,a_2,a_3)}$
- Bernstein polynomial functions second to fourth order, $f_{\text{Bernstein2}-4)}(a_0, a_1, a_2, a_3)$
- Power function (x^{a_0}) and second order power function ($x^{a_0} + a_1 x^{a_2}$).

where a_i represent the background model parameters.

The optimisation of the fit range in each category is based on the obtained highest significance of an Asimov fit (background + signal). In addition, spurious signal uncertainty is included in the significance evaluation. The fit range selection is performed by varying the lower and upper bound mass ranges in 5 GeV steps between 105-115 GeV and 140-160 GeV.

Table 6.12 shows the selected background models for each category, together with the chosen fit range for a SM Higgs boson. Fig. 6.30 shows the results of background only fit with the chosen function in corresponding categories, and as it is seen, the fits describe well the observed distributions.

Category	Function Type	Fit range [GeV]
VBF-enriched	Second-order power function	110–155
High relative p_{T}	Second-order exponential polynomial	105–155
ee high p_{Tt}	Second-order Bernstein polynomial	115–145
ee low p_{Tt}	Second-order exponential polynomial	115–160
$\mu\mu$ high p_{Tt}	Third-order Bernstein polynomial	115–160
$\mu\mu$ low p_{Tt}	Third-order Bernstein polynomial	115–160

TABLE 6.12: The selected background function and fit range in each analysis category.

6.6 Systematic uncertainties

The systematic uncertainties which affect this analysis come from experimental uncertainties on data, from uncertainty on the signal $m_{Z\gamma}$ distribution and from theoretical uncertainties based mostly on the limited knowledge of branching fractions and production cross-sections.

6.6.1 Experimental uncertainties

Table 6.13 shows the main sources of the experimental systematic uncertainties, given as fractions of the total predictions for the ggF, VBF, VBF and ttH production modes. The uncertainty on the 2015-2018 combined integrated luminosity collected with the ATLAS detector is $\pm 1.7\%$ [110, 111]. The uncertainty on the pile-up effect on the lepton and photon identification efficiency is included and is measured to be 0.2%. One more source of the uncertainty comes from the reconstruction of the photons, electrons and muons (described in Sec. 4). The photon reconstruction and identification uncertainty arises mainly from the detector material mismodelling, with non-perfect simulation of the conversion fraction. The photon and electron isolation uncertainty comes from difference between the measured energy distribution in topological cells in data and simulation. Data to Monte Carlo differences are observed in addition for electron and photon electromagnetic energy scales. The same principles of modelling correction applies to muons as well, resulting in additional uncertainties. The

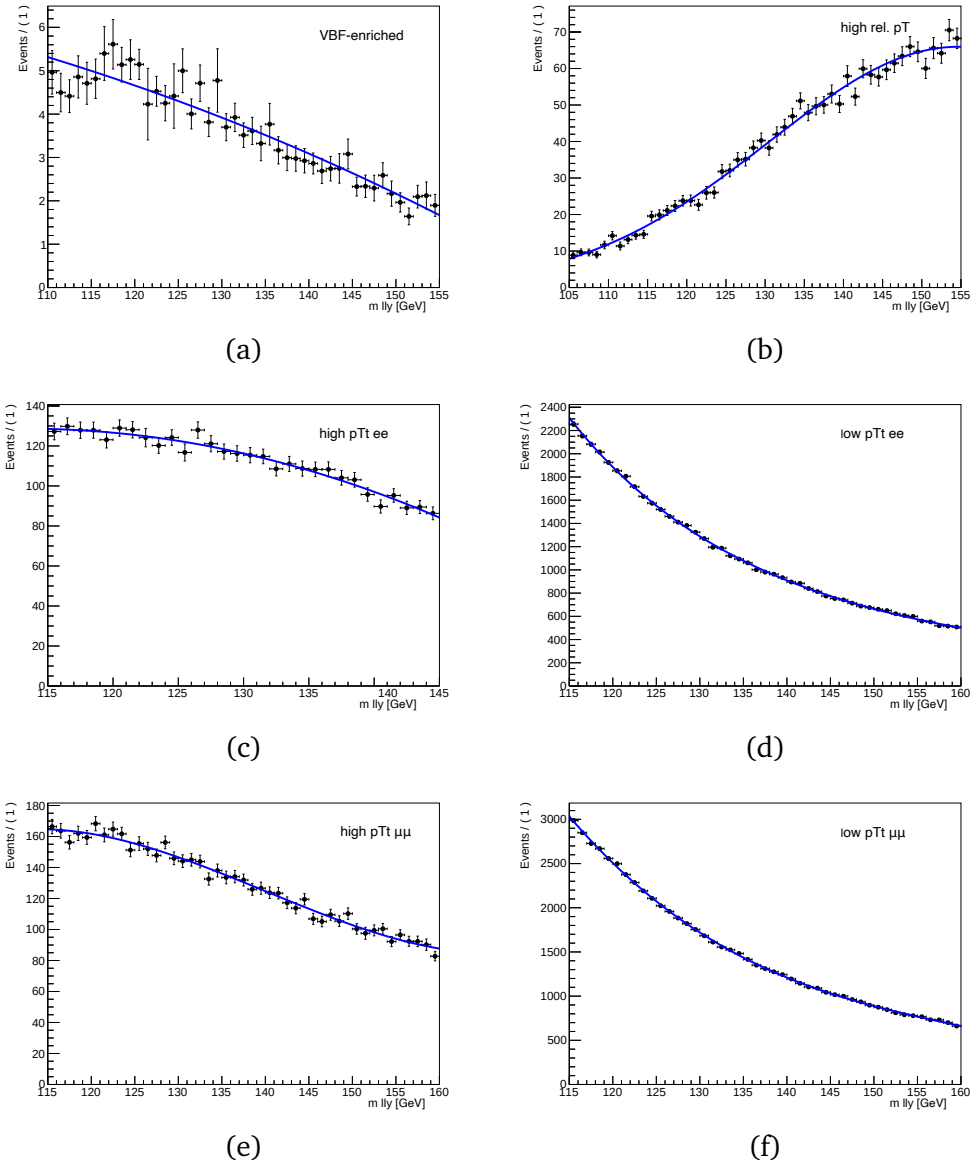

FIGURE 6.30: The background only fit with the chosen function and fit range in each category, in the (a) "VBF-enriched", (b) "high rel. pT", (c) "high pTt ee", (d) "low pTt ee", (e) "high pTt $\mu\mu$", and (f) "low pTt $\mu\mu$", categories for the Higgs Boson search (115-170 GeV).

combined value of all of the sources, as identification, isolation, reconstruction and trigger efficiency, including lepton momentum scale and resolution, is no more than 2.6%, 2.4% and 1.6% for photons, electrons and muons, respectively [1, 48].

The possible contribution from $H \to \mu\mu$ process is estimated from the simulation and is about 1.7% inclusive over all categories, with up to 3.3% in individual categories [112]. Finally, as was mentioned in Sec. 6.5.4, the dominant source of the experimental uncertainty comes from the spurious signal uncertainty. It arises from the choice of background model and its parameters are directly fitted to the data, thus propagating to the statistical uncertainty on the signal yield. The spurious signal is set to be no more than 50% of the statistical error in the expected signal yield per category, as stricter requirement is not possible due to limitation of statistics in background MC. The uncertainty on the spurious signal is evaluated from the maximum number of signal events derived from signal-plus-background fits to $m_{Z\gamma}$ background-only distributions, individually for each category. It is estimated to be 28% on the signal strength. Overall, the introduction of the spurious signal increases the total uncertainty in the expected signal strength by 5.6% because of the large statistical uncertainty.

6.6.2 Systematic uncertainty on the signal $m_{Z\gamma}$ distribution

The systematic uncertainty on the signal arises due to the modelling of the signal invariant mass shape used in the fit to the data to discriminate from the background. The uncertainty varies between analysis channels, such as ggH, VBF, WH, ZH and ttH. For all of these, the $m_{Z\gamma}$ distribution is recomputed after varying the e/γ energy scale, e/γ energy resolution; muon momentum scale or resolution by $\pm 1\sigma$, where σ is its uncertainty.

For the Higgs search, the $m_{Z\gamma}$ distribution with systematic variations is fitted with signal model individually at 125 GeV. The relative difference between different systematic variations on the signal shape parameters (μ_{CB} and σ_{CB}) at 125 GeV is regarded as the signal shape uncertainty.

Systematical uncertainties on the mass position and resolution are summarised in Table 6.13. The dominant uncertainties on the mass resolution σ_{CB} are from the electron and photon energy resolution ($< 3.4\%$) and from the muon momentum resolution ($< 3.6\%$). The uncertainty on the signal position μ_{CB} comes from the uncertainty in electron, photon and muon calibration ($< 0.15\%$). It is less than the Higgs mass uncertainty, which is also applied on the μ_{CB} in each category. The magnitude is 0.19% [85]. The uncertainty on the signal strength is less than 2%.

6.6.3 Theoretical uncertainties

The theoretical uncertainties on the estimated signal yield include QCD scale uncertainties, parton density variations, the strong couplings constant and branching ratios. Most of these can cause migrations between different analysis categories and are therefore computed as uncertainties on each category. They are taken as fully correlated between event categories, and are presented in Table 6.15.

The most important theoretical uncertainties are the QCD scale uncertainty and the PDF uncertainties. The QCD scale uncertainties in VBF, WH, ZH and ttH production modes arise from the mismodelling of the production cross-section and kinematics due to missing higher-order QCD calculations. They take the value of 5.3% and are dominated by the QCD renormalisation and factorisation scales uncertainties

Sources	$H \to Z\gamma$
Luminosity [%]	
Luminosity	1.7
Signal efficiency [%]	
Modelling of pile-up interactions	0.0–0.2
Photon identification efficiency	0.8–1.8
Photon isolation efficiency	0.7–1.9
Electron identification efficiency	0.0–2.3
Electron isolation efficiency	0.0–0.1
Electron reconstruction efficiency	0.0–0.5
Electron trigger efficiency	0.0–0.1
Muon selection efficiency	0.0–0.6
Muon trigger efficiency	0.0–1.6
Jet energy scale	0.0–3.5
Jet resolution	0.0–15
Jet pile-up	0.0–7.5
Jet flavor	0.0–11
Signal modelling on σ_{CB} [%]	
Electron and photon energy resolution	0.5–3.4
Muon – Inner detector resolution	0.0–1.2
Muon – Muon spectrometer resolution	0.0–3.4
Signal modelling on μ_{CB} [%]	
Electron and photon energy scale	0.09–0.15
Muon momentum scale	0.0–0.03
Higgs boson mass measurement	0.19
Background modelling [number of spurious signal events]	
Spurious signal	1.5–39

TABLE 6.13: The main sources of experimental uncertainty for the $H \to Z\gamma$ search. The ranges for the uncertainties cover the variations among different categories, and different production modes (ggF, VBF, VH and ttH). All of the uncertainty values are given as fractions, except for the spurious signal uncertainty, which is given as the absolute number of events. Uncertainties are not listed if systematic sources are negligible.

(5.2%). The uncertainties on PDF and α_S are estimated from the reweighting of the MC. Values of these uncertainties are 2.5% and 1.9%, respectively.

The uncertainties on the branching ratio in the $H \to Z\gamma$ decay channel and total QCD scale ggF cross section uncertainty are provided by the LHC Higgs Cross Section Working Group [26] and are given in Table 6.15. The impact of QCD scale uncertainties on the distribution of signal events in the categories are estimated from scale variations of the Higgs boson p_{T} distribution onto events of NNLOPS ggH125 sample at the reconstruction level, using the Stewart–Tackmann method [113, 26] and inputs from [114, 115, 116]. An additional perturbative uncertainty on the ggH events acceptance in the VBF-enriched and other categories is derived following [117, 118].

An uncertainty on the modelling of the observables that are exploited in the BDT training for the categorisation is derived based on a MADGRAPH5_aMC@NLO/PYTHIA8 sample. Considering that the sample with the $H \to Z\gamma$ decay channel was not available, a sample with the $H \to \gamma\gamma$ decay channel is studied instead at the event generation/truth level in a phase space not identical but similar to the event selection strategy described in Sec. 6.3. The possibility to use a different decay channel at the truth level is derived in addition by the fact that most of the observables entering the BDT training are jet related and are not strongly correlated with the $Z\gamma$ decay. The differences between the nominal ggH125 sample and the alternative MADGRAPH5 sample are studied for each of the BDT variables separately, with the corresponding changes in the definition of the variables in the case of $H \to \gamma\gamma$ decays, where the Z boson was replaced with a photon. The p_{Tt} variable was replaced with the p_T^H due to the changes in the p_{Tt} definition for two different decay channels. The $\Delta\phi_{Z,\gamma}$ and $\Delta R_{min}(Z/\gamma, j_1, j_2)$ variables are not considered due to large shape differences caused by the observable definitions for two decay channels. All BDT observables are shown in Fig. 6.31 and the uncertainty is estimated for each category as the difference between the nominal and alternative MADGRAPH5 samples. The summary of the pertubative category population fraction uncertainties on the ggF process can be found in the Table 6.15.

The underlying event (UE) and parton shower (PS) uncertainties should be computed from a comparison between different parton showering algorithms, mostly PYTHIA8 and Herwig7 and form tune variations using MC reweighting. Currently only test Herwig7 ggF/VBF signal sample is available, and computation of the uncertainties using only truth events from that sample is described below.

The estimation of the UEPS uncertainty is based on a comparison of the NNLOPS ggH and POWHEG VBF samples for the $m_H = 125$ GeV masspoint with the Herwig7 samples. Since the effect of the uncertainty is expected to vary with type of hard scattering and the jet requirements it is therefore necessary to separate different production modes such as ggF and VBF, and apply different jet requirements. This is done in a phase space with the event selection applied as described in Sec. 6.3. The comparison of the predicted transverse momentum spectrum of the Higgs boson between two samples is shown in Fig. 6.32 in terms of the individual jet multiplicity configurations ($N_{jets} < 2$, $N_{jets} = 2$ and $N_{jets} > 2$), separately for the VBF and ggH production modes. As is seen, the alterations between two samples are observed mostly for the case of the selected number of jets equal to two. Resulting differences between the PYTHIA8 a nd Herwig7 samples are estimated by simultaneous reweighting of the truth p_T^H for all cases of jet configurations in the nominal sample to the observed values in the Herwig7 sample. The example of such reweighting is shown in Fig. 6.33, in case of $N_{jets} = 2$, separately for ggH and VBF production modes. The PS and UE uncertainty is estimated individually for each category and for the inclusive case, and the results are presented in the Table 6.14.

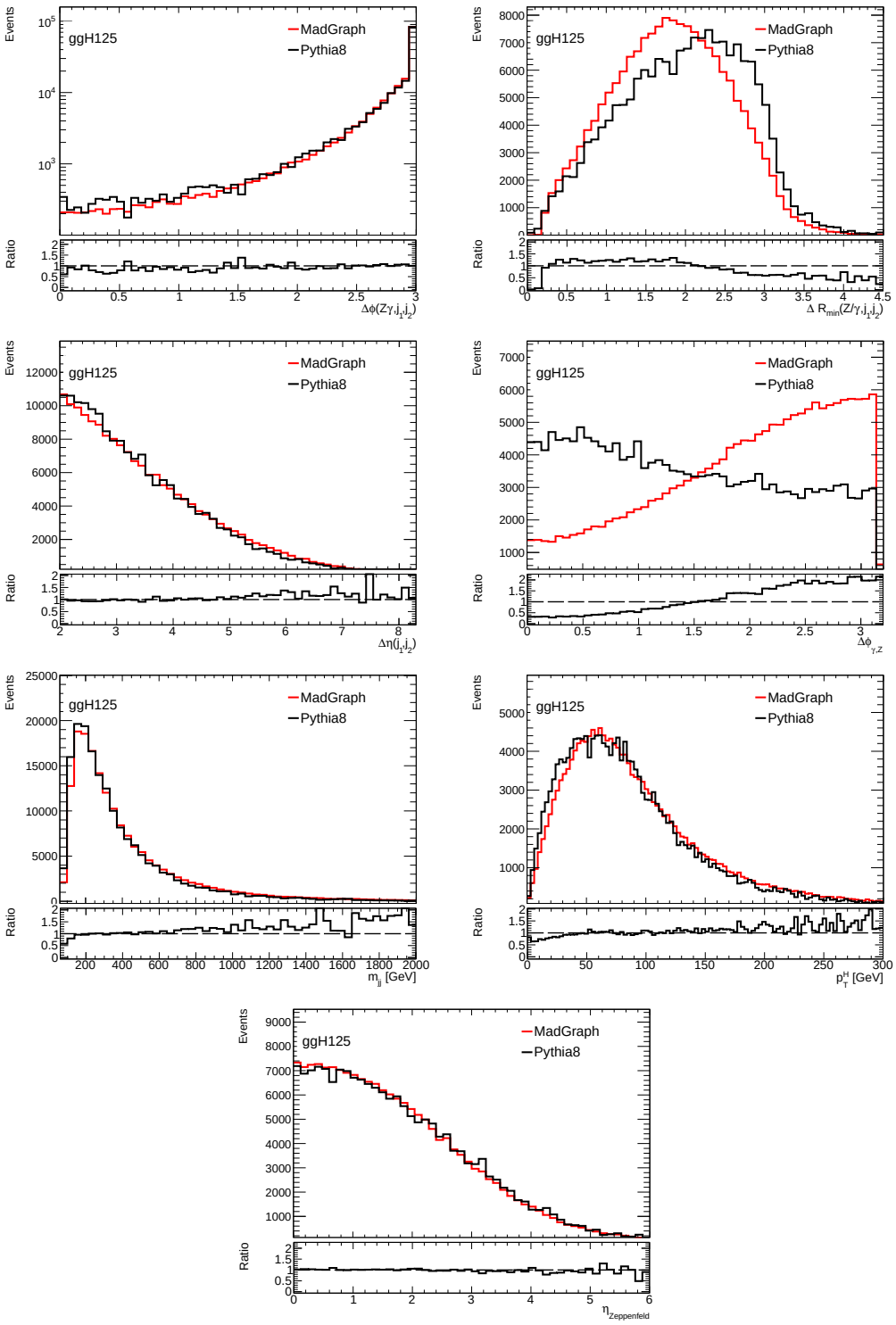

FIGURE 6.31: Event generation/truth-level comparison between different ggH125 Monte Carlo generator predictions for the cases of $H \to Z\gamma$ and $H \to \gamma\gamma$ decay channels, for the observables exploited in the BDT used for the separation of a VBF-topo category. From these plots uncertainty weights were derived for all observables except for the azimuthal separation of the $\Delta\phi_{Z,\gamma}$ and $\Delta R_{min}(Z/\gamma, j_1, j_2)$ as these observables have significantly different shape configurations caused by different Higgs decays.

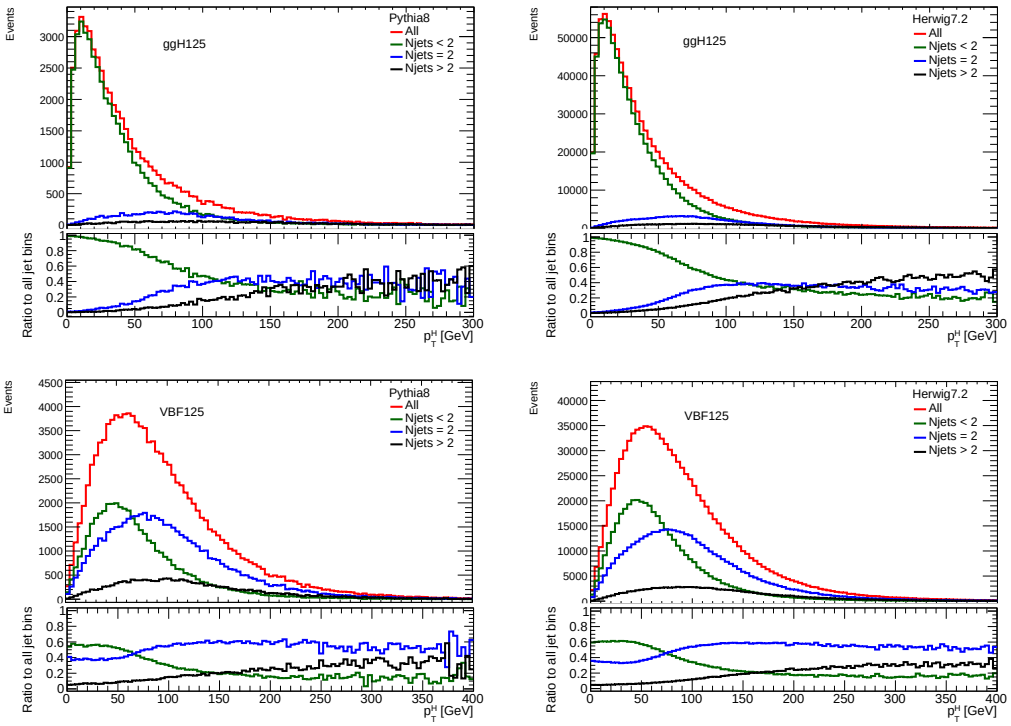

FIGURE 6.32: Truth p_T^H distribution for the cases of $N_{jets} < 2$, $N_{jets} = 2$ and $N_{jets} > 2$, for ggH (top) and VBF (bottom) production modes. Left: nominal PYTHIA8 sample, right: alternative Herwig7 sample.

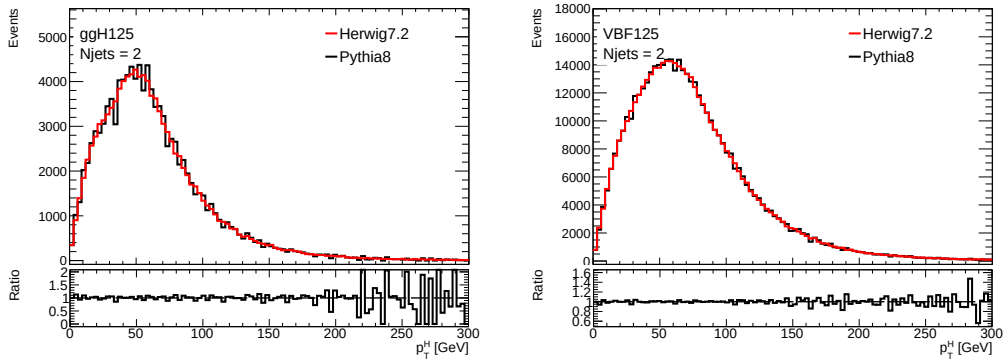

FIGURE 6.33: Truth p_T^H distribution for the case of $N_{jets} = 2$, for ggH (left) and VBF (right) production modes. The distribution in case of nominal PYTHIA8 sample is reweighted to the distribution in case of Herwig7 sample.

Mode	Inclusive	VBF-topo	Rel. pT	High pTt ee	Low pTt ee	High pTt $\mu\mu$	Low pTt $\mu\mu$
ggH	2.07%	1.04%	1.01%	0.30%	2.69%	0.16%	2.53%
VBF	-0.07%	0.47%	0.63%	-0.14%	-0.51%	-0.17%	-0.63%

TABLE 6.14: PS and UE uncertainty for ggH and VBF production modes at $m_H = 125$ GeV, obtained from comparison of the nominal sample PYTHIA8 sample to the alternative Herwig7 sample.

In addition, the ggF NLO MPIOFF full reconstruction sample is used to estimate the UEPS uncertainty as well as by comparison with the nominal NNLO ggF sample following the same principle described for the Herwig7 sample. Results are shown in the Table 6.15. As only the ggF sample is used, the UEPS uncertainty is only applied on the ggF process. The uncertainties obtained using Herwig7 sample are smaller than the errors estimated from the ggF MPIOFF sample, with the impact on final result tested to be negligible (<1%). However, considering that the full Herwig7 sample is not available at the moment, ggF NLO MPIOFF sample uncertainties are used for presenting the final results.

Sources	
Total cross-section and efficiency [%]	
ggF Underlying event	1.3
perturbative order	4.7–9.6
PDF and α_s	1.8–2.8
$B(H \to Z\gamma)$	5.7
Total (total cross-section and efficiency)	7.5–11
Category acceptance [%]	
ggF Underlying event	0.1–11
ggF H p_T perturbative order	0.3–0.4
ggF in VBF-enriched category	37
ggF in high relative p_T category	21
ggF in other categories	10–15
Other production modes	1.0–15
PDF and α_s	0.4–3.5
Total (category acceptance)	11–37

TABLE 6.15: The main sources of theoretical and modelling uncertainties for the $H \to Z\gamma$ search. The ranges for the uncertainties cover the variations among different categories, and different production modes (ggF, VBF, VH and ttH). The combined uncertainty on the total cross-section and efficiency is given assuming the cross-sections predicted by the SM. The uncertainty values are given as relative uncertainties. The uncertainties are on both signal yield, which is called total cross-section and efficiency, and signal decomposition in each category, which is named as category acceptance in the table.

6.7 Statistical methods

A profile-likelihood-ratio test statistic [109] is used to search for a localised excess of events over a smoothly falling background in the $m_{Z\gamma}$ distribution of the data, as well as to quantify its significance and estimate its production cross section and the signal strength (the ratio between the observed event yield and SM expected yield). In general, the likelihood is constructed from two components: background and Higgs boson signal, following Poisson probability terms. It also includes nuisance parameters, which can be described as terms for the systematic uncertainties (Sec. 6.6), parameterised as Gaussian or log-normal priors. The results can be expressed in

terms of signal strength parameter μ, defined as the following ratio

$$\mu = \frac{N_{signal}}{N_{signal}^{SM}}, \tag{6.9}$$

with the number of measured signal events over the expected number in the Standard Model. $\mu = 0$ represents the background-only hypothesis, while $\mu = 1$ identifies the signal-plus-background hypothesis. For a SM Higgs boson decaying to $Z\gamma$, the μ parameter is estimated for each of the categories, and it should be consistent with a single overall value of unity within statistical uncertainties.

Two main approaches exist for statistical interpretations: bayesian and frequentist. The bayesian approach is based on the assumption that hypothesis has an assigned probability. The frequentist approach assumes that hypothesis does not have an assigned probability and probabilities are interpreted as the frequencies of the outcomes of repeatable experiments. The final results presented in Sec. 6.8 rely on the frequentist statistics, and for the limit setting the modified frequentist formalism is used [119]. First, to estimate the significance of a possible observation, the assumption is set for the selected data to contain only background events. Next, the data is tested through the hypothesis test to see if it is compatible with the null hypothesis. Finally, it is possible that the test can shows no presence of any significant excess in data. In that case a limit is set on the ratio of the $H \to Z\gamma$ cross section over the Standard Model expectation.

A detailed description of the statistical methods used in the analysis is provided below.

6.7.1 Likelihood definition

The final results are obtained using unbinned maximum likelihood with a parameter of interest, μ, and *nuisance parameters*, θ. The likelihood can depend on such θ as these parameterise the number of background events, spurious signal terms or theoretical uncertainties. The likelihood function $\mathcal{L}(\mu,\theta)$ is given by the product of a Poisson term, the values of the probability density function $f_{\text{tot}}(m^i_{Z\gamma},\mu,\theta)$ of the invariant mass distribution for each candidate event i and constraint terms $G(\theta)$

$$\mathcal{L}\left((\mu,\theta)\middle|\{m^i_{Z\gamma}\}_{i=1..n}\right) = \frac{\mathrm{e}^{-N(\mu,\theta)}N^n(\mu,\theta)}{n!}\left(\prod_{i=1}^{n} f_{\text{tot}}(m^i_{Z\gamma},\mu,\theta)\right) \times G(\theta). \tag{6.10}$$

In this expression, n is the observed number of events and the expected event yield, N, is the sum of the number of signal events. The contributions to N are $N_{\text{sig}} = L_{\text{int}} \times (\sigma \times BR) \times \varepsilon$, the number of $H \to \mu\mu$ events, $N_{H\mu\mu}$, the number of background events, N_{bkg}, and the spurious signal yield, $N_{\text{spur}}(\theta_{\text{spur}}) = \sigma_{\text{spur}}\theta_{\text{spur}}$, which is the product of the spurious signal uncertainty and the corresponding nuisance parameter. The Higgs search is based on the SM prediction and the corresponding parameter of interest is the signal strength, where we have $N_{\text{sig}} = L_{\text{int}} \times \mu \times (\sigma_{SM}(pp \to H) \times BR_{SM}(H \to Z\gamma) \times BR_{SM}(Z \to ll)) \times \varepsilon$. The function $f_{\text{tot}}(m^i_{Z\gamma},\mu,\theta)$ is built from the component probability density functions of $m_{Z\gamma}$, f_{sig}, $f_{H\mu\mu}$ and f_{bkg}, and from the expected event yields $N^{(c)}_{\text{sig}}$, $N^{(c)}_{\text{spur}}$, $N^{(c)}_{H\mu\mu}$ and $N^{(c)}_{\text{bkg}}$ in the different categories c

$$f_{\text{tot}}(m^i_{Z\gamma}, \mu, \theta) = \frac{1}{N}\sum_c \Big\{ \Big[N^{(c)}_{\text{sig}}(m_H, \mu, \theta_{\text{sig}}) + N^{(c)}_{\text{spur}}(m_H, \theta_{\text{spur}}) \Big] \times f^{(c)}_{\text{sig}}(m^i_{Z\gamma}, \theta_{\text{sig}}) + N^{(c)}_{H\mu\mu}(m_H, \theta_{H\mu\mu}) \times f^{(c)}_{H\mu\mu}(m^i_{ll\gamma}) + N^{(c)}_{\text{bkg}} \times f^{(c)}_{\text{bkg}}(m^i_{Z\gamma}, \theta_{\text{bkg}}) \Big\}, \quad (6.11)$$

where $N^{(c)}_{\text{sig}}$ and θ_{sig} are divided into Higgs production modes (ggH, VBF, WH, ZH, ttH). Especially in the ZH production mode, the cross section of ZH is normalised to the total cross section of $pp \to ZH$ (882.4 fb) due to the lack of ggZH signal samples. The uncertainties in the signal parameterisation, efficiency, bias in the signal yield due to the choice of the background model and $H\mu\mu$ yield uncertainty are included in the full likelihood via nuisance parameters (NP) so that the signal and background yields or parameters of the model become functions of θ. The likelihood is then multiplied by a "constraint" term, which uses the best estimate of each systematic uncertainty. The nuisance parameters are then fitted to the data with the μ parameters. They can be described by either a Gaussian or a Log-normal function. For the uncertainties on the distribution of the signal events in the categories, a Gaussian constraint is used. For the uncertainties on the expected signal yields, the Log-normal form is preferred in order to avoid the negative tails of the Gaussian distribution. For the uncertainties where a Log-normal constraint is used, the affected quantity in the likelihood is multiplied by a term of the form

$$e^{\sqrt{log(1+\sigma^2)}\theta}, \quad (6.12)$$

and the likelihood is multiplied by $G(\theta)$. G is a Gaussian distribution with width equal to one and mean value at zero, σ is the best estimate of the relative uncertainty. For a systematic uncertainty where a Gaussian constraint is used, the quantity affected by the uncertainty in the likelihood is multiplied by a term of the form

$$\mathbf{(1 + \sigma\theta)}, \quad (6.13)$$

where the likelihood is multiplied by $G(\theta)$.

For the theoretical scale uncertainties on the Higgs production cross sections, the log-normal constraints are used. Gaussian constraints are set for the PDF uncertainties. The likelihood then is multiplied by terms for each of the Higgs boson production modes (ggH, VBF, WH, ZH, ttH). The experimental uncertainties are accounted for using the Log-normal constraint.

6.7.2 p-value calculation

In order to make a discovery, the hypothesis test is defined to reject the null hypothesis, meaning that there is no Higgs boson signal with μ equal to 0. The compatibility of the data with the background-only (B-only) hypothesis ($p_0 = 0$) is quantified by the local p_0 or p-value of the data, which gives the probability for a dataset generated in the background-only hypothesis to be in the same or worse agreement with that hypothesis. Only upwards deviations from the B-only hypothesis, which would correspond to a positive signal strength, are considered. A large p_0 therefore corresponds to datasets that agree well with the background-only hypothesis, while a small p_0 suggests a significant positive signal. The p_0 is computed from the q_0 test statistic,

defined as

$$q_0 = \begin{cases} -2\ln\frac{L(0,\hat{\hat{\theta}}(0))}{L(\hat{\mu},\hat{\theta})} & \hat{\mu} \geq 0 \\ 0 & \hat{\mu} < 0 \end{cases} \tag{6.14}$$

where L is the likelihood function described in Section 6.7.1, $\hat{\mu}$ and $\hat{\theta}$ are the best-fit values for μ and θ with all parameters floating and $\hat{\hat{\theta}}(0)$ is the best-fit value of θ in the background-only ($\mu = 0$) hypothesis. If the $\hat{\mu}$ parameter increases, the q_0 value increases as well, corresponding to the disagreement between the the data and background-only hypothesis. That level of disagreement can be expressed as the p_0 value

$$p_0 = \int_{q_{0,\text{obs}}}^{\text{inf}} f(q_0|0, m_H, \hat{\hat{\theta}}(0))dq_0, \tag{6.15}$$

where f is the probability density function of the test statistic under the null hypothesis. A small p_0 occurs only for $q_0 > 0$. The p-value then can be a measure of the probability of observing a dataset under the assumption that there is no signal. Negative fluctuations of the signal are assigned p_0 values to 0.5.

In the expression for $\hat{\mu} > 0$, the numerator corresponds to the best value of the likelihood computed in the background-only hypothesis, while the denominator corresponds to the best value in the signal-plus-background ("S+B") hypothesis including both signal and background. For datasets which are compatible with the background-only hypothesis, both should be of similar magnitude with a small q_0. While in the presence of a signal, the denominator (S+B hypothesis) should be much larger than the numerator (B-only hypothesis), yielding a large value of q_0. In the asymptotic regime, p_0 values can be directly computed from the q_0 values using closed-form "asymptotic formulae" [109].

The term *significance* corresponds to a given p_0 value as the number of standard deviations, Z. At these values the measured p_0 value would be equal to a one-sided tail area of a Gaussian distributed variable with variance of one and zero mean. Typically the value of Z = 5 is used to reject the background-only hypothesis, and the value of Z = 1.64 is used to reject the background-plus-signal hypothesis, meaning $\mu = 1$ can be rejected. The data values can be rejected at a certain confidence level (CL), with a typical number of CL = 95% being used.

The limit setting on the signal strength use the modified frequentist formalism with the CL method based on q_μ statistic [119]

$$q_\mu = \begin{cases} -2\ln\frac{L(\mu,\hat{\hat{\theta}}(\mu))}{L(\hat{\mu},\hat{\theta})} & 0 \leq \hat{\mu} \leq \mu \\ 0 & \hat{\mu} > \mu \\ -2\ln\frac{L(0,\hat{\hat{\theta}}(0))}{L(\hat{\mu},\hat{\theta}(\mu))} & \hat{\mu} < 0 \end{cases} \tag{6.16}$$

where $\hat{\hat{\theta}}(\mu)$ are the best-fit values for θ for a fixed value of μ. Fig. 6.34 shows the relation (a) between the p-value and the observed test statistic q_μ, (b) between the p-value and the significance Z.

The CL_{s+b} p-value is then defined as following:

$$p_\mu = \int_{q_{\mu,\text{obs}}}^{\text{inf}} f(q_\mu|\mu, m_H, \hat{\hat{\theta}}(\mu))dq_\mu, \tag{6.17}$$

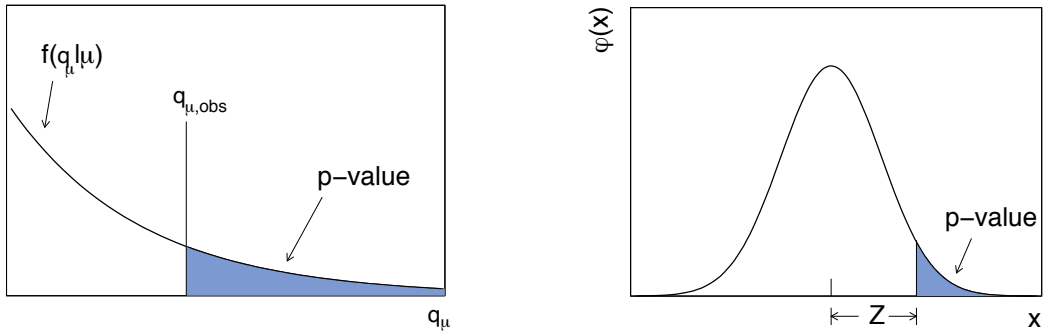

(a) (b)

FIGURE 6.34: (a) Illustration of the relation between the p-value obtained from an observed value of the test statistic. (b) Normal distribution showing the relation between the significance Z and the p-value [109].

where CLs p-value is defined as

$$p'_\mu = \frac{p_\mu}{1 - p_b}, \tag{6.18}$$

and

$$p_b = 1 - \int_{q_{\mu,\text{obs}}}^{\text{inf}} f(q_\mu|0, m_H, \hat{\hat{\theta}}(0))dq_\mu. \tag{6.19}$$

The p'_μ value and the corresponding CLs exclusion are obtained using the asymptotic formulae [109]. Limits at 95% confidence level on μ are obtained by scanning values of the μ hypothesis, identifying the μ_{up} for which this value equals to 0.05.

For the final results of this chapter, both the observed and expected limits are computed using the real data and an Asimov dataset [109] respectively. An Asimov dataset is generated as pseudodata that matches the expected number of background and signal events for a given value of μ.

6.8 Results

As was mentioned in Sec. 6.7, a profile likelihood ratio fit is performed to data. The final results are obtained for the category dependent $Z\gamma$ mass ranges. Figure 6.35 shows the invariant mass distributions with the background-only fit to the data. The expected Higgs boson signal normalised to 20 times the SM prediction is shown as a red dashed curve.

The signal strength parameter μ is defined as the ratio of the measured number of signal events to that expected in the Standard Model. The best-fit value for μ is estimated to be the following

$$\mu = 2.0^{+1.0}_{-0.9}(tot.) = 2.0^{+0.9}_{-0.9}(stat.)^{+0.4}_{-0.3}(syst.) \text{ (obs.)},$$

for the observed value. The expected value, which assumes the presence of the SM Higgs boson, is the following

$$\mu = 1.0^{+0.9}_{-0.9}(tot.) = 1.0^{+0.8}_{-0.8}(stat.)^{+0.3}_{-0.3}(syst.) \text{ (exp.)}.$$

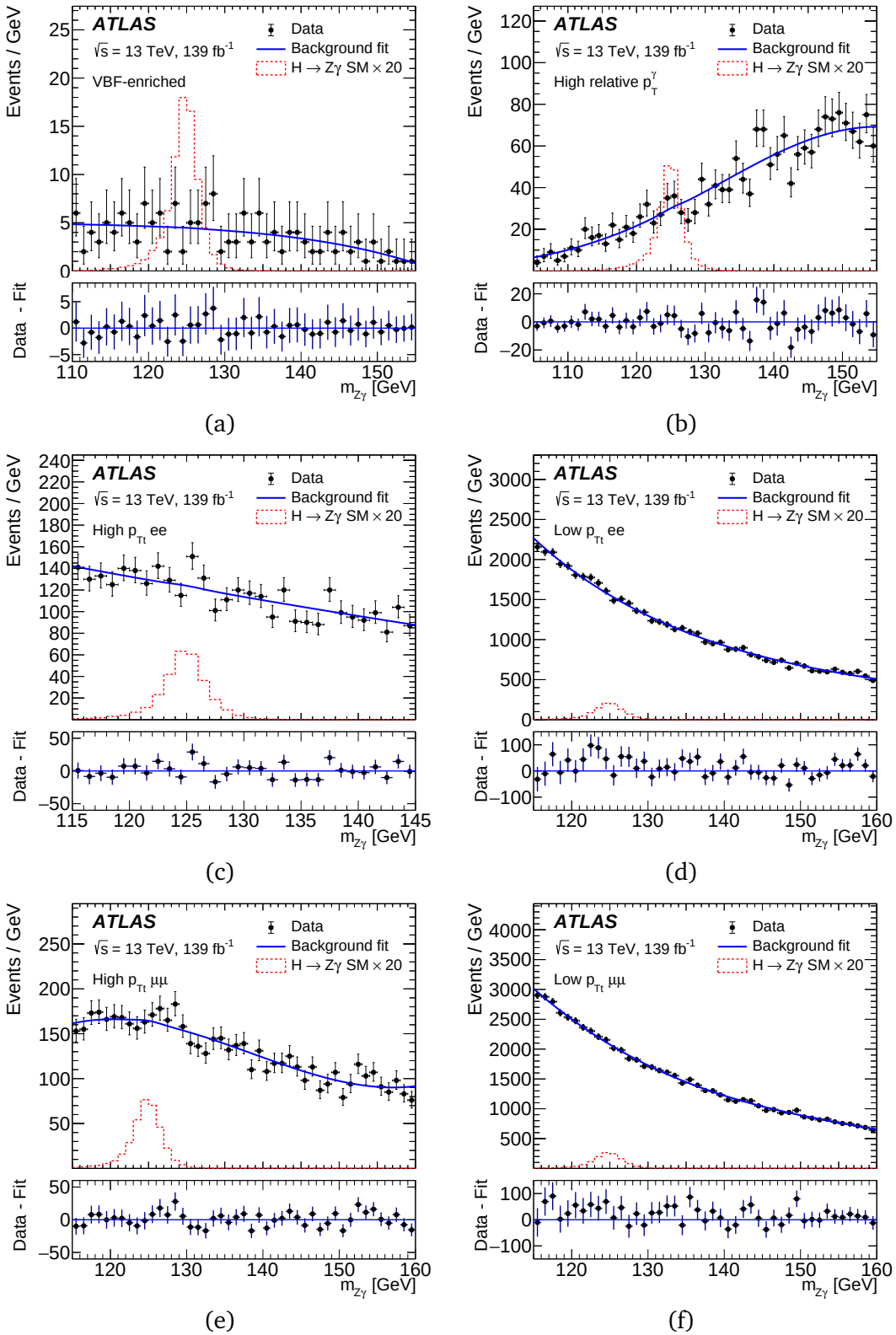

FIGURE 6.35: The $Z\gamma$ invariant mass $m_{Z\gamma}$ distributions for the six event categories: (a) VBF-enriched, (b) High relative p_{T}, (c) High pTt ee, (d) Low pTt ee, (e) High pTt $\mu\mu$, and (f) Low pTt $\mu\mu$. The data is shown with the black dots. The error bars represent only the statistical uncertainty. The solid blue lines show the background-only fits to the data. The red dashed histogram corresponds to the expected signal for a SM Higgs boson with $m_H = 125$ GeV multiplied by a factor of 20. The ratio shows the residuals of the data with respect to the background-only fit.

As it is seen from these values, the analysis is limited statistically.

The observed p-value under the background hypothesis at $m_H = 125$ GeV is 0.013, corresponding to a significance of 2.2 σ, while the expected p-value with an SM Higgs boson is 0.123, and it corresponds to a significance of 1.2 σ.

Considering that no significant signal is observed, upper limits are set on $H \to Z\gamma$ measured production cross section, normalised to the SM expectation. The 95% CL limit on the $H \to Z\gamma$ observed signal strength μ is found to be 3.6 times the SM prediction. The 95% CL limit with the expected μ is set to be 1.7 assuming the background only hypothesis. With the SM Higgs boson decay to $Z\gamma$ assumption, the 95% CL limit on μ is 2.6.

The weighted $m_{Z\gamma}$ distribution over all categories with the corresponding signal-plus-background fitting curve is shown in Figure 6.36. The events are weighted as $\ln 1 + \frac{S_{68}}{B_{68}}$, with S_{68} and B_{68} corresponding to the number of signal and background events respectively in the $m_{Z\gamma}$ mass window, which contains 68% of the expected signal. The invariant mass, $m_{Z\gamma}$, distribution of the data and the signal-plus-background fitting curve in each category is shown in Figures 6.37.

Table 6.16 shows the major groups of uncertainty sources and estimation of their relative errors on the signal strength μ. As is seen from the table, the dominant source of uncertainty on μ is statistical uncertainty. For the systematic uncertainty, the dominant component for the experimental uncertainties comes from the spurious signal uncertainties. Concerning the theoretical uncertainties, the most important impact comes from the QCD scale uncertainties.

Uncertainty	$\Delta\mu/\mu$ (obs.)	$\Delta\mu/\mu$ (exp.)
Statistical uncertainty	43.1%	82.8%
Spurious signal	14.7%	28.4%
e/γ scale, resolution	2.0%	2.4%
Luminosity	1.7%	1.6%
Photon efficiency	1.6%	1.8%
Jet	1.5%	1.1%
Electron, Higgs mass, Muon, $H \to \mu\mu$ normalization, PRW	2.0%	2.1%
QCD scale	6.9%	6.1%
BR($H \to Z\gamma$) uncertainty	5.7%	5.9%
UEPS	2.4%	2.1%
PDF, α_s	2.2%	2.8%
Total	46.7%	88.1%

TABLE 6.16: Relative uncertainies $\Delta\mu/\mu$ in groups.

The top 30 nuisance parameters (NP) rankings affecting the signal strength are presented in Figure 6.38. Figure 6.38 (a) shows the results with the observed data and Figure 6.38 (b) shows the results with the expected data ($\mu = 1$). All of the NPs are similar between the observed data and the Asimov dataset, with no over-constrained or strongly pulled NPs.

The significances for the individual event categories are estimated by implementing an independent signal strength in each category with their simultaneous fit. Table 6.17 shows the significances and signal strengths for the observed and expected data in categories. As is seen, for the observed results, the largest significances are obtained for the categories containing electrons.

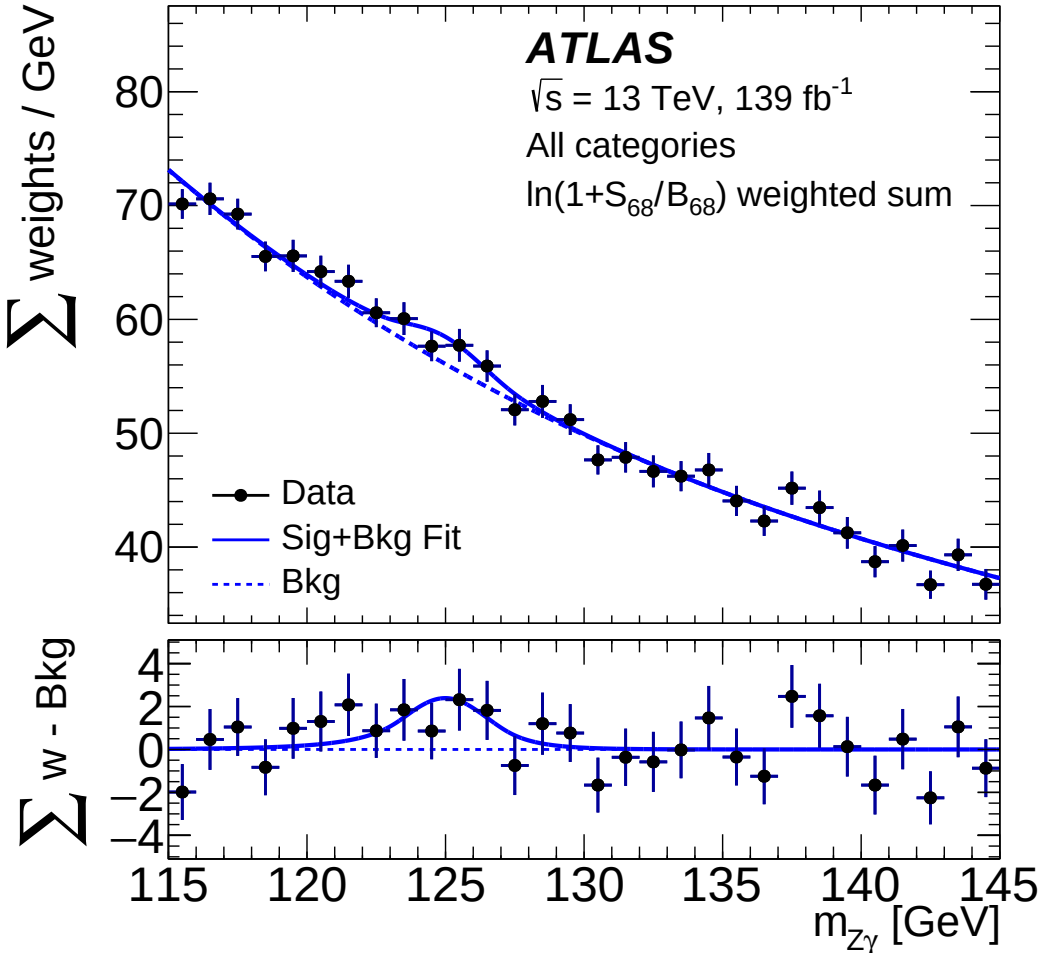

FIGURE 6.36: The weighted $Z\gamma$ invariant mass $m_{Z\gamma}$ distribution. The black dots represent the weighted data. The error bars represent the statistical uncertainty. Events are weighted by $\ln(1 + S_{68}/B_{68})$, where S_{68} and B_{68} are the expected signal and background events in the $m_{Z\gamma}$ window, which contains 68% of the expected signal. The solid blue curve shows the combined fitted signal-plus-background model in all categories fitted simultaneously and the dashed line shows the model of the background component.

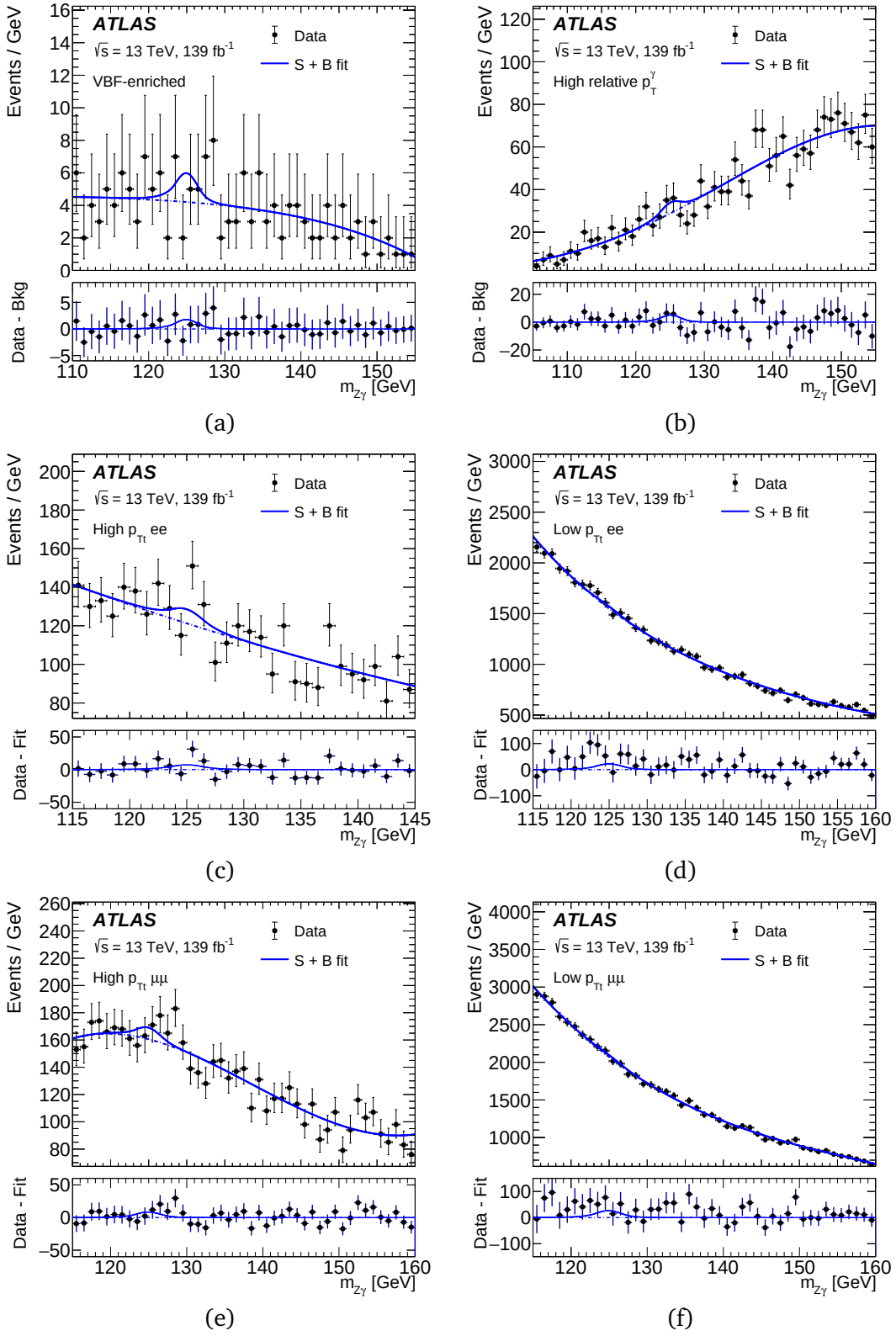

FIGURE 6.37: The $Z\gamma$ invariant mass $m_{Z\gamma}$ distributions for the six event categories: (a) VBF-enriched, (b) High relative p_{T}, (c) High pTt ee, (d) Low pTt ee, (e) High pTt $\mu\mu$, and (f) Low pTt $\mu\mu$. The black dots show data. The error bars represent the statistical uncertainty. The solid blue lines show the signal-plus-background fits to the data. The ratio shows the residuals of the data with respect to the background component of the fit.

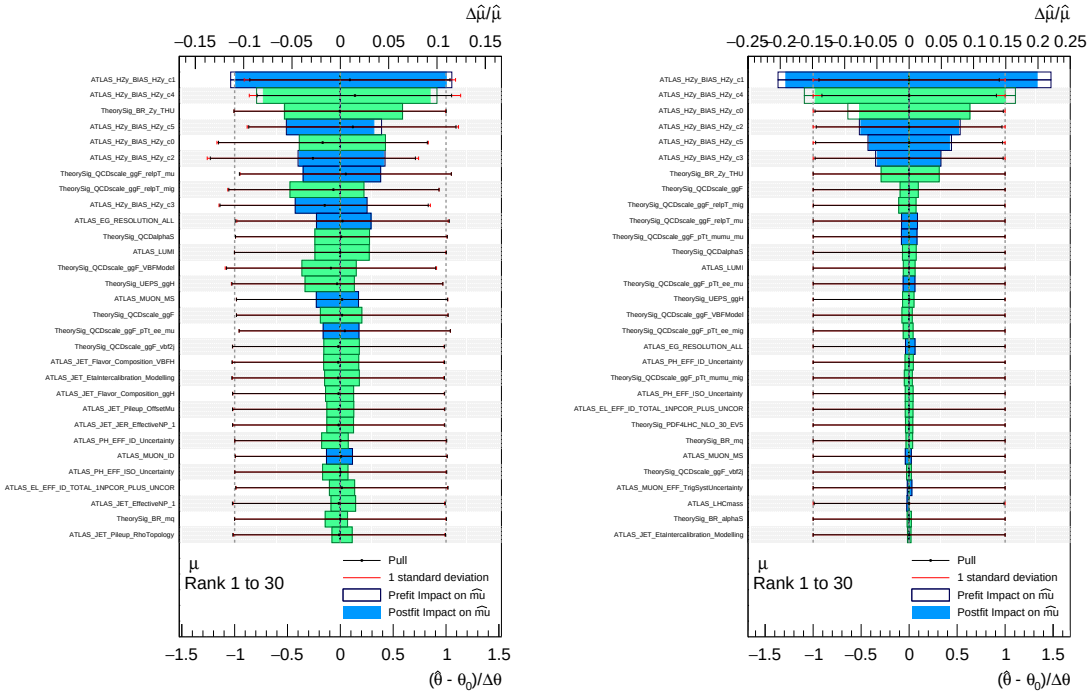

FIGURE 6.38: Rankings of the top 30 NPs affecting the signal strength μ with (a) the observed data and (b) the expected data, using the Asimov ($\mu = 1$) datasets. The empty rectangles correspond to the prefit impact on μ and the filled rectangles show the postfit impact on μ. The black dots show the pulls of the nuisance parameters.

Category	μ	Significance
VBF-enriched	$0.5^{+1.9}_{-1.7}$ $(1.0^{+2.0}_{-1.6})$	0.3 (0.6)
Rel. pT	$1.6^{+1.7}_{-1.6}$ $(1.0^{+1.7}_{-1.6})$	1.0 (0.6)
High pTt ee	$4.7^{+3.0}_{-2.7}$ $(1.0^{+2.7}_{-2.6})$	1.7 (0.4)
Low pTt ee	$3.9^{+2.8}_{-2.7}$ $(1.0^{+2.7}_{-2.6})$	1.5 (0.4)
High pTt $\mu\mu$	$2.9^{+3.0}_{-2.8}$ $(1.0^{+2.8}_{-2.7})$	1.0 (0.4)
Low pTt $\mu\mu$	$0.8^{+2.6}_{-2.6}$ $(1.0^{+2.6}_{-2.5})$	0.3 (0.4)
Combined	$2.0^{+1.0}_{-0.9}$ $(1.0^{+0.9}_{-0.9})$	2.2 (1.2)

TABLE 6.17: Observed and expected signal strengths and significances in each category. The results have good compatibility among categories and between observation and SM prediction.

The limit on the branching ratio B($H \to Z\gamma$), assuming the SM Higgs boson production cross-section, is estimated with the BR theory uncertainties removed. With the SM B($H \to Z\gamma$) being $0.15\% \pm 0.01\%$, the observed upper limit at 95% CL on B($H \to Z\gamma$) is found to be 0.55%. The expected limit on B($H \to Z\gamma$) is estimated to be 0.27% with the background only assumption and with the SM Higgs decay to $Z\gamma$ assumption, the limit on B($H \to Z\gamma$) is 0.39%.

Assuming the SM $\sigma(pp \to H) \cdot B(H \to Z\gamma)$ to be 85 ± 6 fb, the observed significance is found to be 2.2 σ while the expected significance is 1.2 σ. The observed upper limit at 95% CL on $\sigma(pp \to H) \cdot B(H \to Z\gamma)$ is 305 fb. With no Higgs boson decay into $Z\gamma$ assumption, the 95% CL on the expected $\sigma(pp \to H) \cdot B(H \to Z\gamma)$ is 1.7 times the SM prediction, whilst with the presence of the SM Higgs boson decay assumption, the limit is found to be 2.6 times the SM prediction.

The overall obtained improvement, compared with the previous results obtained with 36.1 fb^{-1} of data [118], is about a factor of 2.4 in expected sensitivity. The major improvement with a factor of approximately two comes from the larger analysed dataset and the additional 20% improvement is due to the various optimisations of the analysis, described in previous chapters.

In addition, Figure 6.39 and Figure 6.40 present event displays of the selected data events to illustrate the performance of the ATLAS detector in this analysis. Figure 6.39 shows the candidate Higgs boson decay to $Z\gamma$, with the Z boson decaying into an electron pair. The transverse momenta of the electrons (shown in green) are 51.5 GeV and 39 GeV. The photon candidate (shown in green boxes) is reconstructed as a converted photon with a transverse momentum of 24.5 GeV. The two well-separated tracks correspond to a Z boson, while the two nearby tracks correspond to the photon conversion. The invariant mass of the Z boson is 91.7 GeV and the invariant mass of $Z\gamma$ system is 122.2 GeV. The event is chosen from the low-pTt category. Figure 6.40 shows the Higgs boson decay to $Z\gamma$, with the Z boson decaying into a muon pair. The transverse momenta of the muons (red) are 72 GeVand 20 GeV. The photon candidate is reconstructed as an unconverted photon (green) with a transverse momentum of 32.5 GeV. Two jets are represented by light blue cones, with m_{jj} of 965 GeV. The invariant mass of the Z boson is 91.1 GeV and the invariant mass of $Z\gamma$ system is 125.4 GeV. The event is chosen from the VBF-enriched category.

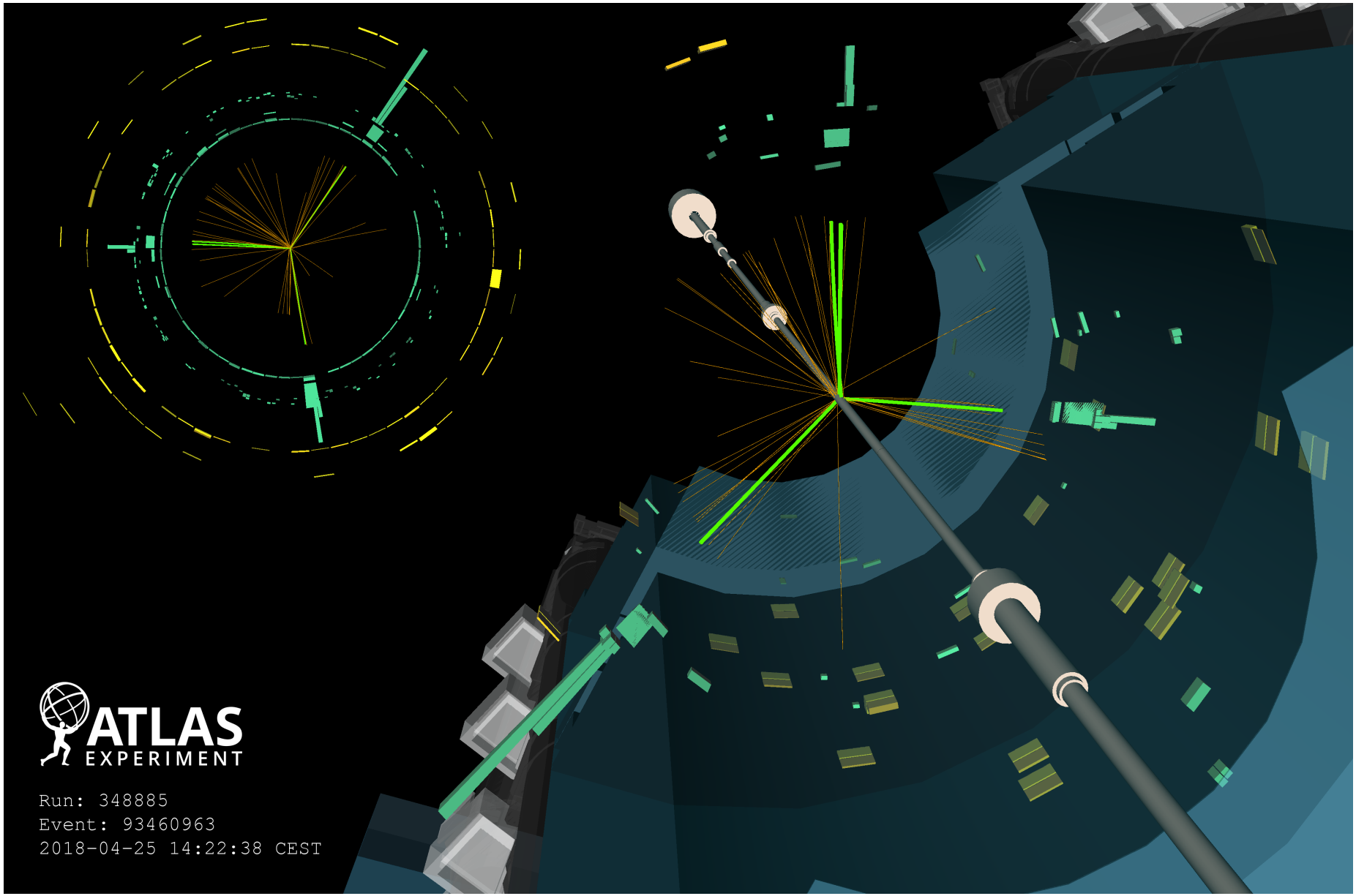

FIGURE 6.39: Event display of a $H \to Z\gamma$ event with the Z boson decaying to e^+e^-. The electrons and the photon, reconstructed as converted, are shown in green. The green boxes correspond to energy deposits in cells of the electromagnetic calorimeter, while yellow boxes correspond to energy deposits in cells of the hadronic calorimeter.

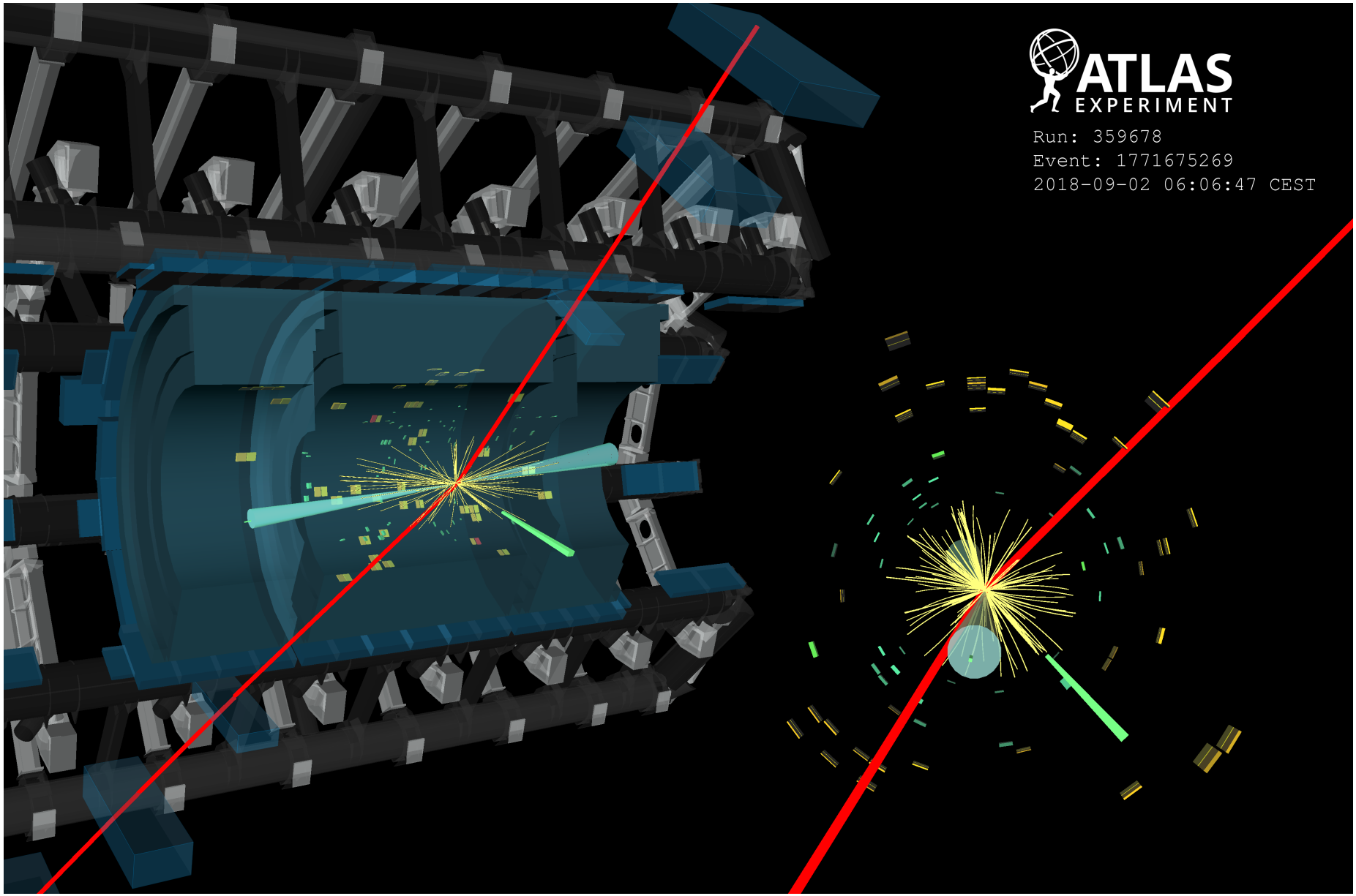

FIGURE 6.40: Event display of a $H \to Z\gamma$ event with the Z boson decaying to $\mu^+\mu^-$. The muons are shown in red and the photon, reconstructed as unconverted, is shown in green. The green boxes correspond to energy deposits in cells of the electromagnetic calorimeter, while yellow boxes correspond to energy deposits in cells of the hadronic calorimeter. Two jets are shown in light blue cones.

7 Conclusions and outlook

After the successful discovery of a particle at the LHC, confirmed later to be the Higgs boson, there is still open question whether it is indeed the particle predicted by the Standard Model. For that it is important to measure precisely all of the Higgs boson's properties, such as mass or branching ratios to various final states. In addition, rare channels as $H \rightarrow Z\gamma$, mediating through the loop diagrams, can be particularly sensitive to the presence of new physics beyond the Standard Model.

The main topic of the current thesis is search for the Standard Model Higgs boson decay into $Z\gamma$. The results are obtained using data collected by the ATLAS experiment at $\sqrt{s}$ = 13 TeV at the LHC in the years from 2015 to 2018, corresponding to an integrated luminosity of 139 fb^{-1}.

The Higgs boson discovery, as well as fulfilment of many research programmes at the LHC, would have been not be possible without excellent detector performance, precise calculations of many theoretical properties of the observed particles, accurate detector calibrations and good particle reconstruction using the analysed data collected at the collider. The work performed for this thesis includes a significant contribution to some of the described fields in the past four years.

The initial work started with the contribution to the studies of the performance of one of the ATLAS sub-detectors - the Transition Radiation Tracker. The TRT provides an important addition to the particle identification system of the ATLAS experiment. Specifically, electrons and photons, which are used later for the Higgs boson search analysis. One of the contributions included the tuning of the high threshold of the front end electronics, which is used to discriminate TRT hits from transition radiation and ionisation. This tuning allows the improvement of data to simulation agreement and accounts for the changing detector gas geometries and different run periods. Another contribution was done to study and improve the performance of the particle energy loss dE/dx in a busy detector environment. The dE/dx parameter can also be used to identify mainly highly ionising particles such as stable massive particles or highly charged particles.

The work continued with the improvements of the photon reconstruction efficiency measurements. One part of these studies is dedicated to the photon identification at the low energy scale using the pure photon sample from radiative Z boson decays. At first, the identification menu is checked in order to have the optimal performance for the search of the Higgs boson decaying to $Z\gamma$. Next, its efficiency is estimated directly from the data and precise corrections of the simulated data are provided. The pure sample of photons from the radiative Z boson decays has been

reused for several other studies, such as study of the photon isolation, and later optimisation of the photon selection for the $H \to Z\gamma$ analysis. The studies of the photon isolation included estimations of the isolation efficiencies from the data, which were obtained for the low photon energies for the first time in ATLAS during the second run.

After the results of the performance studies were well understood and the results were provided to the physics groups, a search for the $H \to Z\gamma$ has been performed. It started with the selection optimisation, where a major improvement comes from the photon identification menu optimisation. The menu has been tuned specifically to improve the signal efficiency of the analysis in the low energy region. It provided a 4% improvement in the analysis sensitivity compared to the previous version. Next, the events are categorised in order to maximise the sensitivity of the analysis. One of these categories has been improved with use of multivariate data analysis, which allowed excellent background to signal separation to be achieved.

Finally, a maximum likelihood fit to data is performed and used to measure the signal strength μ. The best-fit value for μ normalised to the SM prediction is $2.0^{+1.0}_{-0.9}$. The observed data are found to be consistent with the expected background with a p-value of 1.3%, while the expected p-value is 12.3% in the presence of a SM Higgs boson. These p-values correspond to an observed significance of 2.2 standard deviations, while the expected significance corresponds to 1.2 standard deviations. For a Higgs boson mass of 125.09 GeV, the observed 95% CL upper limit on the $\sigma(pp \to H) \cdot B(H \to Z\gamma)$ is 3.6 times the SM prediction. The expected limit on $\sigma(pp \to H) \cdot B(H \to Z\gamma)$ assuming no Higgs boson decay into $Z\gamma$ is 1.7 times the SM prediction, and 2.6 times the SM prediction in the presence of the SM Higgs boson decay.

7.0.1 Outlook

The results of the search of the $H \to Z\gamma$ obtained in the current thesis don't show any significant deviation from the background. However, the statistical component of the uncertainty in the analysis dominates. The improvement in the future can come from both an increased amount of data collected at the LHC and a reduction of the systematic uncertainties. The optimisation of the size of the systematic uncertainties can come from a larger Monte-Carlo simulation dataset. It can help to reduce statistical fluctuations of the templates, used for the background modelling and decrease the spurious signal uncertainty, which is currently the second largest contribution to the sources of uncertainty. One more promising direction of the optimisation can come from use of multivariative techniques, which can allow enhancement of the signal-to-background separation.

The prospects for the $H \to Z\gamma$ search have been studied using 14 TeV proton-proton collisions at the High-Luminosity LHC (HL-LHC) at 3000 fb^{-1}, assuming average pile-up of $\mu = 140$ [120, 121]. They however do not include possible future optimisations of the selection strategies described earlier. Fig. 7.1 shows the precision on the signal strengths expected for several Higgs boson decay channels including $H \to Z\gamma$. The expected significance for a mass of 125 GeV corresponds to 3.9 σ. The expected upper limit at 95% CL on $\sigma(pp \to H) \cdot B(H \to Z\gamma)$ is 0.52 times the SM expected one.

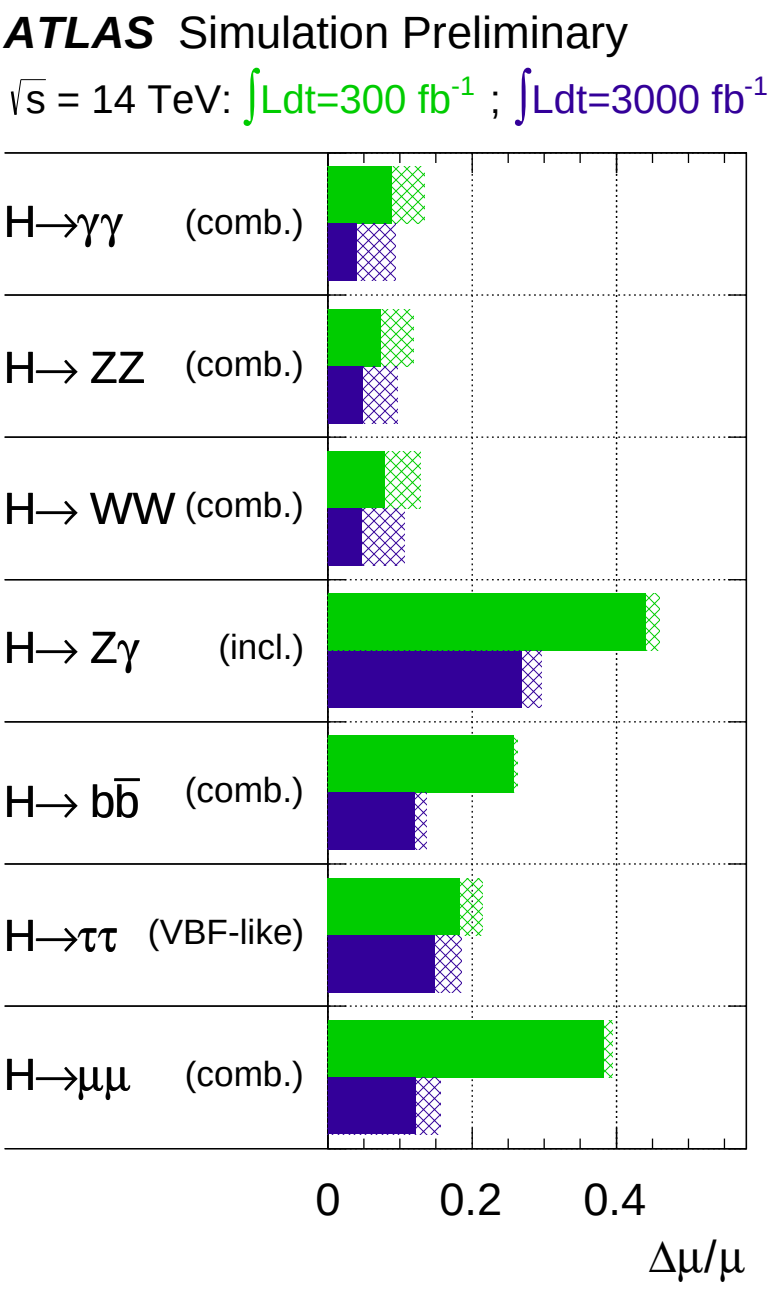

FIGURE 7.1: Relative uncertainty on the signal strength μ for several Higgs final states, assuming a SM Higgs boson with a mass of 125 GeV expected with 3000 fb^{-1} and compared to 300 fb^{-1}, for 14 TeV LHC data [121].

A Additional material on the signal modelling

It is possible that the $H \to \mu\mu$ process can contribute to the $H \to Z\gamma$ process. The effect from the additional contribution of $H \to \mu\mu$ process to the signal parametrisation is checked below, and results are presented in Fig. A.1 and Table A.1. The contribution of the $H \to \mu\mu$ events is negligible.

Category	Resolution [GeV] in $H \to Z\gamma$	Resolution [GeV] in $H \to Z\gamma + H \to \mu\mu$
Inclusive	1.613	1.617
Inclusive ee	1.581	1.584
Inclusive $\mu\mu$	1.629	1.638
e or μ, $BDTG > 0.87$	1.519	1.533
e or μ, $BDTG < 0.87$, $p_{\mathrm{T}}^{\gamma}/m_{ll\gamma} > 0.4$	1.417	1.446
e, BDTG < 0.87, $p_{\mathrm{T}}^{\gamma}/m_{ll\gamma} < 0.4$, $p_{\mathrm{Tt}} > 40$	1.439	1.439
e, BDTG < 0.87, $p_{\mathrm{T}}^{\gamma}/m_{ll\gamma} < 0.4$, $p_{\mathrm{Tt}} < 40$	1.685	1.685
μ, BDTG < 0.87, $p_{\mathrm{T}}^{\gamma}/m_{ll\gamma} < 0.4$, $p_{\mathrm{Tt}} > 40$	1.608	1.631
μ, BDTG < 0.87, $p_{\mathrm{T}}^{\gamma}/m_{ll\gamma} < 0.4$, $p_{\mathrm{Tt}} < 40$	1.662	1.664

TABLE A.1: Resolution for the PDF in each category from $H \to Z\gamma$ and from combination of $H \to Z\gamma$ and $H \to \mu\mu$, for all full simulation signal samples

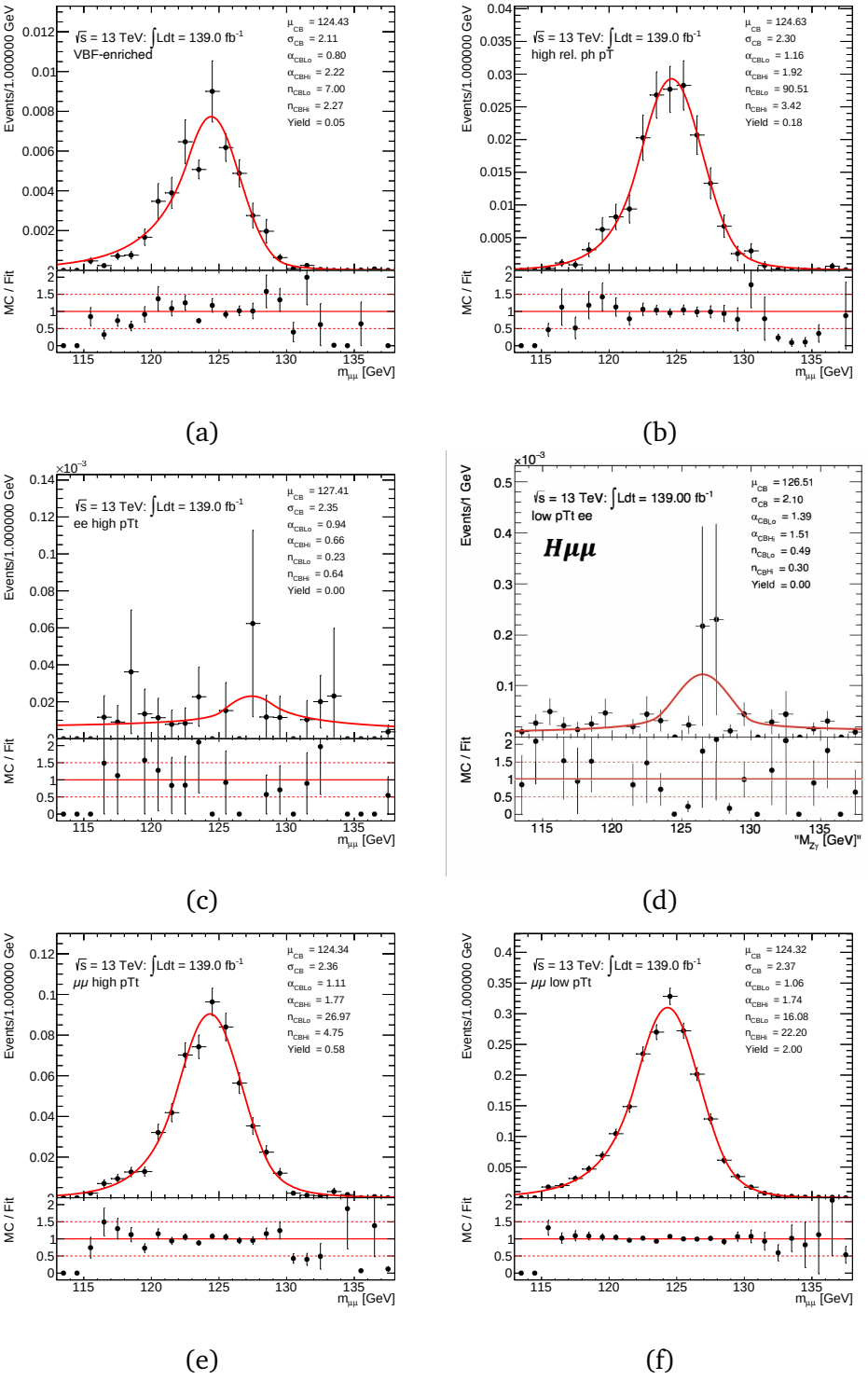

FIGURE A.1: Results of simultaneous fits of DCSB parameters as a function of the invariant mass spectrum of $\mu\mu$ in data derived from all full simulation signal samples, in the (a) "VBF-enriched" , (b) "high rel. pT" , (c) "high pTt ee" , (d) "low pTt ee" , (d) "high pTt $\mu\mu$" , and (e) "low pTt $\mu\mu$", categories for the Higgs Boson search,

Summary

In this thesis a search for the Higgs boson decay into a Z boson and a photon with the ATLAS detector at the LHC is presented. The measurements are based on data collected by the ATLAS detector during the second run of the LHC (2015 to 2018).

In the Standard Model $H \to Z\gamma$ decay is a rare process, having a minute probability of approximately 10^{-3}. Additional complexity comes from considering only leptonic final states (electron or muon) of the Z boson decay, which reduces the final probability of such a process even further:

$$B(H \to Z\gamma) \times B(Z \to ee/\mu\mu) \approx 10^{-4},$$

Using only leptonic final states allows a small background and provides good invariant mass resolution. A search for the $H \to Z\gamma$ process can reveal if Standard Model predictions of the Higgs mechanism are correct or at least shed light on the spectrum of Beyond Standard Model theories if deviations from measured parameters are observed. For example, different branching ratios to those predicted can occur in models with additional charged particles due to their contribution via loop corrections.

Searches for Higgs boson decays can be conducted thanks to particle colliders such as the LHC and detection is possible using an all-purpose detector such as ATLAS. It is essential for a detector to have both excellent performance and particle reconstruction capabilities. The analysis presented in this thesis relies on the correct reconstruction of electrons, muons, and photons, which is achieved with the combination of three main sub-detectors of ATLAS: the inner tracking detector, the calorimeter (electromagnetic and hadronic), and the muon spectrometer. More details are shown in particular for the TRT detector.

I performed several studies on improvement of charged particle identification using the high threshold of the front-end electronics which allows to discriminate TRT hits from transition radiation and ionisation. Next, studies of particle reconstruction mostly in the electromagnetic calorimeter were performed for low energy photons. These studies include improvement of identification performance efficiency and correction of the simulation to correspond to the results obtained from measured data. Photon performance studies are of particular interest for the Higgs boson analysis presented in this thesis as they use the same spectrum of photon energy as in the $H \to Z\gamma$ analysis.

The search for the Higgs boson with decay to a Z boson and a photon uses data with a total integrated luminosity of 139 fb^{-1} of proton-proton collisions at a centre-of-mass energy of 13 TeV. A Higgs boson candidate event must have two same-flavour, opposite-sign leptons (electrons and muons) and a photon. Two steps of selection criteria are applied - firstly, loose selection is used for background estimation, followed

by applied tighter selection for the final results. For the photon selection an improved identification technique was applied which allowed to have higher signal efficiency in the low photon energy region and increased analysis sensitivity by 4%. For the leptons from the Z boson candidate the ones with the invariant mass closest to the Z pole are chosen, with the requirement that $|m_{\ell\ell} - m_Z|$ be less than 10 GeV. Additionally the Z boson candidates are Z-mass constrained and have FSR corrections applied that allow the Higgs boson mass resolution to be improved. Finally, the invariant mass of the Higgs boson candidates is retained between 115 and 170 GeV.

The Higgs boson invariant mass $m_{Z\gamma}$ can be used as an excellent discriminator between signal and background events. The signal includes all of the Higgs production modes (ggF, VBF, WH, ZH and ttH) and the background comes from the SM $Z\gamma$ and from the associated production Z+jets, where jets are misidentified by the detector as photons. In order to further improve signal-to-background separation and enhance sensitivity of the analysis a categorisation with an output of a multivariate discriminant is used. The strategy presented in this thesis exploits the Boosted Decision Tree multivariate method for categorisation, with additional categories based on kinematic characteristics of the Higgs boson candidates. $m_{Z\gamma}$ distribution for each of the categories is later parametrised with analytic functions. It is performed separately for signal and background shapes, where the choice of the function is determined from the modelling. A Double-Sided Crystal Ball function is chosen for the signal shape, and a variety of functions (exponential, Bernstein polynomial and power) are chosen to describe background, depending on the shape obtained in each category.

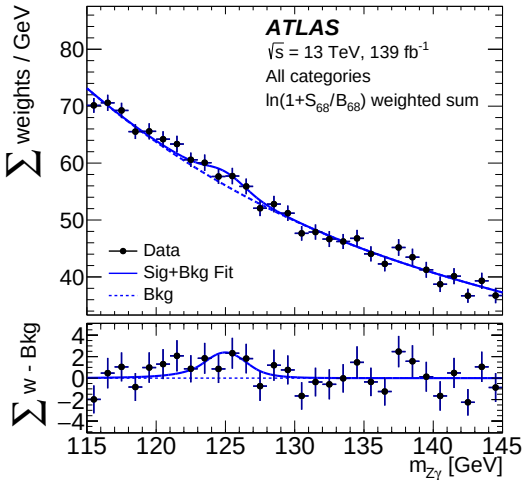

FIGURE S.1: The weighted $Z\gamma$ invariant mass $m_{Z\gamma}$ distribution. Events are weighted by $\ln(1 + S_{68}/B_{68})$, where S_{68} and B_{68} are the expected signal and background events in the $m_{Z\gamma}$ window, which contains 68% of the expected signal.

Finally, a maximum likelihood fit to data is performed for the category dependent $m_{Z\gamma}$ ranges. The weighted $m_{Z\gamma}$ distribution over all categories with the corresponding signal-plus-background fitting curve is shown in Figure S.1. No significant deviation from the background is found, the observed significance is 2.2 standard deviations, while the expected significance is 1.2 standard deviations. For a Higgs boson mass of 125.09 GeV, the observed 95% CL upper limit on the $\sigma(pp \to H) \cdot B(H \to Z\gamma)$ is 3.6 times the SM prediction. The expected limit on $\sigma(pp \to H) \cdot B(H \to Z\gamma)$ assuming no Higgs boson decay into $Z\gamma$ is 1.7 times the SM prediction, and 2.6 times the SM prediction in the presence of the SM Higgs boson decay. Currently results are still limited by the statistics, which can be improved with more data (around 3000 fb^{-1}) collected at the HL-LHC in the future.

Samenvatting

Dit proefschrift beschrijft de zoektocht naar het verval van het Higgs boson in een Z boson en een foton met de ATLAS detector bij de LHC versneller. De metingen zijn gedaan met data verzameld door ATLAS in de tweede run van de LHC (2015 tot en met 2018)

Het verval $H \to Z\gamma$ is een zeldzaam proces in het Standaard Model, met een kans van ongeveer 10^{-3}. Een extra complicatie is dat we alleen de leptonische eindtoestanden (elektron of muon) van het Z boson verval kunnen gebruiken, waardoor de uiteindelijke kans nog kleiner wordt:

$$B(H \to Z\gamma) \times B(Z \to ee/\mu\mu) \approx 10^{-4},$$

Het gebruik van alleen leptonische eindtoestanden maakt een kleine achtergrond mogelijk en zorgt voor een goede invariante massaresolutie. Een zoektocht naar het $H \to Z\gamma$-proces kan uitwijzen of de voorspellingen van het Standaard Model voor het Higgs-mechanisme correct zijn of op zijn minst licht werpen op het spectrum van Beyond Standard Model-theorieën als afwijkingen van de parameters worden gemeten. Er kunnen bijvoorbeeld verschillende vertakkingsverhoudingen optreden in modellen met extra geladen deeltjes vanwege hun bijdrage via luscorrecties.

De zoektocht naar het verval van Higgs-bosonen kan worden uitgevoerd dankzij deeltjesversnellers zoals de LHC en detectie is mogelijk met behulp van een universele detector zoals ATLAS. Het is essentieel voor een detector om zowel uitstekende meetprestaties als het vermogen tot reconstructie van de deeltjes te hebben. De analyse die in dit proefschrift wordt gepresenteerd, is gebaseerd op een nauwkeurige reconstructie van elektronen, muonen en fotonen, die wordt bereikt met de combinatie van drie hoofdsubdetectoren van ATLAS: de inner tracking detector, de calorimeter (elektromagnetisch en hadronisch) en de muonspectrometer. Meer details worden met name getoond voor de TRT-detector

Ik heb verschillende onderzoeken uitgevoerd naar de verbetering van de identificatie van geladen deeltjes met behulp van de hoge threshold van de front-end elektronica die het mogelijk maakt om TRT-hits van transitiestraling en ionisatie te onderscheiden. Vervolgens werden studies uitgevoerd, meestal in de elektromagnetische calorimeter, naar de reconstructie van fotonen met lage energie. Deze studies omvatten verbetering van de efficiëntie van identificatie en correctie van de simulatie om deze overeen te laten komen met echte data. Studies van de fotonidentificatie zijn van bijzonder belang voor de Higgs-bosonanalyse die in dit proefschrift wordt gepresenteerd, omdat ze hetzelfde spectrum van fotonenergieën gebruiken als in de $H \to Z\gamma$-analyse.

De zoektocht naar verval van het Higgs-deeltje naar een Z-boson en een foton gebruikt gegevens met een totale geïntegreerde luminositeit van 139 fb^{-1} aan

proton-proton botsingen bij een massamiddelpuntsenergie van 13 TeV. Een kandidaat botsing met het Higgs-deeltje moet twee leptonen van hetzelfde type (elektronen of muonen) met tegengestelde lading hebben en een foton. Er worden twee selectiestappen toegepast - eerst wordt een losse selectie gebruikt voor het schatten van de achtergrond, gevolgd door een strengere selectie voor de uiteindelijke meting. Voor de fotonselectie werd een verbeterde identificatietechniek toegepast die een hogere signaalefficiëntie in het lage fotonenergiegebied en een met 4% verhoogde analysegevoeligheid mogelijk maakte. Voor de leptonen van de kandidaat Z-boson worden de leptonen gekozen met de invariante massa het dichtst bij de Z-pool, met als eis dat $|m_{\ell\ell} - m_Z|$ kleiner is dan 10 GeV. Bovendien zijn wordt de Z-massa gebruikt om de gemeten massa te corrigeren en zijn er FSR-correcties toegepast waarmee de massa resolutie van de Higgs-boson kan worden verbeterd. Ten slotte blijven Higgs-boson kandidaten met een invariante massa tussen 115 en 170 GeV behouden.

De invariante massa $m_{Z\gamma}$ van het Higgs-deeltje is een uitstekende discriminator tussen signaal- en achtergrondgebeurtenissen. Het signaal omvat alle productiemodi van Higgs (ggF, VBF, WH, ZH en ttH) en de achtergrond is afkomstig van het SM $Z\gamma$ proces en van de productie van Z+jets, waar jets door de detector verkeerd worden geïdentificeerd als fotonen. Om de signaal-naar-achtergrondscheiding verder te verbeteren en de gevoeligheid van de analyse te vergroten, wordt een categorisering met een multivariate discriminant gebruikt. De strategie in dit proefschrift maakt gebruik van de Boosted Decision Tree multivariate methode voor categorisatie, met aanvullende categorieën gebaseerd op kinematische kenmerken van de Higgs-bosonkandidaten. De $m_{Z\gamma}$ distributie voor elk van de categorieën wordt later geparametriseerd met analytische functies. Dit wordt afzonderlijk voor signaal- en achtergrond gedaan, waarbij de keuze van de functie wordt bepaald uit de modellering. Een dubbelzijdige Crystal Ball functie is gekozen voor de signaalvorm, en diverse functies (exponentieel, Bernstein-polynoom en macht) worden gekozen, afhankelijk van de vorm in elke categorie, om de achtergrond te beschrijven,

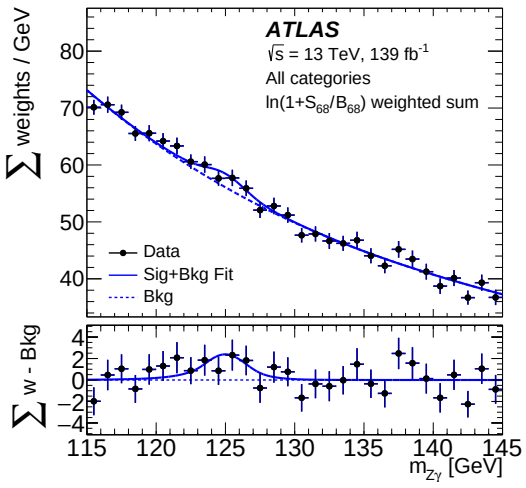

FIGURE S.1: De gewogen $Z\gamma$ invariante massa $m_{Z\gamma}$ verdeling. Het gewicht wordt gegeven door $\ln(1 + S_{68}/B_{68})$, met S_{68} en B_{68} het verwachtte signaal en achtergrond in het $m_{Z\gamma}$ interval, met 68% van het gesimuleerde signaal.

Ten slotte wordt een maximum-likelihood fit van de data uitgevoerd voor de categorieafhankelijke $m_{Z\gamma}$-intervallen. De gewogen $m_{Z\gamma}$ verdeling over alle categorieën met de bijbehorende signaal-plus-achtergrond curve wordt getoond in Figuur S.1. Er wordt geen significante afwijking van de achtergrond gevonden, de waargenomen significantie is 2,2 standaarddeviaties, terwijl de verwachte significantie 1,2 standaarddeviaties is. Voor een Higgs-bosonmassa van 125,09 GeV is de waargenomen 95% CL-bovengrens op de $\sigma(pp \to H) \cdot B(H \to Z\gamma)$ 3,6 keer de SM-voorspelling. De verwachte limiet op $\sigma(pp \to H) \cdot B(H \to Z\gamma)$ ervan uitgaande dat er geen verval van het Higgs-boson in $Z\gamma$ is, is 1,7 keer de SM-voorspelling en 2,6 keer de SM-voorspelling in de aanwezigheid van het verval van het SM Higgs-deeltje.

Momenteel worden de resultaten nog steeds beperkt door de statistische onzekerheid, die kan worden verbeterd met meer data. Ongeveer 3000 fb^{-1} zal in de toekomst bij de HL-LHC worden verzameld.

List of Figures

List of Tables

Bibliography

[1] ATLAS Collaboration, G. Aad et al., *Electron and photon performance measurements with the ATLAS detector using the 2015–2017 LHC proton-proton collision data*, JINST **14** no. 12, (2019) P12006, arXiv:1908.00005 [hep-ex].

[2] ATLAS Collaboration, G. Aad et al., *A search for the $Z\gamma$ decay mode of the Higgs boson in pp collisions at $\sqrt{s} = 13$ TeV with the ATLAS detector*, Phys. Lett. B **809** (2020) 135754, arXiv:2005.05382 [hep-ex].

[3] M. Y. Han and Y. Nambu, *Three-Triplet Model with Double* SU(3) *Symmetry*, Phys. Rev. **139** (1965) B1006–B1010, https://link.aps.org/doi/10.1103/PhysRev.139.B1006.

[4] L. B. Okun, *Leptons and Quarks*. North-Holland, Amsterdam, Netherlands, 1982. http://www.worldscientific.com/worldscibooks/10.1142/9162.

[5] M. E. Peskin and D. V. Schroeder, *An Introduction to quantum field theory*. Addison-Wesley, Reading, USA, 1995. http://www.slac.stanford.edu/~mpeskin/QFT.html.

[6] F. Mandl and G. Shaw, *Quantum Field Theory*. 1985. http://eu.wiley.com/WileyCDA/WileyTitle/productCd-0471496839.html.

[7] S. Glashow, *Partial Symmetries of Weak Interactions*, Nucl. Phys. **22** (1961) 579–588.

[8] S. Weinberg, *A Model of Leptons*, Phys. Rev. Lett. **19** (1967) 1264–1266, https://link.aps.org/doi/10.1103/PhysRevLett.19.1264.

[9] D. J. Gross and F. Wilczek, *Asymptotically Free Gauge Theories. I*, Phys. Rev. D **8** (1973) 3633–3652, https://link.aps.org/doi/10.1103/PhysRevD.8.3633.

[10] D. J. Gross and F. Wilczek, *Asymptotically free gauge theories. II*, Phys. Rev. D **9** (1974) 980–993, https://link.aps.org/doi/10.1103/PhysRevD.9.980.

[11] A. Purcell, *Go on a particle quest at the first CERN webfest. Le premier webfest du CERN se lance à la conquête des particules*, https://cds.cern.ch/record/1473657.

[12] G. A. et al., *Experimental observation of isolated large transverse energy electrons with associated missing energy at s=540 GeV*, Physics Letters B **122** no. 1, (1983) 103 – 116, http://www.sciencedirect.com/science/article/pii/0370269383911772.

[13] P. B. et al., *Evidence for Z0→e+e at the CERN pp collider*, Physics Letters B **129** no. 1, (1983) 130 – 140, http://www.sciencedirect.com/science/article/pii/037026938390744X.

[14] P. Higgs, *Broken symmetries, massless particles and gauge fields*, Physics Letters **12** no. 2, (1964) 132 – 133, http://www.sciencedirect.com/science/article/pii/0031916364911369.

[15] P. W. Higgs, *Broken Symmetries and the Masses of Gauge Bosons*, Phys. Rev. Lett. **13** (1964) 508–509, https://link.aps.org/doi/10.1103/PhysRevLett.13.508.

[16] P. W. Higgs, *Spontaneous Symmetry Breakdown without Massless Bosons*, Phys. Rev. **145** (1966) 1156–1163, https://link.aps.org/doi/10.1103/PhysRev.145.1156.

[17] F. Englert and R. Brout, *Broken Symmetry and the Mass of Gauge Vector Mesons*, Phys. Rev. Lett. **13** (1964) 321–323, https://link.aps.org/doi/10.1103/PhysRevLett.13.321.

[18] *The BEH-Mechanism, Interactions with Short Range Forces and Scalar Particles*, The Universe **1** no. 4, (2013) 55–71.

[19] LEP Working Group for Higgs boson searches, ALEPH, DELPHI, L3, OPAL Collaboration, R. Barate et al., *Search for the standard model Higgs boson at LEP*, Phys. Lett. B **565** (2003) 61–75, arXiv:hep-ex/0306033.

[20] CDF, D0 Collaboration,, *Combined CDF and D0 Upper Limits on Standard Model Higgs Boson Production with up to 8.6 fb^{-1} of Data*, 7, 2011. arXiv:1107.5518 [hep-ex].

[21] ATLAS Collaboration, G. Aad et al., *Observation of a new particle in the search for the Standard Model Higgs boson with the ATLAS detector at the LHC*, Phys. Lett. B **716** (2012) 1–29, arXiv:1207.7214 [hep-ex].

[22] S. C. et al., *Observation of a new boson at a mass of 125 GeV with the CMS experiment at the LHC*, Physics Letters B **716** no. 1, (2012) 30 – 61, http://www.sciencedirect.com/science/article/pii/S0370269312008581.

[23] ATLAS Collaboration, G. Aad et al., *Measurements of the Higgs boson inclusive and differential fiducial cross sections in the 4ℓ decay channel at $\sqrt{s}$ = 13 TeV*, Eur. Phys. J. C **80** no. 10, (2020) 942, arXiv:2004.03969 [hep-ex].

[24] CMS Collaboration, A. M. Sirunyan et al., *Measurements of production cross sections of the Higgs boson in the four-lepton final state in proton-proton collisions at $\sqrt{s} = 13$ TeV*, arXiv:2103.04956 [hep-ex].

[25] ATLAS, CMS Collaboration, G. Aad et al., *Combined Measurement of the Higgs Boson Mass in pp Collisions at $\sqrt{s} = 7$ and 8 TeV with the ATLAS and CMS Experiments*, Phys. Rev. Lett. **114** (2015) 191803, arXiv:1503.07589 [hep-ex].

[26] LHC Higgs Cross Section Working Group Collaboration, D. de Florian et al., *Handbook of LHC Higgs Cross Sections: 4. Deciphering the Nature of the Higgs Sector*, arXiv:1610.07922 [hep-ph].

[27] SNO Collaboration, Q. Ahmad et al., *Direct evidence for neutrino flavor transformation from neutral current interactions in the Sudbury Neutrino Observatory*, Phys. Rev. Lett. **89** (2002) 011301, arXiv:nucl-ex/0204008.

[28] Super-Kamiokande Collaboration, Y. Ashie et al., *Evidence for an oscillatory signature in atmospheric neutrino oscillation*, Phys. Rev. Lett. **93** (2004) 101801, arXiv:hep-ex/0404034.

[29] A. Riotto, *Theories of baryogenesis*, pp. , 326–436. 7, 1998. arXiv:hep-ph/9807454.

[30] M. Carena, I. Low, and C. E. Wagner, *Implications of a Modified Higgs to Diphoton Decay Width*, JHEP **08** (2012) 060, arXiv:1206.1082 [hep-ph].

[31] W. Altmannshofer, M. Bauer, and M. Carena, *Exotic Leptons: Higgs, Flavor and Collider Phenomenology*, JHEP **01** (2014) 060, arXiv:1308.1987 [hep-ph].

[32] C.-W. Chiang and K. Yagyu, *Higgs boson decays to $\gamma\gamma$ and $Z\gamma$ in models with Higgs extensions*, Phys. Rev. D **87** no. 3, (2013) 033003, arXiv:1207.1065 [hep-ph].

[33] G. Branco, P. Ferreira, L. Lavoura, M. Rebelo, M. Sher, and J. P. Silva, *Theory and phenomenology of two-Higgs-doublet models*, Phys. Rept. **516** (2012) 1–102, arXiv:1106.0034 [hep-ph].

[34] M. Sher, *Electroweak Higgs Potentials and Vacuum Stability*, Phys. Rept. **179** (1989) 273–418.

[35] T. P. Cheng and L.-F. Li, *Neutrino masses, mixings, and oscillations in SU(2)×U(1) models of electroweak interactions*, Phys. Rev. D **22** (1980) 2860–2868, https://link.aps.org/doi/10.1103/PhysRevD.22.2860.

[36] J. Schechter and J. Valle, *Neutrino Masses in SU(2) x U(1) Theories*, Phys. Rev. D **22** (1980) 2227.

[37] M. Aoki, S. Kanemura, and O. Seto, *Neutrino Mass, Dark Matter, and Baryon Asymmetry via TeV-Scale Physics without Fine-Tuning*, Phys. Rev. Lett. **102** (2009) 051805, https://link.aps.org/doi/10.1103/PhysRevLett.102.051805.

[38] A. Azatov, R. Contino, A. Di Iura, and J. Galloway, *New Prospects for Higgs Compositeness in $h \to Z\gamma$*, Phys. Rev. D **88** no. 7, (2013) 075019, arXiv:1308.2676 [hep-ph].

[39] L. Evans and P. Bryant, *LHC Machine*, JINST **3** (2008) S08001.

[40] ATLAS Collaboration, *The ATLAS experiment at the CERN Large Hadron Collider*, JINST **3** (2008) S08003.

[41] ATLAS Collaboration, *ATLAS Insertable B-Layer Technical Design Report*, Atlas-tdr-19, 2010, https://cds.cern.ch/record/1291633.

[42] CMS Collaboration, *CMS Physics Technical Design Report, Volume II: Physics Performance*, J. Phys G **34** (2007) 995.

[43] LHCb Collaboration Collaboration, O. Steinkamp, *LHCb Upgrades*, J.Phys.Conf.Ser. **1271** no. LHCb-PROC-2019-007. CERN-LHCb-PROC-2019-007. 1, (2019) 012010. 10 p, https://cds.cern.ch/record/2686662.

[44] T. A. Collaboration, *The ATLAS Experiment at the CERN Large Hadron Collider*, Journal of Instrumentation **3** no. 08, (2008) S08003–S08003, https://doi.org/10.1088/1748-0221/3/08/s08003.

[45] ALICE Collaboration Collaboration, K. e. a. Aamodt, *The ALICE experiment at the CERN LHC. A Large Ion Collider Experiment*, JINST **3** (2008) S08002. 259 p, https://cds.cern.ch/record/1129812, Also published by CERN Geneva in 2010.

[46] ATLAS Collaboration Collaboration,, *ATLAS liquid-argon calorimeter: Technical Design Report*. Technical Design Report ATLAS. CERN, Geneva, 1996. https://cds.cern.ch/record/331061.

[47] ATLAS Collaboration Collaboration,, *ATLAS calorimeter performance: Technical Design Report*. Technical Design Report ATLAS. CERN, Geneva, 1996. https://cds.cern.ch/record/331059.

[48] ATLAS Collaboration, G. Aad et al., *Muon reconstruction performance of the ATLAS detector in proton–proton collision data at $\sqrt{s}$ =13 TeV*, Eur. Phys. J. C **76** no. 5, (2016) 292, arXiv:1603.05598 [hep-ex].

[49] A. Collaboration, *Technical Design Report for the ATLAS Inner Tracker Pixel Detector*, Tech. Rep. CERN-LHCC-2017-021. ATLAS-TDR-030, CERN, Geneva, Sep, 2017. https://cds.cern.ch/record/2285585.

[50] ATLAS Collaboration Collaboration, ATLAS Collaboration, *Operation and performance of the ATLAS semiconductor tracker. Operation and performance of the ATLAS semiconductor tracker*, JINST **9** no. CERN-PH-EP-2014-049. CERN-PH-EP-2014-049, (2014) P08009. 80 p, https://cds.cern.ch/record/1698966, Comments: 60 pages plus author list (80 pages total), 33 figures, 10 tables, submitted to JINST. All figures are available at http://atlas.web.cern.ch/Atlas/GROUPS/PHYSICS/PAPERS/IDET-2013-01/ v2: replaced unreadable labels in Fig. 2.

[51] ATLAS TRT Collaboration, E. Abat et al., *The ATLAS Transition Radiation Tracker (TRT) proportional drift tube: Design and performance*, JINST **3** (2008) P02013.

[52] ATLAS Collaboration, Y. Takubo, *ATLAS IBL operational experience*, PoS **Vertex2016** (2017) 004.

[53] M. C. Aleksa, W. P. Cleland, Y. T. Enari, M. V. Fincke-Keeler, L. C. Hervas, F. B. Lanni, S. O. Majewski, C. V. Marino, and I. L. Wingerter-Seez, *ATLAS Liquid Argon Calorimeter Phase-I Upgrade Technical Design Report*, Tech. Rep. CERN-LHCC-2013-017. ATLAS-TDR-022, Sep, 2013. https://cds.cern.ch/record/1602230. Final version presented to December 2013 LHCC.

[54] ATLAS Collaboration Collaboration„ *ATLAS tile calorimeter: Technical Design Report*. Technical Design Report ATLAS. CERN, Geneva, 1996. https://cds.cern.ch/record/331062.

[55] ATLAS Collaboration, *The ATLAS Experiment at the CERN Large Hadron Collider*, JINST **3** (2008) S08003.

[56] ATLAS Collaboration, *Performance of the ATLAS Trigger System in 2015*, Eur. Phys. J. C **77** (2017) 317, arXiv:1611.09661 [hep-ex].

[57] R. Brun and F. Rademakers, *ROOT: An object oriented data analysis framework*, Nucl. Instrum. Meth. **A389** (1997) 81–86.

[58] ATLAS Collaboration Collaboration„ *Particle Identification Performance of the ATLAS Transition Radiation Tracker*, Tech. Rep. ATLAS-CONF-2011-128, CERN, Geneva, Sep, 2011. http://cds.cern.ch/record/1383793.

[59] ATLAS Collaboration, G. Aad et al., *Search for stable hadronising squarks and gluinos with the ATLAS experiment at the LHC*, Phys. Lett. B **701** (2011) 1–19, arXiv:1103.1984 [hep-ex].

[60] E. Abat et al., *The ATLAS TRT electronics*, JINST **3** (2008) P06007.

[61] P. Cwetanski, *Straw Performance Studies and Quality Assurance for the ATLAS Transition Radiation Tracker*, 2006. https://cds.cern.ch/record/962570. Presented on 22 Jun 2006.

[62] Particle Data Group, K. Nakamura, et al., *Review of Particle Physics*, J. Phys. G **37** (2010) 075021, http://pdg.lbl.gov.

[63] S. Zimmermann, *A search for stable massive particles carrying electric charges in the range of 2e to 6e in proton-proton collisions at $\sqrt{s} = 7$ TeV recorded with the ATLAS detector at the LHC*, Apr, 2013. https://cds.cern.ch/record/1595729. Presented 11 Jun 2013.

[64] W. Blum, W. Riegler, and L. Rolandi, *Particle detection with drift chambers; 2nd ed.* Springer, Berlin, 2008. https://cds.cern.ch/record/1105920.

[65] K. Choi and H. Evans, *TRT high threshold middle bit tuning*, Tech. Rep. ATL-COM-INDET-2015-059, CERN, Geneva, Sep, 2015. https://cds.cern.ch/record/2048151.

[66] N. Belyaev, *TRT PID tool development and optimization*, Tech. Rep. ATL-COM-INDET-2015-080, CERN, Geneva, Oct, 2015. https://cds.cern.ch/record/2064398.

[67] ATLAS Collaboration Collaboration„ *Calibration of the ATLAS Transition Radiation Tracker*, Tech. Rep. ATLAS-CONF-2011-006, CERN, Geneva, Feb, 2011. https://cds.cern.ch/record/1330712.

[68] W. Lampl, S. Laplace, D. Lelas, P. Loch, H. Ma, S. Menke, S. Rajagopalan, D. Rousseau, S. Snyder, and G. Unal, *Calorimeter Clustering Algorithms: Description and Performance*, Tech. Rep. ATL-LARG-PUB-2008-002. ATL-COM-LARG-2008-003, CERN, Geneva, Apr, 2008. https://cds.cern.ch/record/1099735.

[69] W. Lampl et al., *Calorimeter Clustering Algorithms: Description and Performance*, ATL-LARG-PUB-2008-002, 2008, https://cds.cern.ch/record/1099735.

[70] ATLAS Collaboration, *Electron reconstruction and identification in the ATLAS experiment using the 2015 and 2016 LHC proton–proton collision data at* $\sqrt{s} =$ 13 *TeV*, Eur. Phys. J. (2019), arXiv:1902.04655 [hep-ex].

[71] ATLAS Collaboration, *Measurement of the photon identification efficiencies with the ATLAS detector using LHC Run 2 data collected in 2015 and 2016*, Eur. Phys. J. C **79** no. 3, (2019) 205, arXiv:1810.05087 [hep-ex].

[72] R. Frühwirth, *Application of Kalman filtering to track and vertex fitting*, Nuclear Instruments and Methods in Physics Research Section A: Accelerators, Spectrometers, Detectors and Associated Equipment **262** no. 2, (1987) 444 – 450, http://www.sciencedirect.com/science/article/pii/0168900287908874.

[73] T. G. Cornelissen, M. Elsing, I. Gavrilenko, J.-F. Laporte, W. Liebig, M. Limper, K. Nikolopoulos, A. Poppleton, and A. Salzburger, *The global 2track fitter in ATLAS*, Journal of Physics: Conference Series **119** no. 3, (2008) 032013, https://doi.org/10.1088%2F1742-6596%2F119%2F3%2F032013.

[74] ATLAS Collaboration Collaboration,, *Improved electron reconstruction in ATLAS using the Gaussian Sum Filter-based model for bremsstrahlung*, Tech. Rep. ATLAS-CONF-2012-047, CERN, Geneva, May, 2012. https://cds.cern.ch/record/1449796.

[75] ATLAS Collaboration, *Topological cell clustering in the ATLAS calorimeters and its performance in LHC Run 1*, Eur. Phys. J. **C77** (2017) 490, arXiv:1603.02934 [hep-ex].

[76] K. Mistry, M. Fanti, Y. Huang, H. Williams, N. Berger, M. Delmastro, and K. Brendlinger, *Data-MC shower shape comparisons: Supporting documentation for the Photon identification in 2015 and 2016 ATLAS data*, Tech. Rep. ATL-COM-PHYS-2017-363, CERN, Geneva, Apr, 2017. https://cds.cern.ch/record/2258832.

[77] ATLAS Collaboration, *Electron and photon energy calibration with the ATLAS detector using 2015–2016 LHC proton–proton collision data*, JINST **14** (2019) P03017, arXiv:1812.03848 [hep-ex].

[78] A. Hocker et al., *TMVA - Toolkit for Multivariate Data Analysis*, arXiv:physics/0703039 [physics.data-an].

[79] ATLAS Collaboration, *Muon reconstruction performance of the ATLAS detector in proton–proton collision data at* $\sqrt{s} = 13$ *TeV*, Eur. Phys. J. C **76** (2016) 292, arXiv:1603.05598 [hep-ex].

[80] M. Cacciari, G. P. Salam, and G. Soyez, *The anti-k_t jet clustering algorithm*, JHEP **04** (2008) 063, arXiv:0802.1189 [hep-ph].

[81] ATLAS Collaboration, *Jet energy measurement and its systematic uncertainty in proton–proton collisions at* $\sqrt{s} = 7$ *TeV with the ATLAS detector*, Eur. Phys. J. **C75** (2015) 17, arXiv:1406.0076 [hep-ex].

[82] ATLAS Collaboration, *Selection of jets produced in* 13 *TeV proton–proton collisions with the ATLAS detector*, ATLAS-CONF-2015-029, 2015, https://cds.cern.ch/record/2037702.

[83] ATLAS Collaboration, *Tagging and suppression of pileup jets with the ATLAS detector*, ATLAS-CONF-2014-018, 2014, https://cds.cern.ch/record/1700870.

[84] ATLAS Collaboration Collaboration, ATLAS Collaboration, *Measurement of the photon identification efficiencies with the ATLAS detector using LHC Run 2 data collected in 2015 and 2016*, Tech. Rep. arXiv:1810.05087, CERN, Geneva, Oct, 2018. https://cds.cern.ch/record/2643391. * Temporary entry *.

[85] ATLAS and CMS Collaborations, *Combined Measurement of the Higgs Boson Mass in pp Collisions at $\sqrt{s} = 7$ and 8 TeV with the ATLAS and CMS Experiments*, Phys. Rev. Lett. **114** (2015) 191803, arXiv:1503.07589 [hep-ex].

[86] ATLAS Collaboration, *Measurement of the Higgs boson mass in the $H \to ZZ^* \to 4\ell$ and $H \to \gamma\gamma$ channels with $\sqrt{s} = 13$ TeV pp collisions using the ATLAS detector*, Phys. Lett. B **784** (2018) 345, arXiv:1806.00242 [hep-ex].

[87] CMS Collaboration, *Measurements of properties of the Higgs boson decaying into the four-lepton final state in pp collisions at $\sqrt{s} = 13$ TeV*, JHEP **11** (2017) 047, arXiv:1706.09936 [hep-ex].

[88] CMS Collaboration, *A measurement of the Higgs boson mass in the diphoton decay channel*, Phys. Lett. B **805** (2020) 135425, arXiv:2002.06398 [hep-ex].

[89] ATLAS Collaboration, G. Aad et al., *Search for Higgs boson decays to a photon and a Z boson in pp collisions at $\sqrt{s}$=7 and 8 TeV with the ATLAS detector*, Phys. Lett. **B732** (2014) 8–27, arXiv:1402.3051 [hep-ex].

[90] ATLAS Collaboration, M. Aaboud et al., *Searches for the $Z\gamma$ decay mode of the Higgs boson and for new high-mass resonances in pp collisions at $\sqrt{s} = 13$ TeV with the ATLAS detector*, JHEP **10** (2017) 112, arXiv:1708.00212 [hep-ex].

[91] ATLAS Collaboration, *The ATLAS simulation infrastructure*, Eur. Phys. J. C **70** (2010) 823–874, arXiv:1005.4568 [physics.ins-det].

[92] GEANT4 Collaboration, S. Agostinelli et al., *GEANT4 - a simulation toolkit*, Nucl. Instrum. Methods A **506** (2003) 250.

[93] P. Nason and C. Oleari, *NLO Higgs boson production via vector-boson fusion matched with shower in POWHEG*, JHEP **02** (2010) 037, arXiv:0911.5299 [hep-ph].

[94] S. Alioli, P. Nason, C. Oleari, and E. Re, *A general framework for implementing NLO calculations in shower Monte Carlo programs: the POWHEG BOX*, JHEP **06** (2010) 043, arXiv:1002.2581 [hep-ph], (using ATLAS svn revisions r2856 for v1, r3080 for v2 ggF, r3052 for v2 VBF, and r3133 for v2 VH).

[95] P. Nason, *A new method for combining NLO QCD with shower Monte Carlo algorithms*, JHEP **11** (2004) 040, arXiv:hep-ph/0409146.

[96] S. Frixione, P. Nason, and C. Oleari, *Matching NLO QCD computations with Parton Shower simulations: the POWHEG method*, JHEP **11** (2007) 070, arXiv:0709.2092 [hep-ph].

[97] H. B. Hartanto, B. Jager, L. Reina, and D. Wackeroth, *Higgs boson production in association with top quarks in the POWHEG BOX*, Phys. Rev. **D91** no. 9, (2015) 094003, arXiv:1501.04498 [hep-ph].

[98] T. Sjöstrand, S. Mrenna, and P. Skands, *A brief introduction to PYTHIA 8.1*, Comput. Phys. Commun. **178** (2008) 852–867, arXiv:0710.3820 [hep-ph].

[99] J. Alwall, R. Frederix, S. Frixione, V. Hirschi, F. Maltoni, O. Mattelaer, H. S. Shao, T. Stelzer, P. Torrielli, and M. Zaro, *The automated computation of tree-level and next-to-leading order differential cross sections, and their matching to parton shower simulations*, JHEP **07** (2014) 079, arXiv:1405.0301 [hep-ph].

[100] J. Butterworth et al., *PDF4LHC recommendations for LHC Run II*, J. Phys G **43** (2016) 023001, arXiv:1510.03865 [hep-ph].

[101] NNPDF Collaboration, R. D. Ball et al., *Parton distributions for the LHC Run II*, JHEP **04** (2015) 040, arXiv:1410.8849 [hep-ph].

[102] R. Frederix and S. Frixione, *Merging meets matching in MC@NLO*, JHEP **12** (2012) 061, arXiv:1209.6215 [hep-ph].

[103] Long-Bin Chen, Cong-Feng Qiao, Rui-Lin Zhu, *Reconstructing the 125 GeV SM Higgs boson through $l\bar{l}\gamma$*, Phys. Lett. B **726** (2013) 306, arXiv:1211.6058 [hep-ph].

[104] E. Bothmann et al., *Event Generation with Sherpa 2.2*, SciPost Phys. **7** (2019) 034, arXiv:1905.09127 [hep-ph].

[105] ATLAS Collaboration, *The simulation principle and performance of the ATLAS fast calorimeter simulation FastCaloSim*, ATL-PHYS-PUB-2010-013 (2010), https://cds.cern.ch/record/1300517.

[106] ATLAS Collaboration, ATLAS Collaboration, *Measurements of Higgs boson production and couplings in the four-lepton channel in pp collisions at center-of-mass energies of 7 and 8 TeV with the ATLAS detector*, Phys. Rev. D **91** no. 1, (2015) 012006, arXiv:1408.5191 [hep-ex].

[107] ATLAS Collaboration, *Higgs boson production cross-section measurements and their EFT interpretation in the 4ℓ decay channel at $\sqrt{s} = 13$ TeV with the ATLAS detector*, CERN-EP-2020-034 (2020), arXiv:2004.03447 [hep-ex].

[108] A. Hoecker, P. Speckmayer, J. Stelzer, J. Therhaag, E. von Toerne, H. Voss, *TMVA - Toolkit for Multivariate Data Analysis*, Tech. Rep. CERN-OPEN-2007-007, CERN, Geneva, Jul, 2009. https://arxiv.org/abs/physics/0703039.

[109] G. Cowan, K. Cranmer, E. Gross, and O. Vitells, *Asymptotic formulae for likelihood-based tests of new physics*, Eur. Phys. J. **C71** (2011) 1554, arXiv:1007.1727 [physics.data-an], [Erratum: Eur. Phys. J. C **73** (2013) 2501].

[110] ATLAS Collaboration Collaboration,, *Luminosity determination in pp collisions at $\sqrt{s} = 13$ TeV using the ATLAS detector at the LHC*, Tech. Rep. ATLAS-CONF-2019-021, CERN, Geneva, Jun, 2019. https://cds.cern.ch/record/2677054.

[111] G. Avoni et al., *The new LUCID-2 detector for luminosity measurement and monitoring in ATLAS*, JINST **13** no. 07, (2018) P07017.

[112] ATLAS Collaboration, *Search for the Dimuon Decay of the Higgs Boson in pp Collisions at $\sqrt{s} = 13$ TeV with the ATLAS Detector*, Phys. Rev. Lett. **119** (2017) 051802, arXiv:1705.04582 [hep-ex].

[113] I. W. Stewart and F. J. Tackmann, *Theory uncertainties for Higgs and other searches using jet bins*, Phys. Rev. D **85** (2012) 034011, arXiv:1107.2117 [hep-ph].

[114] J. M. Campbell and R. K. Ellis, *MCFM for the Tevatron and the LHC*, Nucl. Phys. Proc. Suppl. **205-206** (2010) 10–15, arXiv:1007.3492 [hep-ph].

[115] S. Gangal and F. J. Tackmann, *Next-to-leading-order uncertainties in Higgs+2 jets from gluon fusion*, Phys. Rev. D **87** no. 9, (2013) 093008, arXiv:1302.5437 [hep-ph].

[116] M. Grazzini and H. Sargsyan, *Heavy-quark mass effects in Higgs boson production at the LHC*, JHEP **09** (2013) 129, arXiv:1306.4581 [hep-ph].

[117] ATLAS Collaboration, *Measurements of Higgs boson properties in the diphoton decay channel with 36 fb^{-1} of pp collision data at $\sqrt{s} = 13$ TeV with the ATLAS detector*, Phys. Rev. D **98** (2018) 052005, arXiv:1802.04146 [hep-ex].

[118] ATLAS Collaboration, *Search for the $Z\gamma$ decay mode of the Higgs boson and for new high-mass resonances in pp collisions at $\sqrt{s} = 13$ TeV with the ATLAS detector*, JHEP **10** (2017) 112, arXiv:1708.00212 [hep-ex].

[119] A. L. Read, *Presentation of search results: The CL_s technique*, J. Phys. G: Nucl. Part. Phys. **28** (2002) 2693.

[120] *Projections for measurements of Higgs boson signal strengths and coupling parameters with the ATLAS detector at a HL-LHC*, Tech. Rep. ATL-PHYS-PUB-2014-016, CERN, Geneva, Oct, 2014. https://cds.cern.ch/record/1956710.

[121] *Update of the prospects for the $H \to Z$ search at the High-Luminosity LHC*, Tech. Rep. ATL-PHYS-PUB-2014-006, CERN, Geneva, May, 2014. https://cds.cern.ch/record/1703276.

Acknowledgements

This thesis has been an immense and challenging journey, it's hard to believe, but it has taken six years to arrive at the finish line. In this text, I wish to sincerely thank each person who has offered me support, encouragement and guidance along the way.

First and foremost, I would like to thank my supervisors, Prof. Nicolo de Groot and Prof. Anatoli Romaniouk for offering me the unique opportunity to pursue a PhD at MEPhI and Radboud University. I'm so grateful for the time they dedicated to setting me on my path and for their careful guidance during the early years of my PhD candidacy. For the final year of my PhD, I'd like to thank them for their encouragement and precious advice in helping me to complete this manuscript.

I would also wish to express my appreciation and thanks to Dr. Tulay Cuhadar Donszelmann, who took care of me and introduced me to the Higgs analysis during my first years in the group. She guided my progress with her great knowledge and support, it was a wonderful experience to share an office with her. I'd also like to thank Frank Filthaut for helping me settle in at Radboud University and CERN, thank you for believing in me and for the brilliant conversations about physics and life.

Thank you to my manuscript committee, Prof. Sijbrand de Jong, Prof. Maxim Khlopov, Dr. Evgeny Soldatov, Prof. Thomas Peitzmann, Dr. Hella Snoek for offering their time to review my thesis, for their careful reading and helpful comments.

I would like to thank again Dr. Evgeny Soldatov for his tremendous support throughout the entirety of this journey and extending back to my years as a bachelor student. I've learnt a lot in physics from him, and I feel very fortunate that he was my very first advisor. Thank you to Dr. Dimitrii Krasnopevtsev for the useful conversations we had over the years, for all the evenings when he helped me find errors in my code and for his patience and kindness during my struggles as I began my journey in data analysis.

Thank you to all of my TRT colleagues, especially to KyungEon Choi for being an amazing guide in the world of TRT software, Eleni Skorda for the fun discussions about TRT and Sweden, Dominik Derendarz, Fred Luehring, Christian Grefe, Peter Hansen, Shion Chen and Kostya Zhukov. Traditional pizza outings in pre-COVID days remains one of the most heartwarming experiences I've had.

Thanks to everyone from E/Gamma group for your kindness, the countless hours of collaboration and for the wonderful ambience and humour during the occasional waves of strict deadlines: Giovanni Marchiori, Nicolas Berger, Heberth Torres, Marcello Fanti, Ximo Poveda and Frued Braren.

I would like to express my appreciation to my colleagues of MEPhI and Radboud University: Nikita, Nastya, Misha, Veronica, Fabrizia, Jeroen, Wouter, Alex. It's been a pleasure to share life at CERN with each of you - I shall miss our lunch dates and

pizza evenings a great deal. Thanks to my office mate Carlo Gottardo for our coffee breaks, physics discussions and chats about life, it's been a pleasure getting to know you. A very special thanks to my previous office mate Tom Powell for the fantastic atmosphere he created, for our numerous adventures throughout Switzerland, for being a wonderful hiking companion and of course for his patience in reading this thesis for grammar.

Thanks to Anastasia Berdnikova and Ruslan Mashinistov for becoming my dear friends and for helping me through the challenging periods of COVID lockdowns. I would like to express my appreciation and thanks to Tatiana Ovsiannikova for being such a great friend and always believing in me, even when I didn't believe myself. Last but certainly not least I would like to thank Daniil Ponomarenko for being the best friend I could ever wish for. Life is often difficult, but we will get through everything.

Finally, I would like to thank my darling mother, father and sister who have supported me throughout my whole life and showed me how to be me.